



Forschungszentrum Karlsruhe
in der Helmholtz-Gemeinschaft

Wissenschaftliche Berichte
FZKA 7419

The LIVE-L1 and LIVE-L3 Experiments on Melt Behaviour in RPV Lower Head

**B. Fluhrer, A. Miassoedov, T. Cron, J. Foit,
X. Gaus-Liu, S. Schmidt-Stiefel, T. Wenz,
I. Ivanov, D. Popov**

**Institut für Kern- und Energietechnik
Programm Nukleare Sicherheitsforschung**

September 2008

Forschungszentrum Karlsruhe

in der Helmholtz-Gemeinschaft

Wissenschaftliche Berichte

FZKA 7419

The LIVE-L1 and LIVE-L3 Experiments on Melt Behaviour in RPV Lower Head

B. Fluhrer, A. Miassoedov, T. Cron, J. Foit, X. Gaus-Liu,
S. Schmidt-Stiefel, T. Wenz,
I. Ivanov¹, D. Popov²

Institut für Kern- und Energietechnik
Programm Nukleare Sicherheitsforschung

¹Technical University of Sofia, Bulgaria

²Kozloduy NPP, Bulgaria

Forschungszentrum Karlsruhe GmbH, Karlsruhe

2008

Für diesen Bericht behalten wir uns alle Rechte vor

Forschungszentrum Karlsruhe GmbH
Postfach 3640, 76021 Karlsruhe

Mitglied der Hermann von Helmholtz-Gemeinschaft
Deutscher Forschungszentren (HGF)

ISSN 0947-8620

urn:nbn:de:0005-074196

Abstract

The sequence of a postulated core melt down accident in the reactor pressure vessel (RPV) of a pressurised water reactor (PWR) involves a large number of complex physical and chemical phenomena. To improve the understanding of possible scenarios of core melt down accidents with core degradation, melt pool formation and relocation in the RPV, possible melt dispersion to the reactor cavity and finally corium concrete interaction and corium coolability in the reactor cavity, the LACOMERA project at the Forschungszentrum Karlsruhe was started in September 2002. The LACOMERA project was a four year action within the 5th Framework programme of the EU and offered research institutions from the EU member Countries and Associated States access to the four large-scale experimental facilities QUENCH, LIVE, DISCO and COMET at the Forschungszentrum Karlsruhe.

Within the LIVE experimental programme two experiments (LIVE-L1 and LIVE-L2) have been performed within the LACOMERA project. The experiment LIVE-L1 is part of this report and was planned and performed in close co-operation with the Technical University Sofia, Bulgaria and the Kozloduy NPP, Bulgaria.

The main objective of the LIVE program is to study the core melt phenomena during the late phase of core melt progression in the RPV both experimentally in large-scale 3D geometry and in supporting separate-effects tests, and analytically using CFD codes in order to provide a reasonable estimate of the remaining uncertainty band under the aspect of safety assessment.

The experiments LIVE-L1 and LIVE-L3 are aimed at investigating the melt pool and crust behaviour during the stages of air circulation at the outer RPV surface with subsequent flooding of the lower head. The initial and boundary conditions in both tests were almost the same except of the pouring position of the melt into the test vessel. In LIVE-L1 the melt was poured in central position and in LIVE-L3 the melt was poured near to the wall of the test vessel. The information obtained in these experiments includes heat flux distribution through the RPV wall in transient and steady state conditions, crust growth velocity and dependence of the crust formation on the heat flux distribution. Supporting post-test analysis contributes to the characterization of solidification processes of binary non-eutectic melts.

The experimental results are being used for the development of mechanistic models to describe the in-core molten pool behaviour, which should then be implemented in severe accident codes like ASTEC.

The present report summarizes the objectives of the LIVE program and presents the main results obtained in the experiments LIVE-L1 and LIVE-L3.

Zusammenfassung

Die Experimente LIVE-L1 und LIVE-L3 zum Schmelzenverhalten im unteren Plenum des RDB

Der Ablauf eines hypothetischen Kernschmelzunfalls in einem Reaktordruckbehälter (RDB) eines Druckwasserreaktors (DWR) beinhaltet eine große Anzahl komplexer physikalischer und chemischer Phänomene. Um das Verständnis über mögliche Ablaufszenarien von Kernschmelzunfällen bezüglich Kernzerstörung zu verbessern, wurde im September 2002 das LACOMERA Projekt am Forschungszentrum Karlsruhe gestartet. Das Ziel des Projektes war die Untersuchung von komplexen Prozessen während der Schmelzenseebildung und Verlagerung im RDB, Schmelzenausbreitung in die Reaktorgrube und Kernschmelze-Betonwechselwirkung und -Kühlung. Das LACOMERA Projekt mit einer Laufzeit von 4 Jahren war Bestandteil des 5. Rahmenprogramms der EU und eröffnete Forschungseinrichtungen der EU Mitgliedsländer und deren angegliederten Staaten den Zugang zu vier Großversuchsanlagen QUENCH, LIVE, DISCO und COMET am Forschungszentrum Karlsruhe.

Innerhalb des LIVE Versuchsprogramms wurden zwei Versuche (LIVE-L1 und LIVE-L2) des LACOMERA Projekts durchgeführt. Das Experiment LIVE-L1 ist Bestandteil dieses Berichts und wurde in Kooperation mit der Technischen Universität Sofia, Bulgarien und dem Kernkraftwerk Kozloduy NPP, Bulgarien geplant und durchgeführt.

Das Hauptziel des LIVE Programms ist es, das Verhalten der Kernschmelze während der späten Phase der Kernzerstörung und –Verlagerung im RDB sowohl experimentell in großem 3-dimensionalen Maßstab und in begleitenden Einzeleffektuntersuchungen als auch analytisch mit CFD Codes zu untersuchen. Dadurch soll eine bessere Einschätzung der Bandbreite der verbleibenden Unsicherheiten unter dem Aspekt der Sicherheitsbewertung ermöglicht werden.

Die Experimente LIVE-L1 und LIVE-L3 untersuchen das Verhalten eines Schmelzensees und einer Schmelzenkruste mit Luftzirkulation an der äußeren Behälterwand des RDB mit nachfolgender Außenflutung des unteren Plenums. Die Anfangs- und Randbedingungen in beiden Versuchen waren bis auf die Eingussposition der Schmelze in den Versuchsbehälter fast identisch. In LIVE-L1 wurde die Schmelze zentral und in LIVE-L3 am Rand in den Versuchsbehälter eingegossen. Die aus den Experimenten gewonnenen Informationen beinhalten Wärmestromverteilungen durch die Wand des RDB in transienten und stationären Versuchsphasen, Krustenwachstumsgeschwindigkeit und die Abhängigkeit der Krustenbildung von der Wärmestromverteilung. Detaillierte Nachuntersuchungen tragen außerdem zur Charakterisierung von Erstarrungsprozessen von nicht-eutektischen Schmelzen bei.

Die experimentellen Ergebnisse sollen weiterhin zur Entwicklung von mechanistischen Modellen verwendet werden, die das Schmelzenseeverhalten im Kern beschreiben sollen und

dann in Systemcodes zur Analyse von schweren Störfällen wie z.B. ASTEC implementiert werden sollen.

Der vorliegende Bericht fasst die Ziele des LIVE Versuchsprogramms zusammen und präsentiert die wichtigen Ergebnisse der Experimente LIVE-L1 und LIVE-L3.

TABLE OF CONTENTS

1	Introduction.....	1
1.1	LIVE as element of the LACOMERA project	1
1.2	Background and objectives of LIVE-L1 and LIVE-L3.....	2
2	LIVE-L1 and LIVE-L3 test design	3
2.1	Test facility description	3
2.2	Melt composition and melt generation	6
2.2.1	Selection of simulant materials	6
2.2.2	Melt composition, preparation and generation.....	7
2.3	Decay heat simulation	8
2.4	Instrumentation and data acquisition	10
3	Progression and test results of LIVE-L1	14
3.1	Preparation and performance of LIVE-L1	14
3.2	Experimental results of LIVE-L1	18
3.2.1	Mass and initial temperature of the melt in LIVE-L1	18
3.2.2	Decay heat simulation in LIVE-L1	19
3.2.3	Melt behaviour in LIVE-L1	20
3.2.4	Heat balance and heat flux in LIVE-L1	23
3.2.4.1	Heat balance at steady state in LIVE-L1	23
3.2.4.2	Heat flux measured by heat flux sensors in LIVE-L1	26
3.2.4.3	Calculated heat fluxes in LIVE-L1	28
3.2.5	Melt surface behaviour in LIVE-L1	33
3.2.6	Post-test analysis in LIVE-L1	34
3.2.6.1	Average melt composition in LIVE-L1	34
3.2.6.2	Crust growth rate in LIVE-L1	35
3.2.6.3	Crust morphology and microstructure in LIVE-L1	40
3.2.6.4	Crust liquidus temperature and crust composition in LIVE-L1	43
3.2.6.5	Crust porosity and crust thermal conductivity in LIVE-L1	47
4	Progression and test results of LIVE-L3.....	50
4.1	Preparation and performance of LIVE-L3	50
4.2	LIVE-L3 test results	56
4.2.1	Mass and initial temperature of the melt in LIVE-L3	56
4.2.2	Decay heat simulation in LIVE-L3.....	57
4.2.3	Melt behaviour in LIVE-L3	58
4.2.4	Heat balance and heat flux in LIVE-L3	60

4.2.4.1	Heat balance at steady state in LIVE-L3.....	60
4.2.4.2	Heat flux measured by heat flux sensors in LIVE-L3	61
4.2.4.3	Calculated heat fluxes in LIVE-L3	63
4.2.4.4	Comparison of the calculated heat fluxes with the measured heat fluxes by the heat flux sensors in LIVE-L3	66
4.2.5	Melt surface behaviour	68
4.2.6	Post-test analysis in LIVE-L3.....	72
4.2.6.1	Average composition of the melt in LIVE-L3	73
4.2.6.2	Crust growth rate in LIVE-L3.....	74
4.2.6.3	Crust morphology in LIVE-L3	78
4.2.6.4	Crust liquidus temperature and crust composition in LIVE-L3	80
4.2.6.5	Crust porosity and crust thermal conductivity in LIVE-L3.....	81
5	Conclusions from the experiments	84
6	References	86
Annex A	Data Acquisition and Instrumentation	88
Annex A.1	LIVE-L1 and LIVE-L3 channel assignments	88
Annex A.2	Drawings of the instrumentation of the LIVE test vessel.....	102
Annex B	Test initial conditions and main parameters	108
Annex C	Test data.....	110
Annex C.1	Test data of LIVE-L1	110
Annex C.2	Test data of LIVE-L3	120

LIST OF TABLES

Table 1: Melt characteristics and preparation	8
Table 2: Characteristics of the LIVE heating system.....	10
Table 3: Test parameter and test phases of the experiment LIVE-L1	14
Table 4: Course of the experiment LIVE-L1	17
Table 5: Geometries of the heat flux zones.....	24
Table 6: Heat balance between the heat transfer through vessel wall and heating power	25
Table 7: Transient and steady state heat fluxes measured by heat flux sensors in LIVE-L1 .	27
Table 8: Heat flux form correction factor for spherical form and wall thickness	28
Table 9: Heat conductivity of AISI316Ti	29
Table 10: Calculated heat fluxes at the steady state of 10 kW and 7 kW heating power in LIVE-L1	30
Table 11: Calculated transient heat fluxes after water flooding in LIVE-L1	31
Table 12: Planned melt composition and melt and crust composition in LIVE-L1	35
Table 13: Heat flux and corresponding crust growth rate in LIVE-L1	37
Table 14: Thickness of the outer layer and the inner layer of the crust in LIVE-L1	40
Table 15: Liquidus temperature determination of $\text{KNO}_3\text{-NaNO}_3$ mixtures.....	44
Table 16: Liquidus temperature and composition of LIVE-L1 crust.....	45
Table 17: The thermal conductivity of the crust layer at the 7 kW steady state period	47
Table 18: Crust heat conductivity and porosity of LIVE-L1	48
Table 19: Test parameter and test phases of the experiment LIVE-L3.....	50
Table 20: Course of the experiment LIVE-L3	55
Table 21: Heat balance between the heat transfer through vessel wall and the heating power in LIVE-L3	61
Table 22: Transient and steady state heat fluxes measured by heat flux sensors in LIVE-L3	63
Table 23: Steady state (2 minutes average value) and transient heat flux distribution in LIVE- L3	65
Table 24: Calculated transient heat fluxes (averaged) after water flooding in LIVE-L3	65
Table 25: Planned and average melt pool composition in the LIVE-L3 test.....	73
Table 26: Crust growth rate, heat flux through the wall and liquidus temperature of the melt measured by CT thermocouples in LIVE-L3	75
Table 27: Liquidus temperature and composition of the crust in LIVE-L3.....	80
Table 28: Thermal conductivities of the crust layers in LIVE-L3	81
Table 29: Crust porosity of LIVE-L3 test	82

LIST OF FIGURES

Figure 1: Picture of the LIVE test vessel with volumetric heating system	3
Figure 2: View from the top of the LIVE test vessel during LIVE-L1	4
Figure 3: Picture of the heating furnace	5
Figure 4: Top view of the LIVE test vessel with pouring spouts	6
Figure 5: $\text{KNO}_3\text{-NaNO}_3$ phase diagram	7
Figure 6: LIVE volumetric heating system	9
Figure 7: Scheme of the LIVE test vessel with some instrumentation	11
Figure 8: Configuration of the LIVE instrumentation plug	12
Figure 9: Flow rate of cooling water in LIVE-L1	16
Figure 10: Initial melt temperature measured in the pouring spout in LIVE-L1	18
Figure 11: Weight of the test vessel and melt release rate in LIVE-L1	19
Figure 12: Heating power distribution between the six heating planes in LIVE-L1	20
Figure 13: Melt pool temperatures at different elevations along the meridian 0° in LIVE-L1 ..	21
Figure 14: Temperatures of the melt pool at different positions at a radius of 174 mm at different times in LIVE-L1	22
Figure 15: Thermal image of the melt surface in LIVE-L1	22
Figure 16: Definition of heat flux zones on the test vessel wall surface	24
Figure 17: Heat balance between heating power and heat transfer through the vessel wall in LIVE-L1	25
Figure 18: Heat balance between the heat transfer through the vessel wall and the heat removed by cooling water in LIVE-L1	26
Figure 19: Measured heat fluxes of the heat flux sensors in LIVE-L1	27
Figure 20: Distribution of the calculated heat flux based on IT thermocouples during the whole experiment LIVE-L1	30
Figure 21: Calculated heat flux distribution along the vessel wall in LIVE-L1	31
Figure 22: Calculated heat flux development after water flooding in LIVE-L1	32
Figure 23: Flow velocity measured at the upper surface of the LIVE-L1 test during 10 kW heating phase	33
Figure 24: View of the test vessel after disassembly of the lid in LIVE-L1	34
Figure 25: Solidification points in the crust temperature measurements of CT2	36
Figure 26: Crust thickness in dependence of the time in LIVE-L1	37
Figure 27: The final crust thickness at the end of the test LIVE-L1	38
Figure 28: Crust thickness along the meridians at 67.5° and 247.5° in LIVE-L1	39
Figure 29: Crust temperature of CT1 in LIVE-L1, 37.6° to the vertical axis	39
Figure 30: Two-layer structure of the crust formed in the LIVE-L1 test	40

Figure 31: SEM-EDX line-scanning of LIVE-L1 crust: Left: crust inner layer; right: crust outer layer	41
Figure 32 Sampling positions at the cross-section of the crust	42
Figure 33: Crust microstructure of a) outer surface; b) middle of the outer layer; c) interface outer layer/inner layer; d) middle of the inner layer and e) inner surface. Magnification: 900x	42
Figure 34: Na and K mole distribution in large grains and in small grains in the crust.....	43
Figure 35: Comparison of determined liquidus temperatures with phase diagram KNO_3 - NaNO_3	45
Figure 36: Crust liquidus temperature and composition in LIVE-L1.	46
Figure 37: Phase diagram and the crust liquidus temperatures in LIVE-L1	46
Figure 38: Pore size distribution of LIVE-L1 crust: top: inner layer, bottom: outer layer	49
Figure 39: Pouring process of the melt into the LIVE test vessel in LIVE-L3	52
Figure 40: Flow rate of cooling water in LIVE-L3	53
Figure 41: Extraction of the melt from the LIVE test vessel in LIVE-L3.....	54
Figure 42: Initial melt temperature measured in the pouring spout in LIVE-L3	56
Figure 43: Weight of the test vessel and melt release rate in LIVE-L3	57
Figure 44: Heating power distribution between the six heating planes in LIVE-L3	58
Figure 45: Melt pool temperatures at different elevations along the meridian 0° in LIVE-L3 .	59
Figure 46: Temperatures of the melt pool at different positions at a radius of 174 mm at different times in LIVE-L3.....	60
Figure 47: Heat balance between heating power, heat through the vessel wall and heat removed by cooling water in LIVE-L3	61
Figure 48: Heat fluxes measured by the heat flux sensors in LIVE-L3	62
Figure 49: Average heat flux values for the five heat flux zones in LIVE-L3	64
Figure 50: Heat flux development after water flooding in LIVE-L3	66
Figure 51: Values of the calculated heat fluxes and measured heat fluxes in LIVE-L3	67
Figure 52: Ratio between calculated heat fluxes and measured heat fluxes in LIVE-L3	67
Figure 53: Thermogram of the melt surface with patterns used for the motion velocity determination.	69
Figure 54: Displacement of the patterns after 2 seconds (the scale is in cm).....	69
Figure 55: Flow velocity measured at the upper surface of the LIVE-L3 test during 10 kW heating phase.....	70
Figure 56: Flow velocity measured at the upper surface of the LIVE-L3 test during power reduction from 10 kW 7 kW.....	70
Figure 57: Flow velocity measured at the upper surface of the LIVE-L3 test during 7 kW heating phase.....	71

Figure 58: View of the test vessel after the end of the experiment LIVE-L3	72
Figure 59: Crust growth rate after water flooding during 10 kW heating period in LIVE-L3 ...	74
Figure 60: Crust thickness profiles at the end of the test LIVE-L3	76
Figure 61: Crust thickness at the end of the test LIVE-L3 along the meridians at 67.5°, 157.5°, 247.5° and 337.5°.....	77
Figure 62: Comparison of the crust thickness at the end of the tests LIVE-L1 and LIVE-L3 along the meridians at 67.5 and 247.5°	77
Figure 63: Line-scanning of the crust cross-section in LIVE-L3: left: inner layer, right: outer layer	78
Figure 64: Crust cross-sections of LIVE-L3 test: a: outer surface, b: middle of the outer layer, c: boundary of the outer/inner layer, d: middle of the inner layer, e: inner layer surface.	79
Figure 65: Comparison of the crust liquidus temperature and the crust composition between LIVE-L1 and LIVE-L3. Crust thickness is 20 mm.	81
Figure 66: Pore size distribution of the crust layers in LIVE-L3: top: outer layer, bottom: inner layer	83

1 Introduction

1.1 *LIVE as element of the LACOMERA project*

The LACOMERA project started in September 2002 at the Forschungszentrum Karlsruhe was part of the 5th Framework Programme of the European Union. The main objective of the project [1] with duration of 4 years was to offer research institutions from the EU Member Countries and Associated States access to four large-scale experimental facilities at the Forschungszentrum Karlsruhe. In these test facilities various large-scale experiments have been performed within the LACOMERA project which aimed at providing data for a better understanding of possible scenarios of core degradation and of different core melt sequences. The results of these experiments can help to improve severe accident management measures and to reduce the severity of the accident consequences.

In detail, the performed experiments concentrated on the following topics:

- Main factors governing the hydrogen source term and melt generation during core quenching (**QUENCH**).
- Study of the late phase of core degradation, onset of melting, formation and stability of melt pools in the reactor pressure vessel (RPV). Regaining of cooling and melt stabilization in the RPV (**LIVE**).
- Location of the melt after failure of the RPV under moderate pressure, with different failure positions. Pressure increase in the reactor pit, the sub-compartments and the containment due to thermal and chemical reactions, such as hydrogen production and burning (**DISCO**).
- Long term concrete erosion during Molten Corium Concrete Interaction (MCCI) and ex-vessel melt coolability (**COMET**).

Eight organisations from five countries participated in preparation, performance and analysis of eight experiments which have been specified within the LACOMERA project. The results of the experiments which have been performed in the QUENCH, DISCO and COMET test facilities have already been documented in [2]-[4].

In the LIVE test facility two experiments have been performed within the LACOMERA project. The experiment LIVE-L1, which is part of this report, was performed in June 2006 [5]. The experiment was designed to investigate the core melt behaviour in the lower plenum of the reactor pressure vessel and the influence of the cooling of the vessel outer surface with water under conditions that may occur during a hypothetical core meltdown accident in the VVER-1000 type reactor. The experiment was planned and performed in close co-operation with the Technical University Sofia, and the Kozloduy Nuclear Power Plant, Bulgaria.

1.2 Background and objectives of LIVE-L1 and LIVE-L3

The sequence of a postulated core melt down accident in the RPV of a pressurised water reactor (PWR) and water-water cooled energy reactor (VVER) involves a large number of complex physical and chemical phenomena, and strongly depends on the accident sequence and the considered reactor design.

In-vessel core melt progression can be divided into the “early” and the “late” phase. While detailed experimental and theoretical information about the early phase is available, large uncertainties exist in the late phase, which is characterised by substantial melting of fuel, formation of in-core melt pools, and melt relocation to and accumulation in the lower head of the RPV. Steady state behaviour of debris and of molten pools in the lower head has been investigated in several experimental studies (e.g. [6], [7]). However, the database for the transient processes during core melting, melt relocation and accumulation is still very limited. For the melt that relocates into the lower head of the vessel, there is a lack of information about e.g. transient heat fluxes to the vessel wall, crust formation, stability and re-melting of melt crusts, as may occur from melt release to steady state and under 3-d geometrical situations.

An improved understanding of these processes can help to define accident management procedures for accident control in present reactors. Therefore the experimental research programme LIVE (Late In-Vessel Phase Experiments) has been defined and started at Forschungszentrum Karlsruhe, in which different important phenomena during the late phase of core melt progression are being investigated [8].

The LIVE programme is divided into three different phases:

- LIVE 1: Melt retention in the lower head
- LIVE 2: Melt relocation to the lower head
- LIVE 3: In-Core melt pool formation

The experiments LIVE-L1 and LIVE-L3 are part of the first phase (LIVE 1). The initial and boundary conditions in the tests LIVE-L1 and LIVE-L3 were almost the same except of the pouring position of the melt into the test vessel. In LIVE-L1 the melt was poured centrally and in LIVE-L3 - near to the wall of the test vessel. Therefore a comparison between the central and lateral melt relocation modes could be realised. The main objective of the two experiments was to gain information on the melt pool and crust behaviour during the stages of air circulation at the outer RPV surface with a subsequent flooding of the lower head. Important phenomena, which shall be investigated, are:

- Transient and steady state melt behaviour.
- Time dependent local heat flux distribution to the lower head.

- Influence of two subsequent cooling modes: In the first phase of the experiments cooling with air at the outer surface followed by the water flooding of the outer surface of the test vessel in the second phase of the test.

2 LIVE-L1 and LIVE-L3 test design

2.1 Test facility description

The LIVE test facility consists of 3 main parts: the test vessel including cooling system, the volumetric heating system and a separate heating furnace. All parts of the LIVE test facility are arranged in a scaffold having three levels. On level 0 (the floor of the experimental hall), all signal cables come together in different control cabinets. Here the measurement signals are collected and transmitted to the control room which is located next to the experimental hall. In the control room, the data acquisition system and online monitoring systems are arranged. On level 0, also the power supply of the heating system and the corresponding hardware to control the heating system is located.

On level 1, the LIVE test vessel is positioned. The LIVE test vessel is a 1:5 scaled RPV of a typical pressurised water reactor (PWR). For the first and second phase of the LIVE experimental program (LIVE 1 and LIVE 2), only the hemispherical bottom of the RPV is used, Figure 1. The inner diameter of the test vessel is 1 m and the wall thickness is ~ 25 mm. The test vessel is fabricated from stainless steel. To investigate the influence of different external cooling conditions on the melt pool behaviour, the test vessel is enclosed by a second vessel (cooling vessel) to be able to cool the test vessel at the outside. The cooling water inlet is located at the bottom of the cooling vessel and the outlet is positioned at the top of the vessel.



Figure 1: Picture of the LIVE test vessel with volumetric heating system

The volumetric heating system located in the LIVE test vessel is also shown in Figure 1. More details on the heating system are given in chapter 2.3.

In Figure 2 a view from the top of the LIVE test vessel during the experiment LIVE-L1 is given. The LIVE test vessel and the cooling vessel are installed on three steel beams and are enclosed by insulation layer. At the top, the test vessel is covered with a lid. This lid consists of a 20 mm stainless steel plate. Under this plate there is a 100 mm layer of insulating material which is surrounded by a 2 mm steel plate. Additionally, there is a shield plate about 8 mm below the insulation layer to protect the lid from the radiation of the hot melt.

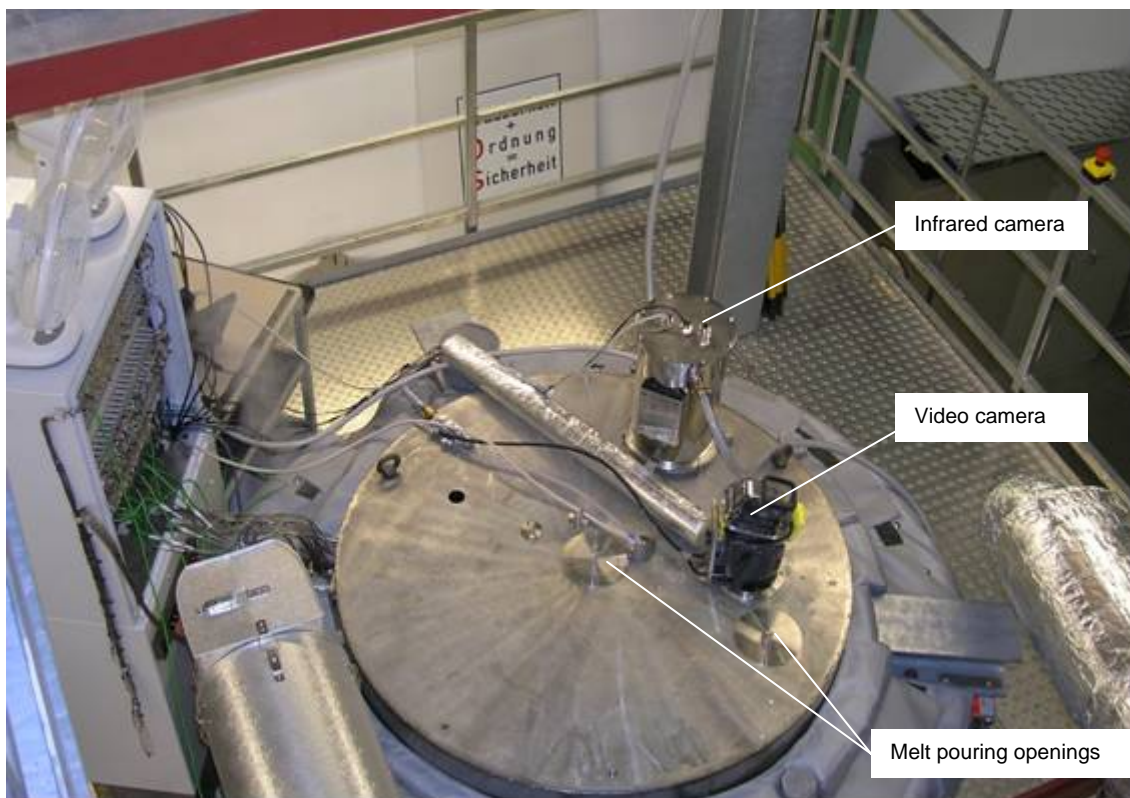


Figure 2: View from the top of the LIVE test vessel during LIVE-L1

The lid has several openings. There are two melt pouring openings to allow pouring of the melt centrally or close to the perimeter of the lower head. There are different small openings to light up the vessel (for optical observation) or to take melt samples during the test. Additionally there are two openings for video observation of the melt surface.

To avoid possible oxidation of the melt in the test vessel, the atmosphere between the melt surface and the upper lid is filled with nitrogen.

To allow transient pouring of the melt into the test vessel, the melt is produced in the external heating furnace, Figure 3. The capacity of this tilting furnace is 220 l volume. From the scaling point of view this corresponds to the most conservative core melt down situation with 100% anticipated melting of the core inventory including both oxidic and metallic components

[9]. The maximum temperature of the heating furnace is 1100 °C. The heating furnace is mounted in a separate scaffold, which is integrated into the scaffold of the test facility. The heating furnace is mounted on a lifting device and is controlled separately. This allows tilting the heating furnace during the pouring process so that the pouring orifice always remains at the same position.



Figure 3: Picture of the heating furnace

When the melt has reached the desired pouring temperature, the furnace is tilted and the melt is discharged with a specified pouring rate into the test vessel via a heated pouring spout. The amount of the discharged melt is defined by the tilting angle and the melt mass flow rate depends on the tilting velocity. There are two pouring spouts available to pour the melt either to the central region or to the perimeter of the test vessel, Figure 4. In addition, the heating furnace is equipped with a vacuum pump; so it is possible to extract the residual melt out of the test vessel back into the heating furnace at the end of the experiment. To

avoid possible oxidation of the melt during melt preparation, the rest atmosphere in the heating furnace is filled with nitrogen.

The control panel of the heating furnace is installed at level 2 of the LIVE test facility. From this level the heating furnace is charged with melt components.

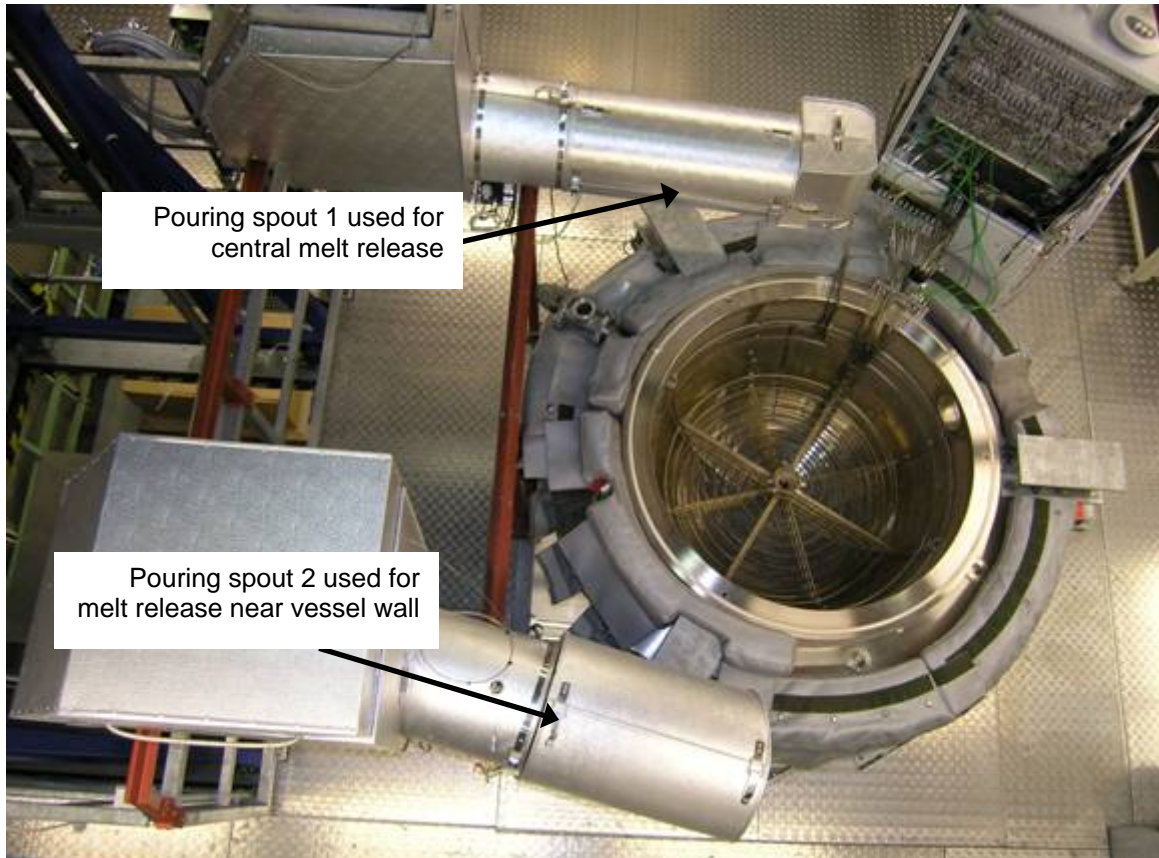


Figure 4: Top view of the LIVE test vessel with pouring spouts

2.2 Melt composition and melt generation

2.2.1 Selection of simulant materials

Simulant materials used in the LIVE program should, to the greatest extent possible, represent the real core materials in important physical properties and in thermo-dynamic and thermo-hydraulic behaviour. Therefore, the applicability of several binary melt compositions as a simulant for the oxidic part of the corium has been investigated. Important criteria for the selection are that the simulant melt should be a non-eutectic mixture of several components with a distinctive solidus-liquidus range of about 100 K, and that the simulant melt should have a similar solidification and crust formation behaviour as the oxidic corium. Moreover, the simulant melt should not be toxic and aggressive against steel and vessel instrumentation. And finally, the temperature range of the simulant melt should not exceed 1000 °C distinctly because of the technical handling and the selection of the volumetric heating system and the heating furnace.

For the first series of experiments a binary mixture of sodium nitrate NaNO_3 and potassium nitrate KNO_3 was chosen, Figure 5. The eutectic composition of this melt is 50-50 mole% and the eutectic temperature is 225 °C [10]. The maximum temperature range between solidus and liquidus is ~60 K and corresponds to a 20-80 mole% NaNO_3 - KNO_3 mixture. This melt can be used in a temperature range from 220 °C (solidification) to 380 °C (chemical decomposition). Due to its solubility for water the applicability of this melt is restricted to dry conditions inside the test vessel.

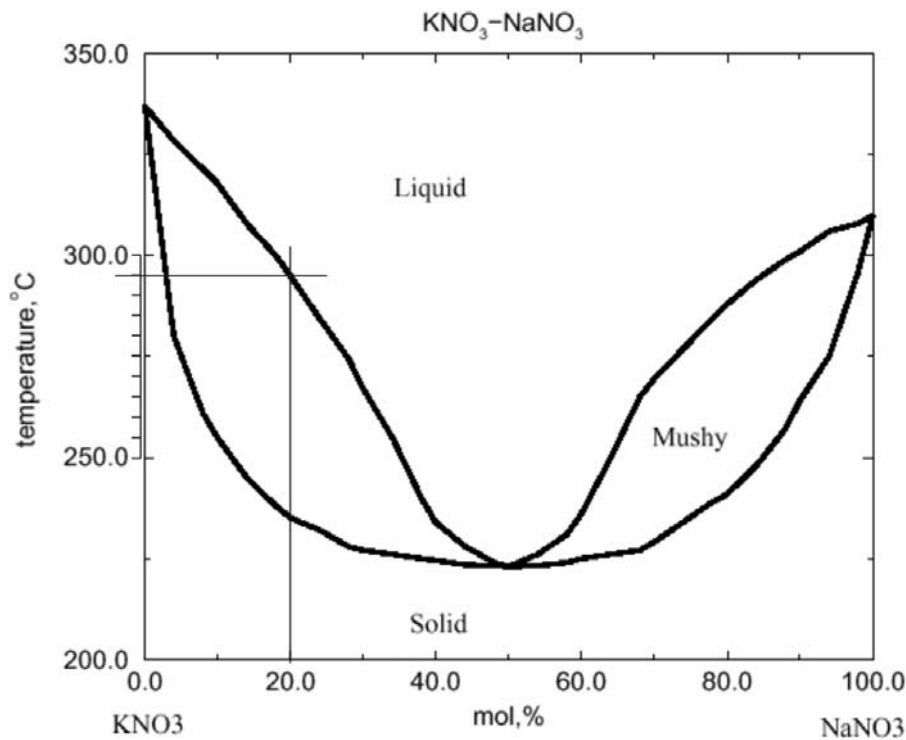


Figure 5: KNO_3 - NaNO_3 phase diagram

2.2.2 Melt composition, preparation and generation

For the experiments LIVE-L1 and LIVE-L3 the 20-80 mole% NaNO_3 - KNO_3 melt composition was used. According to the phase diagram (see Figure 5), the liquidus temperature of this melt is ~280 °C and the solidus temperature ~220 °C [11]. In Table 1 the melt characteristics are described. For the experiment LIVE-L1, being the first experiment with this type of melt in the LIVE test facility, the heating furnace was loaded with 58 kg NaNO_3 and 278 kg KNO_3 powder to produce about 180 l melt of the desired composition.

For the experiment LIVE-L3, the procedure was more complicated, because the residual melt of the previous experiment LIVE-L2 should be recycled. At the end of the experiment LIVE-L2, the residual melt in the test vessel was extracted from the test vessel back into the heating furnace. The composition of this melt was not identical to the original melt composition due to the crust formation in the test vessel. The crust remains in the test vessel and is normally enriched with KNO_3 , because the melting point of this element is higher (337 °C) than

the melting point of NaNO_3 (310 °C). So, the composition of the residual melt has to be determined. Moreover, only part of the melt generated in the furnace was poured into the test vessel during the LIVE-L2 test. Therefore, two melt samples were taken, one at the beginning of the test from the pouring spout and another one from the melt pool just before the melt extraction from the test vessel. Analysis of these melt samples and known mass of the residual melt in the heating furnace allowed to determine the values of NaNO_3 and KNO_3 additives needed to obtain the desired 20-80 mole% NaNO_3 - KNO_3 melt composition.

In both experiments the heating furnace was heated up ~3 days before the test to a temperature of 350 °C and was kept at this temperature until the start of the experiment. During this time the above-melt atmosphere in the heating furnace was filled with nitrogen at 20 l/min to avoid the oxidation and/or chemical decomposition of the melt.

Table 1: Melt characteristics and preparation

Type	NaNO_3	KNO_3
Mole %	20%	80%
Mass %	17.37%	82.63%
Mass	58 kg	278 kg
Total mass	336 kg	
T_{liquidus}	~ 280 °C	
T_{solidus}	~220 °C	
Loading of the furnace	~390 l powder (for $T=20$ °C) ~180 l melt (for $T=350$ °C)	
Pouring mass	120 l (corresponds to ~31 cm melt height)	
Initial temperature	350 °C	
Flow rate of nitrogen covering	20 l/min	

2.3 Decay heat simulation

The volumetric heating system has to simulate the decay heat released from the corium melt. Consequently, the heating system has to produce the heat in the melt as homogeneously as possible. Therefore a heater grid with several independent heating elements was constructed, Figure 6. The heating elements are shrouded electrical resistance wires. The maximum temperature, which the heating system can provide, is limited to 1100 °C. To allow the homogeneous heating of the melt pool, the heating system has six heating planes at different elevations with a distance of about 45 mm. Each heating plane consists of a spirally formed heating element with a distance of ~40 mm between each winding. The heating ele-

ments are located in a special cage to ensure the correct positioning. To realise a homogeneous heating of the melt, each plane can be controlled separately.

The power, which the heating planes can provide, is determined by the length of the heating wire, the corresponding resistance and the supplied voltage. For the dimensioning of the heating system, an input supply voltage of 230 V was assumed. With this voltage, a maximum power of about 28 kW could be realised.

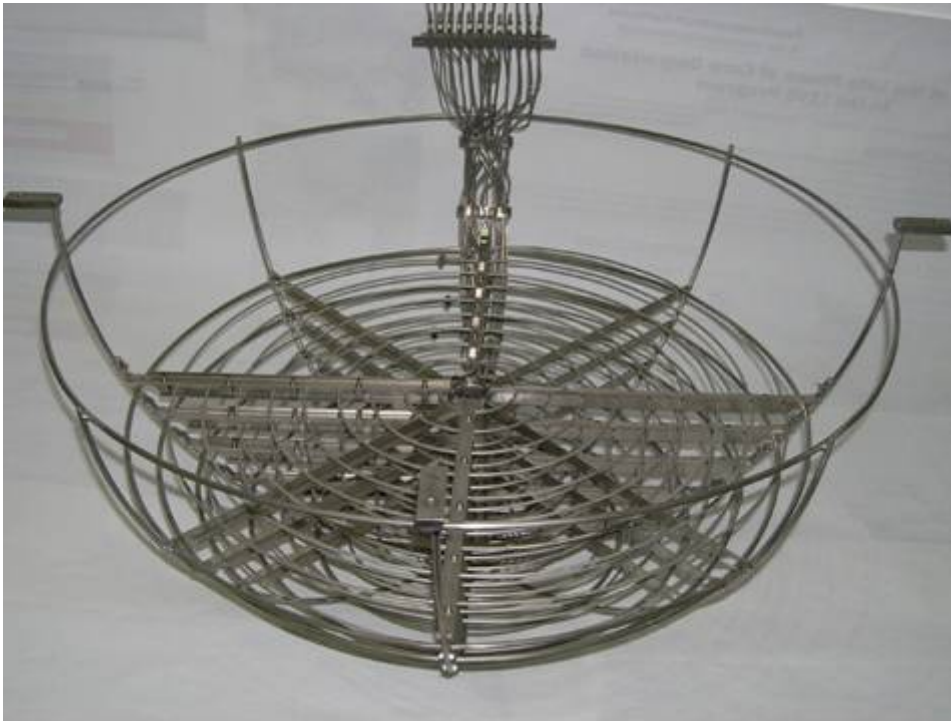


Figure 6: LIVE volumetric heating system

During the commissioning of the heating system, the maximum power of the heating planes has been measured, respectively the corresponding voltage and the current at the clamps of each heating element. The measurements showed that the voltage at the clamps was distinctly lower than the design specification. The measured values varied from 209 to 211 V. This lower voltage results from the power supply of the experimental hall, which provides only ~ 220 V, and from the insulating transformers, which cause additional voltage drop.

Due to the fluctuating voltage at the clamps of the heating elements, the power, which the heating planes can provide, fluctuates as well. The maximum power of the heating planes is given in Table 2 as an average value determined by different measurements. All heating planes together can provide a maximum power of about 24.5 kW.

In Table 2 the vertical position of the heating planes in the test vessel is also given, relating to the inner bottom of the test vessel.

Table 2: Characteristics of the LIVE heating system

Heating plane	Vertical position of the heating planes in the test vessel [mm]	Diameter of the heating elements [mm]	Maximum power measured during commissioning [W]
6	36,4	2	1080
5	90,4	3	2338
4	135,4	4	2715
3	182,4	4	6624
2	233,4	4	6407
1	278,4	4	5300
			Σ 24464

Before the test LIVE-L3, the heating plane 6 has been replaced because of damage during the dismantling of the test LIVE-L2. The new heating plane provides a comparable maximum power as the previous one.

To control the heating system and to avoid the overheating of heating elements, two thermocouples are installed at each heating element: one at the outer region and another one at the inner region of the heating element coil.

The heating system is controlled by a separate PC control and data acquisition system, which is independent from the PC data acquisition system of the measurement data of the instrumentation of the experiment. The programme Visual Designer 4.0 is used to store and to display the data of the heating system. Here, the actual performance of the heating system and also the temperature of the monitoring thermocouples are stored.

2.4 Instrumentation and data acquisition

The LIVE test facility is extensively instrumented to monitor and control the experiment and to collect data for subsequent evaluation. All data are stored on PC data acquisition system running under the Visual Designer 4.0.

In addition, several video systems are used to observe the experiment, including two cameras, which are directed from the upper lid of the test vessel onto the surface of the melt. These systems are particularly useful to observe the pouring process and behaviour of the melt surface. Besides a conventional video camera, an infrared (IR) video camera is installed, viewing through a Zinc selenide (ZnSe) window on the surface of the melt (22 by 17 cm area). This camera operates in the IR wavelength range from 7.5 to 13.0 μm and produces a real-time infrared recording during the transient phases of the test. During the sta-

tionary phases, the infrared pictures are taken every 1 or 5 s according to the needs of the experiment.

Another video camera is installed at the side of the test vessel. With this camera, the pouring process of the melt can be observed in more detail.

To quantify the melt relocation process, the LIVE test vessel is placed onto three weighing cells. The weight of the LIVE test facility is continuously recorded so that the mass flow rate of the discharged melt can be determined post-test by differentiating the recordings of the vessel weight.

Decay power input into the melt is recorded and melt samples are extracted during the tests. Different openings in the upper lid of the test vessel allow pouring of the melt to the central region or close to the perimeter of the lower head. To be able to investigate the crusts, which are formed at the wall of the vessel, the residual melt is extracted out of the vessel at the end of the test.

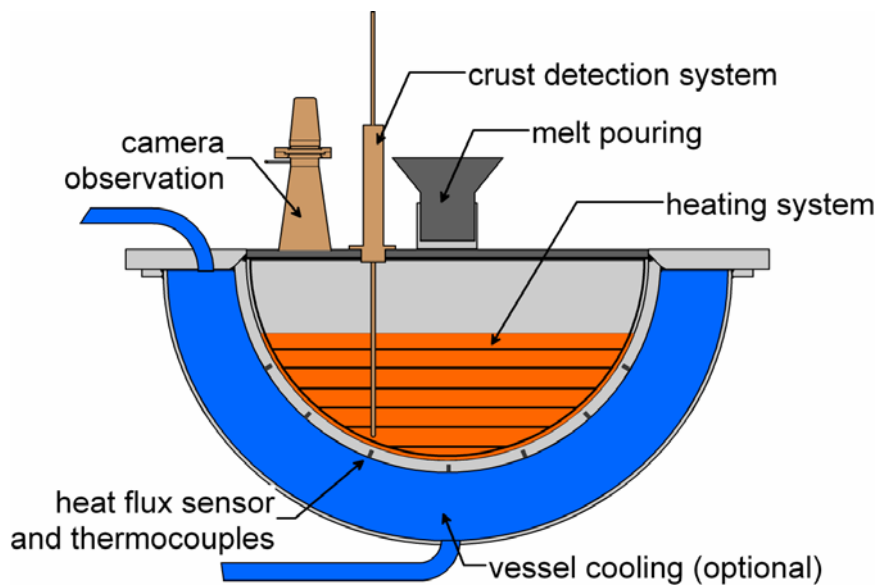


Figure 7: Scheme of the LIVE test vessel with some instrumentation

In Figure 7 a scheme of the LIVE test vessel with some instrumentation is given. The shown crust detection system was unfortunately not available for the experiments LIVE-L1 and LIVE-L3 but is realised in other tests.

To investigate both transient and steady state behaviour of the simulated core melt, an extensive instrumentation of the test vessel is realised. The vessel wall can be equipped with up to 17 instrumented plugs (Figure 8) at different positions along 4 meridians at 67.5° , 157.5° , 247.5° and 337.5° . The axis 0° corresponds to the instrumentation axis, where all signal cables coming from the test vessel are collected and are attached to the first control cabinet. Each plug consists of a heat flux sensor and 5 thermocouples. The thermocouples are protruding into the melt with different distances from the vessel wall (0, 5, 10, 15,

20 mm). The heat flux sensor is part of the vessel wall and is positioned 1 mm below the inner surface of the test vessel. This sensor measures the heat flux and the corresponding temperature.

For the experiment LIVE-L1 only one meridian at 67.5° was instrumented with 5 plugs. In LIVE-L3 the instrumentation was completed with 17 plugs.

To measure the temperature at the outer surface of the vessel wall, 17 thermocouples (named OT) are located at different positions along 4 meridians at 22.5° , 112.5° , 202.5° and 292.5° .

In LIVE-L1 5 thermocouples were installed at the inner vessel wall along the meridian at 112.5° to measure the temperature at the inner vessel wall at different heights (named IT). In LIVE-L3 the number of these thermocouples was increased to 17 along the meridians at 22.5° , 112.5° , 202.5° and 292.5° . These thermocouples (IT) were installed at the same position as the thermocouples at the outer surface of the vessel (OT). So, it was possible to compare the temperatures and to calculate heat fluxes at these positions.

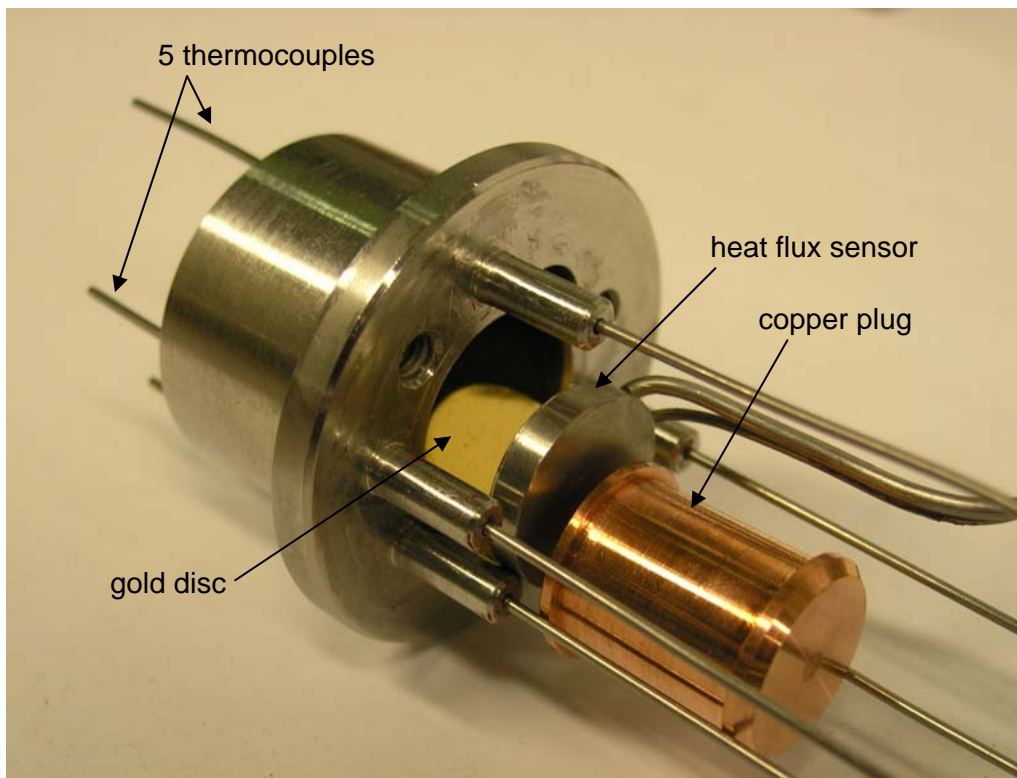


Figure 8: Configuration of the LIVE instrumentation plug

In both experiments, 36 thermocouples were positioned in the melt pool to measure the melt pool temperatures at different positions (named MT). The thermocouples are uniformly distributed in the melt at a distance of 100 mm in horizontal and vertical direction between each other. The thermocouples are mounted at the cage of the volumetric heating system.

To quantify the crust growth at the vessel wall, three thermocouple trees were installed in both experiments. The thermocouple trees were attached at the inner vessel wall along the meridian at 35°. Each thermocouple tree consists of 7 thermocouples. For the first thermocouple tree, which is located at the most lowest point, 420 mm below the upper edge of the test vessel, the length of the thermocouples from the inner vessel wall into the melt is 0, 5, 10, 15, 20, 25, 30 mm. For two other thermocouple trees, which are positioned 320 and 220 mm below the upper edge of the test vessel, the length of the thermocouples from the inner vessel wall into the melt is 0, 3, 6, 9, 12, 15, 18 mm. Here the distance between the thermocouples is smaller comparing to the first thermocouple tree, since thinner crust was expected at these positions.

At the outside of the cooling tank three thermocouples were installed to measure the temperature between the cooling tank and the insulation layer.

The channel assignment of the instrumentation for the data acquisition system is listed in Annex A.1. Instrumentation of the LIVE test vessel is given in Annex A.2.

3 Progression and test results of LIVE-L1

3.1 Preparation and performance of LIVE-L1

The experiment LIVE-L1 was successfully conducted on June 21-22, 2006. The simulated core melt has been generated in the heating furnace as described in the chapter 2.2.2. Several hours before the test, the experimental team made the final preparations of the test, e.g. installing the video cameras and assembling the IR camera. The experiment started with the melt pour from the heating furnace into the test vessel. In Table 3 the main test parameters and the performed test phases of the experiment are summarised. The total melt was discharged in one single pour. The planned initial temperature of the melt was 350 °C and the pouring mass was 120 l. In LIVE-L1, the melt was poured centrally into the test vessel.

Table 3: Test parameter and test phases of the experiment LIVE-L1

LIVE-L1		
21-22.06.2006		
Melt characteristics and preparation		
Type	NaNO ₃	KNO ₃
Mole %	20 %	80 %
Mass %	17.37 %	82.63 %
Mass	58 kg	278 kg
Total mass	336 kg	
Loading of the furnace	~390 l powder (for T=20 °C) ~180 l melt (for T=350°C)	
Pouring Mass	120 l (corresponds to ~31 cm melt height)	
Initial temperature	350 °C	
Flow rate of nitrogen covering in the furnace	20 l/min	
Melt pour		
Position	central	
Number of pours	1	
Furnace tilting velocity	0.5 °/s	
Furnace target angle	80°	
Hold time	50 s	
Pouring spout temperature	350 °C	

Phase 1: Homogeneous heat generation	
Start time	131 s
Boundary conditions	Air
Heating planes	All
Heating power	18 kW at the beginning, stepwise reduction to 10 kW
Maximum melt temperature	360 °C
Phase 2: Start of outer vessel wall cooling	
Start time	7214 s
Boundary conditions	Water, continuous cooling
Cooling water flow rate	~42 g/s
Heating planes	All
Heating power	10 kW
Heat generation	Homogeneous
Phase 3: Reduction of heat generation	
Start time	82682 s
Boundary conditions	Water, continuous cooling
Cooling water flow rate	~47 g/s
Heating planes	All
Heating power	7 kW
Heat generation	Homogeneous
Phase 4: Test termination and melt extraction	
End time	102627 s
Test conditions	Reaching of steady-state conditions in Phase 3
Heating power	0 kW

After the completion of the pouring process, the first test phase with a homogeneous heat generation in the melt started. A heating power of approximately 18 kW was applied by switching all six heating planes simultaneously. To avoid the overheating (and decomposition) of the melt, the power was reduced stepwise to ~10 kW. In the second test phase, after ~7200 s, the flooding of the outer vessel wall was started with a flow rate of about 1.5 kg/s, Figure 9. After the space between the test vessel and the cooling vessel was filled, a cooling rate of about 47 g/s was planned to keep constant throughout the whole experiment. After the experiment LIVE-L1 it was detected that this rate measured by the flowmeter Krohne had an offset of about 5.5 g/s. Therefore the adjusted value of ~47 g/s was not the real cooling rate; taking the offset into account the realized cooling rate amounted to ~42 g/s.

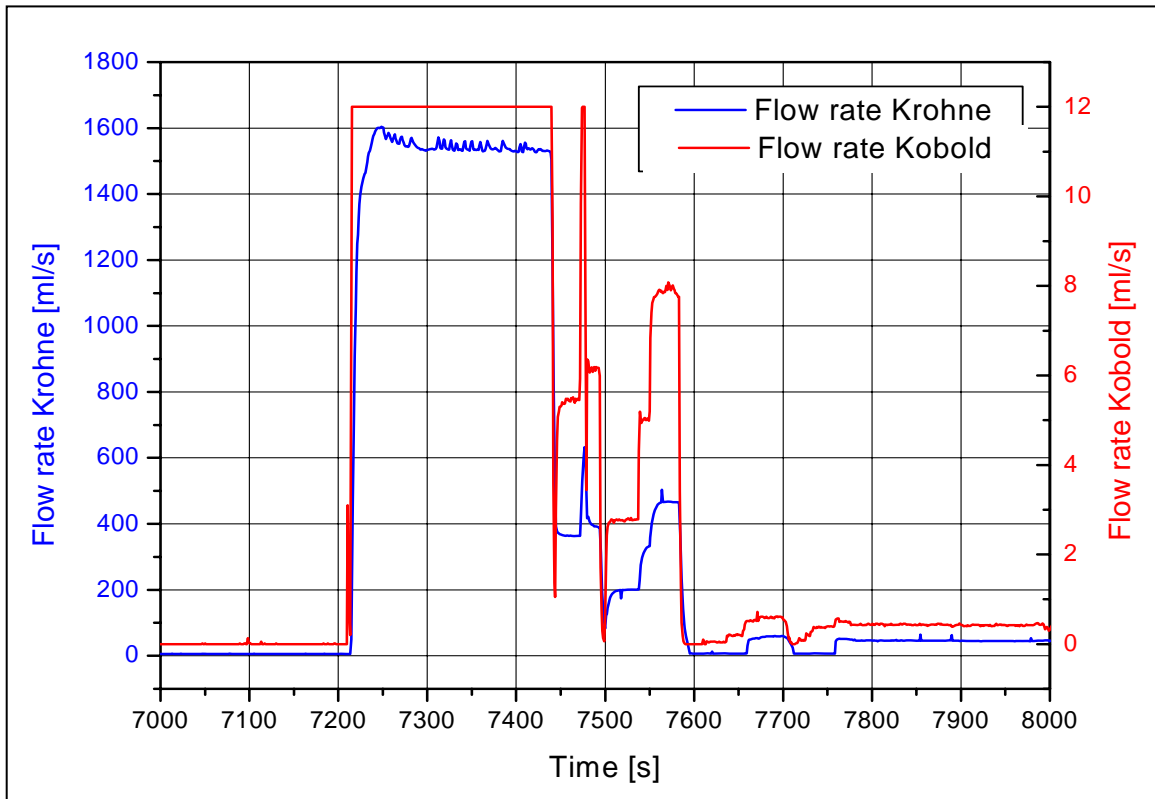


Figure 9: Flow rate of cooling water in LIVE-L1

In LIVE-L1 the measured temperature of the cooling water at the inlet was about 8 °C and the temperature of the cooling water outflow increased to about 80 °C at the beginning and decreased to about 70 °C after about 25000 s. The corresponding temperatures plot is given in Annex C.1.

The homogeneous heating of the melt with 10 kW was continued for about 20 hours to reach the steady state conditions. After about 82000 s, the test phase 3 was started, in which the heating power was reduced to 7 kW to observe the influence of the power reduction on the crust growth and heat flux distribution. This power level was kept for another 6 hours. In the last test phase, the heating power was switched off and the residual melt was extracted from the test vessel back into the heating furnace.

In Table 4 the course of the test LIVE-L1 is described in chronological order.

Table 4: Course of the experiment LIVE-L1

Time of day	Event
21.06.2006	
7:55	Melt temperature in furnace 350 °C
8:50	PC data acquisition start
9:26	Video record start
9:27	Weight of test vessel 1612 kg
9:30	Start of pouring program of heating furnace
9:32	Start of melt pouring into the test vessel
9:33:30	End of melt pouring
9:34	P = 18 kW
9:38	P = 14 kW
9:40	Weight of test vessel 1830 kg
9:59	Video record stop
10:15	P = 12 kW
10:33	P = 10 kW
11:28	Video record start
11:32	Start of flooding of gap between cooling vessel and test vessel (high flow rate)
11:36	Low flow rate set to around 0,047 l/s
12:05	Video record stop
22.06.2006	
8:27	Video record start
8:30	P = 7 kW
10:23	Video record stop
13:40	Weight of test vessel 2209 kg
13:47	Video record start
14:01	Start suction of residual melt
14:15	Suction end, weight of test vessel 2048 kg
14:46	End of video tape

3.2 Experimental results of LIVE-L1

3.2.1 Mass and initial temperature of the melt in LIVE-L1

The experiment LIVE-L1 started with the pouring of the simulated corium melt from the heating furnace centrally into the LIVE test vessel via the preheated pouring spout. The experimental time $t = 0$ s is determined by the temperature increase of the thermocouple ST1 mounted in the pouring spout.

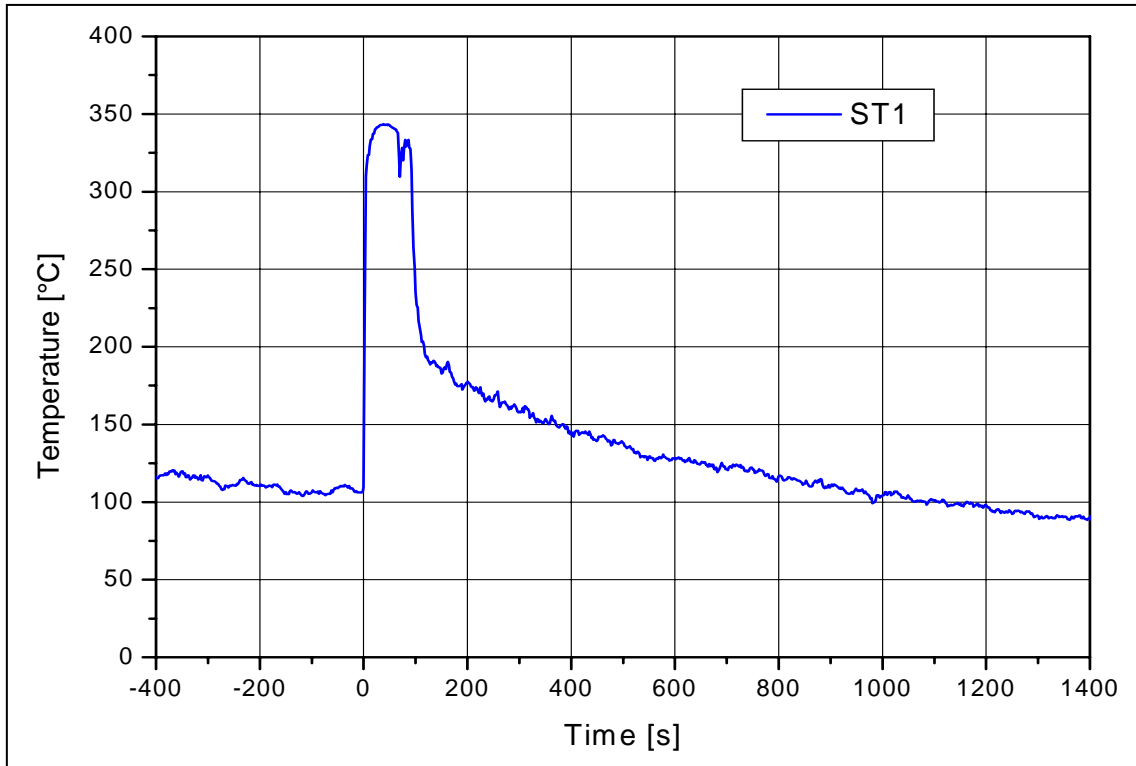


Figure 10: Initial melt temperature measured in the pouring spout in LIVE-L1

In Figure 10, the temperature measurement of the thermocouple ST1 is shown. The initial temperature of the $\text{NaNO}_3\text{-KNO}_3$ melt in the pouring spout was about 343 °C, which is in good agreement with the planned 350 °C.

The mass of the test vessel during the pouring of the melt increased from ~1612 kg to 1831 kg, Figure 11. Therefore about 219 kg of nitrate melt was poured into the test vessel. With a density of about 1868 kg/m^3 for the 20-80 mole% $\text{NaNO}_3\text{-KNO}_3$ melt having the temperature of 343 °C (values taken from [12]), a volume of ~117 l nitrate melt was poured into the test vessel. This value is in good agreement with the planned 120 l melt.

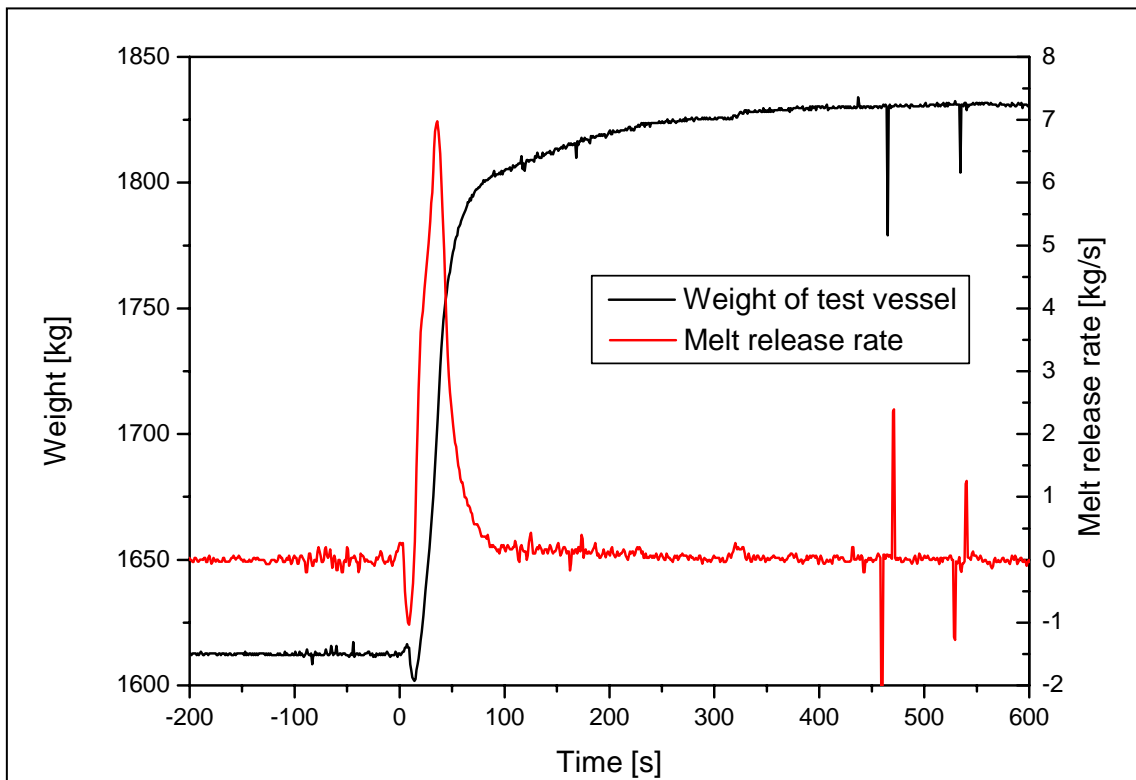


Figure 11: Weight of the test vessel and melt release rate in LIVE-L1

In Figure 11 also the melt release rate is shown. The maximum pouring rate derived from the analysis of the weight of the test vessel was ~ 7 kg/s.

3.2.2 Decay heat simulation in LIVE-L1

After about 131 s after the pouring initiation, the uppermost heating plane was covered with melt and the heating power of approximately 18 kW was applied to heat the melt homogeneously by switching all six heating planes simultaneously. The heating power distribution between the heating planes is shown in Figure 12. It was planned to apply the heating power of 18 kW throughout the test phases 1 and 2, but the temperature of the melt increased over 350 °C and continued to increase. To avoid the melt overheating and chemical decomposition, the heating power was reduced stepwise to about 14 kW after 390 s, then to 12 kW after 2650 s and finally to 10 kW after 3720 s. The disturbances of the power recordings of the heating planes 1 and 2 (see Figure 12) in the upper part of the melt pool were caused by the automatic switch-off of the power when the heater temperatures exceeded 370 °C.

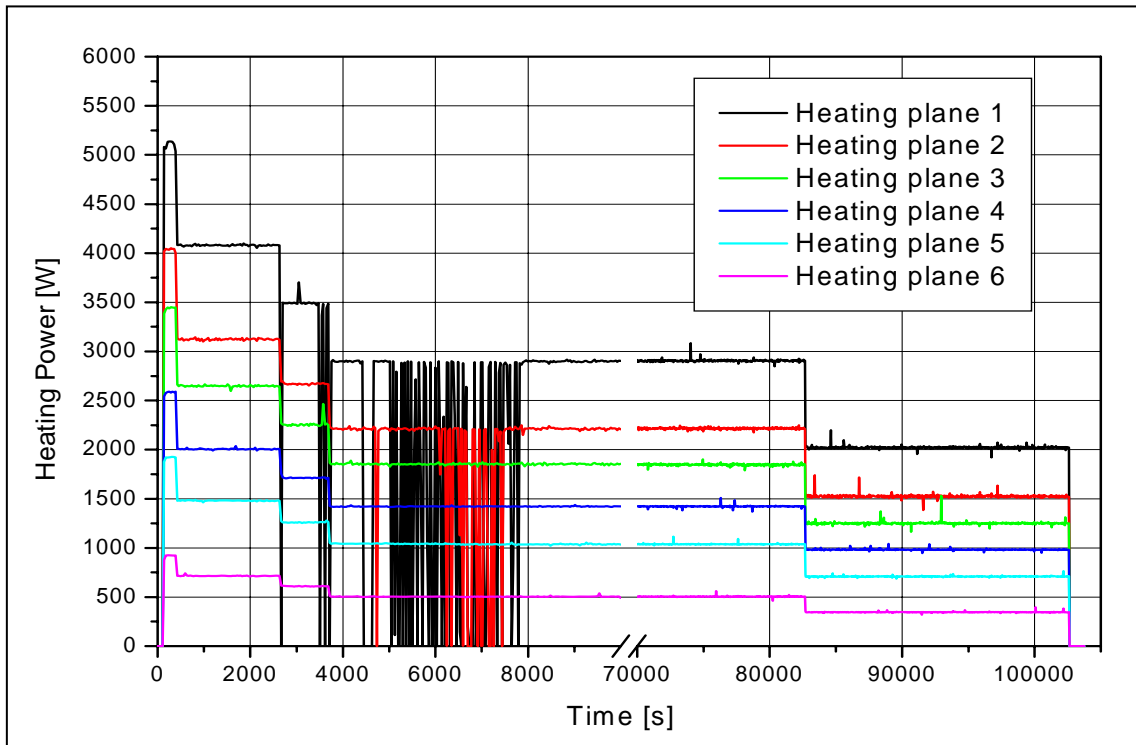


Figure 12: Heating power distribution between the six heating planes in LIVE-L1

The test phases 1 and 2 were performed with the heating power of 10 kW. After 82682 s, the heating power was reduced to 7 kW and the test phase 3 was initiated. After about 102627 s, the heating system was switched off and the test was terminated.

3.2.3 Melt behaviour in LIVE-L1

Shortly after the melt pouring the melt temperatures measured in the melt pool decreased to ~ 300 °C at the bottom of the test vessel and to ~ 330 °C near the melt surface. In Figure 13, the melt pool temperatures at different elevations along the meridian at 0° are shown. After the start of the heating, the melt temperatures started to increase. Due to the high heating power of 18 kW, the melt temperatures increase above 350 °C and therefore, the heating power was reduced to 10 kW. After ~ 7200 s, the test phase 2 was started and the flooding of the outer vessel wall was initiated. The temperatures decreased immediately to ~ 320 °C at the upper part of the melt pool and to ~ 300 °C in the centre of the melt pool.

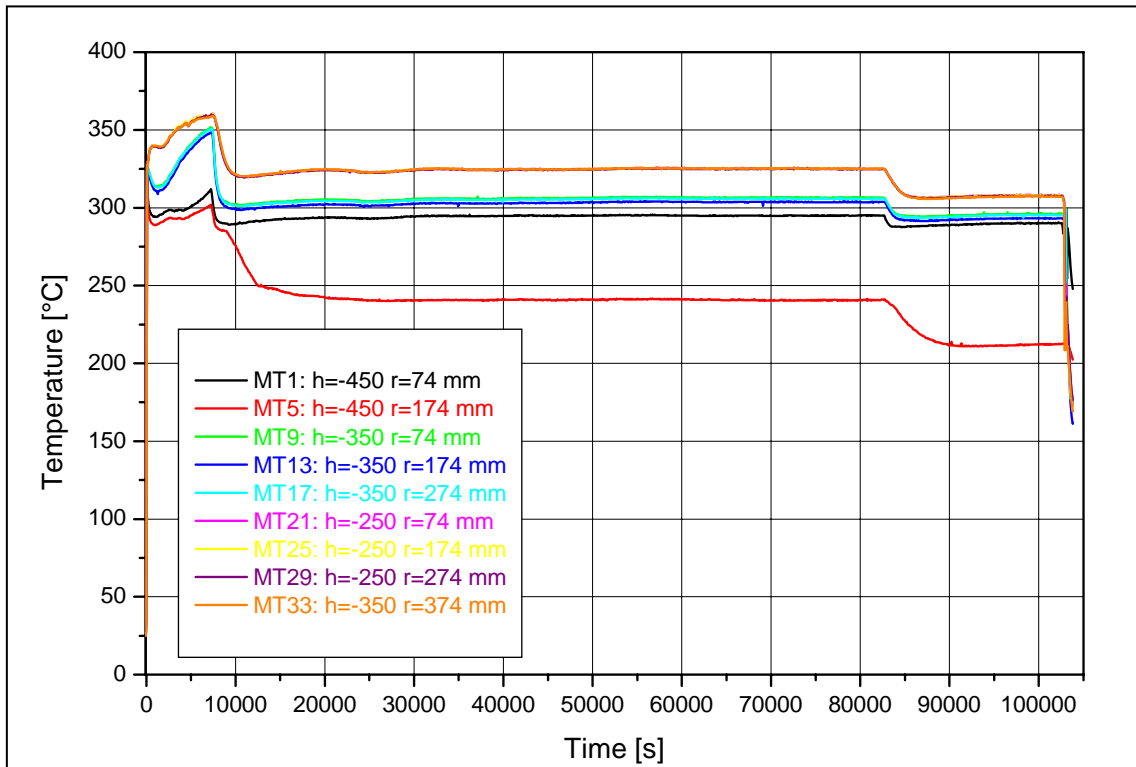


Figure 13: Melt pool temperatures at different elevations along the meridian 0° in LIVE-L1

At the position of the MT5 thermocouple, which is located close to the bottom of the vessel wall, the temperature decreased below the liquidus temperature of the melt indicating the onset of crust formation at this position.

The formation of the crust at the inner vessel wall was also clearly detected by the infrared camera installed at the vessel lid (blue stripe adjacent to the vessel wall in Figure 15).

After about 83000 s, the heating power was reduced to 7 kW. The melt temperatures at all positions decreased accordingly by about 15-20 °C.

The temperature measurements along the meridians 90°, 180° and 270° are similar to the temperature measurements along the meridian 0° and are shown in Annex C.1.

In Figure 14 the temperatures of the melt pool at different positions at the radius of 174 mm at different times are shown. The temperature of the melt at the bottom of the test vessel was always lower than the temperature of the melt at the upper part of the test vessel. At ~20000 s the temperatures at the vessel height 70 mm were already below the liquidus temperature.

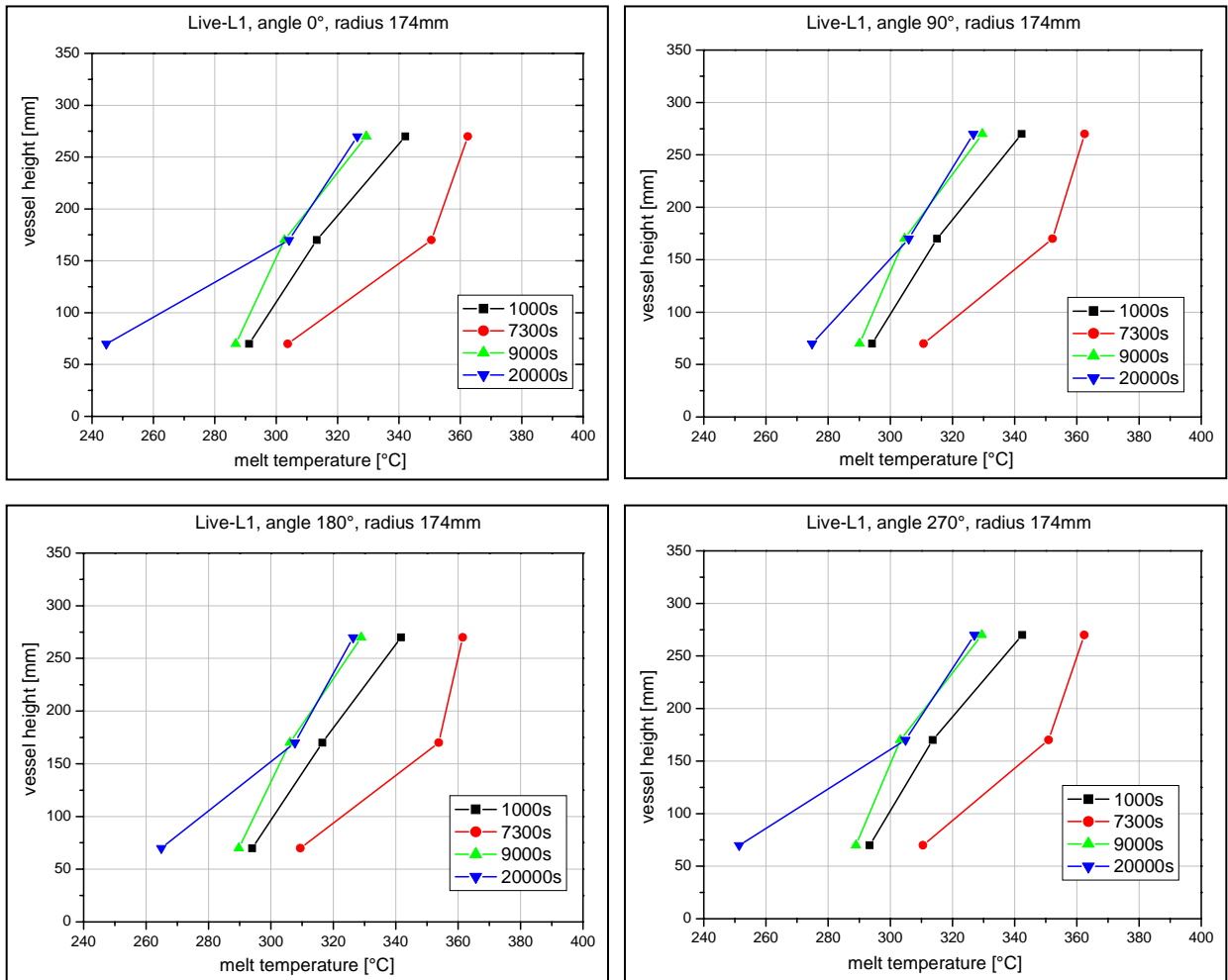


Figure 14: Temperatures of the melt pool at different positions at a radius of 174 mm at different times in LIVE-L1

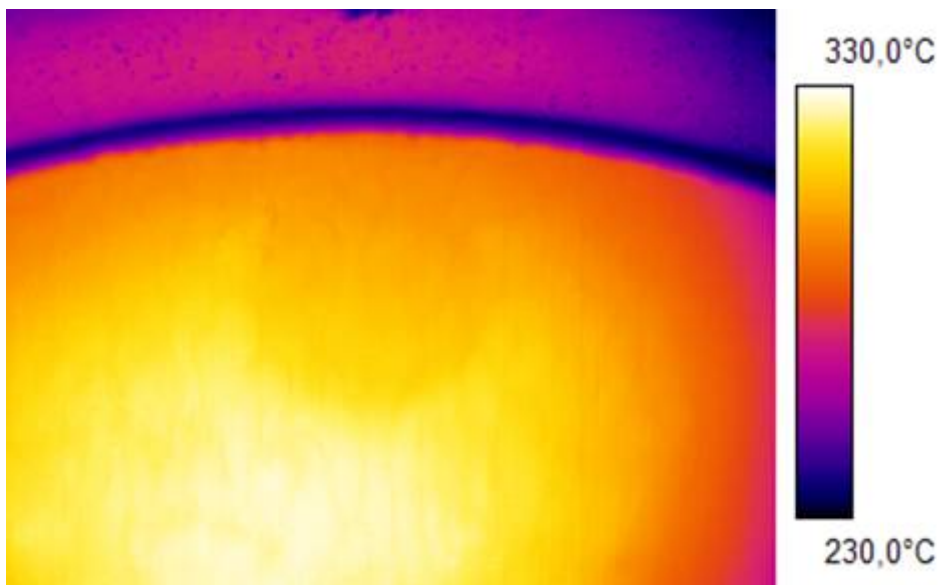


Figure 15: Thermal image of the melt surface in LIVE-L1

3.2.4 Heat balance and heat flux in LIVE-L1

3.2.4.1 Heat balance in the steady state of LIVE-L1

During the thermohydraulic steady state of a severe accident in the lower head of the RPV, a part of the decay heat generated in the melt pool is removed through the bottom hemispheric vessel wall and the rest of the decay heat is released from the melt pool upper surface. The fraction of the heat transferred through the vessel wall is extremely important to determine the cooling effectiveness by external flooding for different heat generation and cooling rates.

The heat through the vessel wall (Q_{wall}) is removed by water which flows from the bottom to the top opening of the cooling vessel in the LIVE test facility. The heat through the test vessel wall and the heat removed by water (Q_{water}) can be calculated based on the measurements of the inner and outer wall temperatures. By comparing these values, the reliability of the temperature measurements in the LIVE facility can be checked.

Therefore, the aim of the heat balance calculation in the test LIVE-L1 are a) to determine the fraction of the heat transferred through the vessel wall during the heating periods of 10 kW and of 7 kW and b) to compare the heat transferred through the vessel wall with the heat removed by cooling water.

To calculate the total heat transferred through the vessel wall, five horizontal heat flux zones are defined on the test vessel wall surface as shown in Figure 16. Each zone has its own local heat flux and surface area. The boundary between each zone under the melt surface is at the middle of the height between two instrumented plugs. Two upper zones are divided by the melt surface. The geometric data of the zones are given in Table 5. The total heat transfer through the vessel wall is the sum of the local heat flux multiplied by the corresponding surface area of the vessel wall:

$$Q_{wall} = \sum q_i \cdot A_i \quad (3.1)$$

where

q_i = local heat flux [W/m²]

A_i = wall inside area of the local heat flux zone [m²]

The heat flux of each zone is calculated accordingly to the vessel wall inner temperature (IT thermocouples) and outer temperature (OT thermocouples). The calculation method is described in detail in Section 3.2.4.2. The temperature measurements of the IT and OT thermocouples are given in Annex C.1. It should be noted that in LIVE-L1 only one meridian at 112.5° was instrumented with IT thermocouples, thus reducing the accuracy of the heat flux calculations.

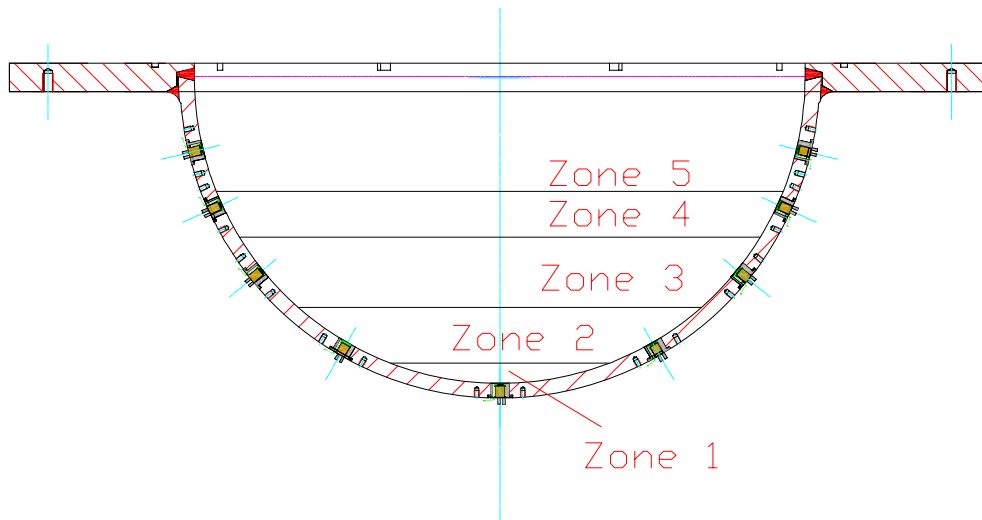


Figure 16: Definition of heat flux zones on the test vessel wall surface

Table 5: Geometries of the heat flux zones

	Plug Nr.	Plug position to flange upper edge [mm]	Height of zone [mm]	Zone inner surface area A_i [m ²]
Zone 1	1	-520	32.5	0.1014
Zone 2	2	-455	91.5	0.2855
Zone 3	6	-337	112.5	0.3510
Zone 4	10	-230	76.5	0.2387
Zone 5	14	-140	183.6	0.5729

In order to calculate the fraction of the heat transported through the vessel wall at steady state conditions, two points are selected at 80000 seconds for the 10 kW period and at 102558 seconds for the 7 kW period. The 30 seconds average value (i.e. 15 s before and 15 s after the time points 80000 s and 102558 s) of the heat transferred through the vessel wall (Q_{wall}) and the heating power ($Q_{heating}$) at this two time points are listed in Table 6. The heat balance shown in Table 6 indicates that the fraction of heat transported through the vessel wall increases with increasing heat generation in the melt pool.

The heat transfer through the vessel wall during the whole test is illustrated in Figure 17. During the steady-state phase with 10 kW heating power, about 84 % of the heat was released through the vessel wall to the cooling water; whereas during the steady-state phase with 7 kW heating power, only about 73 % of the heat was released to the cooling water. The rest of the heat generated in the melt pool was removed from the top of the melt surface.

Table 6: Heat balance between the heat transfer through vessel wall and heating power

Heating period	Time point	Q_{wall}	Q_{heating}	$Q_{\text{wall}}/Q_{\text{heating}}$
10 kW	80000 sec	8348 W	9942 W	84 %
7 kW	102558 sec	5007 W	6832 W	73.3 %

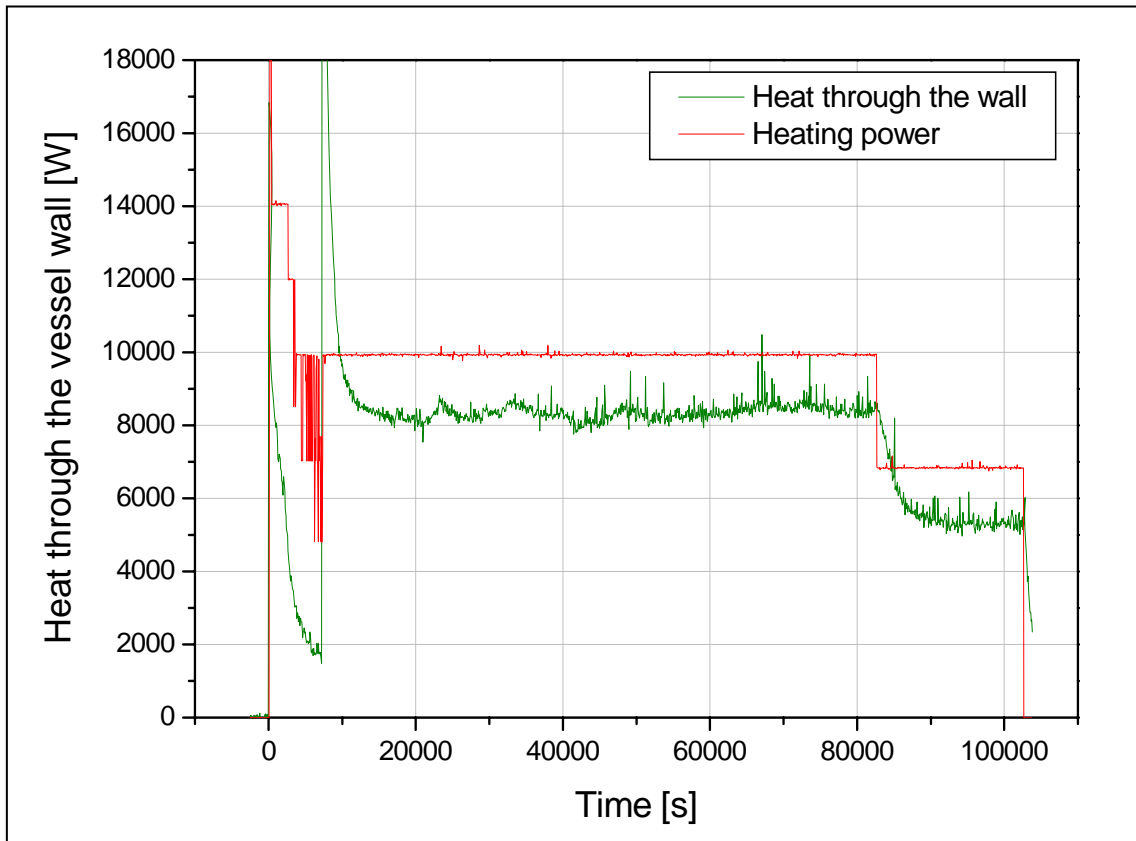


Figure 17: Heat balance between heating power and heat transfer through the vessel wall in LIVE-L1

The heat removed by cooling water (Q_{water}) is calculated according to equation (3.2):

$$Q_{\text{water}} = C_p \cdot (DF1 + DF2) \cdot (AT - ZT) \quad (3.2)$$

where

C_p = specific heat capacity of water = 4.193 J/gK at 10 °C

$DF1$ = mass flow rate Krohne [g/s]

$DF2$ = mass flow rate Kobold [g/s]

AT = cooling water outlet temperature

ZT = cooling water inlet temperature

Disagreements between Q_{water} and Q_{wall} are found in the steady-state. During this phase Q_{water} was significantly higher than Q_{wall} and even higher than the heating power, as shown in Figure 18. The unreliable value of Q_{water} was most probably caused by the position of the reference thermocouple used for the water inlet temperature calibration (ZT). It was placed near a signal cable bundle, which warmed up during the test period. As a consequence, the calibrated water inlet temperature showed lower values than the realistic ones.

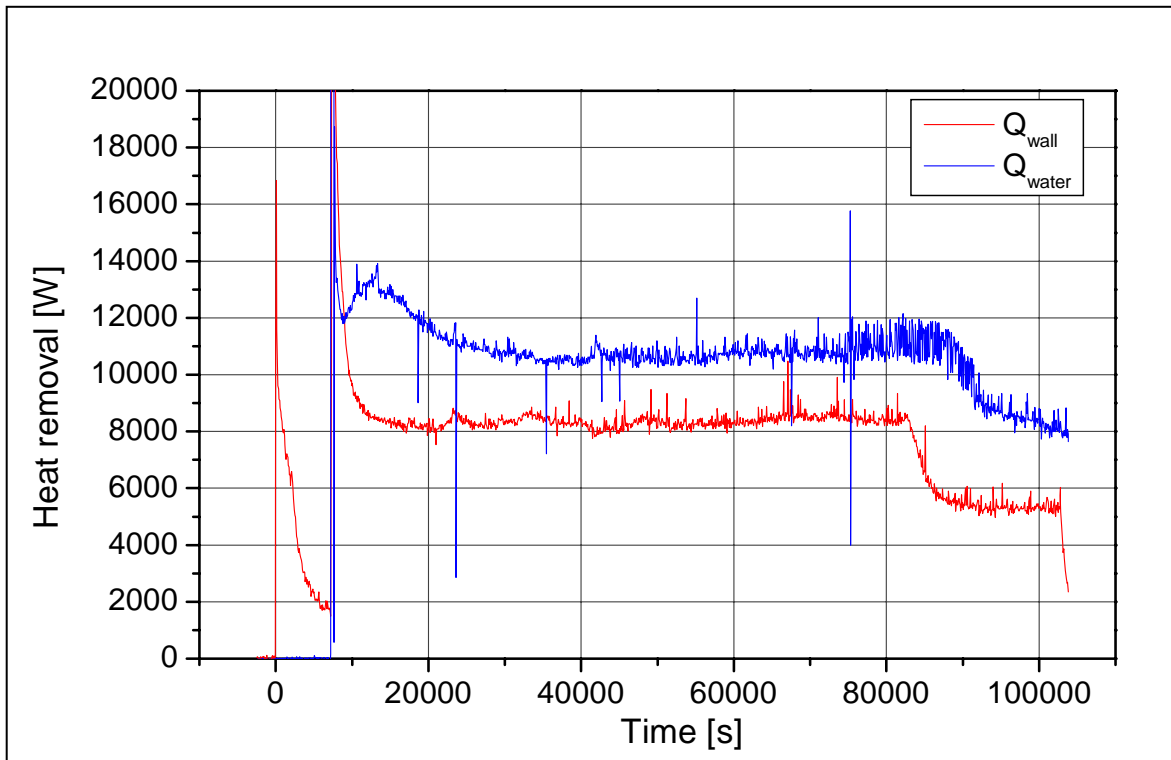


Figure 18: Heat balance between the heat transfer through the vessel wall and the heat removed by cooling water in LIVE-L1

3.2.4.2 Heat flux measured by heat flux sensors in LIVE-L1

In the experiment LIVE-L1 the test vessel wall was equipped with 5 instrumented plugs with 5 commercial heat flux sensors along the meridian at 67.5° . These heat flux sensors are part of the vessel wall and are positioned 1 mm below the inner surface of the test vessel. The position of the heat flux sensors is shown in Figure A- 1 in Annex A.2. The heat fluxes measured by the heat flux sensors are shown in Figure 19. At the time of melt pouring (0 s) and at the time of start of outer vessel cooling (~ 7200 s) high transient heat fluxes have been measured. The values are given in Table 7. In Table 7 the position of the heat flux sensors is also included as angle relating to the vertical central axis of the test vessel. The heat flux sensor HF14 with the angle of 76.5° is positioned about 70 mm above the melt surface, therefore its values should not be taken into account during the evaluation of the test as non-realistic.

At the time of pouring, the maximum transient heat flux of $\sim 65519 \text{ W/m}^2$ is measured by the heat flux sensor HF1 located at the bottom of the test vessel clearly because of the central melt pour. At the time of flooding the maximum heat flux of 92016 W/m^2 was measured by the heat flux sensor HF6. This is as well reasonable since the temperature of the melt at the position of HF6 (183 mm above the test vessel bottom) was significantly higher than at the other positions (see e.g. thermocouple IT7 readings in Figure C- 4).

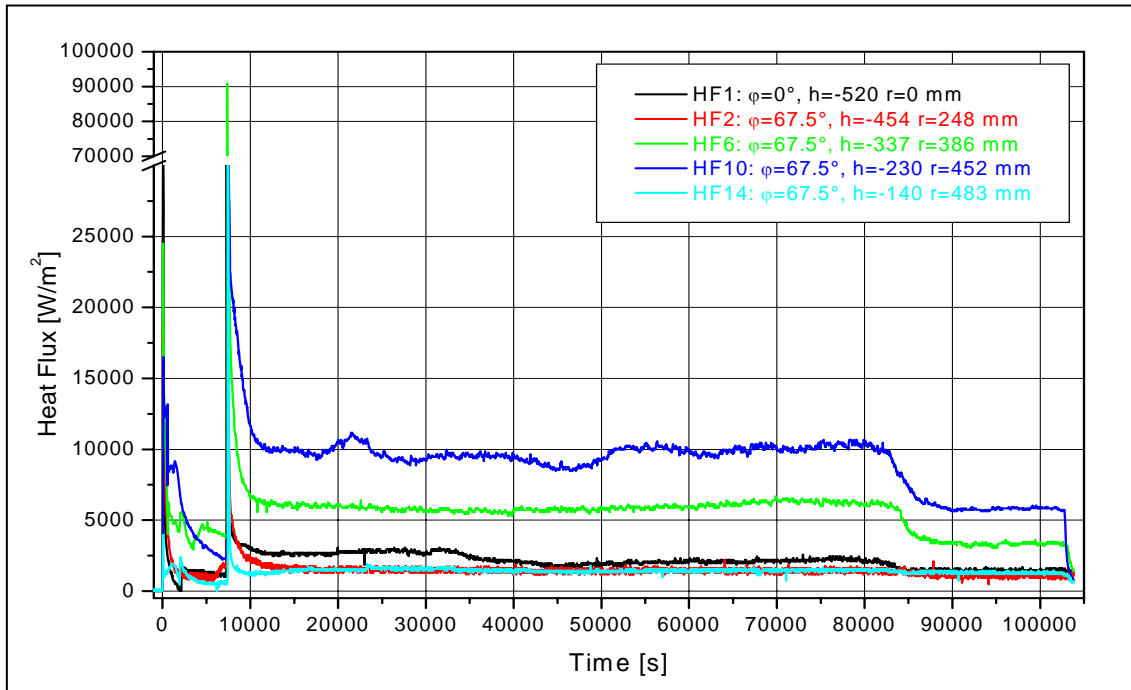


Figure 19: Measured heat fluxes of the heat flux sensors in LIVE-L1

Table 7: Transient and steady state heat fluxes measured by heat flux sensors in LIVE-L1

	Vertical angle [°]	Max. transient q at pouring [W/m ²]	Max. transient q at flooding [W/m ²]	q at 10kW steady state 80064 s	q at 7kW Steady state 102853 s
HF1	0	65519	44705	2245	1470
HF2	30	20862	69228	1432	1075
HF6	51	24500	92016	6143	3233
HF10	65.5	16703	62384	10513	4982
HF14	76.5	4338	49410	1485	1162

In Table 7 the measured heat fluxes at steady state for the test period with 10 kW and with 7 kW heating power are shown. The given values are averaged for 30 s, i.e. the average of all values 15 s before and 15 s after the given time point in Table 7. The heat fluxes at steady state for the 10 kW test period are distinctively lower than the heat fluxes in the transient phases. The highest heat flux is measured by HF10 which is just below the melt surface (the

melt surface is located at the vertical angle of 67.25°), followed by the heat flux sensors HF6 and finally by the heat flux sensors HF2, HF1 and HF14. During the test phase with 7 kW, heating power the same order can be observed.

3.2.4.3 Calculated heat fluxes in LIVE-L1

The heat flux q through a plane wall is given by:

$$q = -k \cdot (OT - IT) / L \quad (3.3)$$

where

q = heat flux [W/m²]

k = thermal conductivity of the wall [W/mK]

OT = wall outside temperature

IT = wall inside temperature

L = wall thickness [m]

To calculate the heat flux through a spherical wall, which is the case for the LIVE test vessel, the heat flux expressed in equation (3.3) should be corrected accordingly. Assuming the inside area of a spherical wall is the same as that of a plane wall, and the spherical wall has also the same thickness as that of the plane wall one can obtain:

$$q_{sph} = q_{pla} \cdot (Ri / Ro) \quad (3.4)$$

where

Ri = radius to the inner spherical wall [m]

Ro = radius to the outer spherical wall [m]

In Table 8, the correction factor “ Ri/Ro ” for the five horizontal heat flux zones is given.

Table 8: Heat flux form correction factor for spherical form and wall thickness

	Zone 1	Zone 2	Zone 3	Zone 4	Zone 5
Thermocouple	IT1/OT1	IT3/OT3	IT7/OT7	IT11/OT11	IT15/OT15
Vertical angle [°]	0	30	51	65.5	76.5
Ri/Ro	0.956	0.956	0.955	0.955	0.955
Wall thickness [mm]	23.3	23.5	23.63	23.76	23.9

The wall thickness is measured at the local positions of IT/OT thermocouples. The groove depth for the IT thermocouples is 0.5 mm, and that for the OT thermocouples is 1 mm.

Therefore the half of the total groove depth should be deducted from the wall thickness. In Table 8 the real wall thickness at the positions of IT/OT thermocouples is given.

The wall of the test vessel is made of stainless steel AISI316Ti, the material number is X6CrNiMoTi17-12-2. The thermal conductivity of this material is taken from [13] and is shown in Table 9.

Table 9: Heat conductivity of AISI316Ti

Temperature [K]	300	400	600
Thermal conductivity [W/(mK)]	13.4	15.2	18.3

Since the working temperature of the test vessel for the LIVE-L1 test is between 300 K and 400 K, following equation can be obtained from the data in Table 9. The temperatures are given in K.

$$k(T) = 13.4 + 0.018 \cdot (T - 300) \quad (3.5)$$

The temperature difference between the inside and the outside wall in equation (3.3) can be determined by the wall inside temperature which was measured by IT thermocouples and the wall outside temperature which was measured by OT thermocouples (Table 8). The IT and OT thermocouples are located at 112.5° of the vessel horizontal angle and at the same vertical level as the plugs with the heat flux sensors in each heat flux zone.

In the following, the results of the calculation of the heat fluxes based on the measurement of the inner wall temperature by IT thermocouples are described in detail.

The calculated heat fluxes based on the IT/OT values during the whole test LIVE-L1 are shown in Figure 20. The results show that the highest heat flux at the steady state is in the Zone 4 (heat flux q_{IT11}), which is just below the melt surface (the melt surface is located at the vertical angle of 67.25°). The second highest heat flux zone is in the Zone 3 (q_{IT7}), the level below the Zone 4. The lowest heat flux is at the vertical angle of 30° (Zone 2) and above the melt surface (Zone 5).

In Table 10, the heat fluxes are given as a 30 seconds average at the steady state of 10 kW and 7 kW heating periods. These values are also illustrated in Figure 21. Figure 21 also demonstrates that by increasing the heat generation in the melt pool, the intensity of the heat transfer through the vessel wall shifts upwards. E.g. during the 10 kW heating period the heat flux in the Zone 4 is twice of that in Zone 3, and 4 to 6 times higher than in the Zones 2 and 1.

It is also observed that during the 10 kW steady state test period, the heat flux in the Zone 4 fluctuated. However, this phenomenon was not observed in the LIVE-L3 test.

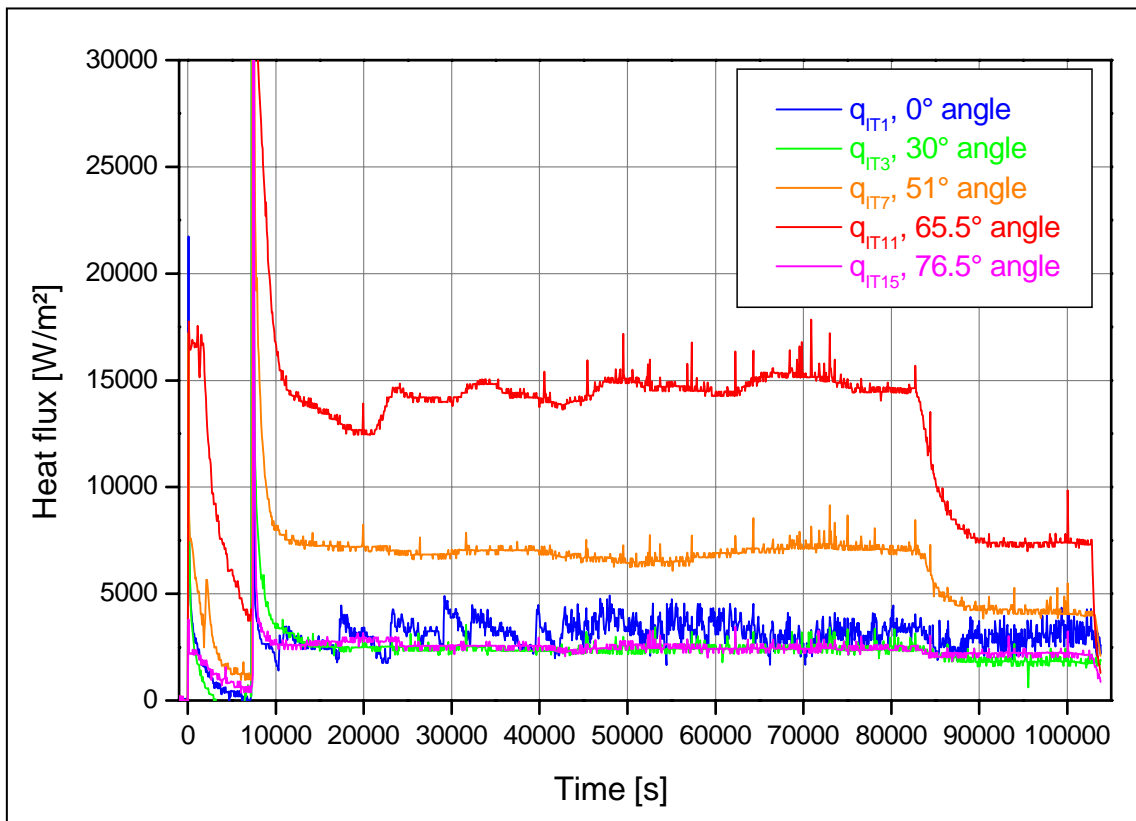


Figure 20: Distribution of the calculated heat flux based on IT thermocouples during the whole experiment LIVE-L1

Table 10: Calculated heat fluxes at the steady state of 10 kW and 7 kW heating power in LIVE-L1

Heat flux	Area zone	Vertical angle [°]	q at 10kW Time: 80064sec	q at 7kW Time: 102853sec
q_{IT1}	Zone 1	0	3322	3327
q_{IT3}	Zone 2	30	2421	1930
q_{IT7}	Zone 3	51	7052	4153
q_{IT11}	Zone 4	65.5	14525	6793
q_{IT15}	Zone 5	76.5	2409	2056

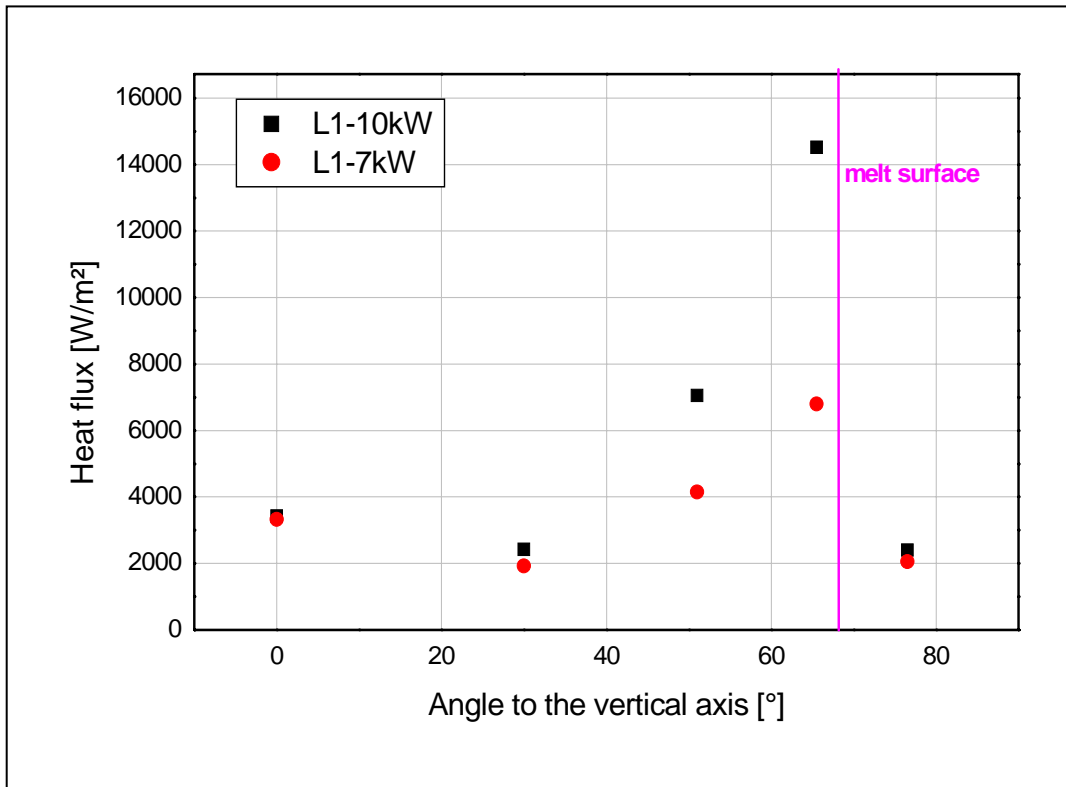


Figure 21: Calculated heat flux distribution along the vessel wall in LIVE-L1

Two transient phases during the LIVE-L1 test are characterised by a pronounced increase of the heat flux through the vessel wall. One was at the beginning of the test when the melt was poured in the test vessel; the other one was at the beginning of the external water flooding at ~7200 seconds. The heat flux reached its maximum at the moment of water flooding (Figure 22) with the highest value of 169 kW/m² observed in the Zone 3. Subsequently, the heat flux rapidly decreased in about 6 minutes, and then continued to decrease slowly to the steady-state value (Figure 22). The slow reduction of the heat flux took about three to four hours. In Table 11, the time of flooding, the time of the transition from fast reduction to slow reduction of heat flux and the maximum heat fluxes are given.

Table 11: Calculated transient heat fluxes after water flooding in LIVE-L1

	Start of flooding [s]	Transition time point to the slowly reduction of q [s]	Time point to the q steady state [s]	Max. q [W/m ²]	q at the transition time [W/m ²]
Zone 1	7248	7600	~11000	92537	4950
Zone 2	7282	7600	~15000	139998	11000
Zone 3	7335	7640	~25750	168752	22000
Zone 4	7384	7660	~21000	152067	32500

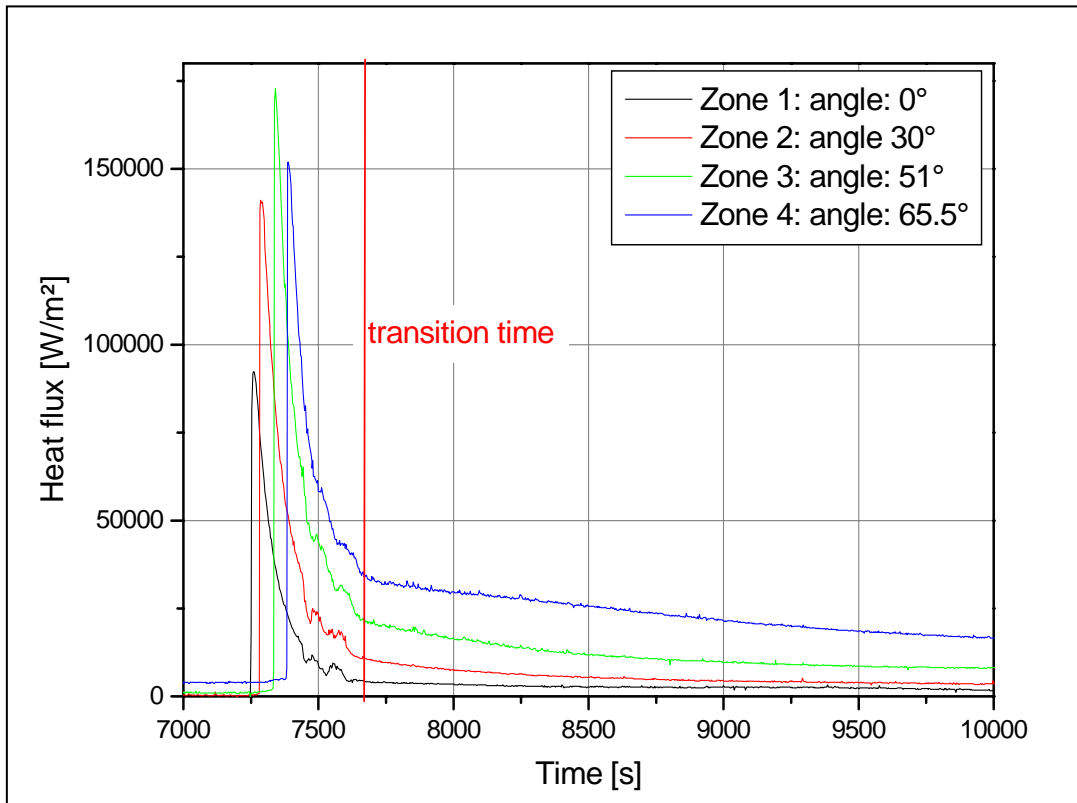


Figure 22: Calculated heat flux development after water flooding in LIVE-L1

Besides the calculation of the heat fluxes with the measurements of the IT/OT thermocouples, the heat fluxes are also calculated with the wall inside temperatures measured by PT thermocouples of the instrumented plugs (situated at the vessel inner surface, e.g. PT11), see Figure C- 9 to Figure C- 14 in Annex C.

A comparison between the calculated heat fluxes will be given in chapter 4.2.4.4.

3.2.5 Melt surface behaviour in LIVE-L1

As it is described in the section 2.4, the infrared camera is installed at the lid of the facility to observe the melt surface behaviour near to the vessel wall. The recorded thermograms are used to measure the temperature distribution on the surface of the molten pool and to identify the convection patterns in the fluid during different stages of experiments.

The analysis of recordings shows a complex picture of the fluid motion at the upper surface, the general trend being that the fluid is transported from the center of the pool to the vessel outer wall. To quantify the flow velocity, the IR pictures were analysed similarly to particle image velocimetry (PIV). Instead of seeds used in PIV, moving areas of the melt surface with distinctive patterns were used (examples are given in the section 4.2.5 where similar analysis of the LIVE-L3 test is described), assuming that they follow the flow dynamics. The displacement of the patterns after 2 seconds was determined and the flow velocity was calculated. In LIVE-L1 the flow velocity of the upper surface has been analysed only for the first steady state phase of the test with 10 kW heat generation. The results of the measurements are presented in Figure 23. The X axis is given in the dimensionless term R/R_{ves} where R is the starting radial position of the analysed point and R_{ves} is the vessel radius (50 cm). The complex motion pattern leads to a large scatter of the results, the calculated velocities are within the range 0.1-0.3 cm/s.

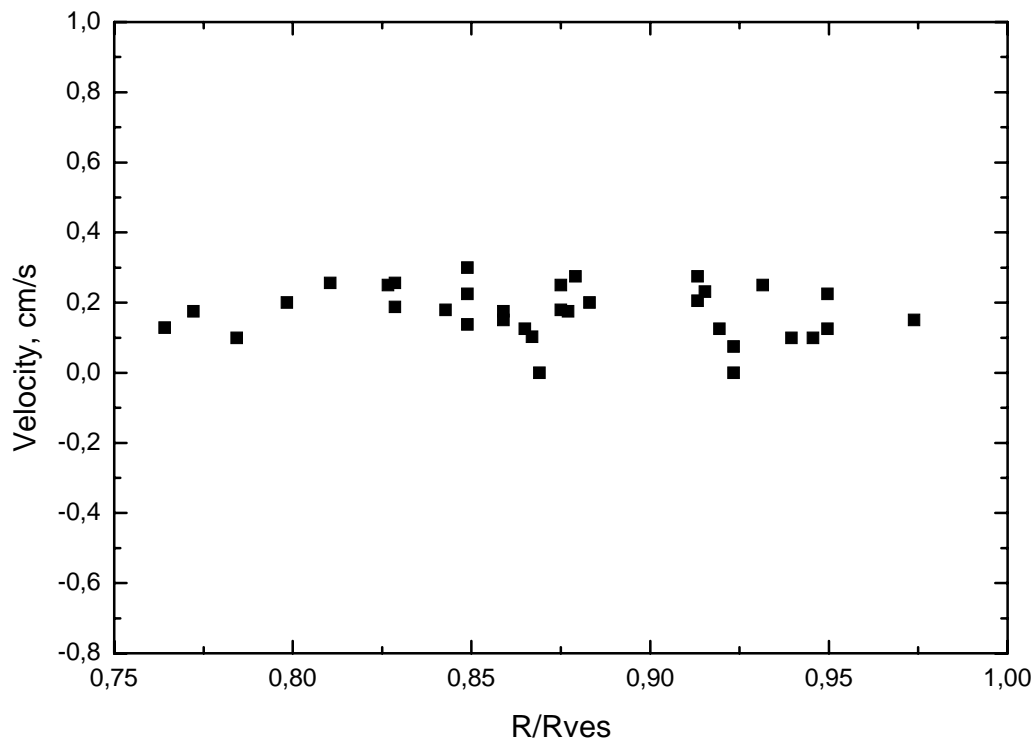


Figure 23: Flow velocity measured at the upper surface of the LIVE-L1 test during 10 kW heating phase.

3.2.6 Post-test analysis in LIVE-L1

As mentioned in chapter 3.2.1, about 218 kg of nitrate melt, corresponding to 117 l, was poured into the test vessel at the beginning of the test. At the end of the test, 161 kg of liquid melt was extracted into the heating furnace, thus resulting in 57 kg of the crust after the 7 kW heating period. The mass of the crust corresponds to 26 % of the original amount of the initial poured melt mass.

After the extraction of the melt and after the cool down of the test facility, the disassembly of the test rig was started. In Figure 24 a view of the test vessel after removing of the top lid of the test vessel is shown. The crust which was formed during the test at the vessel wall can be seen clearly. The thickness of the crust was measured along the section 67.5°-247.5° and different samples were taken to investigate the crust characteristics and composition. In the following chapters, the detailed post-test analysis is described.



Figure 24: View of the test vessel after disassembly of the lid in LIVE-L1

3.2.6.1 Average melt composition in LIVE-L1

To determine the melt composition at the beginning and at the end of the test, two material samples were collected. Sample 1 was taken from the crust formed at the pouring spout and its composition corresponds to the composition of the original melt. Sample 2 was collected by a stainless steel rod which was inserted into the melt pool just before the end of the test.

The analysis of these melt samples is important in two aspects: 1) for the comparison of the real melt composition with the composition planned for the test and 2) for the evaluation of the changes in the melt composition caused by the crust formation and depletion of the high temperature melt component KNO_3 .

The composition of the melt samples was analysed with the cation determination method. The results are shown in Table 12. They clearly demonstrate that the real composition (Sample 1) was very close to the planned one.

Table 12: Planned melt composition and melt and crust composition in LIVE-L1

	Planned	Before test (sample L1-M1)	End of test (sample L1-M2)	Inner Crust to the melt pool (sample L1-C1)	Outer Crust to the vessel wall Sample (L1-C2)
KNO_3 [mole%]	80	79.9	78.3	91.5	91.3
NaNO_3 [mole%]	20	20.1	21.7	8.5	8.7
Na/K ratio [mole/mole]	0.25	0.25	0.28	0.09	0.09
KNO_3 [w%]	82.6	82.6	81.1	92.8	92.6
NaNO_3 [w%]	17.4	17.4	18.9	7.2	7.4

The composition of the melt at the end of the test is depleted of KNO_3 meaning that the initial KNO_3 fraction was reduced by ~1.7 mole% during the experiment. This demonstrates the fact, that the high temperature melt component KNO_3 is enriched in the crust according to the phase diagram shown in Figure 5. This observation is in a good agreement with the post-test chemical analysis of the crust performed at two locations, Table 12, which indicated that the amount of KNO_3 in the crust has been increased to ~91 mole% compared to the initial value of 80 mole%. The detailed analysis of crust composition is given in chapter 3.2.6.4.

3.2.6.2 Crust growth rate in LIVE-L1

The crust growth rate can be determined by the temperature profiles measured by the thermocouple trees (CT1* to CT3*). The measurements of the thermocouple trees throughout the whole experiment are given in Annex C.1. Figure 25 shows a section of the temperature profiles of the thermocouple tree CT2 during the test. The X axis shows the time after flooding, which means the time 0 s is related to the start of flooding after about 7200 s. Before the flooding initiation no crust was formed at the location of the CT2 thermocouple tree (all measured temperatures are above the liquidus, as shown in Figure 25).

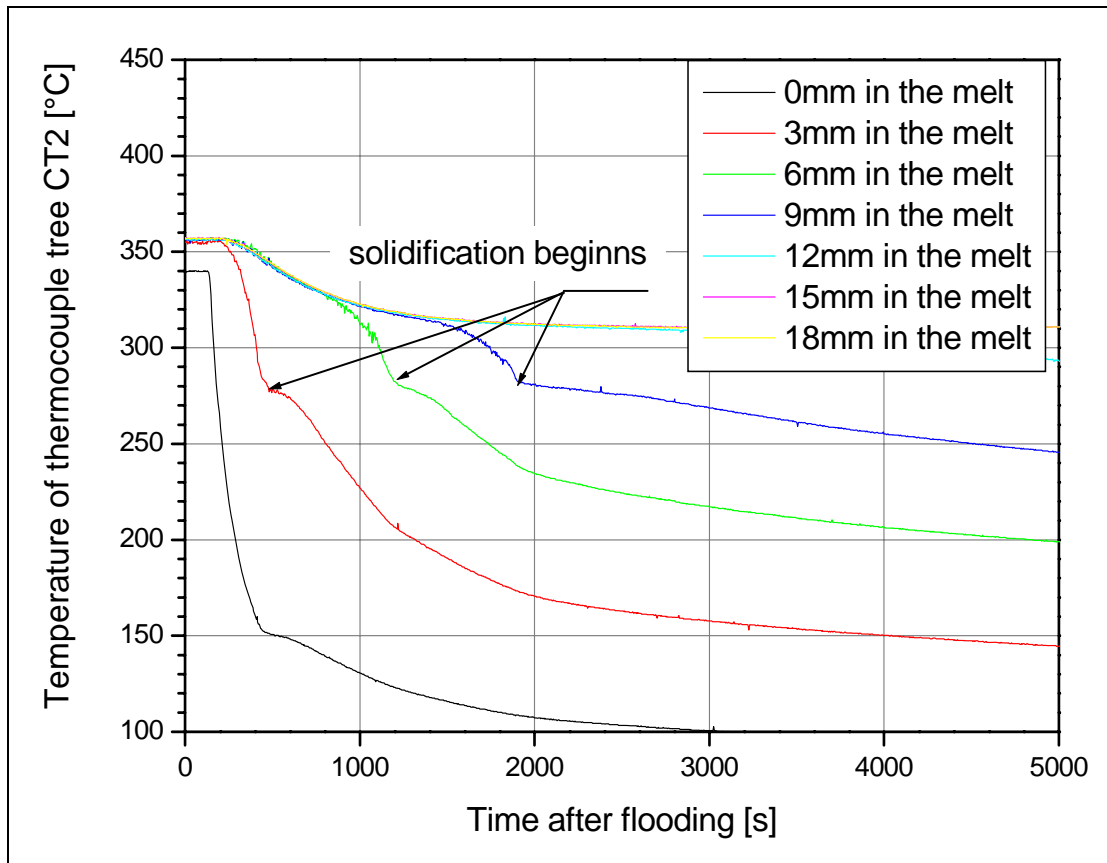


Figure 25: Solidification points in the crust temperature measurements of CT2

The disturbances in the decreasing temperature curves indicate the beginning of melt solidification. Based on the stagnation time and the position of the temperature measurement, the crust growth rate was determined.

Figure 26 shows the crust development over the time at three different heights along the vessel wall. At the position of the lowest thermocouple tree, CT1, the crust thickness exceeds the measurement range. Therefore, the final thickness of the crust at this position could not be determined by the thermocouple tree. This problem was solved in later tests by increasing the distance between the thermocouples in CT1 from 5 mm to 8 mm.

The dependence of the crust growth rate on the transient heat flux through the vessel wall during the crust formation periods was studied. Following the assumptions about the heat flux are given: at the position of CT1, the heat flux is the sum of 70% q_{IT3} and 30% q_{IT7} (calculated transient heat flux at the time of solidification); at the position of CT2, the local heat flux corresponds to q_{IT7} and at the position of CT3, the local heat flux corresponds to q_{IT11} . In Table 13 the local transient heat fluxes through the wall and the corresponding crust growth rate are listed.

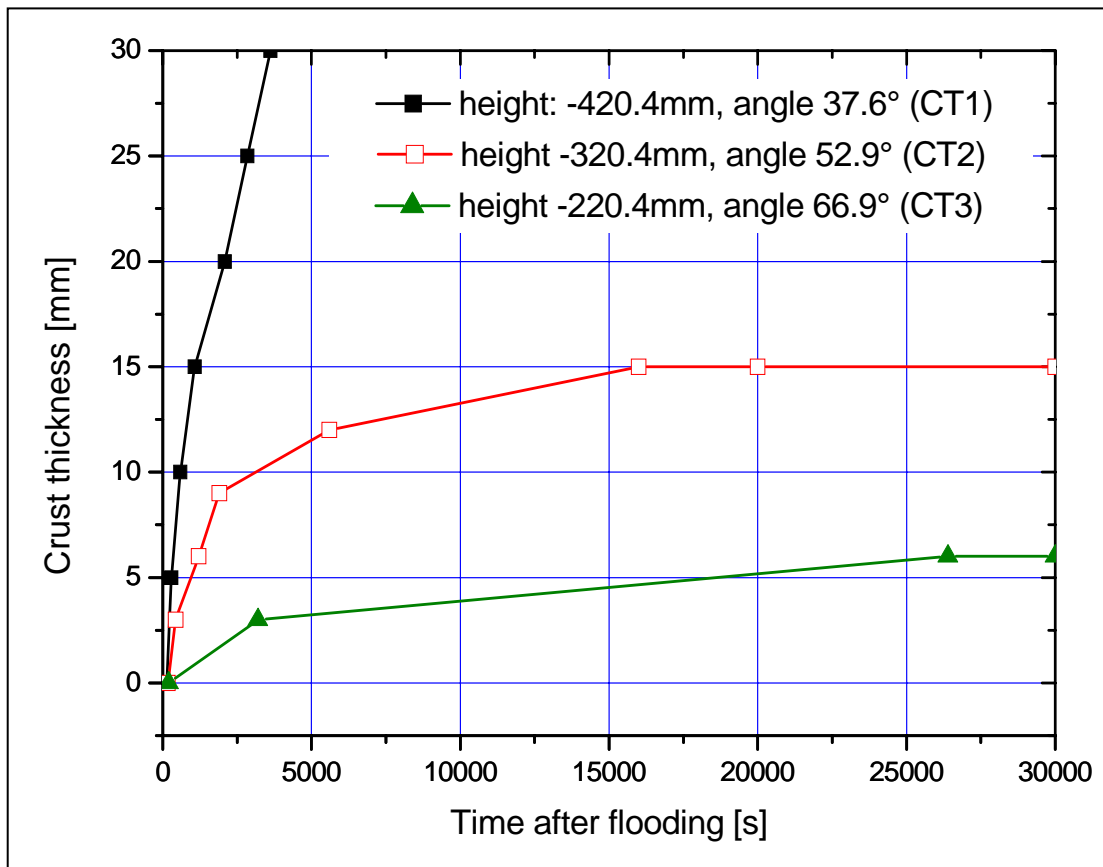


Figure 26: Crust thickness in dependence of the time in LIVE-L1

Table 13: Heat flux and corresponding crust growth rate in LIVE-L1

CT1 (37.6°) mm in melt	q [W/m ²]	Crust growth rate [mm/s]	CT2 (52.9°) mm in melt	q [W/m ²]	Crust growth rate [mm/s]	CT3 (66.9°) mm in melt	q [W/m ²]	Crust growth rate [mm/s]
0	110564		3	97408		3	125033	
5	29788	0.0313	6	22638	0.0118	6	15706	0.0010
10	12040	0.0164	9	12467	0.0039*	9	14826	0.0001
15	8193	0.0102	12	9448	0.0043*	12		liquid
20	5645	0.0056*	15	7275	0.0008	15		liquid
25	4895	0.0058*	18		liquid	18		liquid
30	3299	0.0065	21		liquid	21		liquid

Furthermore, Table 13 shows that the crust growth rate was considerably higher at the beginning of flooding and was reduced later on. It was observed that at a certain time period, a quasi metallurgical steady-state of the crust growth approaches [14], i.e. the crust grows with a constant rate during this phase. These periods are marked with "*" in Table 13. Comparing

the heat flux during the metallurgical steady state with those given in Table 11, it can be concluded that the steady growth of the crust took place during the period of slow reduction of heat flux during the transient state.

For nuclear safety it is important to determine the time period from the beginning of water cooling to the melt thermohydraulic steady state, at which the crust thickness remains quasi constant (the slow reduction of residual heat is not considered). This time period is also called as the “characteristic time” in different publications [15]. It was determined for the position of CT2 during the LIVE-L1 test and amounted to 13000 seconds or 217 minutes. In [15] it is reported that the characteristic time for such a 20-80 mole% $\text{NaNO}_3\text{-KNO}_3$ melt is 16-160 minutes to reach a constant heat flux from the melt pool to the crust interface (neglecting the latent heat release during the solidification process). Analysis of the CT2 results in the LIVE-L1 test does not agree with these predictions.

The final thickness of the crust is given in Figure 27. The crust thickness at the bottom of the test vessel can be higher than the real one, since a small amount of melt was not extracted back to the heating furnace at the end of the test due to technical reasons.

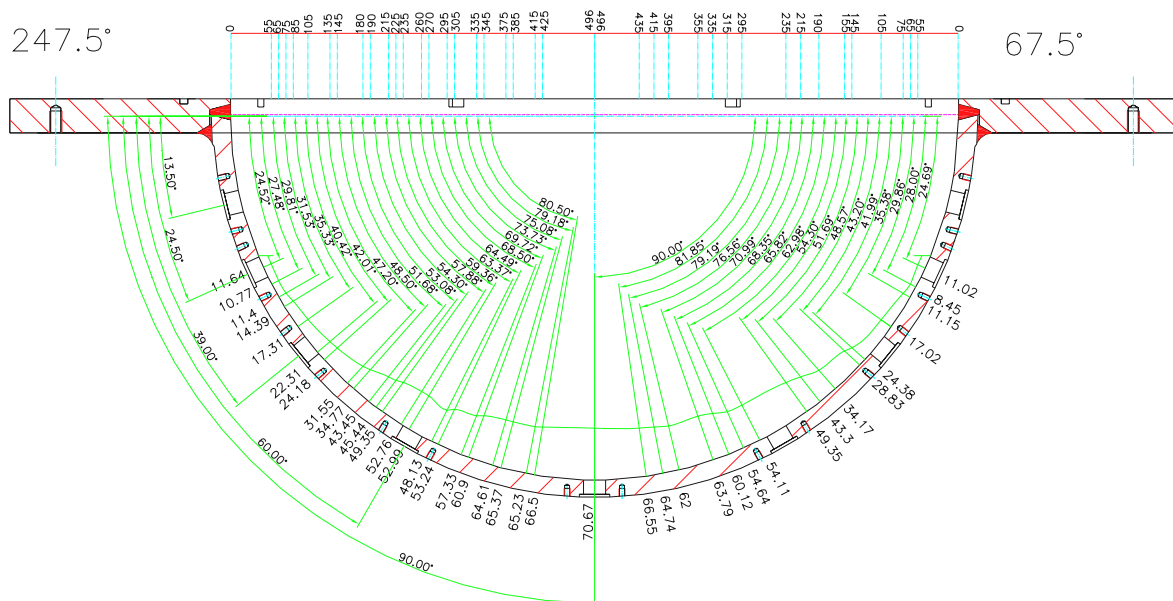


Figure 27: The final crust thickness at the end of the test LIVE-L1

The final crust thickness is also presented in Figure 28. Here the crust thickness along the meridians at 67.5° and at 247.5° is shown. The X axis shows the angle to the horizontal axis, which means that the angle 90° is the bottom of the test vessel and the angle 0° is the upper edge of the test vessel. In LIVE-L1 the thickness of the crust was highest at the bottom of the test vessel. In Figure 28 also the positions of the heat flux sensors are shown.

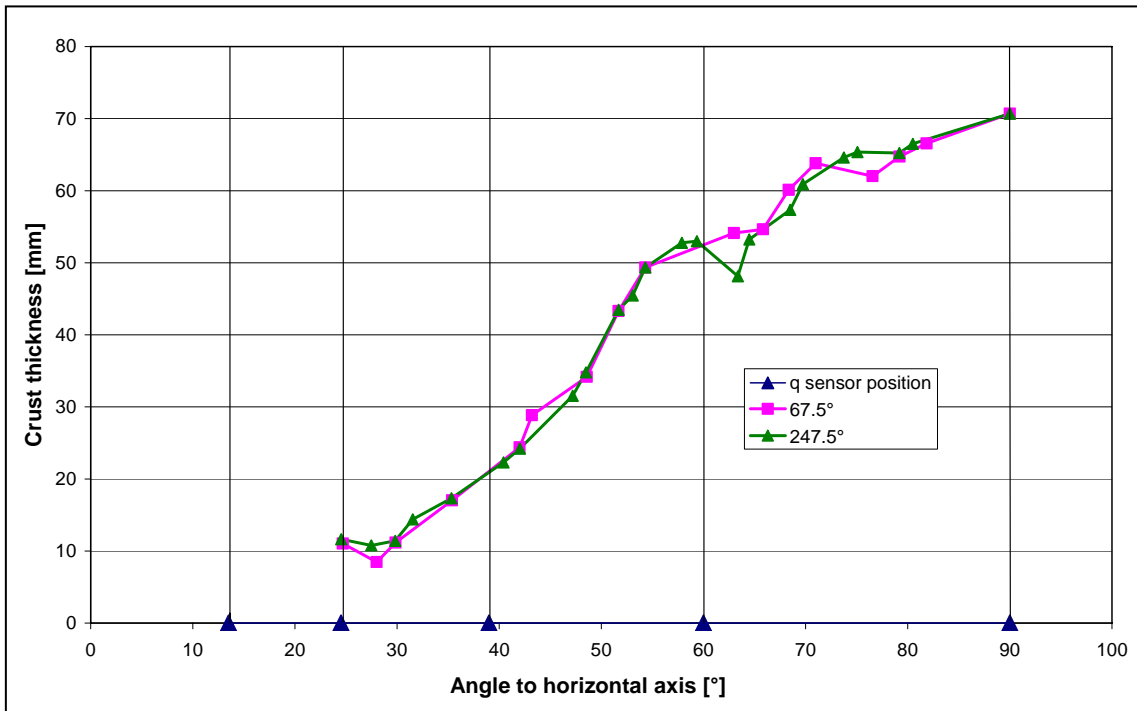


Figure 28: Crust thickness along the meridians at 67.5° and 247.5° in LIVE-L1

The final thickness of the crust can be influenced by gap formation between the crust and the vessel wall. This gap can be formed due to the shrinkage of the crust upon cool-down. Gap formation is indicated by the temperature readings of the thermocouple CT11 of the thermocouple tree CT1, located 0 mm in the melt, Figure 29.

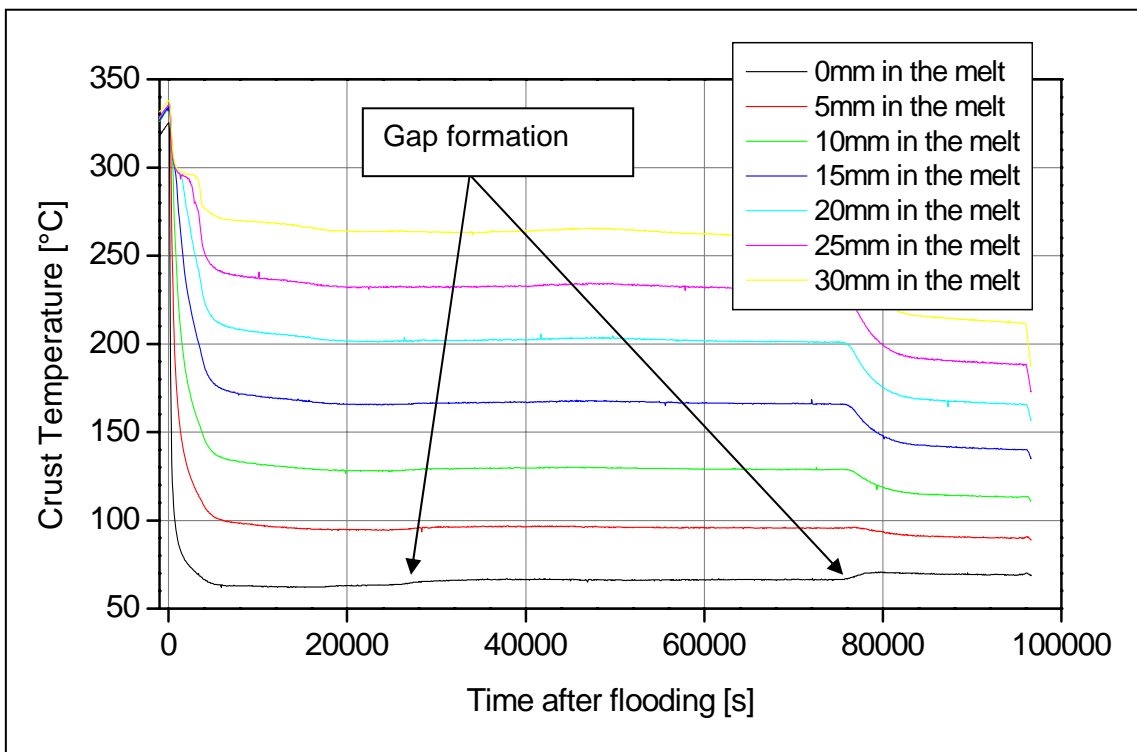


Figure 29: Crust temperature of CT1 in LIVE-L1, 37.6° to the vertical axis

However, the increase of temperature during the 10 kW and 7 kW heating periods is not consistent with the crust growth process assuming that no gap between the crust and the vessel wall was formed. At other positions where the crust layer is thinner, like at CT2 and CT3, such phenomenon is not obviously observed. One of the possible explanations could be that the thermocouple is embedded in the crust at the beginning of the crust formation process. As the crust becomes thicker and its temperature decreases, the crust can be detached from the vessel wall (shrinkage) and the thermocouple CT11 is entrained by the crust and is removed from the vessel wall. As a consequence, the crust turns warmer due to the reduced heat conduction caused by the gap formation.

3.2.6.3 Crust morphology and microstructure in LIVE-L1

Two-layer structure of the crust was observed post-test, as shown in Figure 30. The outer layer was formed during the 10 kW heating period and the inner layer was formed during the 7 kW heating period. The outer layer is hard and solid, whereas the inner layer is fragile. The thickness of the two crust layers are measured at three positions as shown in Table 14.

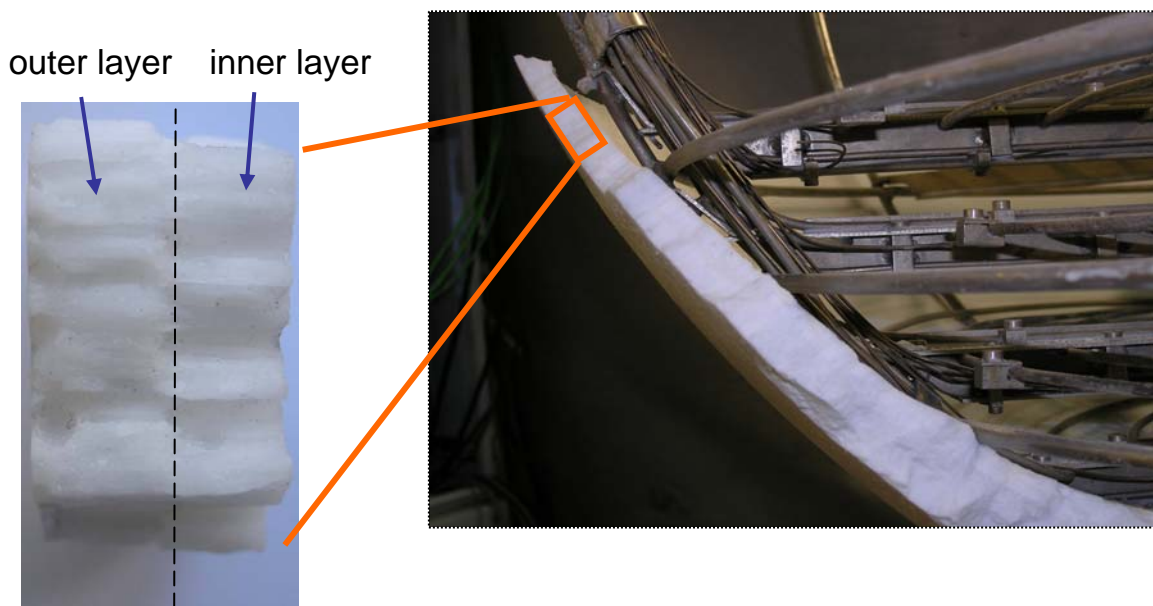


Figure 30: Two-layer structure of the crust formed in the LIVE-L1 test

Table 14: Thickness of the outer layer and the inner layer of the crust in LIVE-L1

	Position 1	Position 2	Position 3
Angle [°]	62	51	41.4
Radius [mm]	421	385.6	306
Total crust thickness [mm]	13	20.9	34.3
Outer layer thickness [mm]	7.5	14.2	24.3
Inner layer thickness [mm]	5.5	6.7	10

The crust microstructure is examined with SEM-EDX line-scanning and point analysis. The cross-section of a 20 mm thick sample of the crust was ground and coated with carbon for SEM-EDX analysis. Figure 31 shows the overview of the crust inner and outer layers. A SEM-EDX line-scanning has been performed at the green line position indicated in the pictures, and the count spectra of Na and K elements are given below each picture.

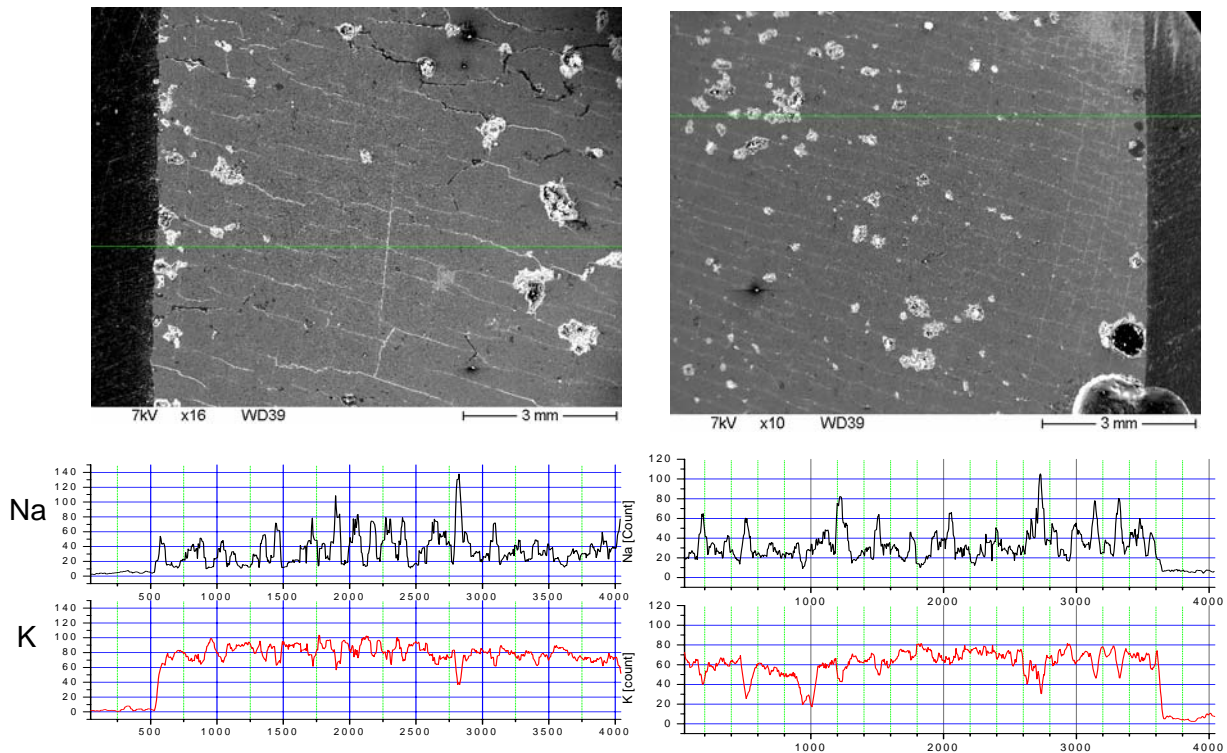


Figure 31: SEM-EDX line-scanning of LIVE-L1 crust: Left: crust inner layer; right: crust outer layer

Microscopic cracks are observed in the crust inner layer, which are responsible for the fragile characteristic of this layer. The SEM-EDX line-scanning of both inner layer and outer layers shows different enrichment of K and Na in the crust. The heterogeneous elemental distribution indicates that the crust was formed under constitutional supercooling conditions. Under this condition, the local melt temperature ahead of the crust solidification front is below the local melt liquidus temperature [16]. More details of the microstructure can be revealed in Figure 33.

SEM-pictures at 900 magnification were taken at the following positions: crust inner surface (in), in the middle of the inner layer (in-mid), at the boundary inner layer/outer layer (mid), in the middle of the outer layer (mid-out) and at the outer surface (out) (Figure 32).

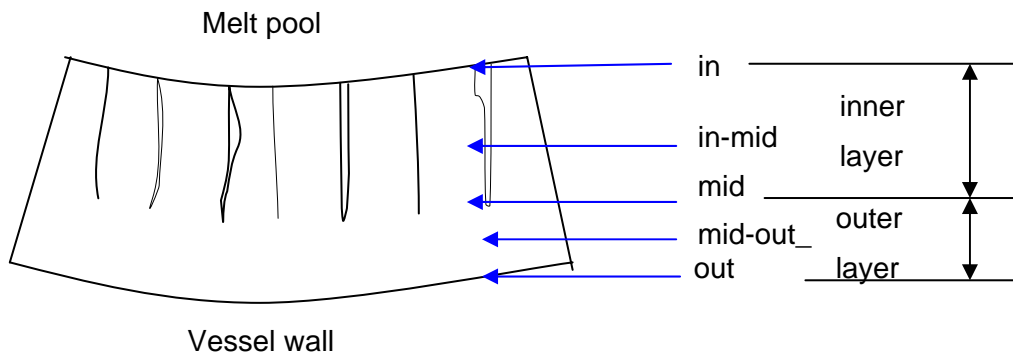


Figure 32 Sampling positions at the cross-section of the crust

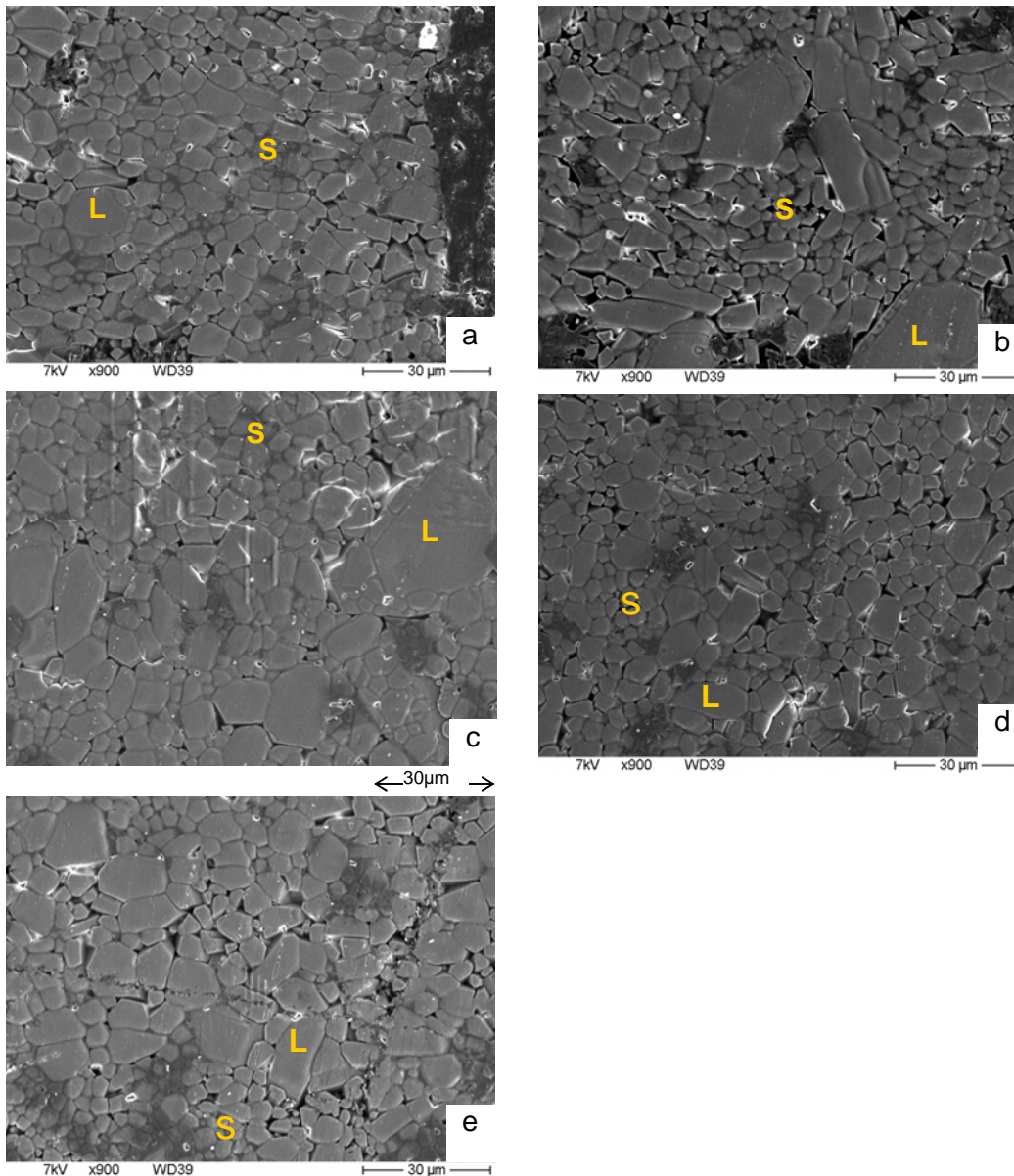


Figure 33: Crust microstructure of a) outer surface; b) middle of the outer layer; c) interface outer layer/inner layer; d) middle of the inner layer and e) inner surface. Magnification: 900x

Elemental quantitative analysis is performed at the position of “L” (large grain) and “S” (small grain) in the SEM-pictures in Figure 33. The elemental distribution is illustrated in Figure 34. Certain errors can be induced to the analysis due to e.g. other alkali compounds which were selected for the alkali standard calibration (no commercial alkali nitrate standard can be found), and to the random selection of large and small crystal grains.

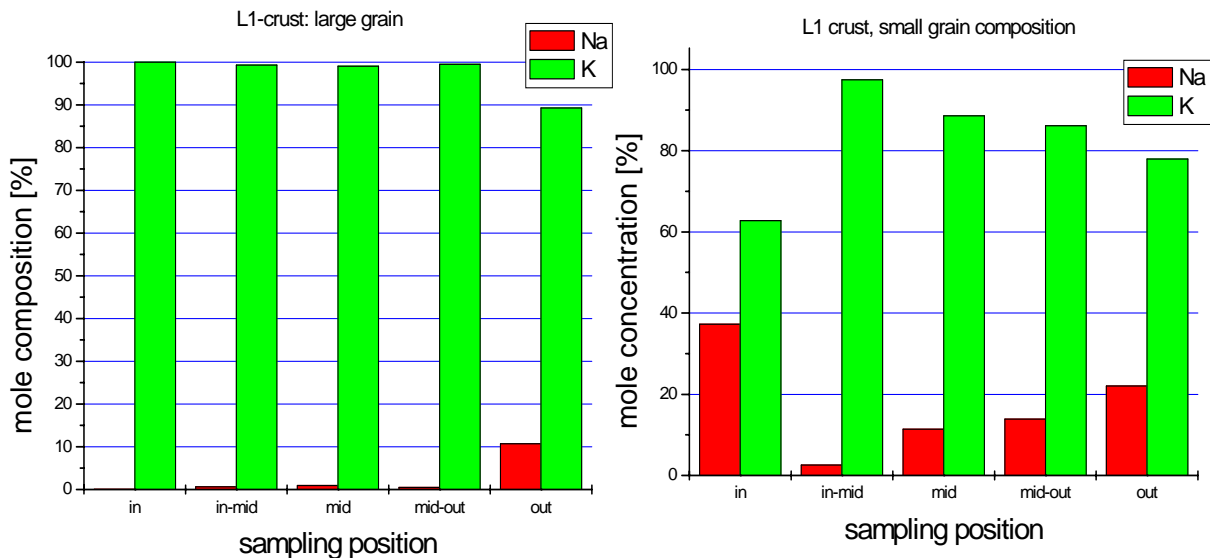


Figure 34: Na and K mole distribution in large grains and in small grains in the crust

Given the measurement inaccuracy, the following trends regarding the elemental distribution were observed:

- Large grains are enriched with the refractory compound KNO_3 , whereas small grains are enriched with NaNO_3 . Since refractory elements are enriched in crystal dendrites during solidification process, the position of large grains corresponds to the original dendrites in the crust.
- The concentration of Na and K both in large grains and in small grains across the crust thickness is different. The degree of segregation of Na and K in the crystal grains depends on the crust growth rate and the diffusion rate of NaNO_3 in the crust front to the melt pool.

3.2.6.4 Crust liquidus temperature and crust composition in LIVE-L1

The liquidus temperature of the crust is an important parameter for the calculation of melt pool heat transfer, since based on phase diagram, the liquidus temperature of the local melt ahead of the crust, which is one of the boundary conditions for the melt pool heat transfer calculation, can be deduced from the crust liquidus temperature. In addition, crust liquidus temperature indicates the local crust composition, which reflects the crust formation process.

Two methods are applied to determine the liquidus temperature of the crust. In the first method a melting temperature equipment named “Optimelt” is used. It measures the optic change of a powder specimen located in a capillary tube with a defined rising rate of temperature. When the specimen is completely melted, or in other words, the melt is completely clear, the liquidus temperature is reached. The second method is a furnace test. In this test, the specimen is first melted and then the temperature change in the melt is measured during cool-down. At the liquidus point, the melt temperature stagnates for a while (due to the latent heat), and then decreases further.

The “Optimelt” method is a fast and convenient one. Another advantage of this method is that it needs small amount of specimen material. However, the liquidus temperature measured with “Optimelt” is several degrees higher than the liquidus temperature measured in the furnace test. In the contrary, the results of the furnace test are very reliable. Due to this fact, we have correlated the “Optimelt” tests with the furnace test. For the determination of the liquidus temperature of the crust, the crust sample was measured first with “Optimelt”, and then the liquidus temperature was calculated from the furnace test results.

To check the accuracy of the $\text{KNO}_3\text{-NaNO}_3$ phase diagram, the liquidus temperatures of nitrate salt mixtures from 0 mole% to 20 mole% NaNO_3 have been determined..

Table 15 and Figure 35 show the results of the standard liquidus temperature from our measurements. The liquidus temperatures of our measurements are considerably lower than the liquidus temperatures of the phase diagram cited in [10].

Table 15: Liquidus temperature determination of $\text{KNO}_3\text{-NaNO}_3$ mixtures

mole% of NaNO_3	Furnace test	Cited phase diagram
20	281	295
18	288	299
16	294	303
14	298	308
12	302	313
10	307	318
8	311	322
6	318	325
4	323	328
2	328	333
0	337	337

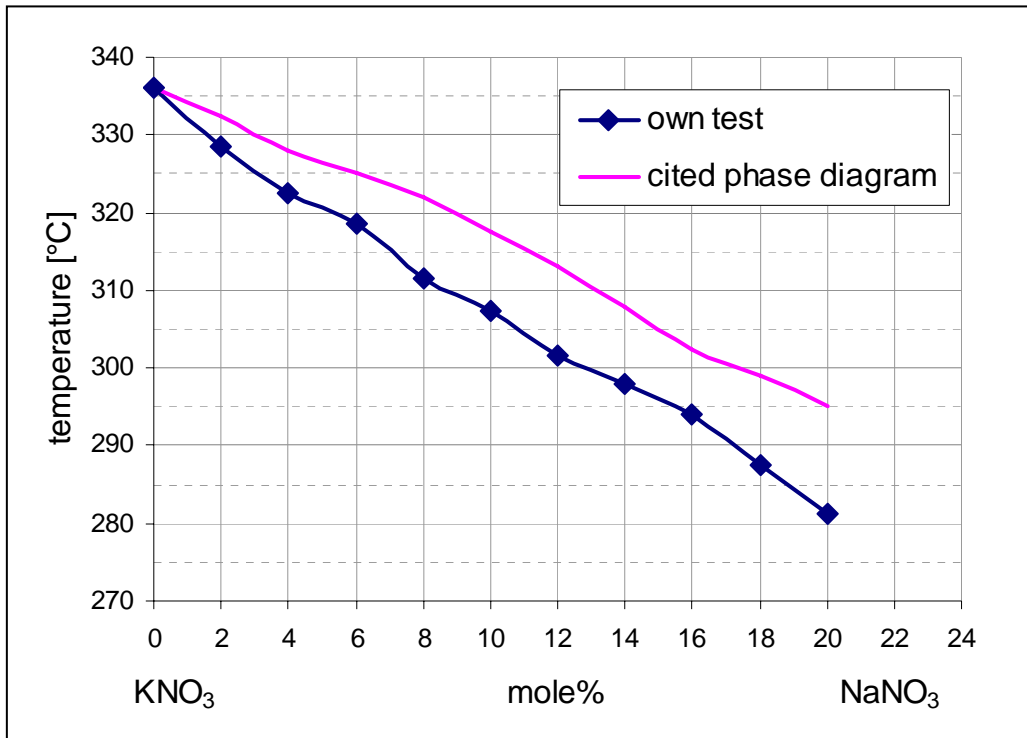


Figure 35: Comparison of determined liquidus temperatures with phase diagram KNO_3 - NaNO_3

Two crust samples 20 mm and 34.6 mm thick were taken for the measurement of the liquidus temperature. For each sample, the same positions used for the SEM-EDX point analysis were studied (see Figure 32).

The local liquidus temperatures and the composition of the crust formed in LIVE-L1 are shown in Table 16 and in Figure 36.

Table 16: Liquidus temperature and composition of LIVE-L1 crust

	Crust thickness 20 mm		Crust thickness 34.6 mm	
	liquidus temp [°C]	NaNO_3 mole%	liquidus temp [°C]	NaNO_3 mole%
in	319	5.7	319	5.7
in-mid	306	10.3	284	19.1
mid	314	7.3	304	11.0
mid-out	281	20.0	281	20.0
out	287	18.3	306	10.3

Higher crust liquidus temperatures are observed at the crust outer surface, i.e. at the boundary of the two layers and at the crust inner surface. At the beginning of water cooling, the local melt composition amounts to the melt pool composition, corresponding to the theoretical crust liquidus temperature of about 328°C (Figure 37).

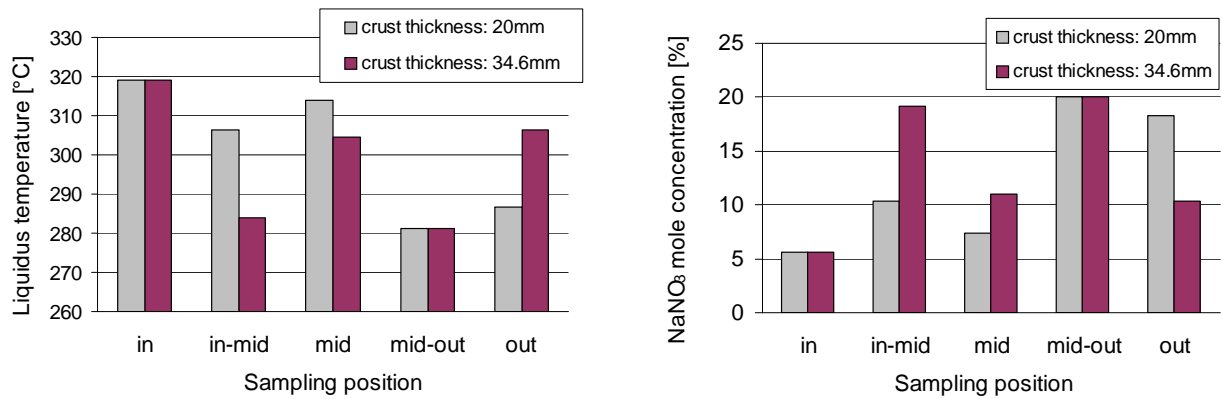


Figure 36: Crust liquidus temperature and composition in LIVE-L1.

As the crust grows further, it is enriched with KNO₃, and therefore the local melt ahead of the crust front is enriched with NaNO₃. This results in decreasing melt liquidus temperature and in decreasing crust liquidus temperature. When the local melt composition approaches to 43% of NaNO₃, the crust liquidus temperature amounts to about 283°C, which is the melt pool liquidus temperature. The post-test analysis demonstrates that the crust position “mid-out” corresponds to this condition during the crust growth process. As the melt pool reaches the thermohydraulic steady state, at which the crust growth rate approaches zero, the concentration gradient of NaNO₃ ahead of the crust disappears, thus the crust liquidus temperature increases again. The crust positions at the end of the 10 kW and 7 kW phases, which are denoted as “mid” and “in”, respectively, correspond to such a condition (Figure 37).

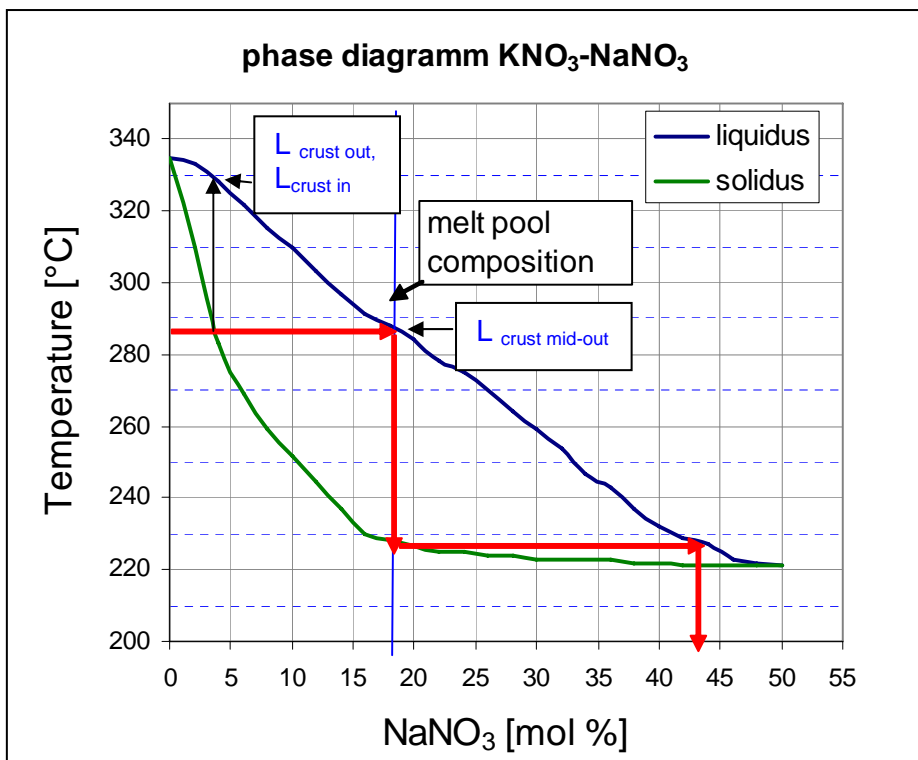


Figure 37: Phase diagram and the crust liquidus temperatures in LIVE-L1

3.2.6.5 Crust porosity and crust thermal conductivity in LIVE-L1

Crust thermal conductivity is an important parameter for the calculation of heat transfer through the crust and the vessel wall. Furthermore, the effective crust conductivity is usually used as an input parameter for the codes applied to describe the melt pool behaviour in the vessel lower head. Usually, the crust thermal conductivity is taken from the literature for the heat transfer calculation. The analysis of the experiment showed, however, that the crust thermal conductivity is not a constant value. The crust thermal conductivity depends on the crust structure, e.g. the porosity of the crust. Since crust structure and porosity strongly depend on different cooling rates or crust growth rates, the crust thermal conductivity is a parameter depended on the crust growth rate.

The crust thermal conductivity can be indirectly measured in the LIVE tests at the positions of thermocouple trees. The crust thermal conductivity of the inner layer and the outer layer of the crust can be calculated at the steady state according to equation (3.6):

$$k = q \cdot L / (\Delta T) \quad (3.6)$$

where

k = thermal conductivity of the crust [W/mK]

q = heat flux at the position of thermocouple tree at steady state [W/m²]

ΔT = temperature difference between the thermocouples

L = distance between the thermocouples [m]

Table 17: The thermal conductivity of the crust layer at the 7 kW steady state period

	Thermocouple	Temp. range [°C]	L [mm]	ΔT [K]	q [W/m ²]	k [W/mK]
	inner layer (crust layer to melt)					
CT2*	CT25-CT27	189-255	6	66	4064	0.368
CT3*	CT32-CT34	128-230	6	102	7386	0.424
	outer layer (crust layer to wall)					
CT1*	CT11-CT17	70-215	30	145	2478.2	0.511
CT2*	CT21-CT25	65-189	12	124	4064	0.392
CT3*	CT31-CT32	74-128	3	54	7386	0.408

In Table 17, the crust thermal conductivity of the inner crust layer and the outer crust layer are calculated for the 7 kW steady state period. The error can be about 10% due to the assumption that the calculated heat fluxes at the positions of the IT thermocouples along the meridian at 112.5° are the same as the heat fluxes at the positions of the thermocouple trees CT1 to CT3 along the meridian at 35°.

The values given in the Table 17 indicate that the lower part of the crust has a better thermal conductivity than the upper part of the crust.

The crust porosity and the distribution of the pore size have been measured with an Hg-porosimeter. The pore size distribution in Figure 38 shows that the porosity of the inner layer is mainly contributed by the macroscopic cracks and pores, whereas the porosity of the outer layer is mainly determined by middle size and super-fine pores. Generally, the crust inner layer is denser than the outer layer. The porosity measurements are in a good agreement with the observation by SEM (Figure 31), in which the inner layer is characterized by macroscopic cracks. The macroscopic cracks were very likely generated after the extraction of the melt at the end of the test. At this moment, the crust was cooled down very fast. Concerning this effect, the inner crust must have been even denser during the experiment than the results of porosity analysis show.

It is worth to note that the porosity in the same crust layer considerably varies from one position to another. Two samples of each crust layer were analysed, and the results obtained are within 25 % - 30 % range for both inner and outer layers of the crust, Table 18. In the same table, the bulk density and the pore distribution of the four crust samples are given.

Table 18: Crust heat conductivity and porosity of LIVE-L1

	Total porosity [%]	Bulk density [g/cm ³]	Pore distribution	
			100-2 μ m [%]	2-0.001 μ m [%]
Inner layer Sample I	4.1	2.06	62.6	30.4
Inner layer Sample II	5.1	2.00	81.1	18.9
Outer layer Sample I	6.4	2.02	48.9	51.1
Outer layer Sample II	8.2	2.13	60.7	39.3

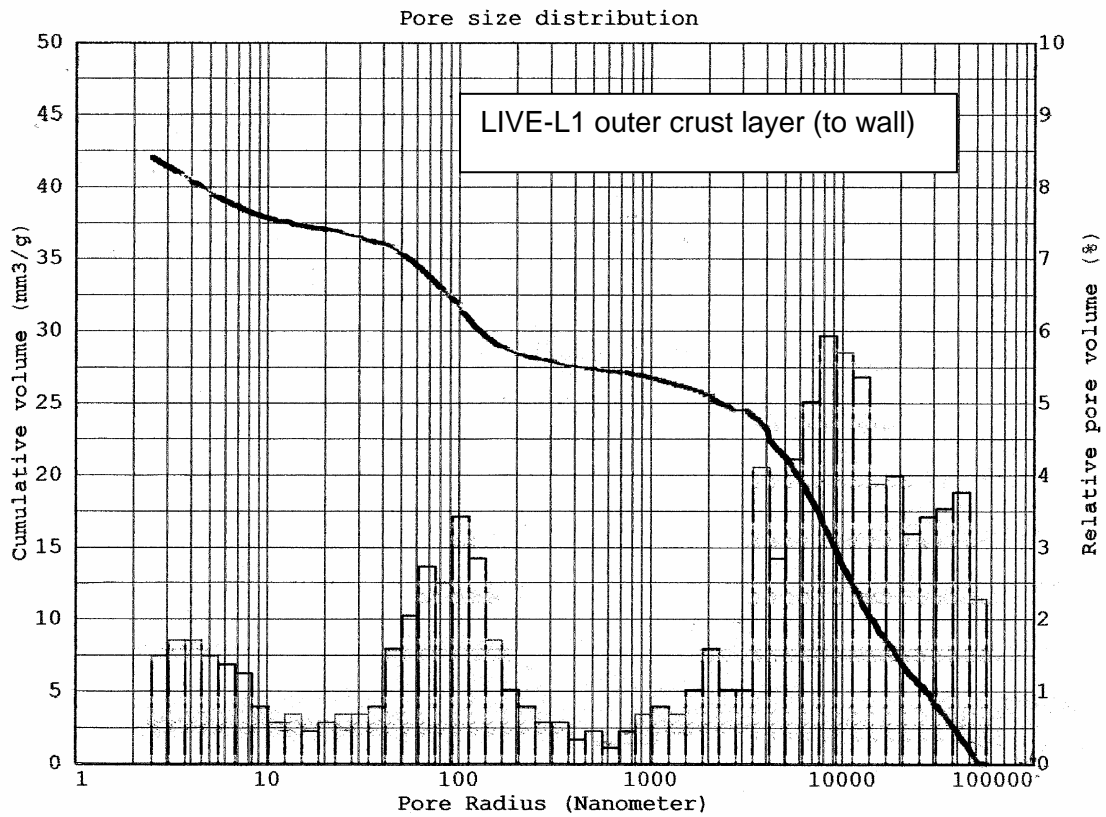
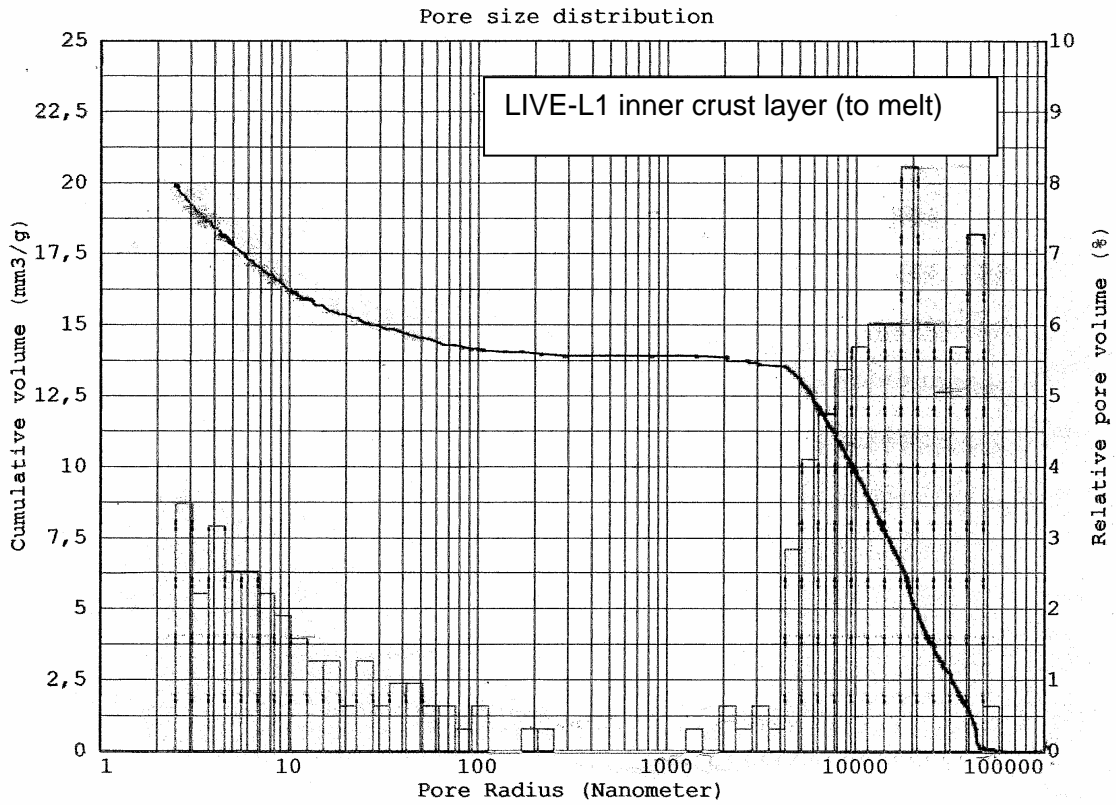


Figure 38: Pore size distribution of LIVE-L1 crust: top: inner layer, bottom: outer layer

4 Progression and test results of LIVE-L3

4.1 Preparation and performance of LIVE-L3

The experiment LIVE-L3 was successfully conducted on May 7-8, 2007. The experiment LIVE-L3 has been prepared and performed nearly identically in comparison with the experiment LIVE-L1. In Table 19 the main test parameters and the performed test phases of the experiment are summarised. The melt was discharged in one single pour and the planned initial temperature of the melt was 350 °C. The pouring mass was 120 l. The only difference between LIVE-L1 and LIVE-L3 experiments was the pouring position. In LIVE-L3 the melt was poured at the wall of the test vessel in contrary to LIVE-L1, where the melt was poured centrally to the test vessel.

Table 19: Test parameter and test phases of the experiment LIVE-L3

LIVE-L3	
7-8.05.2007	
Melt characteristics and preparation	
Type	NaNO ₃ KNO ₃
Mole %	20 % 80 %
Mass %	17.37 % 82.63 %
Mass	58 kg 278 kg
Total mass	336 kg
Loading of the furnace	Completion of residual melt of LIVE-L2 ~180 l melt (for T=350°C)
Pouring Mass	120 l (corresponds to ~31 cm melt height)
Initial temperature	350 °C
Flow rate of nitrogen covering in the furnace	20 l/min
Melt pour	
Position	Lateral
Number of pours	1
Furnace tilting velocity	0.5 °/s
Furnace target angle	80°
Hold time	50 s
Pouring spout temperature	350 °C

Phase 1: Homogeneous heat generation	
Start time	111 s
Boundary conditions	Air
Heating planes	All
Heating power	18 kW at the beginning, stepwise reduction to 10 kW
Maximum melt temperature	370 °C
Phase 2: Start of outer vessel wall cooling	
Start time	7199 s
Boundary conditions	Water, continuous cooling
Cooling water flow rate	~47 g/s
Heating planes	All
Heating power	10 kW
Heat generation	Homogeneous
Phase 3: Reduction of heat generation	
Start time	83100 s
Boundary conditions	Water, continuous cooling
Cooling water flow rate	~47 g/s
Heating planes	All
Heating power	7 kW
Heat generation	Homogeneous
Phase 4: Test termination and melt extraction	
End time	102900 s
Test conditions	Reaching of steady-state conditions in Phase 3
Heating power	0kW

The pouring process of the melt into the LIVE test vessel in the experiment LIVE-L3 is presented in Figure 39. After the completion of the pouring process, the test phases were performed in the same chronological order as in the LIVE-L1 test. In the first test phase with a homogeneous heat generation a heating power of approximately 18 kW was applied by switching all six heating planes simultaneously. To avoid the overheating of the melt, the power was reduced stepwise to ~10 kW. In the second test phase, after ~7200 s, the flooding of the outer vessel wall was started with a flow rate of about 1.5 kg/s. After the space between the test vessel and the cooling vessel was filled, a cooling rate of about 47 g/s was planned to keep constant throughout the whole experiment.

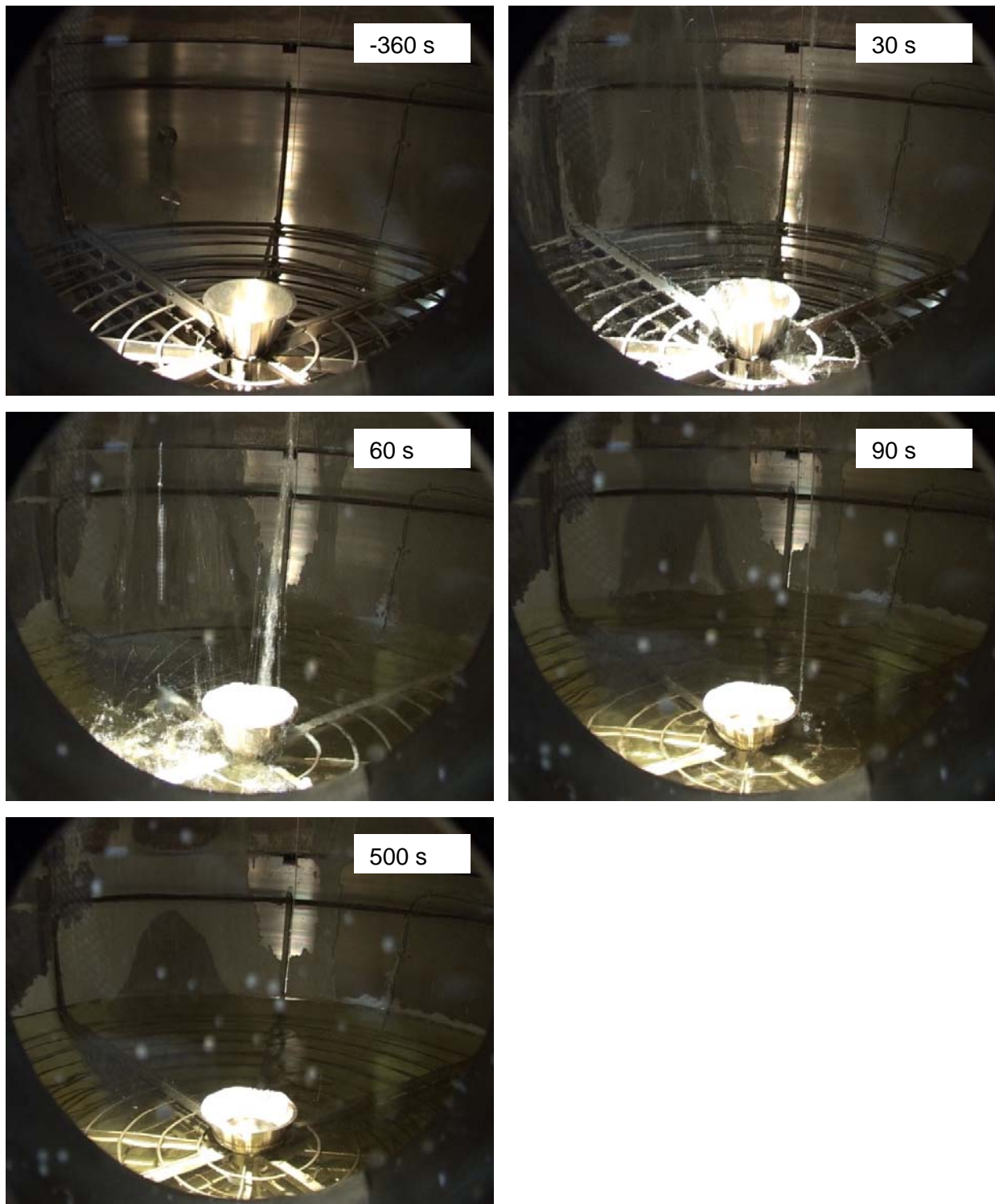


Figure 39: Pouring process of the melt into the LIVE test vessel in LIVE-L3

In LIVE-L1 only a cooling rate of ~ 42 g/s could be realized due to an offset of the flowmeter Krohne. In LIVE-L3, the flowmeter Kobold with a measurement range of 0-12 ml/s was replaced by another flowmeter with a measurement range of 0-200 ml/s (DN10), Figure 40. Therefore, after the flooding of the space between the cooling vessel and the test vessel, the total cooling rate could be adjusted using the new flowmeter. The flowmeter Krohne was

closed and thus the offset was not relevant. For this reason, the cooling rate in LIVE-L3 agreed with the planned value of 47 g/s.

In LIVE-L3 the measured temperature of the cooling water at the inlet was about 16 °C and the temperature of the cooling water outflow increased at the beginning to ~90 °C and decreased to ~60 °C after about 30000 s. The corresponding temperatures plot is given in Annex C.2.

The homogeneous heating of the melt with 10 kW was continued for about 20 hours to reach the steady state conditions. After about 82000 s, the test phase 3 was started, in which the heating power was reduced to 7 kW to observe the influence of the power reduction on the crust growth and heat flux distribution. This power level was kept for another 6 hours. In the last test phase, the heating power was switched off and the residual melt was extracted from the test vessel back into the heating furnace. In Figure 41, pictures from the extraction of the melt from the test vessel are shown.

Additionally, in Table 20 the course of the test LIVE-L3 is described in chronological order.

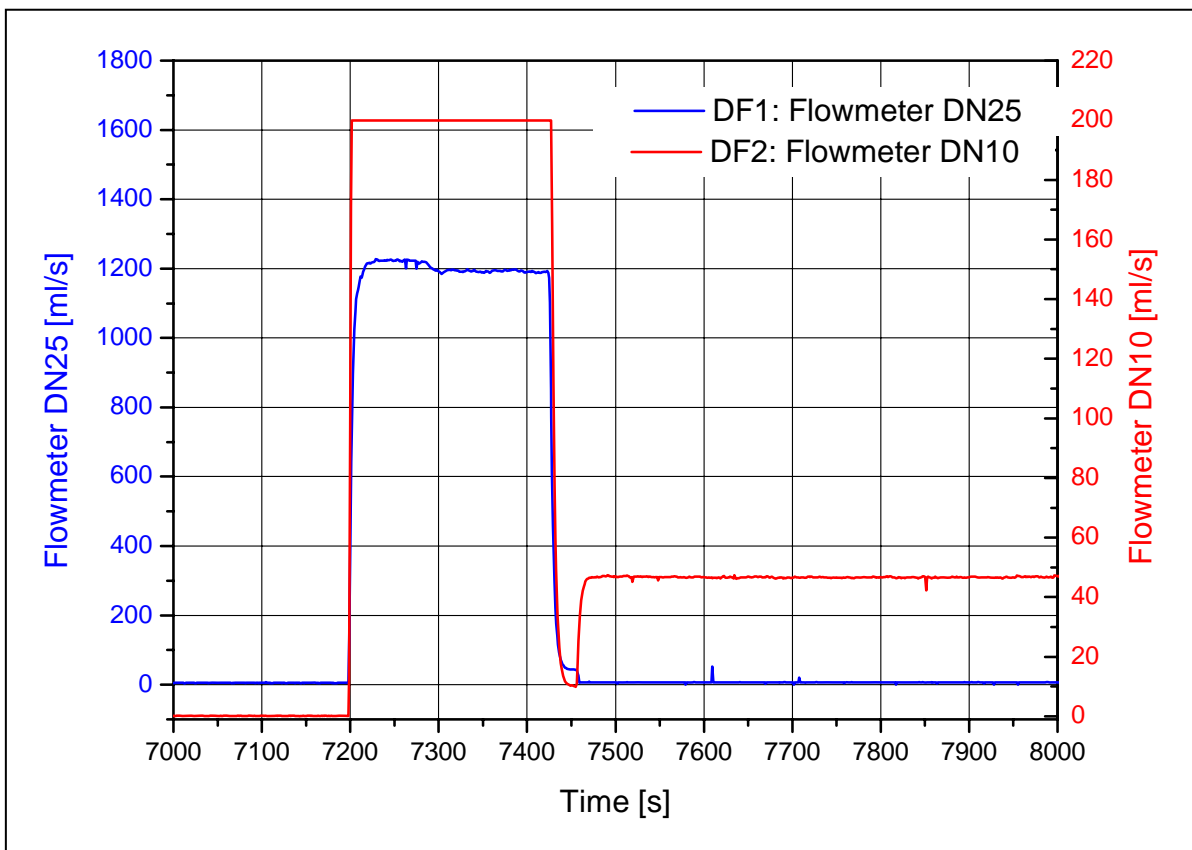


Figure 40: Flow rate of cooling water in LIVE-L3

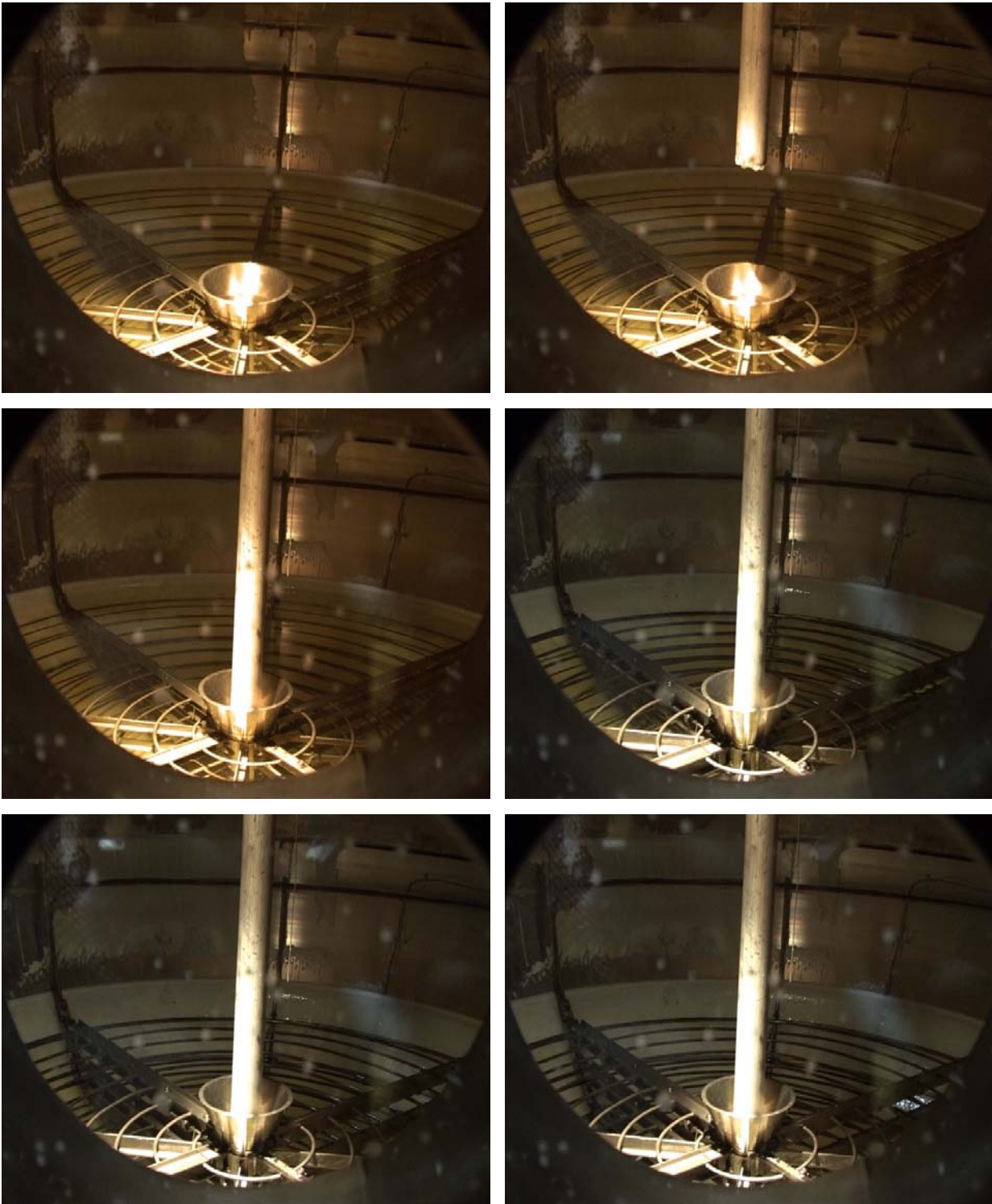


Figure 41: Extraction of the melt from the LIVE test vessel in LIVE-L3

Table 20: Course of the experiment LIVE-L3

Time of day	Event
07.05.2007	
8:03	Melt temperature in furnace 350 °C
8:55	PC data acquisition start
8:55	Weight of test vessel 1599 kg
8:58	Video record start
8:59	IR camera record start
9:00	Start of pouring program of heating furnace
9:04	Heating system on, P = 18 kW
9:08	P = 14 kW
9:12	Weight of test vessel 1812 kg
9:20	First material probe through central pouring opening
9:45	P = 12 kW
10:03	P = 10 kW
11:02	Start of flooding of gap between cooling vessel and test vessel (high flow rate)
11:06	Low flow rate set to around 0,047 l/s
15:21	Second material probe through central pouring opening
08.05.2007	
8:00	P = 7 kW
13:14	Third material probe through central pouring opening
13:24	Video record start
13:29	Weight of test vessel 2224 kg
13:30	Start suction of residual melt
13:31	Suction end, weight of test vessel 2058 kg
13:35:20	PC data acquisition stop

4.2 LIVE-L3 test results

4.2.1 Mass and initial temperature of the melt in LIVE-L3

Similarly to the LIVE-L1 test, the experiment LIVE-L3 started with the pouring of the simulated corium melt from the heating furnace into the LIVE test vessel via the preheated pouring spout. The difference to the experiment LIVE-L1 was that the melt was poured close to the test vessel wall. The experimental time $t = 0$ s is determined by the first response of the ST1 thermocouple located in the pouring spout.

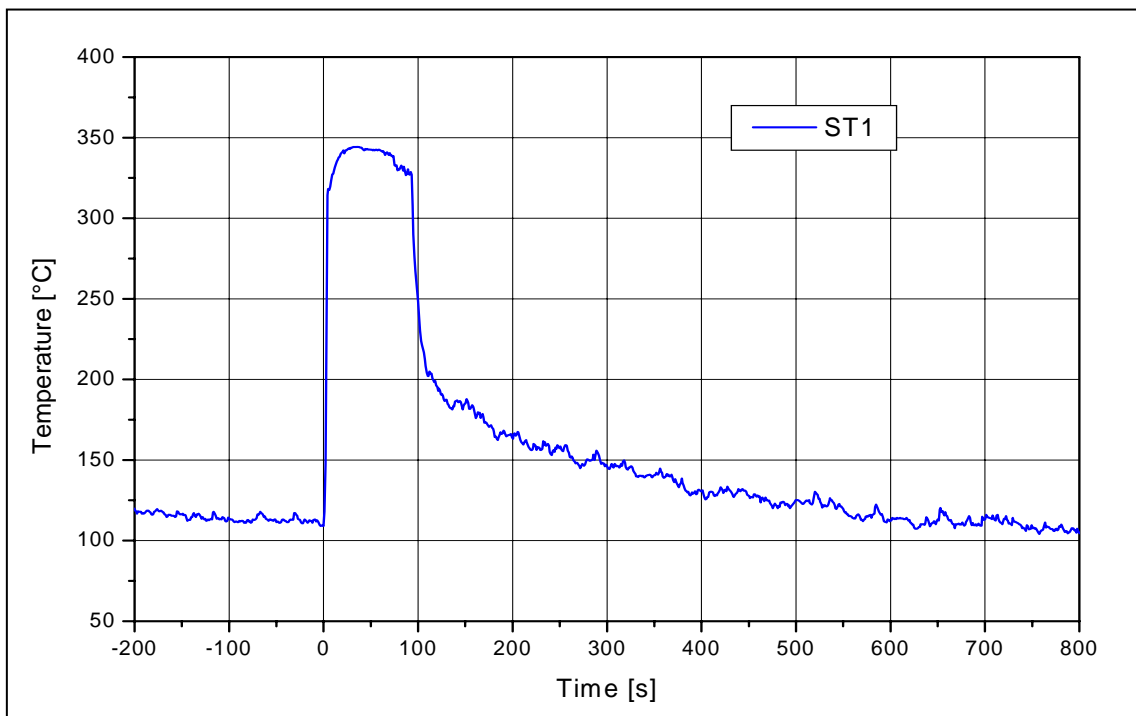


Figure 42: Initial melt temperature measured in the pouring spout in LIVE-L3

In Figure 42, the temperature measurement of the thermocouple ST1 is shown. The initial temperature of the $\text{NaNO}_3\text{-KNO}_3$ melt in the pouring spout was about 343 °C, which is in good agreement with the planned 350 °C.

The mass of the test vessel during the pouring of the melt rose from about 1597 kg to 1820 kg, Figure 43. Therefore about 223 kg of nitrate melt has been poured into the test vessel. With a density of about 1868 kg/m^3 for a 20-80 mole% $\text{NaNO}_3\text{-KNO}_3$ melt with a temperature of 344 °C, determined in [12], a volume of ~119,4 l nitrate melt has been poured into the test vessel. This value is very close to the planned volume of melt of 120 l.

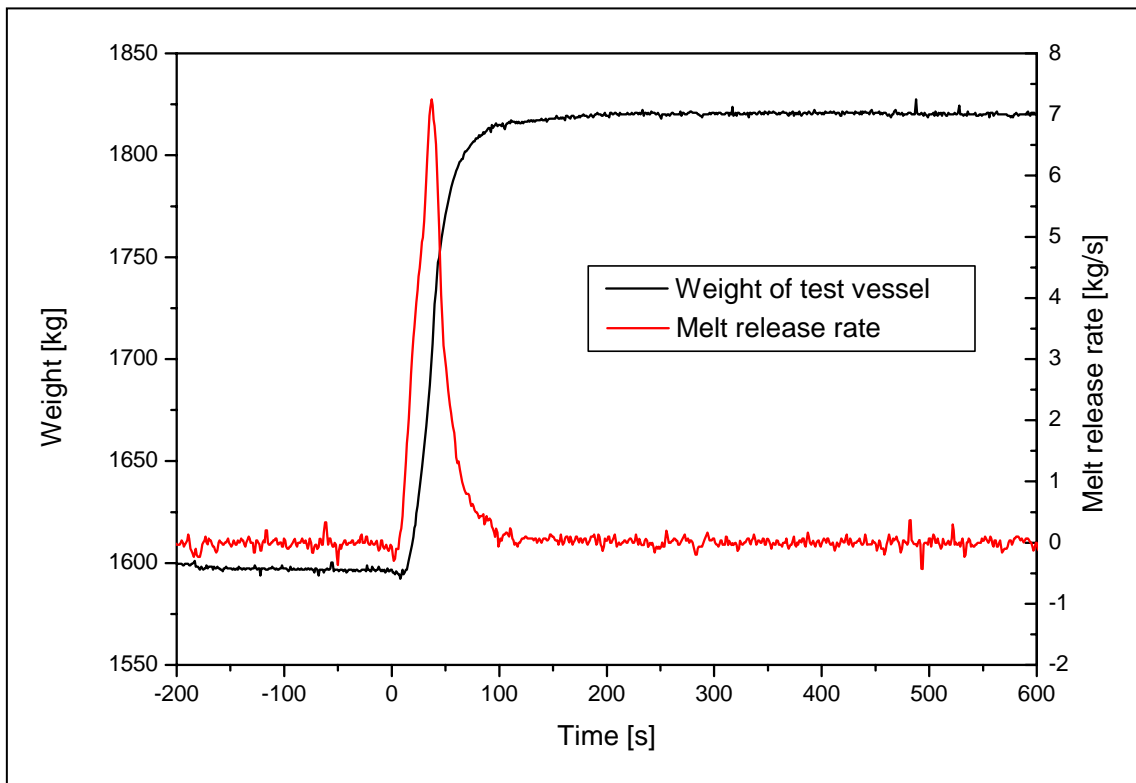


Figure 43: Weight of the test vessel and melt release rate in LIVE-L3

In Figure 43 the melt release rate is shown. The maximum pouring rate derived from the analysis of the weight of the test vessel was ~ 7 kg/s.

4.2.2 Decay heat simulation in LIVE-L3

To compare LIVE-L3 with the test LIVE-L1 (to observe the influence of different melt pouring positions) the same power generation rate was applied. The heating power distribution between the heating planes is shown in Figure 44.

After about 111 s from the pouring initiation, the top heating plane was covered with melt and a heating power of approximately 18 kW was applied to heat the melt homogeneously by switching all six heating planes simultaneously. Then the heating power was reduced step-wise to about 14 kW after 365 s, then to 12 kW after 2580 s and finally to 10 kW after 3660 s. There were also some disturbances of the heating planes 1 and 2 at the upper part of the melt pool due to the automatic switch-off of the power when the heater temperature exceeded 370 °C as in LIVE-L1. However, after the start of flooding of the outer vessel wall after 7199 s, the heat transfer was higher and the temperature measured at the heating elements decreased significantly.

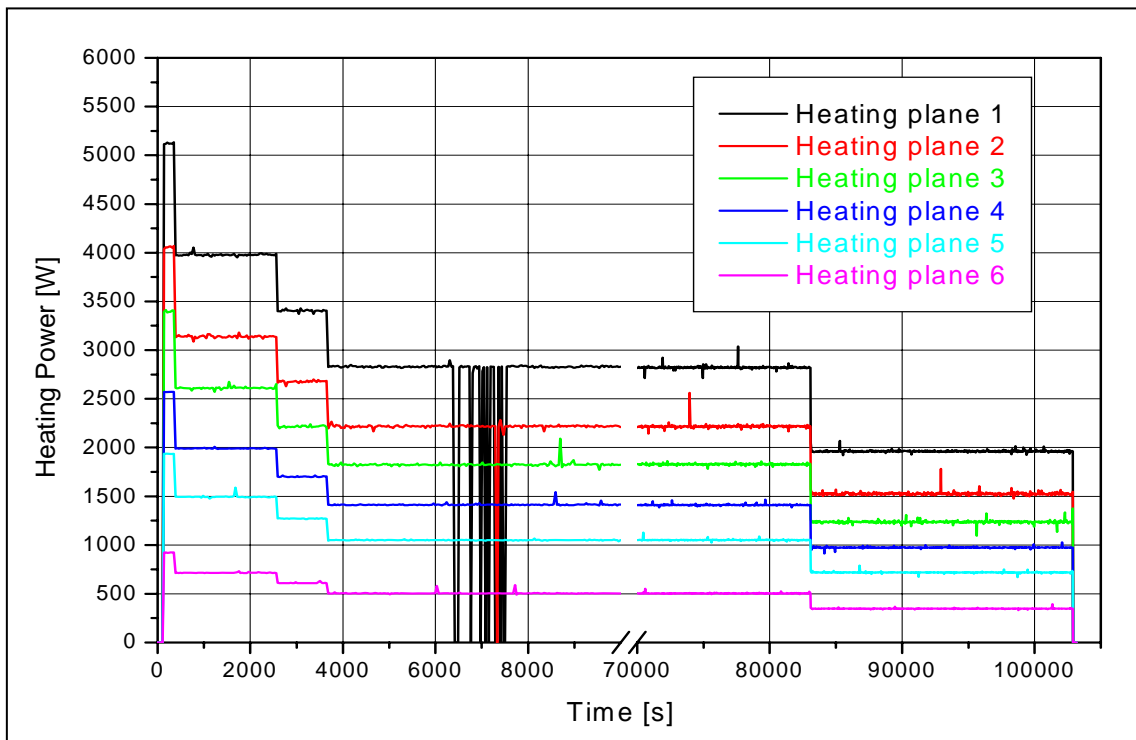


Figure 44: Heating power distribution between the six heating planes in LIVE-L3

The test phases 1 and 2 were performed with the heating power of 10 kW. After 83100 s, the heating power was reduced to 7 kW and the test phase 3 was started. After about 102900 s, the heating system was switched off terminating the experiment.

4.2.3 Melt behaviour in LIVE-L3

Generally, the measured melt temperatures in LIVE-L3 are similar to the measured melt temperatures in LIVE-L1, no significant differences were observed.

After the melt pouring, the melt temperatures measured inside the melt pool decreased to ~ 300 °C at the bottom of the test vessel and to ~ 330 °C near the melt surface. In Figure 45, the melt pool temperatures at different elevations along the meridian at 0° are shown. After the start of heating, the melt temperatures started to increase. The heating power was reduced stepwise to 10 kW after 3660 s. After ~ 7200 s, the test phase 2 was started and the flooding of the outer vessel wall was initiated. The temperatures decreased immediately to ~ 320 °C at the upper part of the melt pool and to ~ 300 °C in the centre of the melt pool.

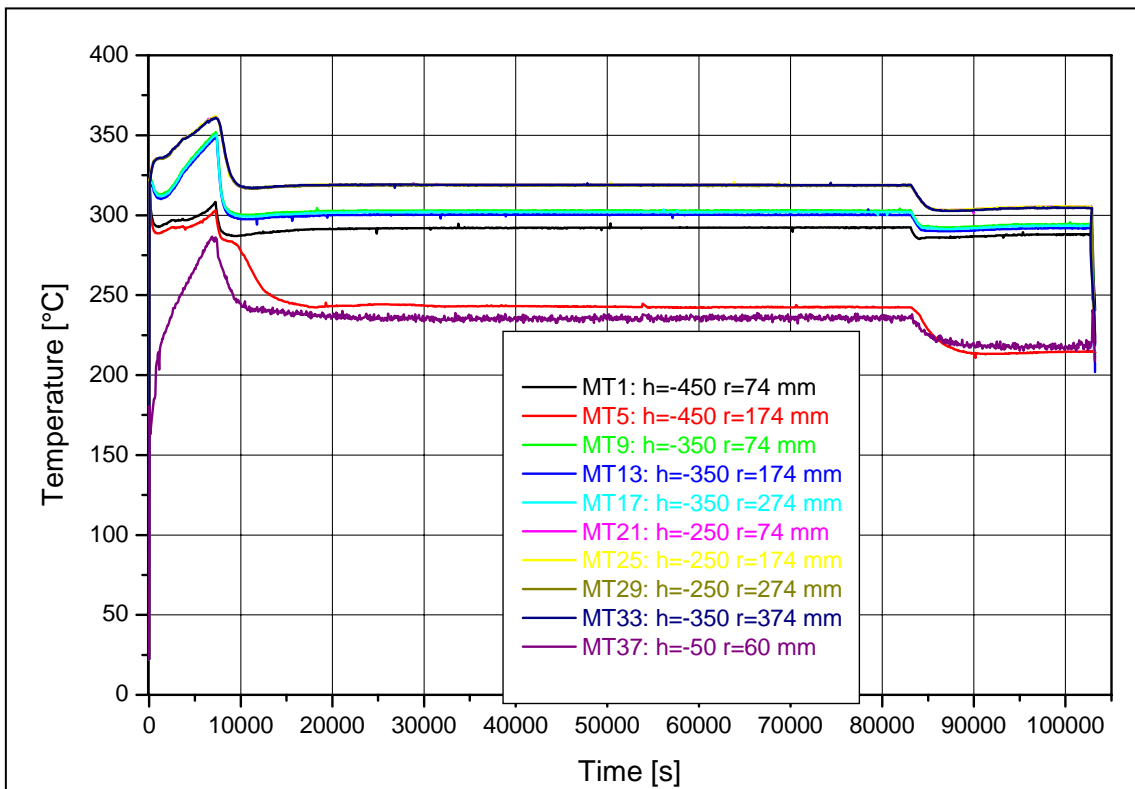


Figure 45: Melt pool temperatures at different elevations along the meridian 0° in LIVE-L3

At the position of the thermocouple MT5, which is situated near the bottom of the vessel wall, the temperature decreased below the liquidus temperature of the melt and therefore a crust is formed at this position. The crust formation at the wall of the test vessel could be investigated in more detail with the help of the thermocouple trees, as discussed in the chapter 4.2.6.2.

After about 83000 s, the heating power was reduced to 7 kW. The melt temperatures at all positions decreased by about 15-20 °C.

The temperature measurements along the meridians 90° , 180° and 270° are similar to the temperature measurements along the meridian 0° and are shown in Annex C.2.

In Figure 46 the temperatures of the melt pool are shown at different positions at a radius of 174 mm for different times. The temperature of the melt at the bottom of the test vessel was always lower than the temperature of the melt at the upper part of the test vessel. At 20000 s the temperatures at the vessel height 70 mm at all angles remained below the liquidus temperature.

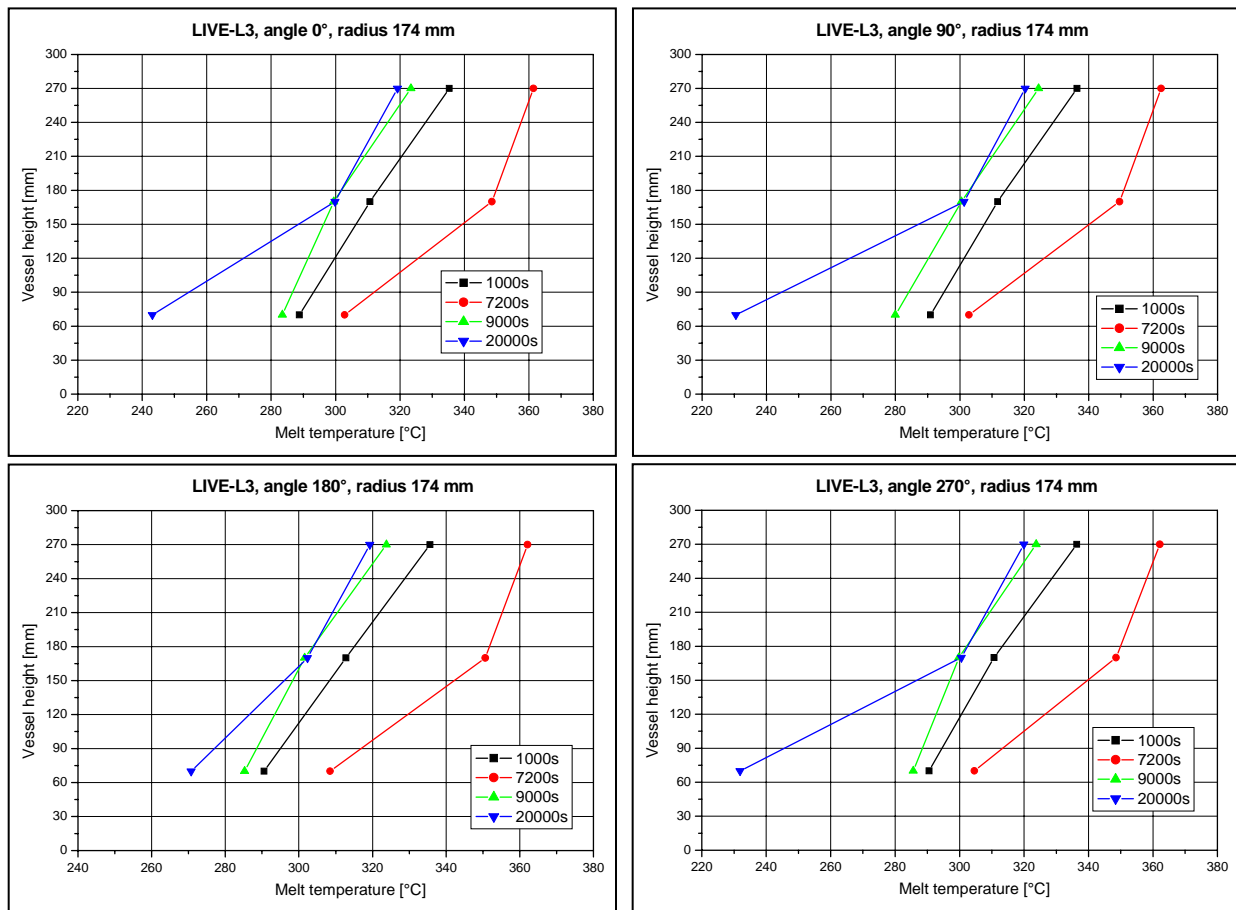


Figure 46: Temperatures of the melt pool at different positions at a radius of 174 mm at different times in LIVE-L3

4.2.4 Heat balance and heat flux in LIVE-L3

4.2.4.1 Heat balance in the steady state of LIVE-L3

The calculation method for the heat balance in LIVE-L3 is the same as for the LIVE-L1 test. In the LIVE-L3 test, different to the LIVE-L1 test, the vessel wall was equipped with plugs and inside wall thermocouples (IT) at the whole circumference (in 90° distance horizontally). The complete instrumentation assures an accurate measurement of the melt and crust behaviour. The heat transfer through the vessel wall during the test period is illustrated in Figure 47. Good agreement is achieved between heat transfer through the wall and heat removal by cooling water.

The ratio between the heat transferred through the vessel wall Q_{wall} and total the heating power ($Q_{heating}$) at the steady state of 10 kW and 7 kW is listed in Table 21. Compared to the $Q_{wall} / Q_{heating}$ ratio determined in the LIVE-L1 test, see Table 6, more heat was transported through the vessel wall in the LIVE-L3 test. One reason may be that the water flow rate in LIVE-L3 was about 47 g/s, whereas in LIVE-L1 the water flow rate was about 42 g/s. The increase of the water flow rate leads to a higher heat removal especially at low heating power, as can be observed during the 7 kW heating period. Another reason could be the dis-

placement of the thermocouple IT10 (measurements of the inner wall temperature) in Zone 4 in the LIVE-L1 test. IT10 measured a higher value than the realistic one since IT10 was detached from the vessel wall as the thermocouple was embedded in the crust and the crust shrank and spalled from the vessel wall.

Table 21: Heat balance between the heat transfer through vessel wall and the heating power in LIVE-L3

Heating period	Time point	Q_{water}	Q_{wall}	Q_{heating}	$Q_{\text{wall}}/Q_{\text{heating}}$
10kW	60001-60180 s	8412 W	8539 W	9833 W	86.8%
7kW	94811-95031 s	5844 W	5477 W	6768 W	80.9%

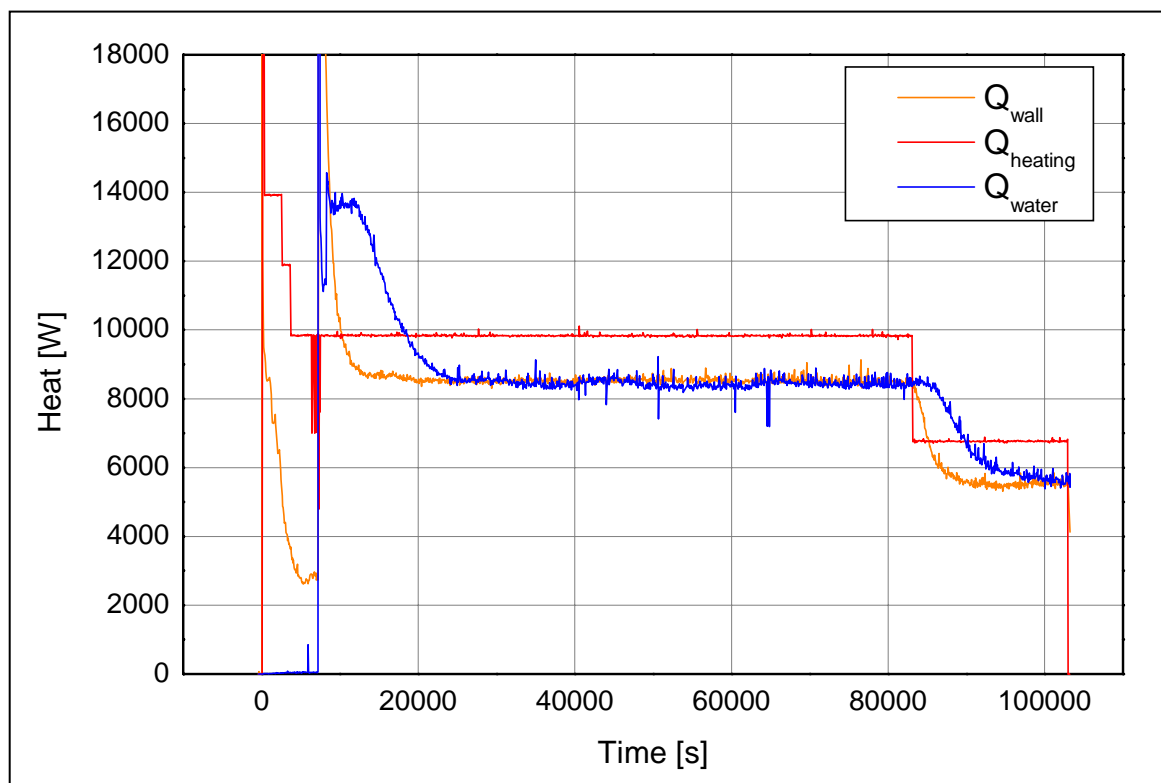


Figure 47: Heat balance between heating power, heat through the vessel wall and heat removed by cooling water in LIVE-L3

4.2.4.2 Heat flux measured by heat flux sensors in LIVE-L3

As already mentioned, the instrumentation of the test vessel with plugs in LIVE-L3 was completed with 17 instrumented plugs. Therefore, 17 heat flux sensors were available to measure the heat flux through the vessel wall. The positions of the heat flux sensors and the instrumented plugs are shown in Figure A- 1 in Annex A.2. In Figure 48 the measured heat fluxes of all heat flux sensors are presented. At the time of pouring (0 s) and at the time of start of outer vessel cooling (~7200 s) high transient heat fluxes were measured. The values

are given in Table 22. The position of the heat flux sensors as defined by the horizontal and vertical angle is also given in Table 22. The horizontal angle relates to the instrumentation axis at 0°, where all signal cables from the test vessel are collected and are attached to the first control cabinet. The vertical angle relates to the vertical central axis of the test vessel.

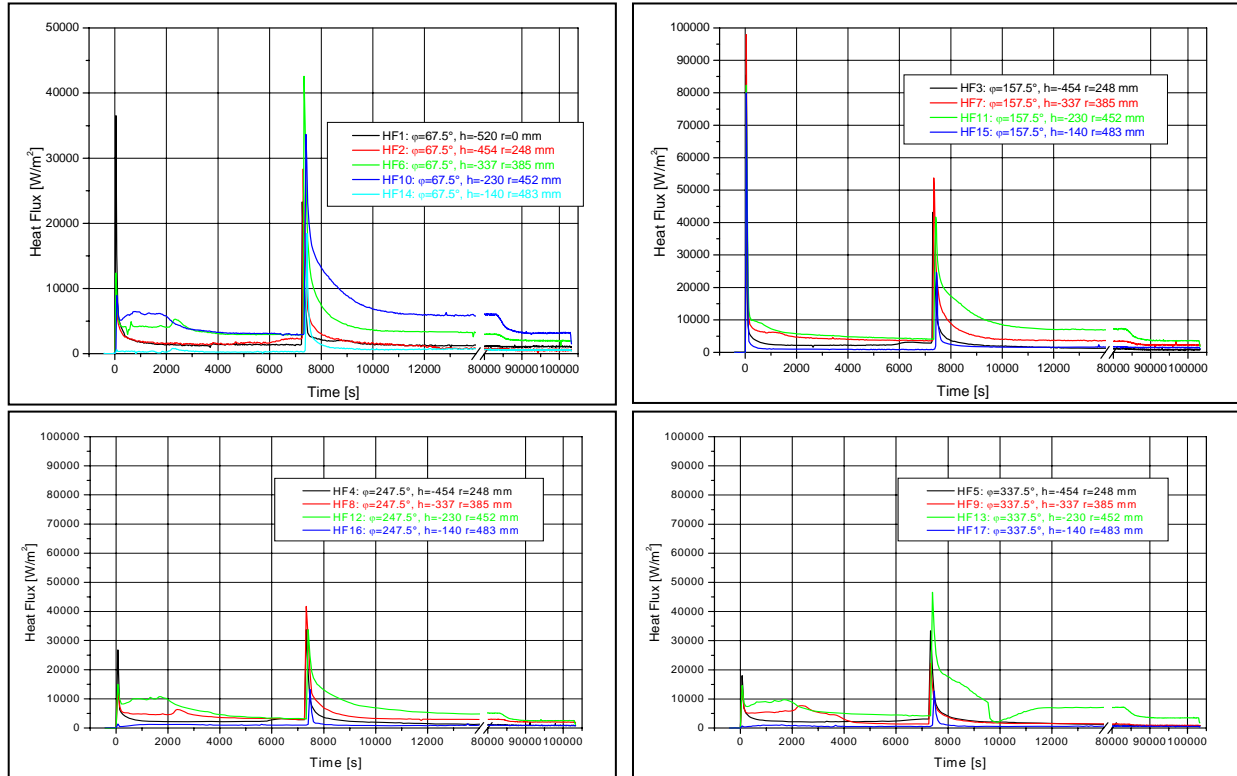


Figure 48: Heat fluxes measured by the heat flux sensors in LIVE-L3

The heat flux sensors along the meridian at 157.5° are located directly below the pouring position of the melt. Therefore these heat flux sensors showed the highest transient heat fluxes during the pouring of the melt. The maximum heat flux of 104391 W/m² was measured by the heat flux sensor HF7. The lowest heat fluxes were measured at the positions opposite to the melt pour. Only after about 3000 s the situation homogenised and the heat flux decreased to about 5000 kW/m² at all four orientations. The asymmetric behaviour of the heat fluxes in the initial phase of the test was probably caused by a different crust thickness distribution.

At the time of flooding, the maximum heat flux was significantly lower as at the time of pouring and was also measured by HF7 with 53775 W/m². All values for the maximum transient heat flux during flooding are between 20000 and 50000 W/m². In LIVE-L1 the maximum heat flux during flooding was clearly higher with ~92000 W/m² measured by HF6.

In Table 22 the measured heat fluxes during the steady-state for the test period with 10 kW and with 7 kW are also shown. These values are averaged over 2 minutes i.e. the average of all values measured 1 minute before and 1 minute after the time listed in Table 22. Compar-

ing the heat fluxes along the four meridians, it can be seen, that also at steady state, the highest heat fluxes were measured along the meridian at 157.5°.

Table 22: Transient and steady state heat fluxes measured by heat flux sensors in LIVE-L3

	Horiz. angle [°]	Vertical angle [°]	Max. transient q at pouring [W/m ²]	Max. transient q at flooding [W/m ²]	q at 10kW steady state 65000 s	q at 7kW steady state 95000 s
HF1	0	0	38246	24043	1151	1106
HF2	67.5	30	10063	28991	683	554
HF6	67.5	51	13583	43014	2991	2019
HF10	67.5	65.5	9158	35172	6120	3152
HF14	67.5	76.5	606	23439	617	559
HF3	157.5	30	92617	47866	1063	841
HF7	157.5	51	104391	53775	3397	2311
HF11	157.5	65.5	82797	44064	7280	3640
HF15	157.5	76.5	85089	28516	1694	1476
HF4	247.5	30	92617	47866	1063	841
HF8	247.5	51	16801	48408	2953	2009
HF12	247.5	65.5	15808	33751	5216	2523
HF16	247.5	76.5	1676	21226	931	854
HF5	337.5	30	30499	45811	1047	883
HF9	337.5	51	21927	23429	1370	930
HF13	337.5	65.5	14621	47144	7075	3523
HF17	337.5	76.5	744	20388	698	623

4.2.4.3 Calculated heat fluxes in LIVE-L3

The calculation method is the same as for the LIVE-L1 test presented in the chapter 3.2.4.3. As in LIVE-L1, the heat flux is calculated based on the wall inside temperature (IT) and the plug temperature (PT*1). The temperature measurements of the IT, PT and OT thermocouples are given in Annex C.2. The heat fluxes calculated with the IT/OT and the PT/OT values are also shown in Annex C.2. In Figure 49 the calculated IT/OT heat flux values have been averaged for every heat flux zone (Figure 16). Comparing with the LIVE-L1 test the similar trend is observed: the highest heat flux is located in the Zone 4 ($q_{IT10-13}$), which is just below the melt surface. In LIVE-L3 the average heat flux in the Zone 4 is higher than in LIVE-L1, but lower than in Zones 3 (q_{IT6-9}) and 5 ($q_{IT14-17}$). In Zone 1 (q_{IT1}) and Zone 2 (q_{IT2-5}) the heat fluxes are comparable.

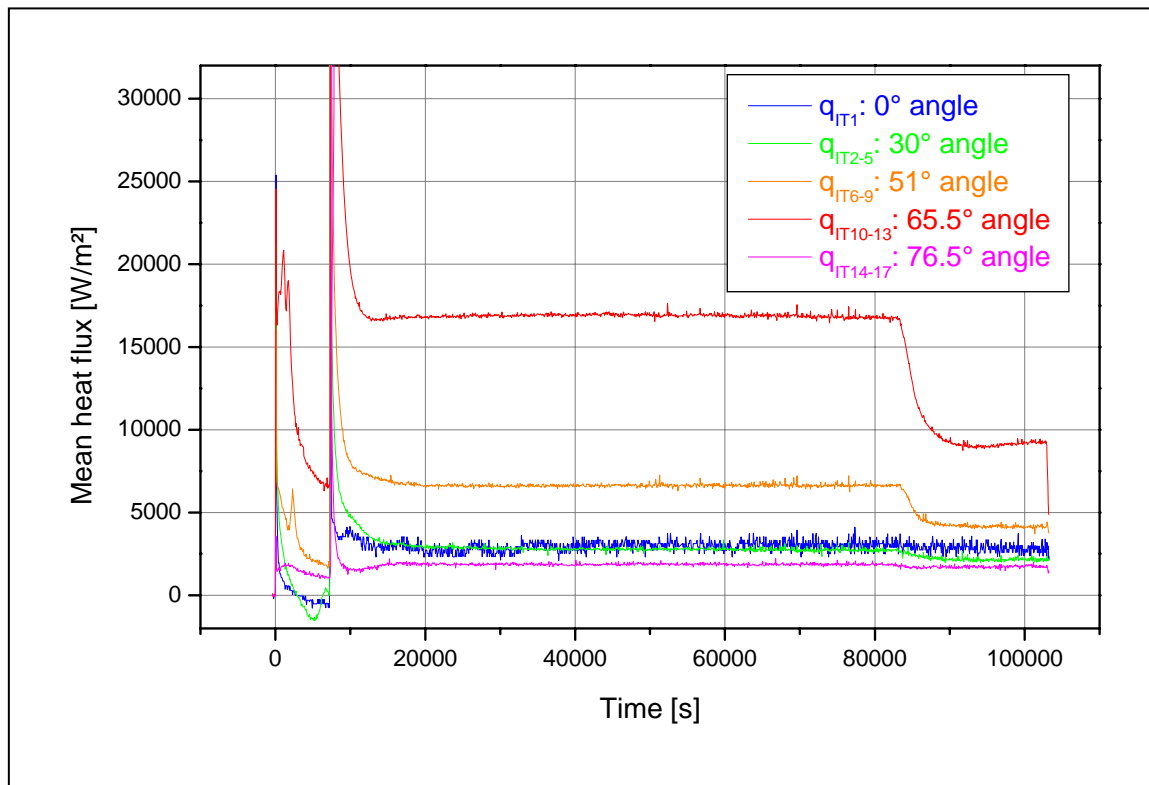


Figure 49: Average heat flux values for the five heat flux zones in LIVE-L3

In Table 23, the heat fluxes calculated with the IT/OT values as 2 minutes average values at the steady state during the 10 kW (time point 65000 s) and 7 kW (time point 95000 s) heating periods are listed. The results show that the heat fluxes within one zone differ considerably from each other. In the same table, the maximum transient heat fluxes during pouring and during flooding are shown, also calculated based on the IT/OT measurements. The transient heat fluxes during flooding are significantly higher than the transient heat fluxes during pouring of the melt. This can be explained by the asymmetry in the crust formation and different crust thicknesses.

The averaged transient heat fluxes for four heat flux zones after water flooding are shown in Figure 50 and Table 24. Similarly to LIVE-L1, the maximum heat transfer was detected in the Zone 3, followed by Zone 4 and Zone 2. The maximum heat fluxes are slightly higher than those observed in the LIVE-L1 test and the heat flux during the LIVE-L3 test reached faster steady state conditions.

Table 23: Steady state (2 minutes average value) and transient heat flux distribution in LIVE-L3

Plug. Nr	Area zone	Heat flux q_{IT} [W/m ²]	q at 10 kW steady state 65000 s	q at 7kW steady state 95000sec	Max. transient q at pouring [W/m ²]	Max. transient q at flooding [W/m ²]
1	1	q_{IT1}	3126	2875	64941	98755
2-5	2	q_{IT2} (22.5°)	2876	2244	31689	142180
		q_{IT3} (112.5°)	2277	1777	34376	143326
		q_{IT4} (202.5°)	3946	2839	27126	138494
		q_{IT5} (292.5°)	2180	1678	18238	144462
6-9	3	q_{IT6} (22.5°)	7477	4843	29027	180680
		q_{IT7} (112.5°)	6422	3986	17969	179717
		q_{IT8} (202.5°)	6028	3911	10700	176148
		q_{IT9} (292.5°)	6874	3821	21548	177124
10-13	4	q_{IT10} (22.5°)	18305	9726	36886	165867
		q_{IT11} (112.5°)	15466	7997	31859	162897
		q_{IT12} (202.5°)	18077	9626	29866	164337
		q_{IT13} (292.5°)	15872	8582	35090	164587
14-17	5	q_{IT14} (22.5°)	1825	1562	12935	90050
		q_{IT15} (112.5°)	2055	1859	6792	90885
		q_{IT16} (202.5°)	2352	2117	13701	96997
		q_{IT17} (292.5°)	1383	1299	4564	89554

Table 24: Calculated transient heat fluxes (averaged) after water flooding in LIVE-L3

	Start of flooding [s]	Transition time point to the slowly reduction of q [s]	Time point to the q steady state [s]	Max. q [W/m ²]	q at the transition time [W/m ²]
Zone 1	7235	7450	~7450	98755	~6000
Zone 2	7263	7450	~9500	141462	~20000
Zone 3	7317	7500	~11000	177341	~38000
Zone 4	7365	7600	~11400	164215	~52000

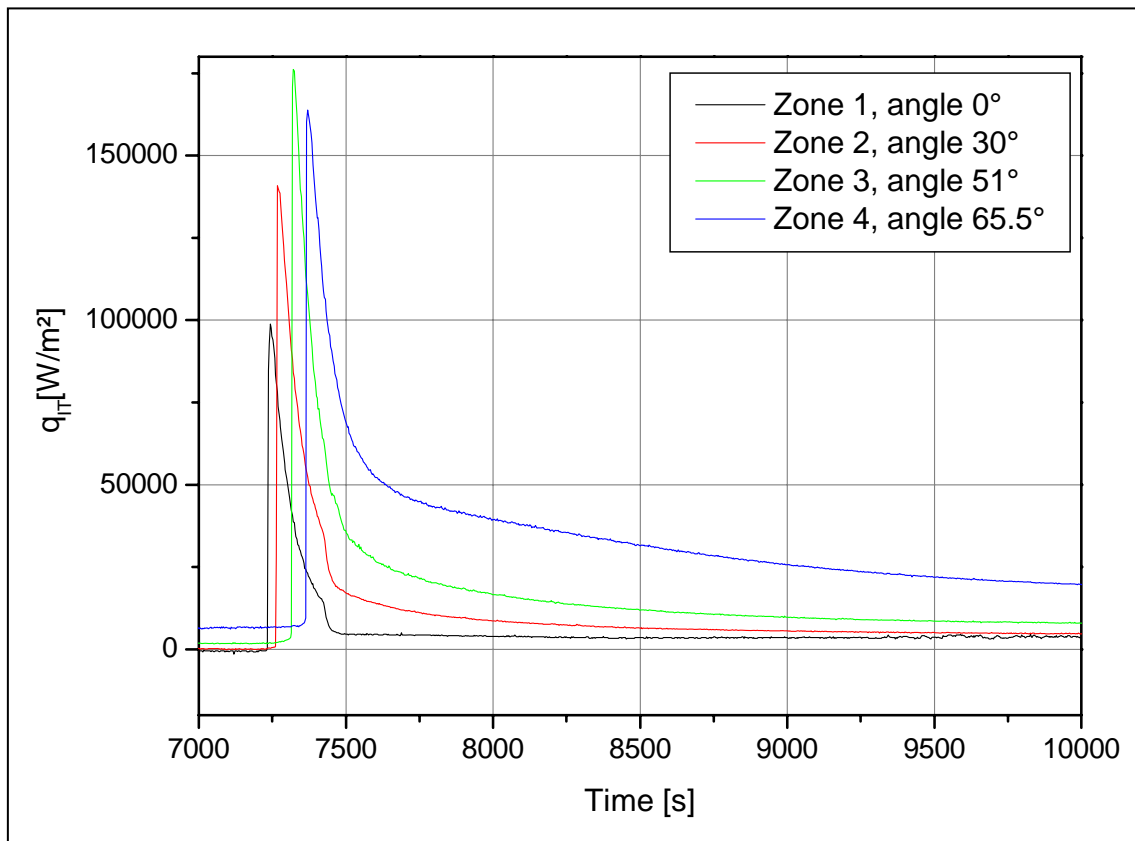


Figure 50: Heat flux development after water flooding in LIVE-L3

4.2.4.4 Comparison of the calculated heat fluxes with the measured heat fluxes by the heat flux sensors in LIVE-L3

A comparison of the calculated heat fluxes according to IT and PT values with the heat fluxes measured by the heat flux sensors for the LIVE-L3 test was performed. The comparison of the heat fluxes based on the IT/OT values with the measured heat fluxes is restricted because the IT/OT thermocouples are positioned at the same height in the test vessel but are displaced by 45° to the positions of the heat flux sensors (the IT/OT thermocouples are positioned along the meridians at 22.5° , 112.5° , 202.5° and 292.5° and the heat flux sensors are positioned along the meridians at 67.5° , 157.5° , 247.5° and 337.5°). Due to the different positions it is possible that the conditions concerning crust formation, crust thickness or the flow conditions of the melt are also different. Therefore, the measured heat fluxes are also compared with the heat fluxes calculated with the PT*1 thermocouples. The PT*1 thermocouples are part of the instrumented plugs and are positioned at the wall inner surface (0 mm).

In Figure 51 the heat flux values of the heat flux sensors and the heat fluxes calculated with the IT and PT thermocouples as 3 minutes average values at the time point 60000 s are shown for all 17 measurement positions.

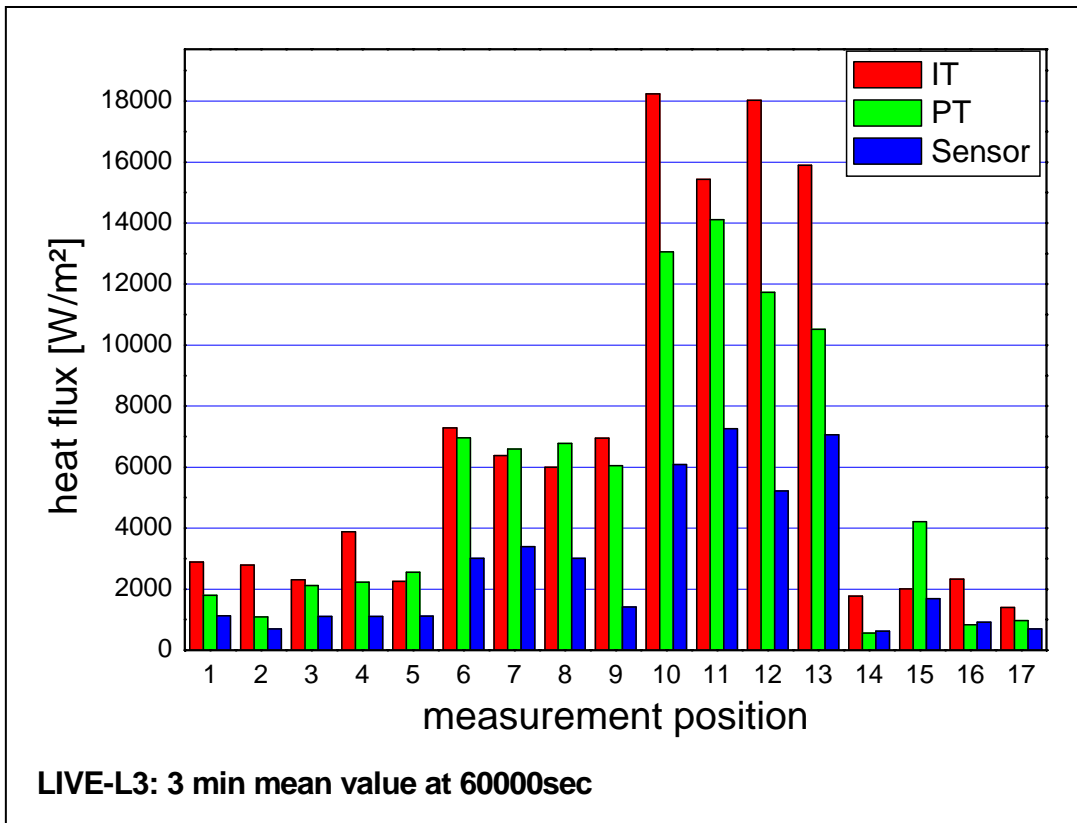


Figure 51: Values of the calculated heat fluxes and measured heat fluxes in LIVE-L3

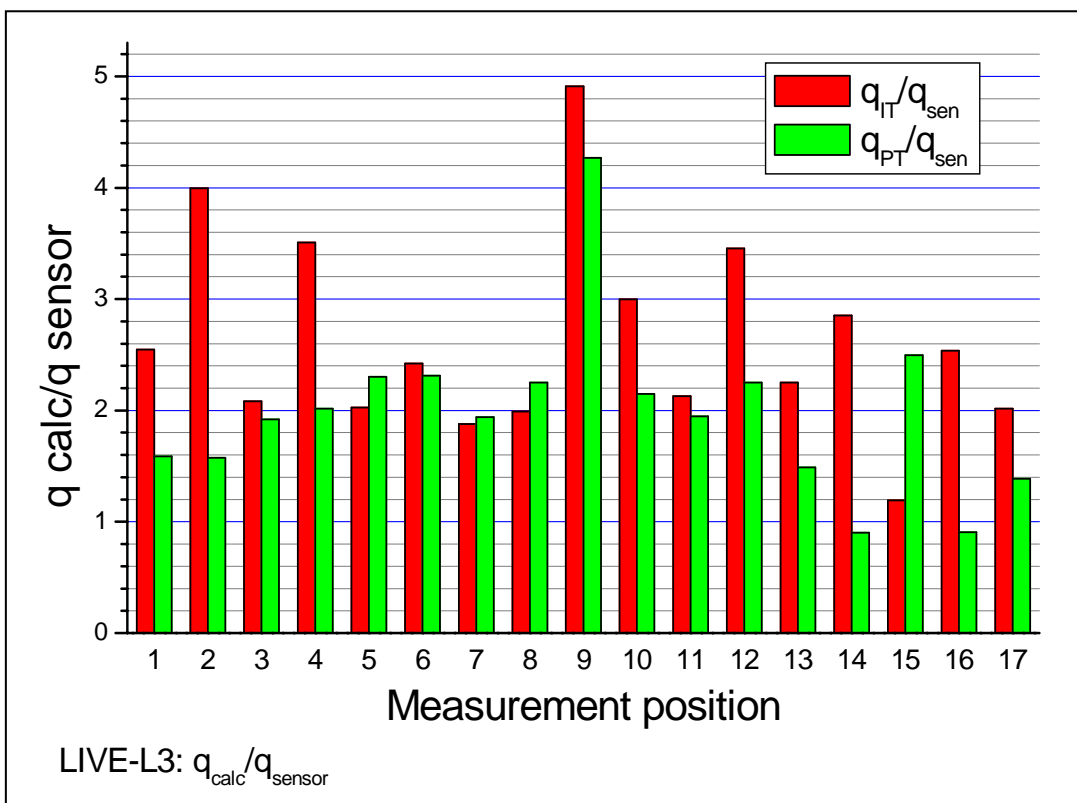


Figure 52: Ratio between calculated heat fluxes and measured heat fluxes in LIVE-L3

In Figure 52, the ratio between the calculated heat fluxes and the measured heat fluxes is shown. Both figures show that the heat flux sensor values are significantly lower than the calculated values. Furthermore Figure 52 shows that the sensor values do not correlate with the calculated values from one measurement position to another. Moreover, it was found that the sensor values are inconsistent comparing the results of the two tests and the accuracy of the measurements becomes questionable. The major problem of the heat flux sensors is their calibration and their installation into the plug and into the test vessel. Most probably, the heat resistance inside the plugs varies from one plug to another. The different cooling conditions during the test influence to a major extent the contact between the plug components, changing therefore the plug heat resistance.

The heat fluxes calculated with the PT values are also lower than the heat fluxes calculated with the IT values. Partly this can be due to the different position in the test vessel but also to other reasons. The PT thermocouples are also part of the instrumented plugs of the heat flux sensors. The PT thermocouples are arranged perpendicular to the inner vessel wall instead of horizontal as it is the case for the IT thermocouples. Therefore, the measurement position in the PT thermocouple is not exactly known.

The conclusion is that the heat fluxes calculated with the IT/OT values are reliable.

4.2.5 Melt surface behaviour

The analysis of the behaviour of the upper melt surface of the LIVE-L3 test was performed in the same way as described in the section 3.2.5. Figure 53 and Figure 54 show the technique used to determine the velocity distribution at the upper melt surface. The darker area at the middle of the pictures is a reflection of the camera lenses from the melt surface. This influences the temperature measurements of the melt surface, but is not important for the analysis of the fluid motion. The areas of thermograms having distinctive patterns were identified (point 1 in Figure 53) and their displacement after 2 seconds was determined (point 2 in Figure 53 and Figure 54). Three phases of the LIVE-L3 test were analysed:

- steady state phase at 10 kW,
- transient phase during the power reduction from 10 kW to 7 kW,
- steady state phase at 7 kW.

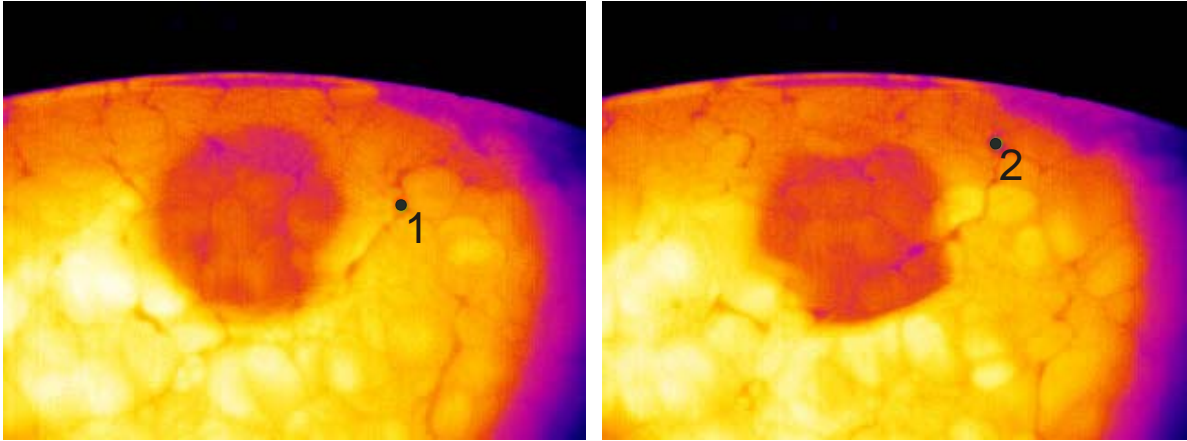


Figure 53: Thermogram of the melt surface with patterns used for the motion velocity determination.

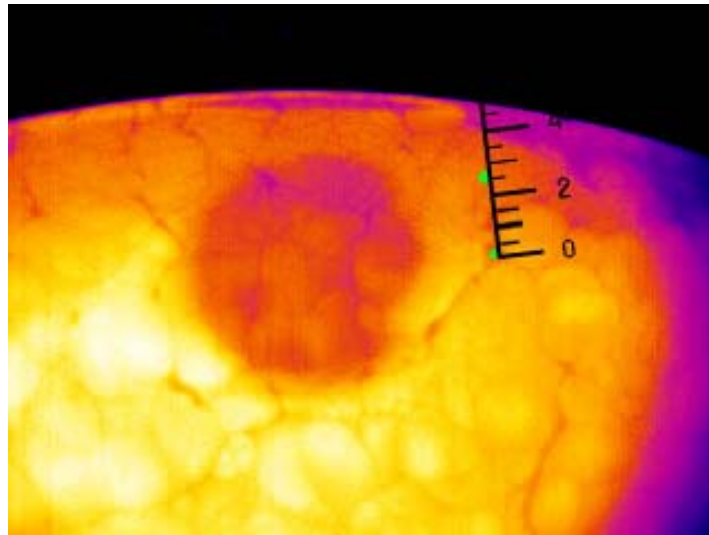


Figure 54: Displacement of the patterns after 2 seconds (the scale is in cm).

The calculated flow velocities are summarised in Figure 55 to Figure 57. The X axis is given in the dimensionless term R/R_{vel} where R is the starting radial position of the analysed point and R_{ves} is the vessel radius (50 cm). The results of the analysis indicate that the flow velocity is within the following range:

- 0.7-1.25 cm/s in the steady state phase at 10 kW,
- 0.5-1.25 cm/s in the transient phase during the power reduction from 10 kW to 7 kW,
- 0.25-0.75 cm/s in the steady state phase at 7 kW.

As it was expected, the decrease of the flow velocity with decreasing heat generation can be reported. However, the comparison with the LIVE-L1 test indicates that the velocity measured in similar conditions during 10 kW phase of the LIVE-L1 test is lower (0.1-0.3 cm/s). The reason for the deviation is not clear at the moment.

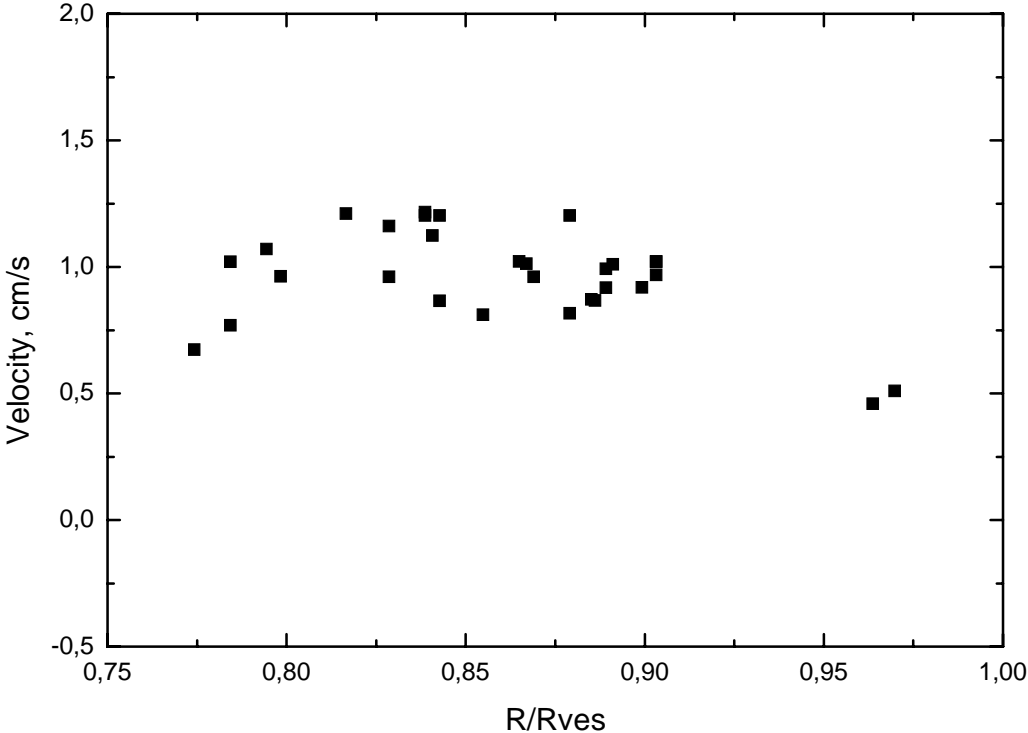


Figure 55: Flow velocity measured at the upper surface of the LIVE-L3 test during 10 kW heating phase.

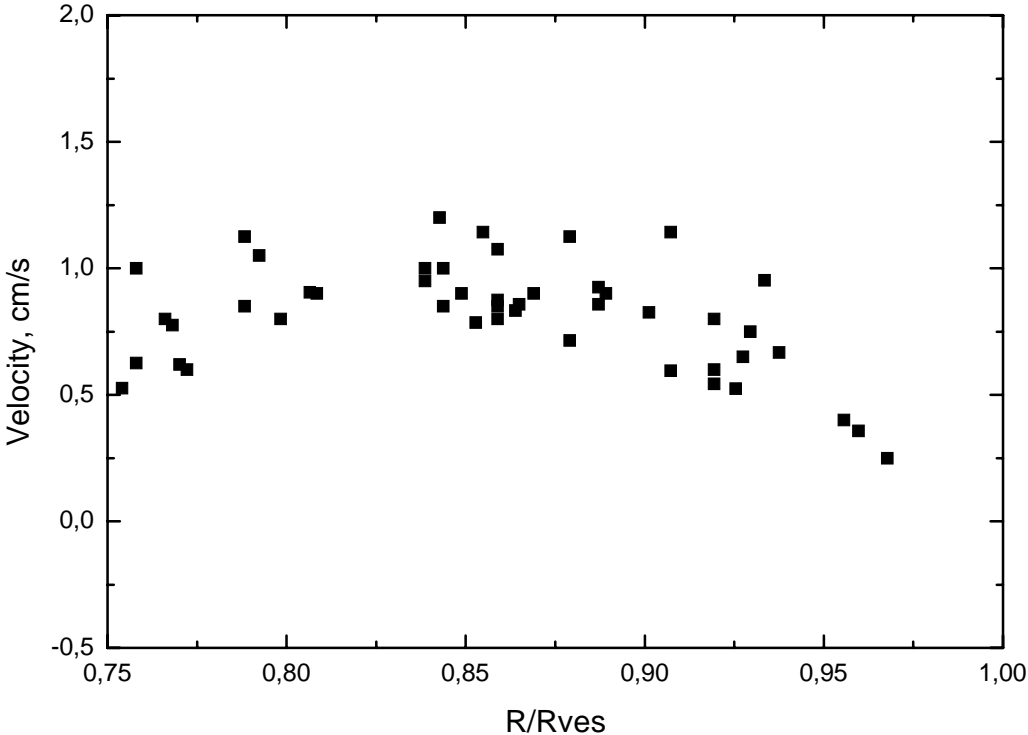


Figure 56: Flow velocity measured at the upper surface of the LIVE-L3 test during power reduction from 10 kW 7 kW.

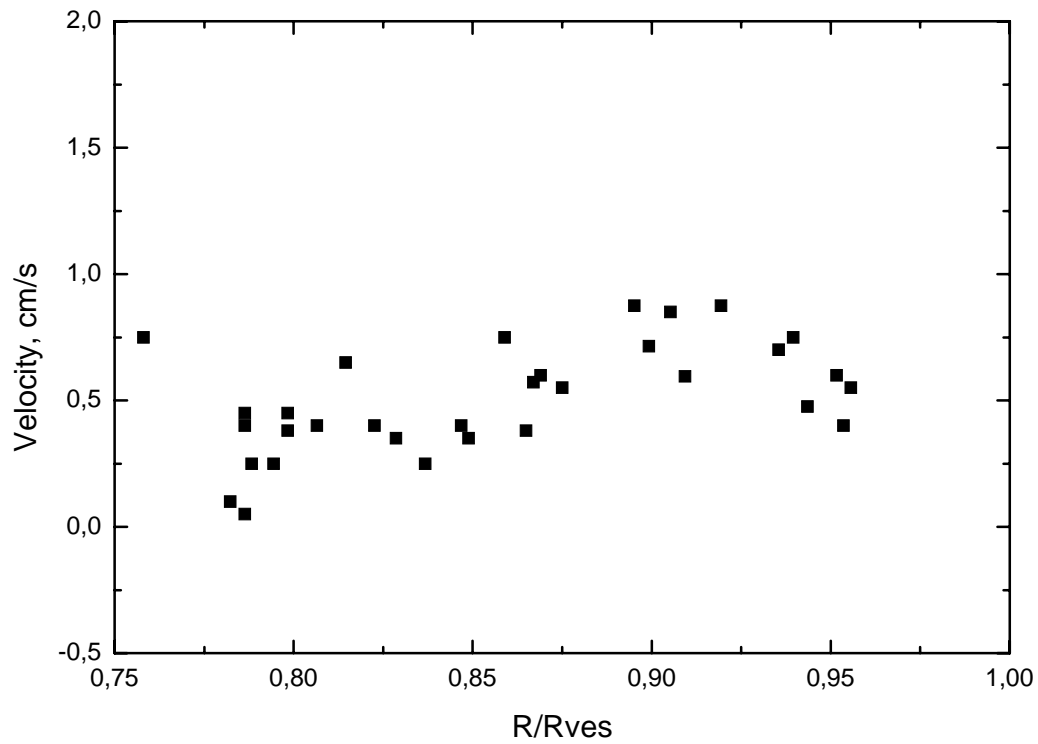


Figure 57: Flow velocity measured at the upper surface of the LIVE-L3 test during 7 kW heating phase.

4.2.6 Post-test analysis in LIVE-L3

As mentioned in chapter 4.2.1, about 223 kg of nitrate melt, corresponding to 119.4 l, was poured into the test vessel at the beginning of the test. About 2 kg of the 223 kg melt was spilled on the steel cover of the upper lid during the pouring process. At the end of the test, 169 kg of melt was extracted back into the heating furnace. Thus, the mass of the crust formed on the vessel wall at the end of the test is 52 kg, which corresponds to 23.5 % of the total melt mass in the test vessel (compare to 57 kg and 26% measured in LIVE-L1).

After the extraction of the melt and after the cool down of the test facility, the disassembly of the test rig was started. In Figure 58 a view of the test vessel after removing of the lid of the test vessel is shown. At the upper part of the test vessel residual solidified melt from the lateral melt pouring at the vessel wall can be seen. At the lower part of the test vessel, there is the crust which was formed during the test.



Figure 58: View of the test vessel after the end of the experiment LIVE-L3

The thickness of the crust was measured along the sections 67.5° - 247.5° and 157.5° - 337.5° and different samples were taken to investigate the crust characteristics and composition. In the following chapters, the detailed post-test analysis is described.

4.2.6.1 Average composition of the melt in LIVE-L3

To determine the melt pool composition in LIVE-L3, four samples were analysed. Sample 0 was taken after the test from the crust on the upper lid of the test vessel and represents the original melt composition. Sample 1 was taken from the melt pool 20 minutes after the melt pouring. At this time, there was no water cooling. Thus, there was only the crust, which was formed during the first contact between the melt and the test vessel during pouring process. This crust melted gradually in time due to the high heating power. Sample 2 and Sample 3 were taken during the steady state phases of the 10 kW heating period and the 7 kW heating period respectively. The samples were taken by inserting and quickly removing a stainless steel rod into the melt pool. Under these conditions, the melt solidified on the rod surface under supercooling conditions and the segregation of Na and K during the solidification process is kept as low as possible. The composition of the melt samples is shown in Table 25.

Table 25: Planned and average melt pool composition in the LIVE-L3 test

	Planned	Before test (Sample 0)	20 min after pouring (Sample 1)	10 kW steady state (Sample 2)	7 kW steady state (Sample 3)
K [mole%]	80	78.1	78.4	77.8	77.2
Na [mole%]	20	21.9	21.6	22.2	22.8
Na/K ratio [mole/mole]	0.25	0.28	0.28	0.29	0.30
KNO₃ [w%]	82.635	80.9	81.2	80.6	80.1
NaNO₃ [w%]	17.365	19.1	18.8	19.4	19.9

Comparing the results of Sample 0 with Sample 1 analysis, the melt sample taken by the stainless steel rod has a slight enrichment in KNO₃. This can be explained by the equilibrium partition law during the solidification of a two-compound mixture, despite the fast melt solidification. Due to the same reason, the remaining melt pool is depleted with KNO₃ as the crust grew during the 10 kW and 7 kW heating periods, which is demonstrated by Sample 2 and Sample 3. At the end of the test, the initial KNO₃ fraction was reduced by ~1 mole%. This observation is in a good agreement with the post-test chemical analysis of the crust, which remained in the test vessel, see chapter 4.2.6.4.

4.2.6.2 Crust growth rate in LIVE-L3

The development of the crust thickness at the positions of the thermocouple trees (CT) is shown in Figure 59. In this figure, the X axis shows the time after flooding, which means the time 0 s is related to the start of flooding after about 7200 s. The measurements of the thermocouple trees over the whole experiment are given in Annex C.2.

Figure 59 also shows that the characteristic time is reached faster than in LIVE-L1. At the position of CT2, the characteristic time is 7085 s, or 118 minutes. This value is still lower than the predictions given in [15] (16-160 min).

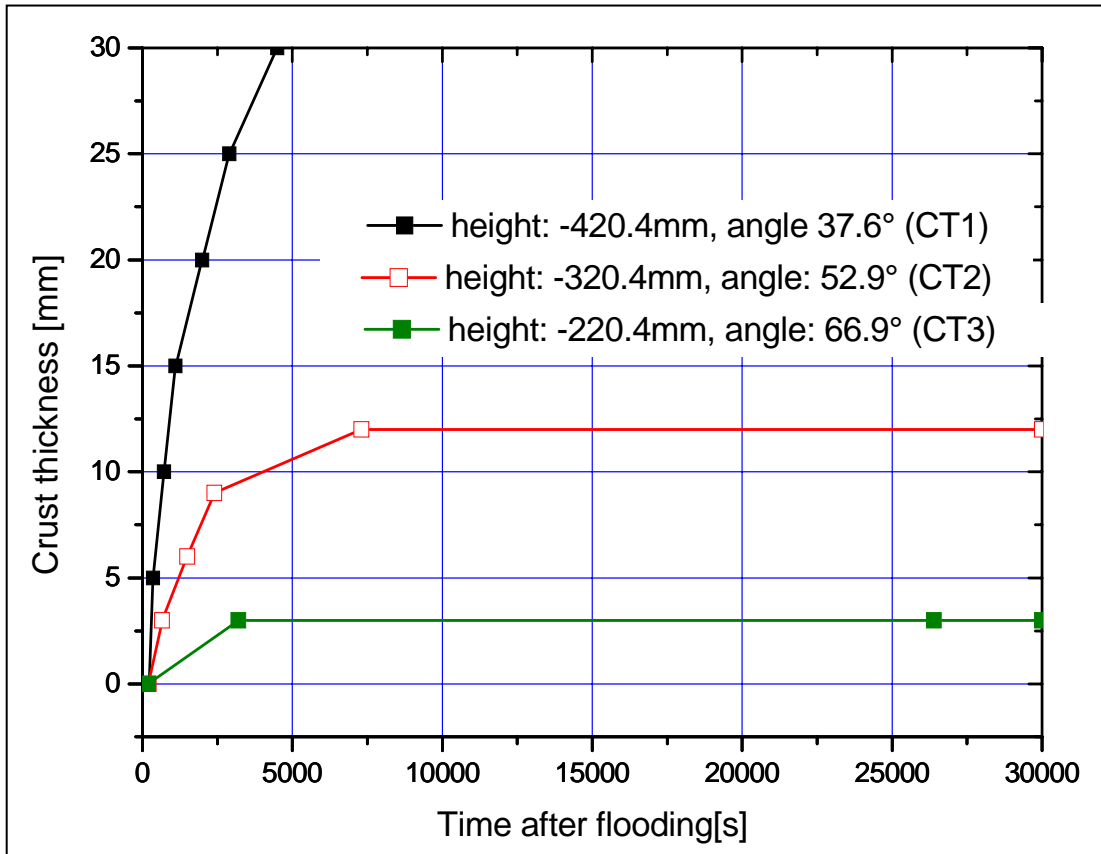


Figure 59: Crust growth rate after water flooding during 10 kW heating period in LIVE-L3

The steady state behaviour of crust growth is examined during the 10 kW heating period in the LIVE-L3 test. In Table 26, the crust growth rate, the transient heat flux through the wall and the liquidus temperature of the melt are given. For the transient heat flux, assuming that: at the position of CT1, the heat flux is the sum of 70 % q_{IT2} and 30 % q_{IT6} ; at the position of CT2, the local heat flux corresponds to q_{IT6} and at the position of CT3, the local heat flux corresponds to q_{IT10} . Table 26 shows that the crust growth rate was considerably higher at the beginning of the test in comparison with the crust growth rate in LIVE-L1. It is also found that similarly to LIVE-L1, at the same CT position, the steady state of crust growth took place at the same crust thickness and in the similar heat transfer range. For example, at the position of CT1, the crust grew at a steady rate of 0.005 - 0.007 mm/s at the crust thickness of 20 to

25 mm. At the position of CT2, the crust grew at a steady rate of 0.003 - 0.004 mm/s at the crust thickness of 6 – 9 mm. During the steady state of solidification process, the crust composition is close to the melt pool composition and the liquidus temperature of the local melt ahead of the crust is significantly lower than the melt pool liquidus temperature.

The melt liquidus temperatures measured by CT thermocouples are between 275 - 280°C. These values are higher than the theoretically predicted local melt liquidus temperature ahead of the crust front. Since the crust was formed under the constitutional supercooling conditions, the solidification takes place in the range between the melt pool liquidus temperature (~284°C) and the local liquidus temperature (~230°C). However, since the characteristic dimensions of the thermocouples and the crust boundary layer are similar (~1 mm) it is not possible to obtain the exact temperature values in the boundary layer ahead the propagating crust front.

Table 26: Crust growth rate, heat flux through the wall and liquidus temperature of the melt measured by CT thermocouples in LIVE-L3

CT1 (37.6°) mm in melt	q_{wall} [W/m²]	Crust growth rate [mm/s]	T_{liq} of the melt [°C]	CT2 (52.9°) mm in melt	q_{wall} [W/m²]	Crust growth rate [mm/s]	T_{liq} of the melt [°C]
0	32191		285	0	62899		283
5	18197	0.0376	287	3	19261	0.0067	285
10	12332	0.0172	277	6	11652	0.0038	282
15	8980	0.0111	278	9	8867	0.0032	283
20	6729	0.0066	278	12	7536	0.0006	284
25	5829	0.0053	280	15		liquid	
30	5054	0.0031	282	18		liquid	
CT3 (66.9°) mm in melt	q_{wall} [W/m²]	Crust growth rate [mm/s]	T_{liq} of the melt [°C]				
0	122097		300				
3	20739	0.0010	288				
6			liquid				

After the end of the test, the crust thicknesses along the four meridians at 67.5°, 157.5°, 247.5° and 337.5° were measured and correspond to the steady state conditions at the end of the heating period with 7 kW. The crust thickness profiles are shown in Figure 60.

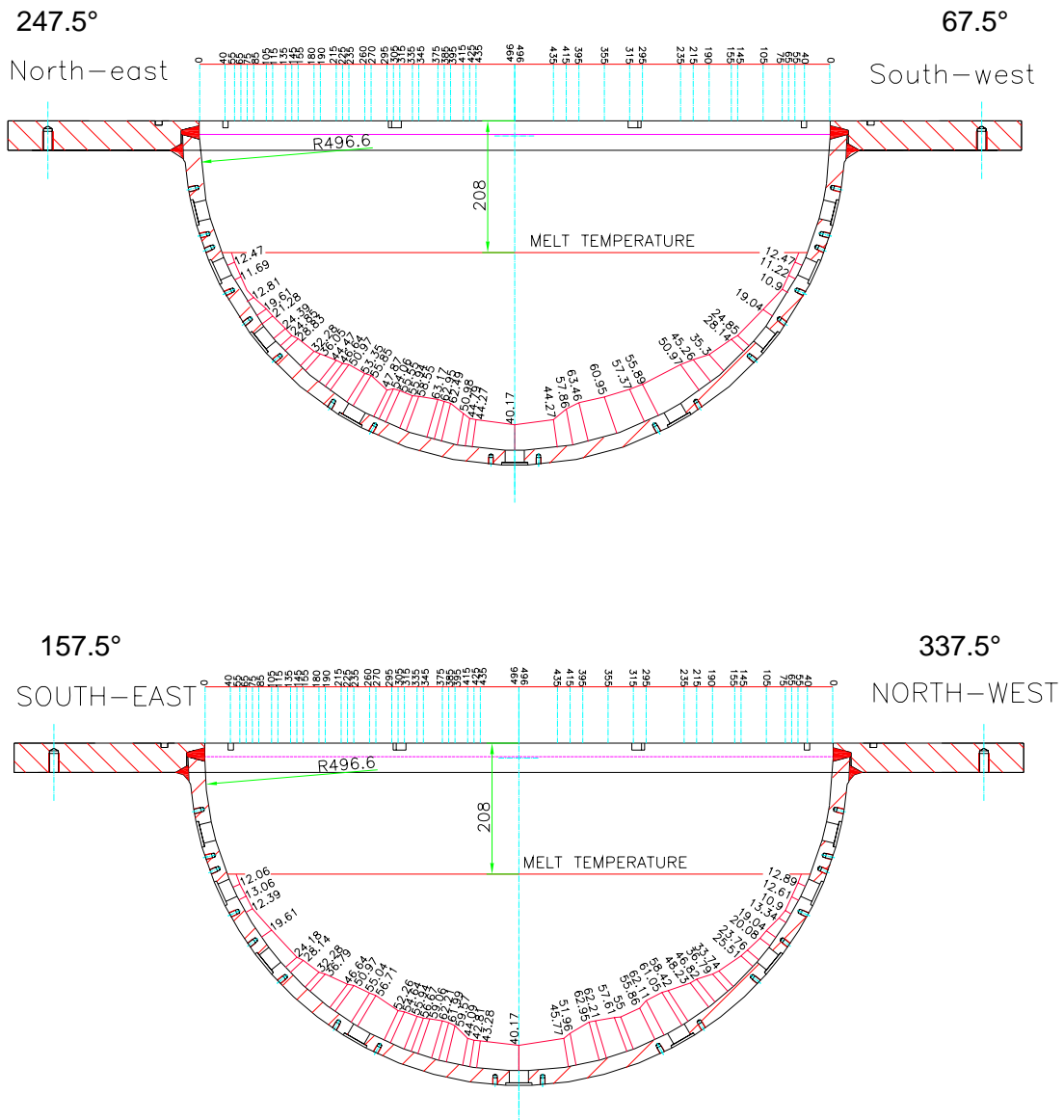


Figure 60: Crust thickness profiles at the end of the test LIVE-L3

In Figure 61, the crust thickness at the end of the test along the meridians 67.5°, 157.5°, 247.5° and 337.5° is shown. The X axis shows the angle to the horizontal axis, which means that the angle 90° is the south pole of the test vessel and the angle 0° corresponds to the upper edge of the test vessel. In Figure 61 also the positions of the heat flux sensors are shown. In LIVE-L3 the thickest crust was formed at the angle between 60° to 85°. In comparison to LIVE-L1, Figure 62, the crust at the bottom of the test vessel was thinner. This can be due to the extraction of the melt at the end of the test. Part of the crust may have been destroyed due to the insertion of the extraction device in LIVE-L3, whereas in LIVE-L1 a part of the melt pool was not extracted back into the heating furnace and remained at the bottom of the vessel.

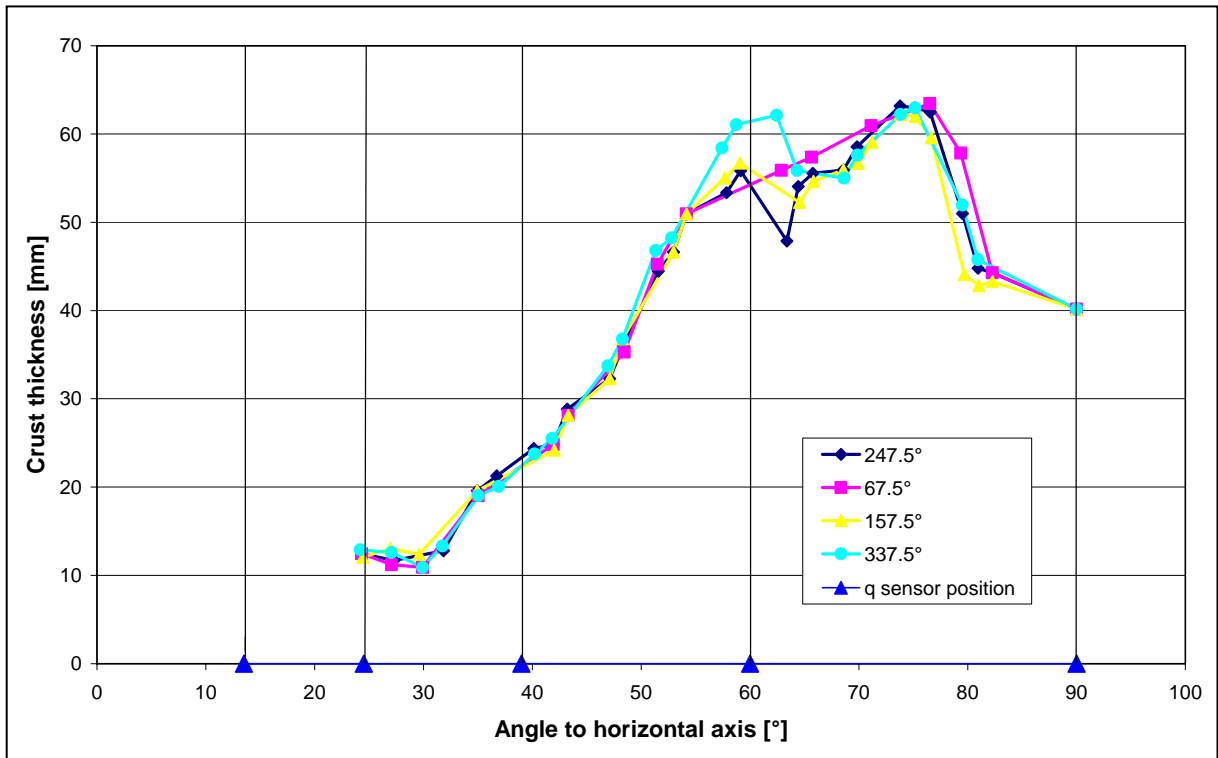


Figure 61: Crust thickness at the end of the test LIVE-L3 along the meridians at 67.5°, 157.5°, 247.5° and 337.5°

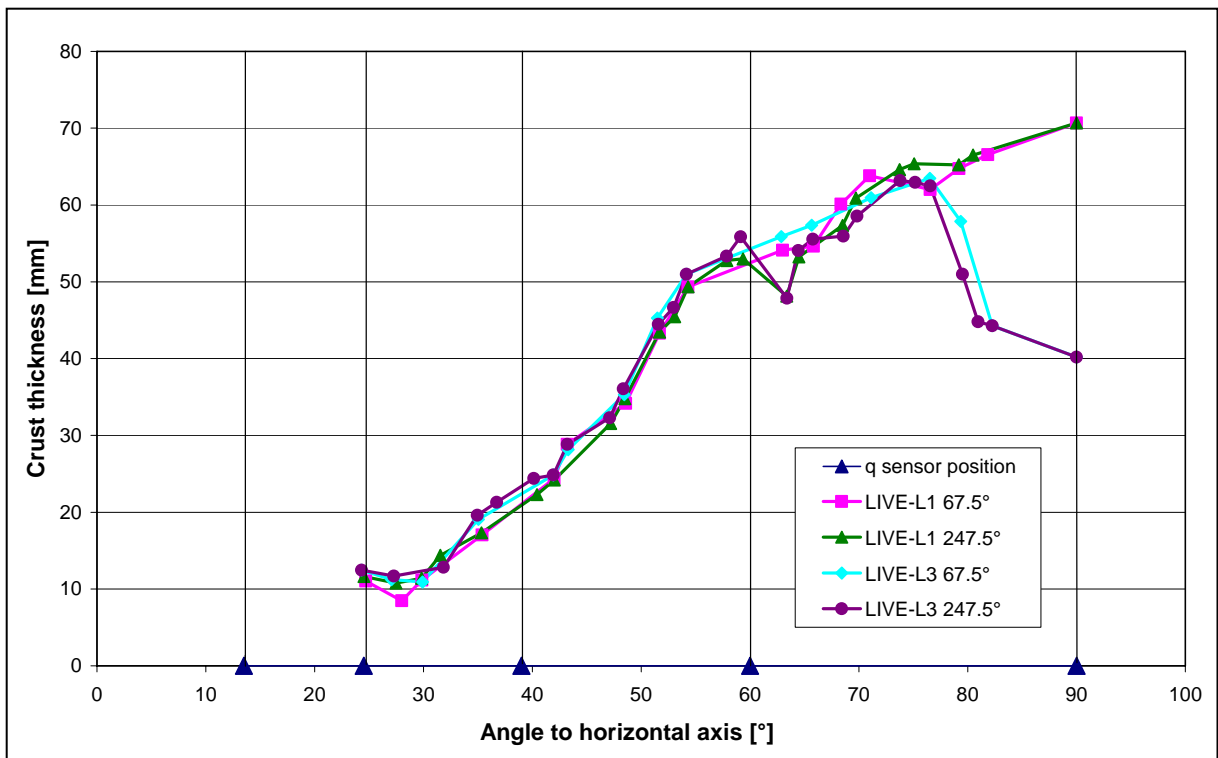


Figure 62: Comparison of the crust thickness at the end of the tests LIVE-L1 and LIVE-L3 along the meridians at 67.5 and 247.5°

4.2.6.3 Crust morphology in LIVE-L3

SEM-EDX line-scanning was performed on the cross-section of a 20 mm thick crust sample. Figure 63 shows the overview pictures of the crust inner layer adjacent to the melt pool and the outer layer adjacent to the vessel wall. The count spectra of Na and K elements at the position of the green line are shown under the SEM pictures. Macroscopically the crust is more compact than the crust formed in the LIVE-L1 test. Similarly to LIVE-L1, Na and K are alternatively enriched across the crust layer. However, the crust compositions near the crust inner surface and the crust outer surface are more homogeneous than those in the middle of the crust layers. The homogeneity at the outer surface can be a result of supercooling conditions at the beginning of water flooding. In this process the crust grows so fast that the solidification temperature is below the solidus temperature. Thus K and Na can not be segregated during solidification. The homogeneity of crust composition at the inner surface can be a result of the very little growth rate of the crust and the crust is formed under almost equilibrium conditions.

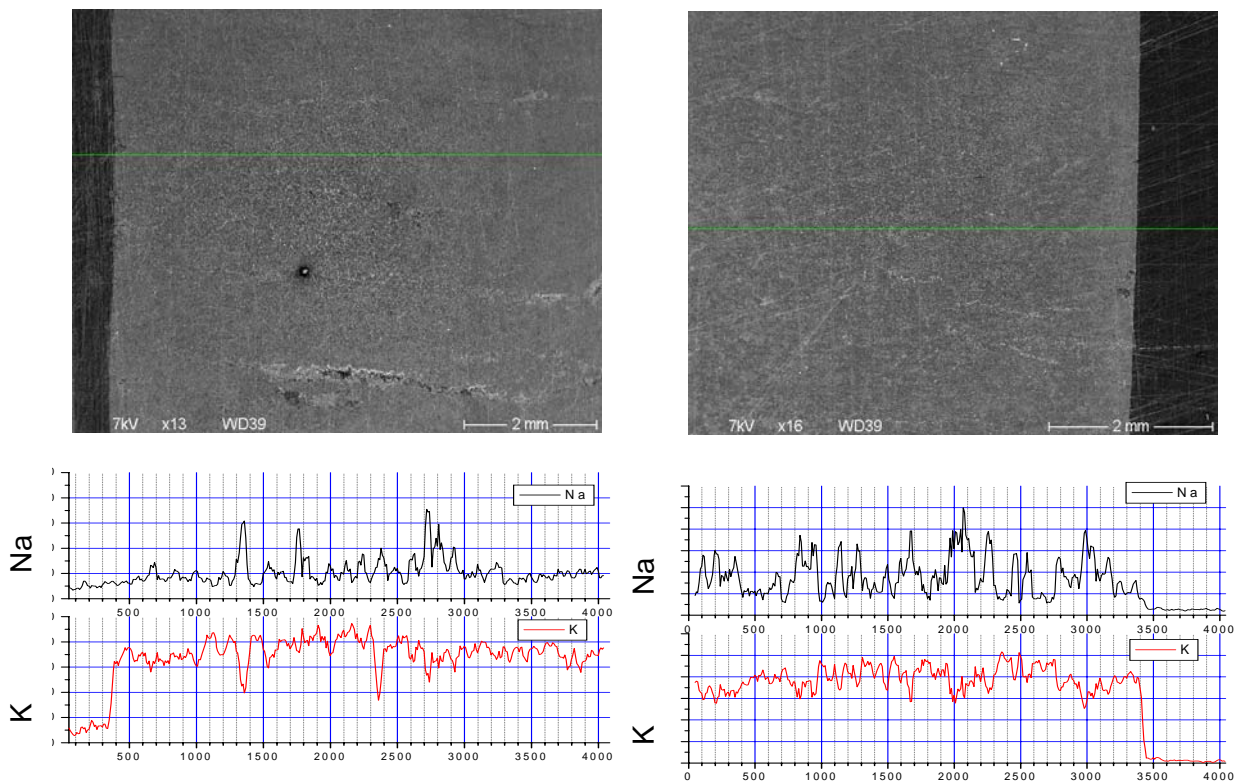


Figure 63: Line-scanning of the crust cross-section in LIVE-L3: left: inner layer, right: outer layer

The microstructure of the crust at the crust outer surface, in the middle of the outer layer, at the boundary of the two layers, in the middle of the inner layer and at the inner surface are shown in Figure 64. The distribution of the grain size is very different among the five positions. At the crust outer surface (a), at the two-layer boundary (c) and at the inner surface (e),

the particle size distribution is very heterogeneous. Both very large particles and very small particles present a high fraction. In the picture (c), which is located at the two-layer boundary, signs of dendrites can be observed. In the contrary, in the middle of the crust layers, pictures (b) and (d) in Figure 64, the particle size is relatively homogenous.

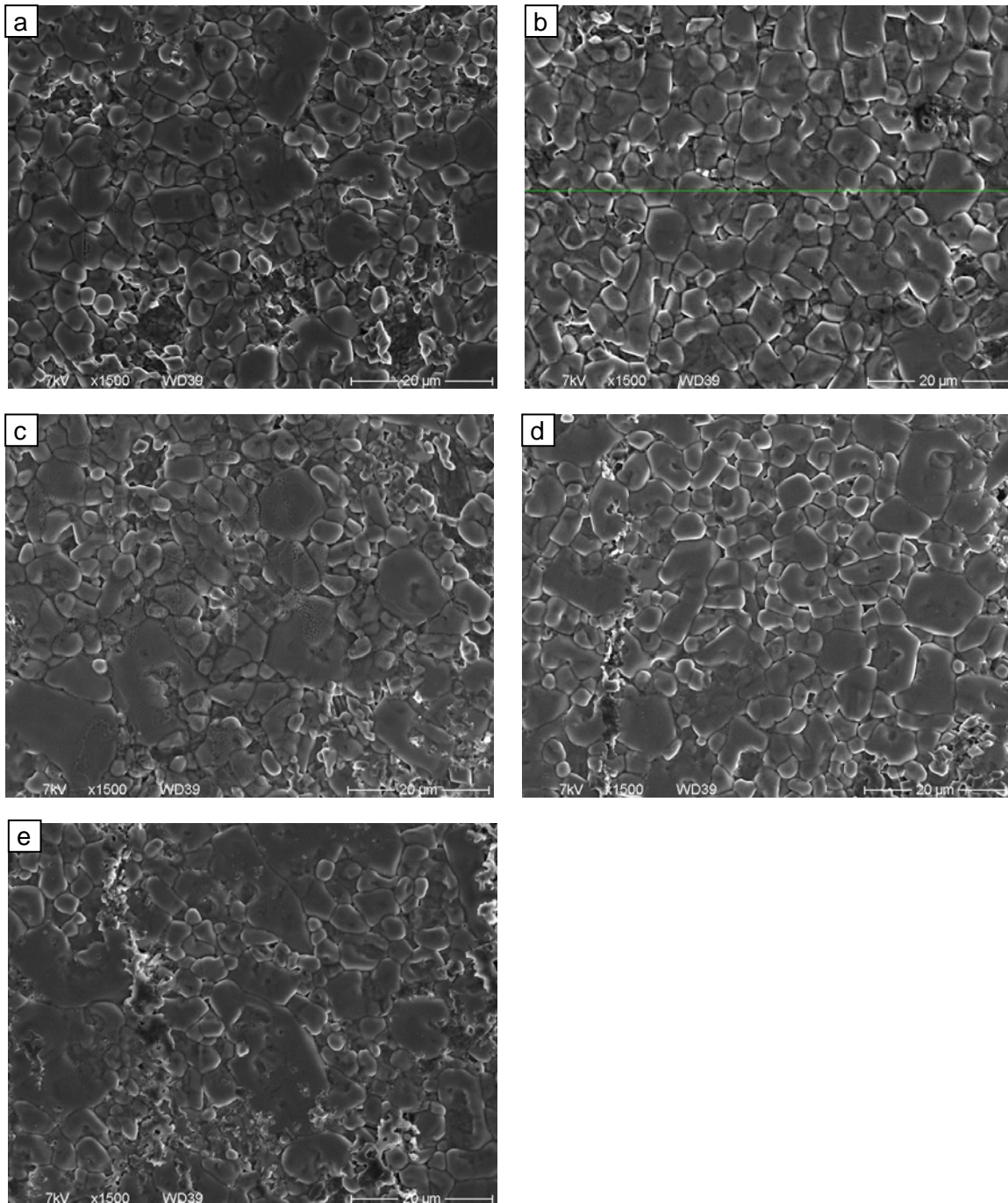


Figure 64: Crust cross-sections of LIVE-L3 test: a: outer surface, b: middle of the outer layer, c: boundary of the outer/inner layer, d: middle of the inner layer, e: inner layer surface.

4.2.6.4 Crust liquidus temperature and crust composition in LIVE-L3

The method of liquidus temperature determination was the same as for LIVE-L1. Two crust samples were used for the analysis, one from the upper (thinner) part of the crust, the other one from the crust piece with a thickness of 20 mm. For the upper sample, the outer crust layer and the inner crust layer were analysed, whereas for the sample with a thickness of 20 mm, five positions along the cross-section of the crust have been measured (Figure 32). The crust liquidus temperatures and the compositions of the crust in the LIVE-L3 test are shown in Table 27.

Table 27: Liquidus temperature and composition of the crust in LIVE-L3

Crust position	Upper range		Crust position	20 mm thick crust piece	
	Liquidus temp [°C]	mole% of NaNO ₃		Liquidus temp [°C]	mole% of NaNO ₃
inner layer	310	8.9	in	316	5.7
outer layer	308	9.4	in-mid	297	19.1
			mid	307	11.0
			mid-out	286	20.0
			out	303	10.3

The same trend is observed as in the LIVE-L1 test: the liquidus temperatures at the crust outer surface and the inner surface are higher than those inside the crust layer.

Some differences were also observed: the crust liquidus temperature in LIVE-L3 (crust outer layer) is higher than those in LIVE-L1 during the 10 kW heating period, but lower than in LIVE-L1 during the 7 kW heating period (crust inner layer). Taking into account the crust growth rates at the position of CT2 in Table 13 and Table 26, and the liquidus temperatures shown in Figure 65, following explanation could be proposed: In the case of LIVE-L3, the crust growth rate is lower than in LIVE-L1, so that the enrichment of NaNO₃ in the local melt is not very high. At the same time, there is more time for NaNO₃ diffusion from the local melt to the melt pool. This leads to the fact the local melt composition is more approached to the melt pool composition. Therefore, the crust formed during a slow growth rate has a higher liquidus temperature.

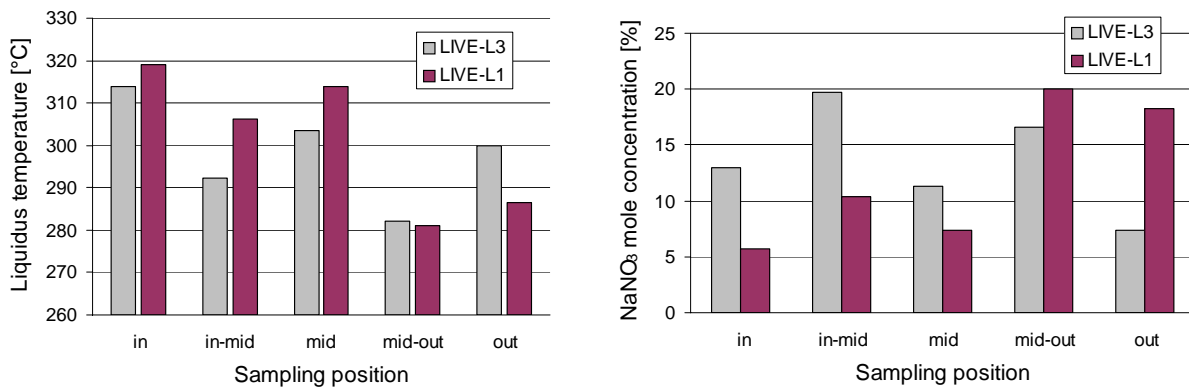


Figure 65: Comparison of the crust liquidus temperature and the crust composition between LIVE-L1 and LIVE-L3. Crust thickness is 20 mm.

4.2.6.5 Crust porosity and crust thermal conductivity in LIVE-L3

The crust thermal conductivity is calculated using the same approach as described in chapter 3.2.6.5. However, more accurate results were obtained in the LIVE-L3 calculation, since the heat flux selected for the calculation is located at the meridian at 22.5° horizontally (q_{IT2} , q_{IT6} , q_{IT10} and q_{IT14}), which is near by the thermocouple trees at 35°. In Table 28, the calculation parameters and the thermal conductivities of the inner crust layer and the outer crust layer at different heights are listed.

Table 28: Thermal conductivities of the crust layers in LIVE-L3

	Thermocouple	Temp. range [°C]	L [mm]	ΔT [K]	Q [W/m ²]	k W/(mK)
Inner layer (crust layer to melt)						
CT2*, 52.9°	CT25-CT27	262-205	6	57	4754	0.494
CT3*, 66.9°	CT32-CT34	130-228	6	98	9903	0.605
Outer layer (crust layer to wall)						
CT1*, 37.6°	CT11-CT17	78-212	30	134	2925	0.653
CT2*, 52.9°	CT21-CT25	79-205	12	126	4754	0.454
CT3*, 66.9°	CT31-CT32	70-130	3	60	9903	0.495

As in LIVE-L1, significant differences in the crust thermal conductivity were observed also in the LIVE-L3 test. The highest crust thermal conductivity was measured at the lower part of the crust (CT1*). It reduces gradually to about 0.45 W/mK at the middle range of the crust (CT2*), which is almost equivalent to the thermal conductivity of the liquid melt, and it in-

creases slightly again at the upper range of the crust (CT3*). Similarly to LIVE-L1, the crust inner layer has slightly higher thermal conductivity than the crust outer layer.

The crust porosity in the LIVE-L3 test is given in Table 29. In general, the crust inner layer is denser than the crust outer layer. In comparison with the results of LIVE-L1 in 3.2.6.5, the LIVE-L3 crust has a lower porosity. This is probably the reason that the LIVE-L3 crust has generally higher thermal conductivity than the LIVE-L1 crust.

Table 29: Crust porosity of LIVE-L3 test

	Total porosity [%]	Bulk density [g/cm ³]	Pore distribution	
			100-2µm [%]	2-0.001µm [%]
Inner layer	2.5	2.07	67.6	32.4
Outer layer	3.3	2.04	51.3	48.7

The detailed pore distribution of the crust inner layer and the outer layer formed during the LIVE-L3 test is illustrated in Figure 66.

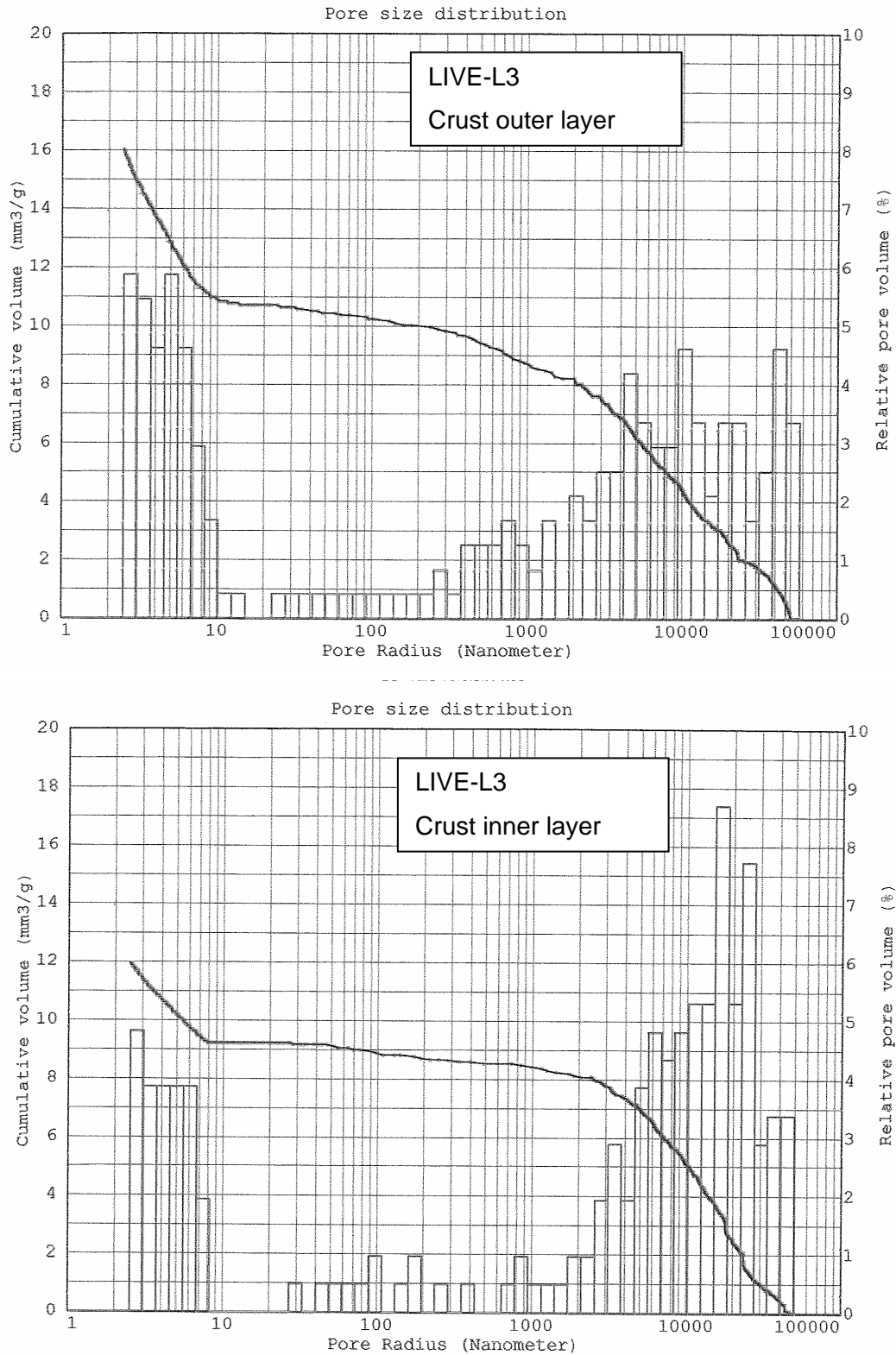


Figure 66: Pore size distribution of the crust layers in LIVE-L3: top: outer layer, bottom: inner layer

5 Conclusions from the experiments

The LIVE experimental facility is designed to study the molten pool behaviour in the RPV lower head in order to complement the experimental data obtained in the earlier programs and to provide new results for the development and improvement of mechanistic models applied for the description of the late in-vessel phase of the core melt progression.

The objective of the performed LIVE-L1 and LIVE-L3 tests was to study the influence of the melt relocation mode on the vessel thermal loads in the transient phase and on the long-term melt behaviour and crust formation in the steady state conditions. Another objective of these tests was to study the melt behaviour and heat flux distribution through the vessel wall during two cooling modes a) with air circulation at the outer vessel wall followed by b) flooding the outside vessel wall with water. Therefore, the initial and boundary conditions in the tests LIVE-L1 and LIVE-L3 were the same except that the melt was poured at the center in the LIVE-L1 and near to the vessel wall in the LIVE-L3 test.

The heat flux distribution at the vessel wall has been measured with heat flux sensors and has been calculated with the help of thermocouples, which were positioned at the inner and outer vessel wall surface. In both experiments the measurements and the calculations clearly indicate two peaks: one after the melt pouring and a second one after the start of the outer vessel wall cooling. The maximum heat fluxes during the vessel cooling were measured and calculated in the area just below the melt surface. Generally, the evaluation of the heat flux measurement and calculation showed that the accuracy of the heat flux sensor values is not sufficient. The heat flux calculation with the IT/OT thermocouples provides the most reliable data. Therefore the heat flux distribution in future tests will be evaluated based on the measurements of the inner and outer wall (using IT/OT thermocouples).

The position of the melt pour has only minor influence on the melt temperature and heat flux distribution in the long-term. However, in the transient phase of the LIVE-L3 test an asymmetric distribution of the heat flux was observed with higher heat fluxes measured at the pouring position. Asymmetry in the crust form and crust thickness at the end of the test due to the lateral pouring position in LIVE-L3 was not observed. The main reason for this phenomenon is that with the high heating power of 10 kW in the test phase 1 without water cooling of the vessel wall, the melt crusts formed during the melt pouring have been remelted. Therefore, same conditions as in LIVE-L1 have been created and the crust growth rates and the final crust thicknesses in both experiments are comparable.

The post-test analysis shows that the crust formed in the LIVE-L3 experiment is less porous and therefore has higher thermal conductivity than the crust formed in the LIVE-L1 test.

The results of the experiments will be used for the validation of codes applied for safety assessment and planning of accident mitigation concepts.

Acknowledgements

This work has been partially sponsored by the European Commission in the 5th Framework Programme under the LACOMERA contract No. FIR1-CT2002-40158

6 References

- [1] A. Miassoedov, et al., "Large Scale Experiments on Core Degradation, Melt Retention and Coolability (LACOMERA)", 2003, Proc. FISA-2003. EU Research in Reactor Safety, Luxembourg, November 10-13, 2003.
- [2] A. Miassoedov, et al., "Results of the QUENCH-L1, DISCO-L1 and COMET-L1 Experiments Performed Within the LACOMERA Project at the Forschungszentrum Karlsruhe", 2005, Proc. 13th International Conference on Nuclear Engineering (ICONE13), Beijing, China, May 16-20, 2005, CD-ROM, Paper 50607.
- [3] A. Miassoedov, et al., "Results of the QUENCH-L2, DISO-L2 and COMET-L2 Experiments Performed Within the LACOMERA Project at the Forschungszentrum Karlsruhe", 2006, Proc. 14th International Conference on Nuclear Engineering (ICONE14), Miami, Florida, USA, July 17-20, 2006, CD-ROM, Paper 89343.
- [4] H. Alsmeyer, et al., "The COMET-L1 Experiment on Long-Term Concrete Erosion and Surface Flooding", Proc. 11th International Topical Meeting on Nuclear Reactor Thermal-Hydraulics (NURETH-11), Avignon, France, October 2-6, 2005.
- [5] A. Miassoedov, et al., "Results of the LIVE-L1 Experiment on Melt Behaviour in RPV Lower Head Performed within the LACOMERA project at the Forschungszentrum Karlsruhe", 2007, Proc. 15th International Conference on Nuclear Engineering (ICONE15), Nagoya, Japan, April 22-26, 2007, Paper 10227.
- [6] O. Kymäläinen, H. Tuomisto, T.G. Theofanous, "In-vessel retention of corium at the Loviisa plant", Nuclear Engineering and Design 169 (1997) pp.109-130.
- [7] S. Abalin, I. Gnidoi, V. Semenov, V. Strizhov, A. Surenkov, "The Results and Analysis of the RASPLAV Salt Tests", Rasplav Seminar 2000, Munich, Germany, 14-15 November 2000.
- [8] B. Fluhrer, et al., "The Experimental Programme LIVE to investigate In-Vessel Core Melt Behaviour in the Late Phase", Jahrestagung Kerntechnik 2005, Nürnberg, INFORUM GmbH, 2005, pp. 198-201.
- [9] Deutsche Risikostudie Kernkraftwerke, Phase B-: eine Untersuchung / Ges. für Reaktorsicherheit. Im Auftr. d. Bundesministers für Forschung u. Technologie. - Köln: Verl. TÜV Rheinland, 1990, ISBN 3-88585-809-6.
- [10] E.M. Levin, C.R. Robbins, H.F. McMurdie, 1985, "Phase Diagrams For Ceramists Vol. 1: Oxides and Salts", Amercian Ceramic Society, ISBN-10: 0916094049.
- [11] B.R. Sehgal, Z.L. Yang, "Ex-vessel Core Melt Stabilization Research; On the Experiments with Simulant Materials at KTH", SAM-ECOSTAR-P11/001, KTH, Stockholm ,

- Sweden, January 2001.
- [12] H.M. Goodwin, and R.D. Mailey, "On the Density, Electrical Conductivity and Viscosity of Fused Salts and Their Mixtures", *The Physical Review - American Physical Society*, January, 1908, pp. 40.
- [13] F.P. Incropera, D. P. DeWitt, "Introduction to heat transfer", John Wiley & Sons, New York, 2002, ISBN 0-471-38649-9.
- [14] M. P. Flemings, "Solidification Processing", McGraw-Hill Inc., New York, 1974, pp. 59-61, ISBN 0-07-021283-X.
- [15] H. Combeau, B. Appolaire, J.M. Seiler, "Interface temperature between solid and liquid corium in severe accident situations: a comprehensive study of characteristic time delay needed for reaching liquidus temperature", OECD/CSNI MASCA2 Seminar, Cadarache, France, 11-12 October 2007.
- [16] Robert E. Reed-Hill, "Physical Metallurgy Principles", 2nd ed., Van Nostrand Reinhold, University Ser. in Basic Engineering, pp. 381-398, ISBN: 0-442-26868-8, 1973.

Annex A Data Acquisition and Instrumentation

Annex A.1 LIVE-L1 and LIVE-L3 channel assignments

Table A-1 lists all signals that were registered on the PC data acquisition system for the experiment LIVE-L1 and Table A- 2 lists all signals that were registered on the PC data acquisition system for the experiment LIVE-L3.

All signal cables are attached to a control cabinet, which is positioned near the LIVE test vessel. The temperature signals are all single-ended signals. The reference junctions of thermocouples are traditionally maintained at 0°C. This is assumed in thermocouple calibration tables. In the LIVE experiments, the reference junction is situated in the control cabinet and has ambient temperature. To overcome this error of a non-zero thermocouple reference junction, the temperature of the reference point is measured by three PT-100 sensors (named RT) that are attached at the connector blocks of the thermocouples. This temperature is then used to correct the temperature measured by the thermocouples.

Table A-1: LIVE-L1 channel assignment for PC data acquisition system

Nr.	Designation	Category	Sensor	Position			Channel Number	Remarks
				Angle ϕ	Radius [mm]	Depth [mm]		
1	ST1	Spout temperature	NiCr/Ni	-	-	-	1	ST = Spout Temperature
2	MT1	Melt temperature	NiCr/Ni	0	74	450	2	MT = Melt Temperature
3	MT2	Melt temperature	NiCr/Ni	90	74	450	3	
4	MT3	Melt temperature	NiCr/Ni	180	74	450	4	Reference point:
5	MT4	Melt temperature	NiCr/Ni	270	74	450	5	Angle 0 = Instrumentation axis
6	MT5	Melt temperature	NiCr/Ni	0	174	450	6	Radius 0 = Middle of the tet vessel
7	MT6	Melt temperature	NiCr/Ni	90	174	450	7	Depth 0 = Flange upper edge
8	MT7	Melt temperature	NiCr/Ni	180	174	450	8	
9	MT8	Melt temperature	NiCr/Ni	270	174	450	9	
10	MT9	Melt temperature	NiCr/Ni	0	74	350	10	
11	MT0	Melt temperature	NiCr/Ni	90	74	350	11	
12	MT11	Melt temperature	NiCr/Ni	180	74	350	12	
13	MT12	Melt temperature	NiCr/Ni	270	74	350	13	
14	MT13	Melt temperature	NiCr/Ni	0	174	350	14	
15	MT14	Melt temperature	NiCr/Ni	90	174	350	15	
16	MT15	Melt temperature	NiCr/Ni	180	174	350	16	
17	MT16	Melt temperature	NiCr/Ni	270	174	350	17	
18	MT17	Melt temperature	NiCr/Ni	0	274	350	18	
19	MT18	Melt temperature	NiCr/Ni	90	274	350	19	
20	MT19	Melt temperature	NiCr/Ni	180	274	350	20	
21	MT20	Melt temperature	NiCr/Ni	270	274	350	21	
22	MT21	Melt temperature	NiCr/Ni	0	74	250	22	
23	MT22	Melt temperature	NiCr/Ni	90	74	250	23	
24	MT23	Melt temperature	NiCr/Ni	180	74	250	24	
25	MT24	Melt temperature	NiCr/Ni	270	74	250	25	

26	MT25	Melt temperature	NiCr/Ni	0	174	250	26
27	MT26	Melt temperature	NiCr/Ni	90	174	250	27
28	MT27	Melt temperature	NiCr/Ni	180	174	250	28
29	MT28	Melt temperature	NiCr/Ni	270	174	250	29
30	MT39	Melt temperature	NiCr/Ni	0	274	250	30
31	MT30	Melt temperature	NiCr/Ni	90	274	250	31
32	MT31	Melt temperature	NiCr/Ni	180	274	250	32
33	MT32	Melt temperature	NiCr/Ni	270	274	250	33
34	MT33	Melt temperature	NiCr/Ni	0	374	250	34
35	MT34	Melt temperature	NiCr/Ni	90	374	250	35
36	MT35	Melt temperature	NiCr/Ni	180	374	250	36
37	MT36	Melt temperature	NiCr/Ni	270	374	250	37
38	OT1	Outer wall temperature	NiCr/Ni	292.5	36.35	518	191
39	OT2	Outer wall temperature	NiCr/Ni	22.5	260	451	192
40	OT3	Outer wall temperature	NiCr/Ni	112.5	260	451	193
41	OT4	Outer wall temperature	NiCr/Ni	202.5	260	451	194
42	OT5	Outer wall temperature	NiCr/Ni	292.5	260	451	195
43	OT6	Outer wall temperature	NiCr/Ni	22.5	404	327	196
44	OT7	Outer wall temperature	NiCr/Ni	112.5	404	327	197
45	OT8	Outer wall temperature	NiCr/Ni	202.5	404	327	198
46	OT9	Outer wall temperature	NiCr/Ni	292.5	404	327	199
47	OI10	Outer wall temperature	NiCr/Ni	22.5	474	216	200
48	OI11	Outer wall temperature	NiCr/Ni	112.5	474	216	201
49	OI12	Outer wall temperature	NiCr/Ni	202.5	474	216	202
50	OI13	Outer wall temperature	NiCr/Ni	292.5	474	216	203
51	OI14	Outer wall temperature	NiCr/Ni	22.5	506	121	204
52	OI15	Outer wall temperature	NiCr/Ni	112.5	506	121	205
53	OI16	Outer wall temperature	NiCr/Ni	202.5	506	121	206
54	OI17	Outer wall temperature	NiCr/Ni	292.5	506	121	207
55	IT1	Inner wall temperature	NiCr/Ni	112.5	35	520	49

OT = Temperature of the vessel
outer surface

Reference point:
Angle 0 = Instrumentation axis
Radius 0 = Middle of the test vessel
Depth 0 = Flange upper edge

IT = Temperature of the vessel

56	IT3	Inner wall temperature	NiCr/Ni	112.5	249	455	51	inner surface
57	IT7	Inner wall temperature	NiCr/Ni	112.5	387	337	55	
58	IT11	Inner wall temperature	NiCr/Ni	112.5	453	230	59	
59	IT15	Inner wall temperature	NiCr/Ni	112.5	484	140	63	
60	OOT1	Outer temp. cooling tank	NiCr/Ni	300	38	730	46	
61	OOT2	Outer temp. cooling tank	NiCr/Ni	300	428	587	47	OOT = Temperature of the cooling tank outer surface
62	OOT3	Outer temp. cooling tank	NiCr/Ni	300	670	250	48	
63	PT11	Temperature of plug 1	NiCr/Ni	0	0	520	68	PT = Plug temperature
64	PT12	Temperature of plug 1	NiCr/Ni	0	0	520	69	Position refers to the upper edge of the instrumentation plug
65	PT13	Temperature of plug 1	NiCr/Ni	0	0	520	70	
66	PT14	Temperature of plug 1	NiCr/Ni	0	0	520	71	
67	PT15	Temperature of plug 1	NiCr/Ni	0	0	520	72	
68	PT21	Temperature of plug 2	NiCr/Ni	67.5	248.18	454	146	
69	PT22	Temperature of plug 2	NiCr/Ni	67.5	248.18	454	147	Angle 0 = Instrumentation axis
70	PT23	Temperature of plug 2	NiCr/Ni	67.5	248.18	454	148	Radius 0 = Middle of the test vessel
71	PT24	Temperature of plug 2	NiCr/Ni	67.5	248.18	454	149	Depth 0 = Flange upper edge
72	PT25	Temperature of plug 2	NiCr/Ni	67.5	248.18	454	150	Designation of the "b" number of PT"ab" 1 = 0 mm 2 = 5 mm 3 = 10 mm 4 = 15 mm 5 = 20 mm length of the thermocouple from the inner vessel wall into the melt
73	PT61	Temperature of plug 6	NiCr/Ni	67.5	385.75	337	152	
74	PT62	Temperature of plug 6	NiCr/Ni	67.5	385.75	337	153	
75	PT63	Temperature of plug 6	NiCr/Ni	67.5	385.75	337	154	
76	PT64	Temperature of plug 6	NiCr/Ni	67.5	385.75	337	155	
77	PT65	Temperature of plug 6	NiCr/Ni	67.5	385.75	337	156	
78	PT101	Temperature of plug 10	NiCr/Ni	67.5	451.69	230	158	
79	PT102	Temperature of plug 10	NiCr/Ni	67.5	451.69	230	159	
80	PT103	Temperature of plug 10	NiCr/Ni	67.5	451.69	230	160	
81	PT104	Temperature of plug 10	NiCr/Ni	67.5	451.69	230	161	
82	PT105	Temperature of plug 10	NiCr/Ni	67.5	451.69	230	162	
83	PT141	Temperature of plug 14	NiCr/Ni	67.5	482.66	140	164	
84	PT142	Temperature of plug 14	NiCr/Ni	67.5	482.66	140	165	
85	PT143	Temperature of plug 14	NiCr/Ni	67.5	482.66	140	166	

86	PT144	Temperature of plug 14	NiCr/Ni	67.5	482.66	140	167
87	PT145	Temperature of plug 14	NiCr/Ni	67.5	482.66	140	168
88	HFT1	Heat flux sensor temp.	NiCr/Ni	0	0	520	67
89	HFT2	Heat flux sensor temp.	NiCr/Ni	67.5	248.18	454	145
90	HFT6	Heat flux sensor temp.	NiCr/Ni	67.5	385.75	337	151
91	HFT10	Heat flux sensor temp.	NiCr/Ni	67.5	451.69	230	157
92	HFT14	Heat flux sensor temp.	NiCr/Ni	67.5	482.66	140	163
93	HF1	Heat flux	WFS	0	0	520	169
94	HF2	Heat flux	WFS	67.5	248.18	454	170
95	HF6	Heat flux	WFS	67.5	385.75	337	174
96	HF10	Heat flux	WFS	67.5	451.69	230	178
97	HF14	Heat flux	WFS	67.5	482.66	140	182
98	CT11	TC-Tree 1	NiCr/Ni	35	260	420.4	208
99	CT12	TC-Tree 1	NiCr/Ni	35	260	420.4	209
100	CT13	TC-Tree 1	NiCr/Ni	35	260	420.4	210
101	CT14	TC-Tree 1	NiCr/Ni	35	260	420.4	211
102	CT15	TC-Tree 1	NiCr/Ni	35	260	420.4	212
103	CT16	TC-Tree 1	NiCr/Ni	35	260	420.4	213
104	CT17	TC-Tree 1	NiCr/Ni	35	260	420.4	214
105	CT21	TC-Tree 2	NiCr/Ni	35	404	320.4	215
106	CT22	TC-Tree 2	NiCr/Ni	35	404	320.4	216
107	CT23	TC-Tree 2	NiCr/Ni	35	404	320.4	217
108	CT24	TC-Tree 2	NiCr/Ni	35	404	320.4	218
109	CT25	TC-Tree 2	NiCr/Ni	35	404	320.4	219
110	CT26	TC-Tree 2	NiCr/Ni	35	404	320.4	220
111	CT27	TC-Tree 2	NiCr/Ni	35	404	320.4	221
112	CT31	TC-Tree 3	NiCr/Ni	35	474	220.4	222
113	CT32	TC-Tree 3	NiCr/Ni	35	474	220.4	223
114	CT33	TC-Tree 3	NiCr/Ni	35	474	220.4	224
115	CT34	TC-Tree 3	NiCr/Ni	35	474	220.4	225

Position refers to the upper edge of the instrumentation plug

Reference point:

Angle 0 = Instrumentation axis

Radius 0 = Middle of the test vessel

Depth 0 = Flange upper edge

CT = Crust Temperature

Position refers to the mounting position of the TC-Tree

Reference point:

Angle 0 = Instrumentation axis

Radius 0 = Middle of the test vessel

Designation of the "b" number of

CT"ab" different for a = 1 and

a = (2,3)

1 = 0 mm (0 mm)

2 = 5 mm (3 mm)

3 = 10 mm (6 mm)

4 = 15 mm (9 mm)

5 = 20 mm (12 mm)

6 = 25 mm (15 mm)

7 = 30 mm (18 mm)

116	CT35	TC-Tree 3	NiCr/Ni	35	474	220.4	226	length of the thermocouple from inner wall into the melt
117	CT36	TC-Tree 3	NiCr/Ni	35	474	220.4	227	
118	CT37	TC-Tree 3	NiCr/Ni	35	474	220.4	228	
119	RT1	Temp. Control Cabinet	Pt-100					RT = Resistance Thermometer
120	RT2	Temp. Control Cabinet	Pt-100					
121	RT3	Temp. Control Cabinet	Pt-100					
122	AT1	Temp. cool. water outflow	NiCr/Ni	inside bow of overflow rod			230	flowmeter 0-2 l/s flowmeter 0-12 ml/s
123	ZT1	Temp. cooling water inflow	NiCr/Ni	behind flowmeter			231	
124	KT1	Temp. condensate outflow	NiCr/Ni	behind condensator			232	
125	W1	Weight of test vessel	W. cells	-			233	
126	DF1	Flow rate cooling water	Krohne	inside cooling water inlet			234	
127	DF2	Flow rate cooling water	Kobold	inside cooling water inlet			235	

Table A- 2: LIVE-L3 channel assignment for PC data acquisition system

Nr.	Designation	Category	Sensor	Position			Channel Number	Remarks
				Angle ϕ	Radius [mm]	Depth [mm]		
1	ST1	Shout temperature	NiCr/Ni	-	-	-	1	ST = Shout Temperature
2	MT1	Melt temperature	NiCr/Ni	0	74	450	2	MT = Melt Temperature
3	MT2	Melt temperature	NiCr/Ni	90	74	450	3	
4	MT3	Melt temperature	NiCr/Ni	180	74	450	4	Reference point:
5	MT4	Melt temperature	NiCr/Ni	270	74	450	5	Angle 0 = Instrumentation axis
6	MT5	Melt temperature	NiCr/Ni	0	174	450	6	Radius 0 = Middle of the tet vessel
7	MT6	Melt temperature	NiCr/Ni	90	174	450	7	Depth 0 = Flange upper edge
8	MT7	Melt temperature	NiCr/Ni	180	174	450	8	
9	MT8	Melt temperature	NiCr/Ni	270	174	450	9	
10	MT9	Melt temperature	NiCr/Ni	0	74	350	10	
11	MT10	Melt temperature	NiCr/Ni	90	74	350	11	
12	MT11	Melt temperature	NiCr/Ni	180	74	350	12	
13	MT12	Melt temperature	NiCr/Ni	270	74	350	13	
14	MT13	Melt temperature	NiCr/Ni	0	174	350	14	
15	MT14	Melt temperature	NiCr/Ni	90	174	350	15	
16	MT15	Melt temperature	NiCr/Ni	180	174	350	16	
17	MT16	Melt temperature	NiCr/Ni	270	174	350	17	
18	MT17	Melt temperature	NiCr/Ni	0	274	350	18	
19	MT18	Melt temperature	NiCr/Ni	90	274	350	19	
20	MT19	Melt temperature	NiCr/Ni	180	274	350	20	
21	MT20	Melt temperature	NiCr/Ni	270	274	350	21	
22	MT21	Melt temperature	NiCr/Ni	0	74	250	22	
23	MT22	Melt temperature	NiCr/Ni	90	74	250	23	
24	MT23	Melt temperature	NiCr/Ni	180	74	250	24	
25	MT24	Melt temperature	NiCr/Ni	270	74	250	25	

26	MT25	Melt temperature	NiCr/Ni	0	174	250	26
27	MT26	Melt temperature	NiCr/Ni	90	174	250	27
28	MT27	Melt temperature	NiCr/Ni	180	174	250	28
29	MT28	Melt temperature	NiCr/Ni	270	174	250	29
30	MT39	Melt temperature	NiCr/Ni	0	274	250	30
31	MT30	Melt temperature	NiCr/Ni	90	274	250	31
32	MT31	Melt temperature	NiCr/Ni	180	274	250	32
33	MT32	Melt temperature	NiCr/Ni	270	274	250	33
34	MT33	Melt temperature	NiCr/Ni	0	374	250	34
35	MT34	Melt temperature	NiCr/Ni	90	374	250	35
36	MT35	Melt temperature	NiCr/Ni	180	374	250	36
37	MT36	Melt temperature	NiCr/Ni	270	374	250	37
38	MT37	Temperature above melt	NiCr/Ni	0	60	50	38
39	OT1	Outer wall temperature	NiCr/Ni	292.5	36.35	518	191
40	OT2	Outer wall temperature	NiCr/Ni	22.5	260	451	192
41	OT3	Outer wall temperature	NiCr/Ni	112.5	260	451	193
42	OT4	Outer wall temperature	NiCr/Ni	202.5	260	451	194
43	OT5	Outer wall temperature	NiCr/Ni	292.5	260	451	195
44	OT6	Outer wall temperature	NiCr/Ni	22.5	404	327	196
45	OT7	Outer wall temperature	NiCr/Ni	112.5	404	327	197
46	OT8	Outer wall temperature	NiCr/Ni	202.5	404	327	198
47	OT9	Outer wall temperature	NiCr/Ni	292.5	404	327	199
48	OT10	Outer wall temperature	NiCr/Ni	22.5	474	216	200
49	OT11	Outer wall temperature	NiCr/Ni	112.5	474	216	201
50	OT12	Outer wall temperature	NiCr/Ni	202.5	474	216	202
51	OT13	Outer wall temperature	NiCr/Ni	292.5	474	216	203
52	OT14	Outer wall temperature	NiCr/Ni	22.5	506	121	204
53	OT15	Outer wall temperature	NiCr/Ni	112.5	506	121	205
54	OT16	Outer wall temperature	NiCr/Ni	202.5	506	121	206
55	OT17	Outer wall temperature	NiCr/Ni	292.5	506	121	207

OT = Temperature of the vessel
outer surface

Reference point:
Angle 0 = Instrumentation axis
Radius 0 = Middle of the test vessel
Depth 0 = Flange upper edge

56	IT1	Inner wall temperature	NiCr/Ni	292.5	35	520	49
57	IT2	Inner wall temperature	NiCr/Ni	22.5	249	455	50
58	IT3	Inner wall temperature	NiCr/Ni	112.5	249	455	51
59	IT4	Inner wall temperature	NiCr/Ni	202.5	249	455	52
60	IT5	Inner wall temperature	NiCr/Ni	292.5	249	455	53
61	IT6	Inner wall temperature	NiCr/Ni	22.5	387	337	54
62	IT7	Inner wall temperature	NiCr/Ni	112.5	387	337	55
63	IT8	Inner wall temperature	NiCr/Ni	202.5	387	337	56
64	IT9	Inner wall temperature	NiCr/Ni	292.5	387	337	57
65	IT10	Inner wall temperature	NiCr/Ni	22.5	453	230	58
66	IT11	Inner wall temperature	NiCr/Ni	112.5	453	230	59
67	IT12	Inner wall temperature	NiCr/Ni	202.5	453	230	60
68	IT13	Inner wall temperature	NiCr/Ni	292.5	453	230	61
69	IT14	Inner wall temperature	NiCr/Ni	22.5	484	140	62
70	IT15	Inner wall temperature	NiCr/Ni	112.5	484	140	63
71	IT16	Inner wall temperature	NiCr/Ni	202.5	484	149	64
72	IT17	Inner wall temperature	NiCr/Ni	292.5	484	140	65
73	OOT1	Outer temp. cooling tank	NiCr/Ni	300	38	730	46
74	OOT2	Outer temp. cooling tank	NiCr/Ni	300	428	587	47
75	OOT3	Outer temp. cooling tank	NiCr/Ni	300	670	250	48
76	PT11	Temperature of plug 1	NiCr/Ni	0	0	520	68
77	PT12	Temperature of plug 1	NiCr/Ni	0	0	520	69
78	PT13	Temperature of plug 1	NiCr/Ni	0	0	520	70
79	PT14	Temperature of plug 1	NiCr/Ni	0	0	520	71
80	PT15	Temperature of plug 1	NiCr/Ni	0	0	520	72
81	PT21	Temperature of plug 2	NiCr/Ni	67.5	248.18	454	146
82	PT22	Temperature of plug 2	NiCr/Ni	67.5	248.18	454	147
83	PT23	Temperature of plug 2	NiCr/Ni	67.5	248.18	454	148
84	PT24	Temperature of plug 2	NiCr/Ni	67.5	248.18	454	149
85	PT25	Temperature of plug 2	NiCr/Ni	67.5	248.18	454	150

IT = Temperature of the vessel inner surface

OOT = Temperature of the cooling tank outer surface

PT = Plug temperature

Position refers to the upper edge of the instrumentation plug

Reference point:

Angle 0 = Instrumentation axis

Radius 0 = Middle of the test vessel

Depth 0 = Flange upper edge

116	PT91	Temperature of plug 9	NiCr/Ni	337.5	385.75	337	80
117	PT91	Temperature of plug 9	NiCr/Ni	337.5	385.75	337	81
118	PT93	Temperature of plug 9	NiCr/Ni	337.5	385.75	337	82
119	PT94	Temperature of plug 9	NiCr/Ni	337.5	385.75	337	83
120	PT95	Temperature of plug 9	NiCr/Ni	337.5	385.75	337	84
121	PT101	Temperature of plug 10	NiCr/Ni	67.5	451.69	230	158
122	PT102	Temperature of plug 10	NiCr/Ni	67.5	451.69	230	159
123	PT103	Temperature of plug 10	NiCr/Ni	67.5	451.69	230	160
124	PT104	Temperature of plug 10	NiCr/Ni	67.5	451.69	230	161
125	PT105	Temperature of plug 10	NiCr/Ni	67.5	451.69	230	162
126	PT111	Temperature of plug 11	NiCr/Ni	157.5	451.69	230	134
127	PT112	Temperature of plug 11	NiCr/Ni	157.5	451.69	230	135
128	PT113	Temperature of plug 11	NiCr/Ni	157.5	451.69	230	136
129	PT114	Temperature of plug 11	NiCr/Ni	157.5	451.69	230	137
130	PT115	Temperature of plug 11	NiCr/Ni	157.5	451.69	230	138
131	PT121	Temperature of plug 12	NiCr/Ni	247.5	451.69	230	110
132	PT122	Temperature of plug 12	NiCr/Ni	247.5	451.69	230	111
133	PT123	Temperature of plug 12	NiCr/Ni	247.5	451.69	230	112
134	PT124	Temperature of plug 12	NiCr/Ni	247.5	451.69	230	113
135	PT125	Temperature of plug 12	NiCr/Ni	247.5	451.69	230	114
136	PT131	Temperature of plug 13	NiCr/Ni	337.5	451.69	230	86
137	PT132	Temperature of plug 13	NiCr/Ni	337.5	451.69	230	87
138	PT133	Temperature of plug 13	NiCr/Ni	337.5	451.69	230	88
139	PT134	Temperature of plug 13	NiCr/Ni	337.5	451.69	230	89
140	PT135	Temperature of plug 13	NiCr/Ni	337.5	451.69	230	90
141	PT141	Temperature of plug 14	NiCr/Ni	67.5	482.66	140	164
142	PT142	Temperature of plug 14	NiCr/Ni	67.5	482.66	140	165
143	PT143	Temperature of plug 14	NiCr/Ni	67.5	482.66	140	166
144	PT144	Temperature of plug 14	NiCr/Ni	67.5	482.66	140	167
145	PT145	Temperature of plug 14	NiCr/Ni	67.5	482.66	140	168

146	PT151	Temperature of plug 15	NiCr/Ni	157.5	482.66	140	140
147	PT152	Temperature of plug 15	NiCr/Ni	157.5	482.66	140	141
148	PT153	Temperature of plug 15	NiCr/Ni	157.5	482.66	140	142
149	PT154	Temperature of plug 15	NiCr/Ni	157.5	482.66	140	143
150	PT155	Temperature of plug 15	NiCr/Ni	157.5	482.66	140	144
151	PT161	Temperature of plug 16	NiCr/Ni	247.5	482.66	140	116
152	PT162	Temperature of plug 16	NiCr/Ni	247.5	482.66	140	117
153	PT163	Temperature of plug 16	NiCr/Ni	247.5	482.66	140	118
154	PT164	Temperature of plug 16	NiCr/Ni	247.5	482.66	140	119
155	PT165	Temperature of plug 16	NiCr/Ni	247.5	482.66	140	120
156	PT171	Temperature of plug 17	NiCr/Ni	337.5	482.66	140	92
157	PT172	Temperature of plug 17	NiCr/Ni	337.5	482.66	140	93
158	PT173	Temperature of plug 17	NiCr/Ni	337.5	482.66	140	94
159	PT174	Temperature of plug 17	NiCr/Ni	337.5	482.66	140	95
160	PT175	Temperature of plug 17	NiCr/Ni	337.5	482.66	140	96
161	HFT1	Heat flux sensor temperature	NiCr/Ni	0	0	520	67
162	HFT2	Heat flux sensor temperature	NiCr/Ni	67.5	248.18	454	145
163	HFT3	Heat flux sensor temperature	NiCr/Ni	157.5	248.18	454	121
164	HFT4	Heat flux sensor temperature	NiCr/Ni	247.5	248.18	454	97
165	HFT5	Heat flux sensor temperature	NiCr/Ni	337.5	248.18	454	73
166	HFT6	Heat flux sensor temperature	NiCr/Ni	67.5	385.75	337	151
167	HFT7	Heat flux sensor temperature	NiCr/Ni	157.5	385.75	337	127
168	HFT8	Heat flux sensor temperature	NiCr/Ni	247.5	385.75	337	103
169	HFT9	Heat flux sensor temperature	NiCr/Ni	337.5	385.75	337	79
170	HFT10	Heat flux sensor temperature	NiCr/Ni	67.5	451.69	230	157
171	HFT11	Heat flux sensor temperature	NiCr/Ni	157.5	451.69	230	133
172	HFT12	Heat flux sensor temperature	NiCr/Ni	247.5	451.69	230	109
173	HFT13	Heat flux sensor temperature	NiCr/Ni	337.5	451.69	230	85
174	HFT14	Heat flux sensor temperature	NiCr/Ni	67.5	482.66	140	163
175	HFT15	Heat flux sensor temperature	NiCr/Ni	157.5	482.66	140	139

Position refers to the upper edge of the instrumentation plug

Reference point:
Angle 0 = Instrumentation axis
Radius 0 = Middle of the test vessel
Depth 0 = Flange upper edge

176	HFT16	Heat flux sensor temperature	NiCr/Ni	247.5	482.66	140	115
177	HFT17	Heat flux sensor temperature	NiCr/Ni	337.5	482.66	140	91
178	HF1	Heat flux	HFS	0	0	520	169
179	HF2	Heat flux	HFS	67.5	248.18	454	170
180	HF3	Heat flux	HFS	157.5	248.18	454	171
181	HF4	Heat flux	HFS	247.5	248.18	454	172
182	HF5	Heat flux	HFS	337.5	248.18	454	173
183	HF6	Heat flux	HFS	67.5	385.75	337	174
184	HF7	Heat flux	HFS	157.5	385.75	337	175
185	HF8	Heat flux	HFS	247.5	385.75	337	176
186	HF9	Heat flux	HFS	337.5	385.75	337	177
187	HF10	Heat flux	HFS	67.5	451.69	230	178
188	HF11	Heat flux	HFS	157.5	451.69	230	179
189	HF12	Heat flux	HFS	247.5	451.69	230	180
190	HF13	Heat flux	HFS	337.5	451.69	230	181
191	HF14	Heat flux	HFS	67.5	482.66	140	182
192	HF15	Heat flux	HFS	157.5	482.66	140	183
193	HF16	Heat flux	HFS	247.5	482.66	140	184
194	HF17	Heat flux	HFS	337.5	482.66	140	185
195	CT11	TC-Tree 1	NiCr/Ni	35	260	420.4	208
196	CT12	TC-Tree 1	NiCr/Ni	35	260	420.4	209
197	CT13	TC-Tree 1	NiCr/Ni	35	260	420.4	210
198	CT14	TC-Tree 1	NiCr/Ni	35	260	420.4	211
199	CT15	TC-Tree 1	NiCr/Ni	35	260	420.4	212
200	CT16	TC-Tree 1	NiCr/Ni	35	260	420.4	213
201	CT17	TC-Tree 1	NiCr/Ni	35	260	420.4	214
201	CT21	TC-Tree 2	NiCr/Ni	35	404	320.4	215
203	CT22	TC-Tree 2	NiCr/Ni	35	404	320.4	216
204	CT23	TC-Tree 2	NiCr/Ni	35	404	320.4	217
205	CT24	TC-Tree 2	NiCr/Ni	35	404	320.4	218

CT = Crust Temperature

Position refers to the mounting position of the TC-Tree

Reference point:

Angle 0 = Instrumentation axis

Radius 0 = Middle of the test vessel

Designation of the "b" number of

CT"ab" different for a = 1 and

a = (2,3)

206	CT25	TC-Tree 2	NiCr/Ni	35	404	320.4	219	1 = 0 mm (0 mm)
207	CT26	TC-Tree 2	NiCr/Ni	35	404	320.4	220	2 = 5 mm (3 mm)
208	CT27	TC-Tree 2	NiCr/Ni	35	404	320.4	221	3 = 10 mm (6 mm)
209	CT31	TC-Tree 3	NiCr/Ni	35	474	220.4	222	4 = 15 mm (9 mm)
210	CT32	TC-Tree 3	NiCr/Ni	35	474	220.4	223	5 = 20 mm (12 mm)
211	CT33	TC-Tree 3	NiCr/Ni	35	474	220.4	224	6 = 25 mm (15 mm)
212	CT34	TC-Tree 3	NiCr/Ni	35	474	220.4	225	7 = 30 mm (18 mm)
213	CT35	TC-Tree 3	NiCr/Ni	35	474	220.4	226	length of the thermocouple from
214	CT36	TC-Tree 3	NiCr/Ni	35	474	220.4	227	inner wall into the melt
215	CT37	TC-Tree 3	NiCr/Ni	35	474	220.4	228	
216	RT1	Temp. Control Cabinet	Pt-100					RT = Resistance Thermometer
217	RT2	Temp. Control Cabinet	Pt-100					
218	RT3	Temp. Control Cabinet	Pt-100					
219	AT1	Temp. cool. water outflow	NiCr/Ni	inside bow of overflow rod			230	redundancy
220	AT2	Temp. cool. water outflow	NiCr/Ni	inside bow of overflow rod			229	
221	ZT1	Temp. cooling water inflow	NiCr/Ni	behind flowmeter			231	
222	KT1	Temp. condensate outflow	NiCr/Ni	behind condenser			232	
223	W1	Weight of test vessel	W. cells	-			233	
224	DF1	Flow rate cooling water	Krohne	inside cooling water inlet			234	flowmeter 0-2 l/s
225	DF2	Flow rate cooling water	Kobold	inside cooling water inlet			235	flowmeter 0-12 ml/s

Annex A.2 Drawings of the instrumentation of the LIVE test vessel

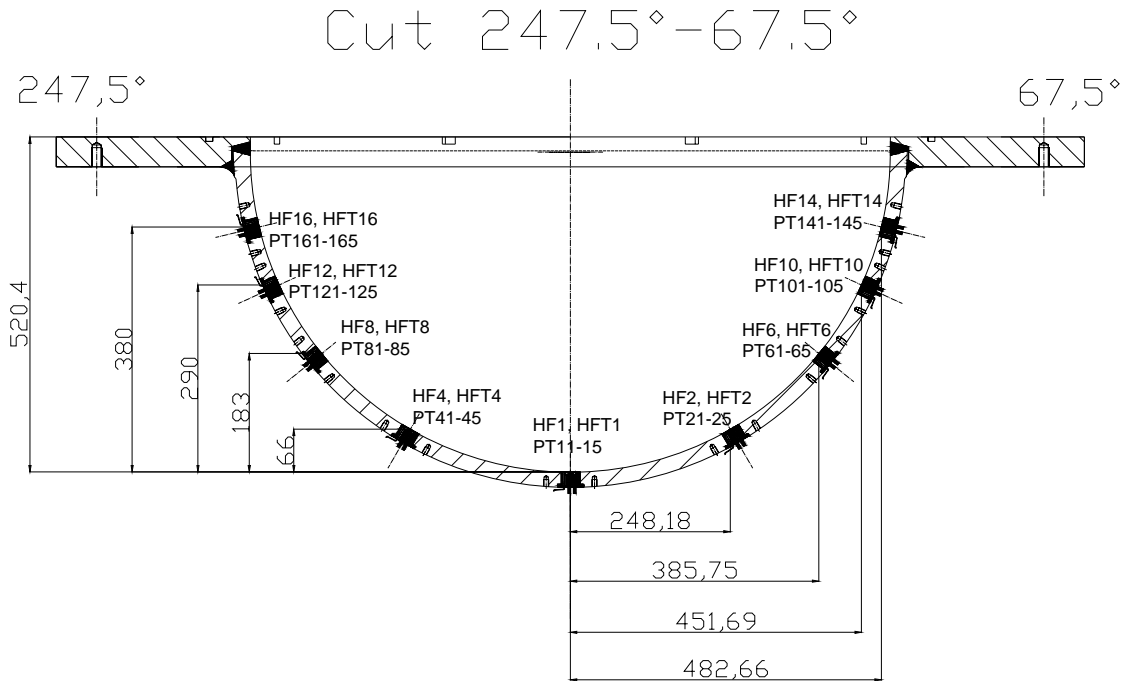


Figure A- 1: Positions of the instrumented plugs along the meridians at 67.5° and 247.5° . In LIVE-L1 only the meridian at 67.5° was instrumented.

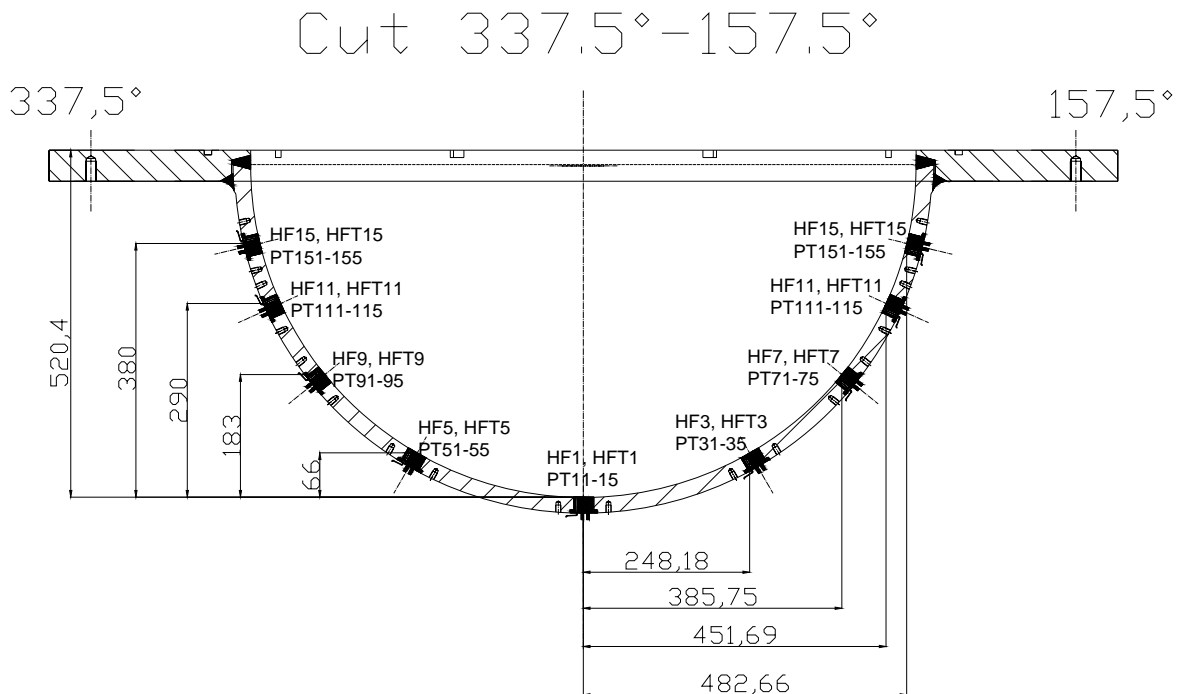


Figure A- 2: Positions of the instrumented plugs along the meridians at 157.5° and 337.5° . In LIVE-L1 only the meridian at 67.5° was instrumented.

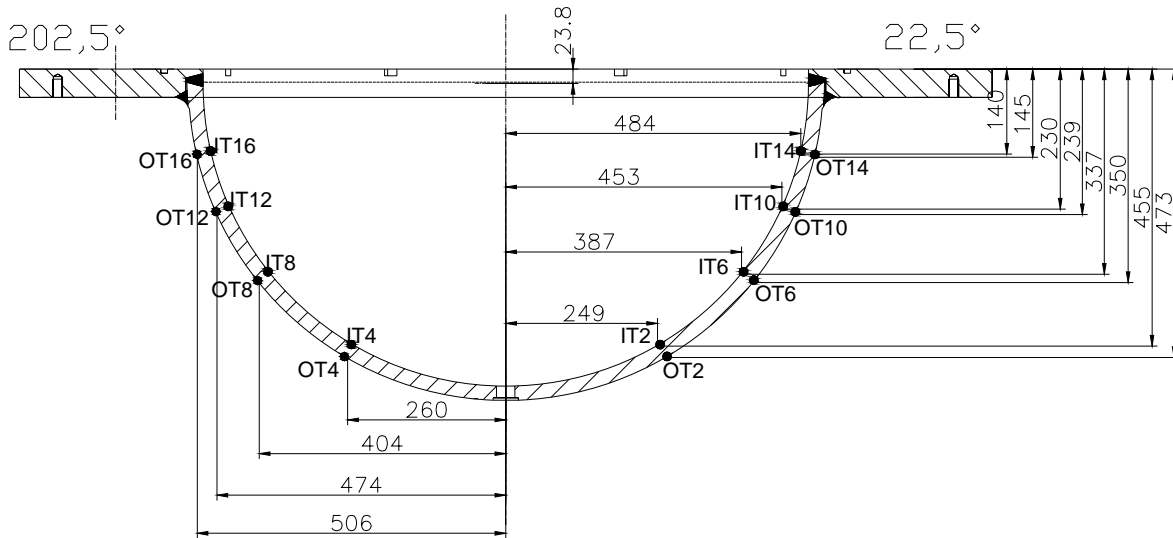
Cut $202,5^\circ - 22,5^\circ$ 

Figure A- 3: Positions of the IT and OT thermocouples along the meridians at $22,5^\circ$ and $202,5^\circ$. In LIVE-L1 only the meridian at $112,5^\circ$ was instrumented with IT thermocouples.

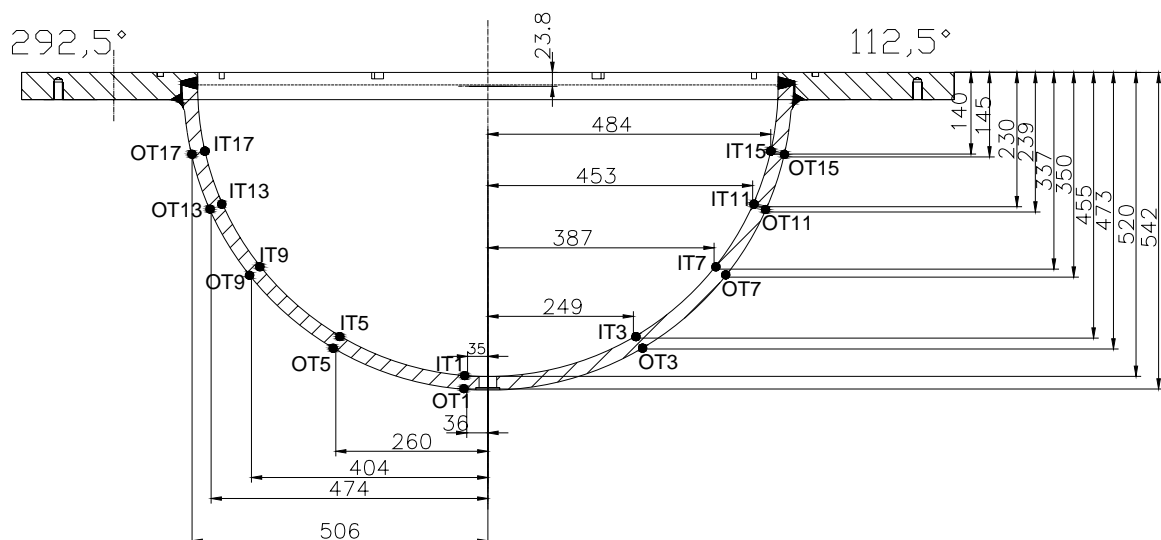
Cut $292,5^\circ - 112,5^\circ$ 

Figure A- 4: Positions of the IT and OT thermocouples along the meridians at $112,5^\circ$ and $292,5^\circ$. In LIVE-L1 only the meridian at $112,5^\circ$ was instrumented with IT thermocouples.

Cut 0° - 180°

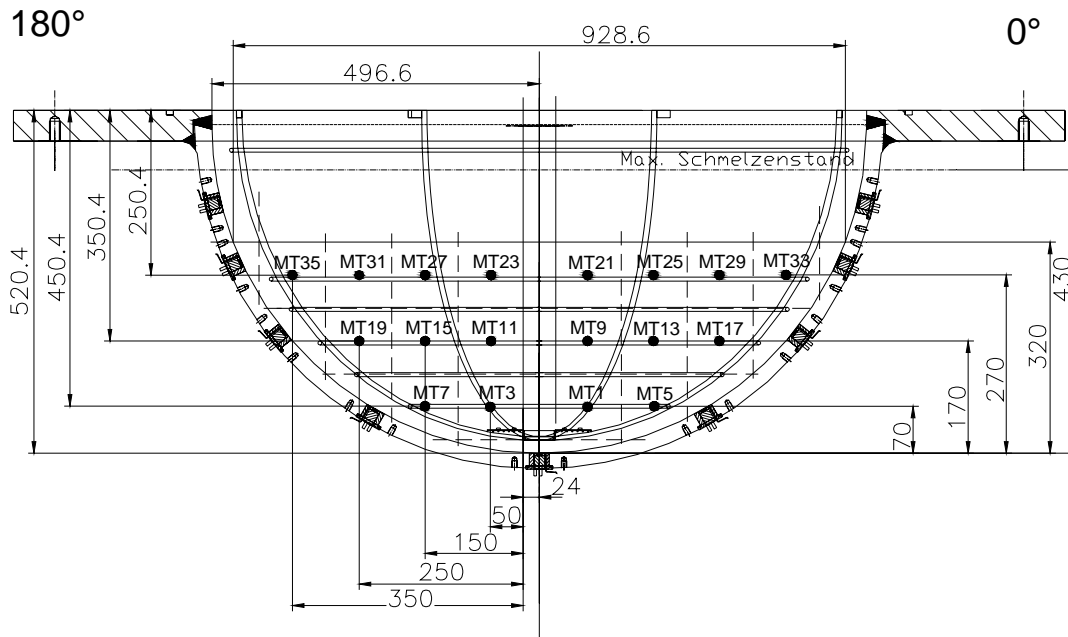


Figure A- 5: Positions of the MT thermocouples in the section 0° - 180°

Cut 90° - 270°

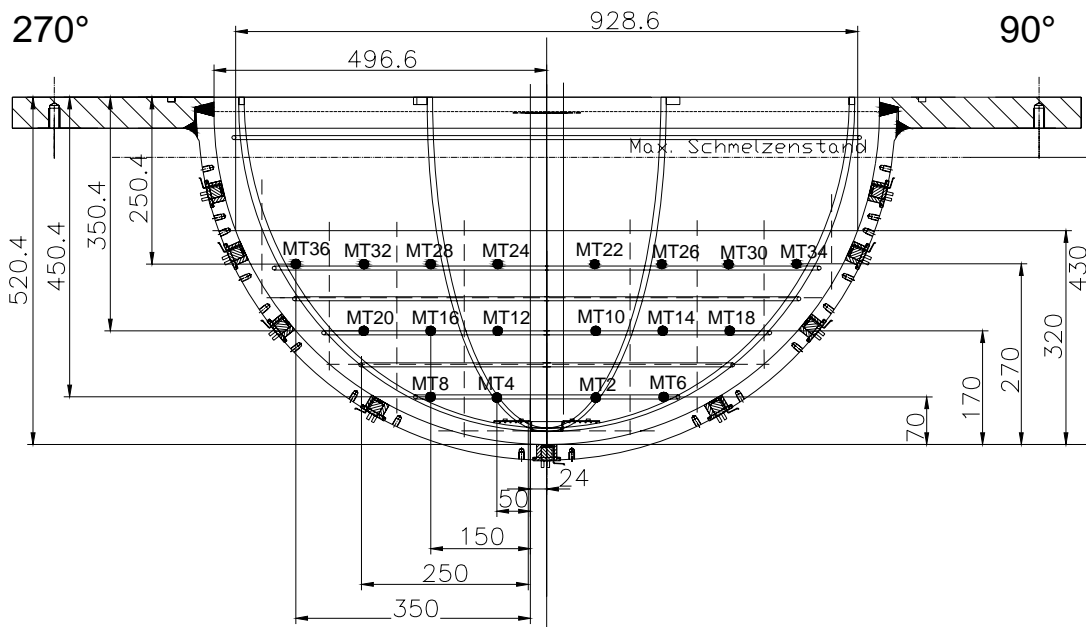


Figure A- 6: Positions of the MT thermocouples in the section 90° - 270°

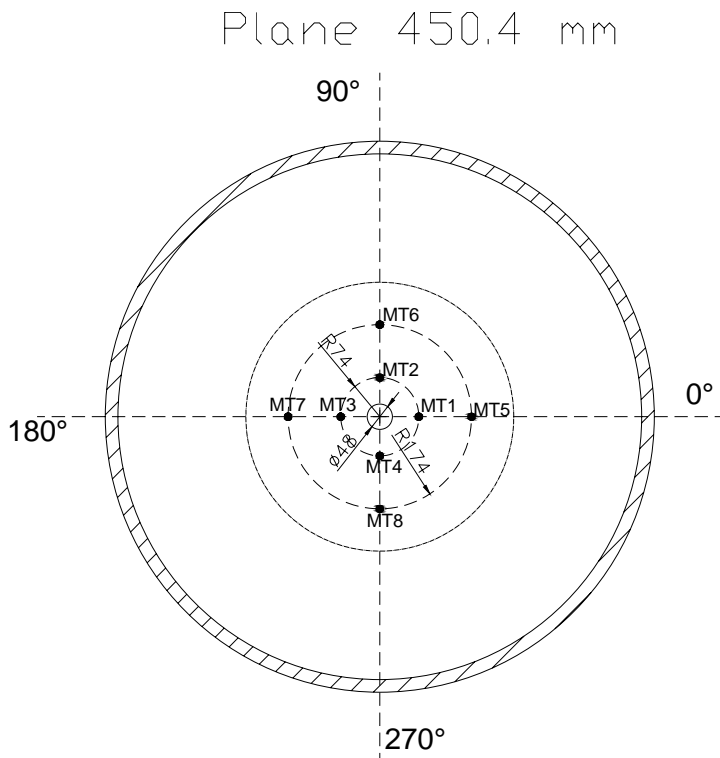


Figure A- 7: Orientation of the MT thermocouples at the plane 450.4 mm. Reference point is the upper edge of the LIVE test vessel.

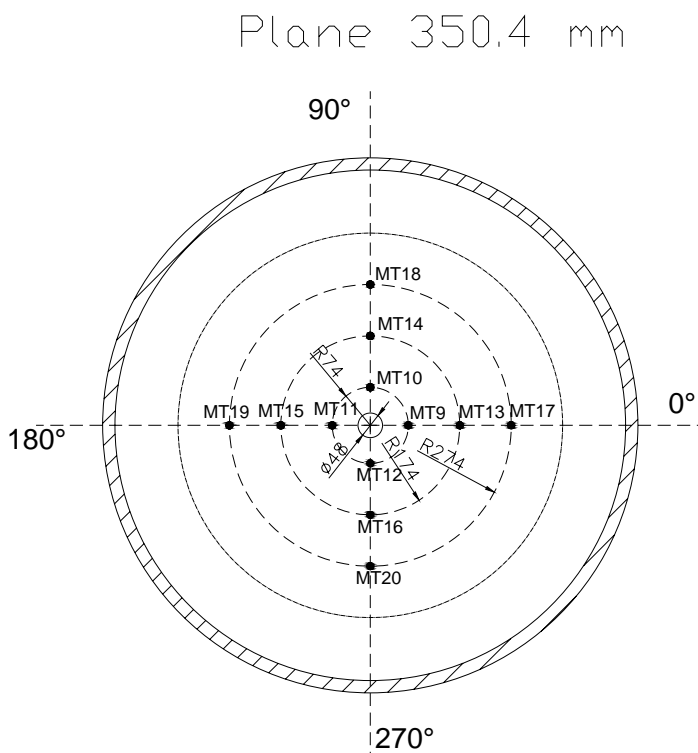


Figure A- 8: Orientation of the MT thermocouples at the plane 350.4 mm. Reference point is the upper edge of the LIVE test vessel.

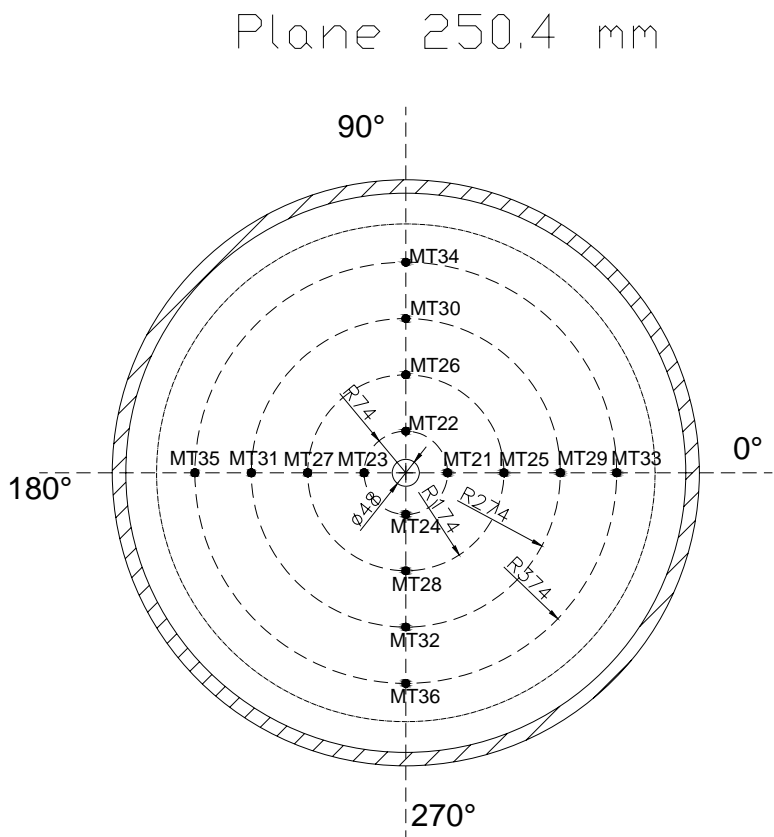


Figure A- 9: Orientation of the MT thermocouples at the plane 250.4 mm. Reference point is the upper edge of the LIVE test vessel.

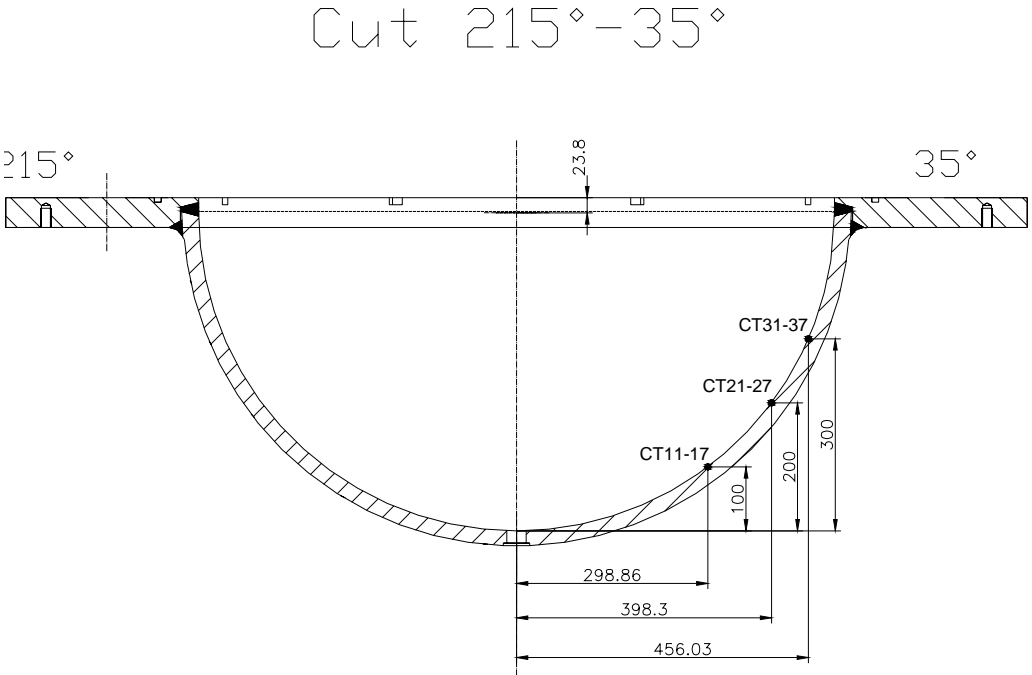


Figure A- 10: Positions of the thermocouple trees along the meridian at 35°.

Cut South - North

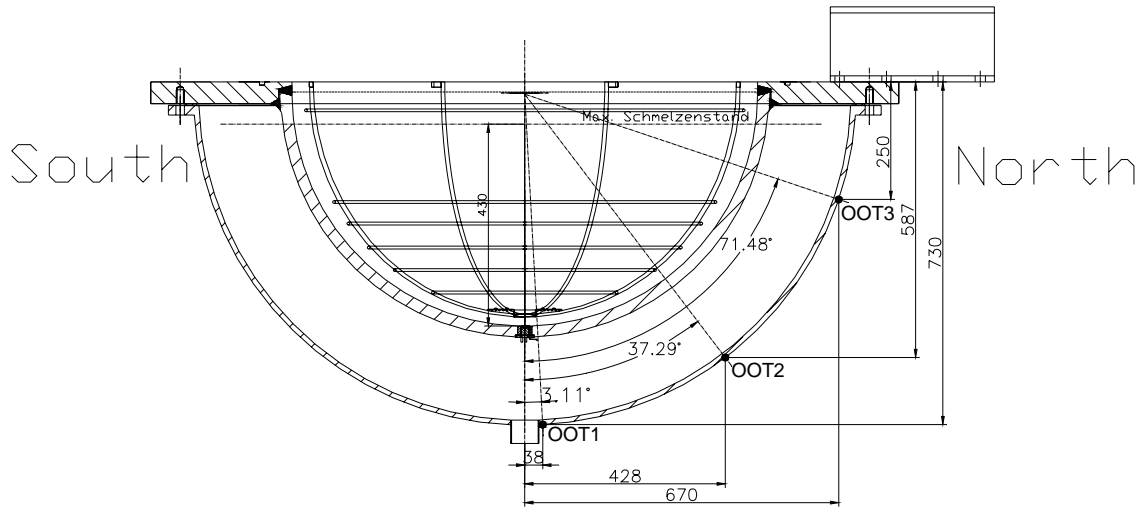


Figure A- 11: Positions of the thermocouples at the outer surface of the cooling tank.

Annex B Test initial conditions and main parameters

	LIVE-L1 21/22.06.2006		LIVE-L3 7/8.05.2007	
Melt characteristics and preparation				
Type	NaNO ₃	KNO ₃	NaNO ₃	KNO ₃
Mole %	20 %	80 %	20 %	80 %
Mass %	17,37 %	82,63 %	17,37 %	82,63 %
Mass	58 kg	278 kg	58 kg	278 kg
Total mass	336 kg		336 kg	
Loading of the furnace	~390 l powder (for T=20 °C) ~180 l melt (for T=350°C)			
Pouring Mass	120 l (corresponds to ~31 cm melt height)		120 l (corresponds to ~31 cm melt height)	
Initial temperature	350 °C		350 °C	
Flow rate of nitrogen covering	20 l/min		20 l/min	
Melt pour				
Position	central		lateral	
Number of pours	1		1	
Furnace tilting velocity	0.5 °/s		0.5 °/s	
Furnace target angle	80°		80°	
Hold time	50 s		50 s	
Trace heating pouring spout	350 °C		350 °C	
Phase 1: Homogeneous heat generation				
Start time	131 s		111 s	
Boundary conditions	Air		Air	
Heating planes	All		All	
Heating power	18 kW at the beginning, step-wise reduction to 10 kW		18 kW at the beginning, step-wise reduction to 10 kW	
Maximum melt temperature	350 °C		370 °C	
Phase 2: Start of outer vessel wall cooling				
Start time	7214 s		7199 s	
Boundary conditions	Water, continuous cooling		Water, continuous cooling	

Cooling water flow rate	~42 g/s	~47 g/s
Heating planes	All	All
Heating power	10 kW	10 kW
Heat generation	Homogeneous	Homogeneous
Phase 3: Reduction of heat generation		
Start time	82682 s	83100 s
Boundary conditions	Water, continuous cooling	Water, continuous cooling
Cooling water flow rate	~47 g/s	~47 g/s
Heating planes	All	All
Heating power	7 kW	7 kW
Heat generation	Homogeneous	Homogeneous
Phase 4: Test termination and melt extraction		
End time	102627 s	102900 s
Test conditions	Reaching of steady-state conditions in Phase 3	Reaching of steady-state conditions in Phase 3
Heating power	0 kW	0kW

Annex C Test data

This appendix provides plots of the experimental results, which are not shown in the main part of the report.

Annex C.1 Test data of LIVE-L1

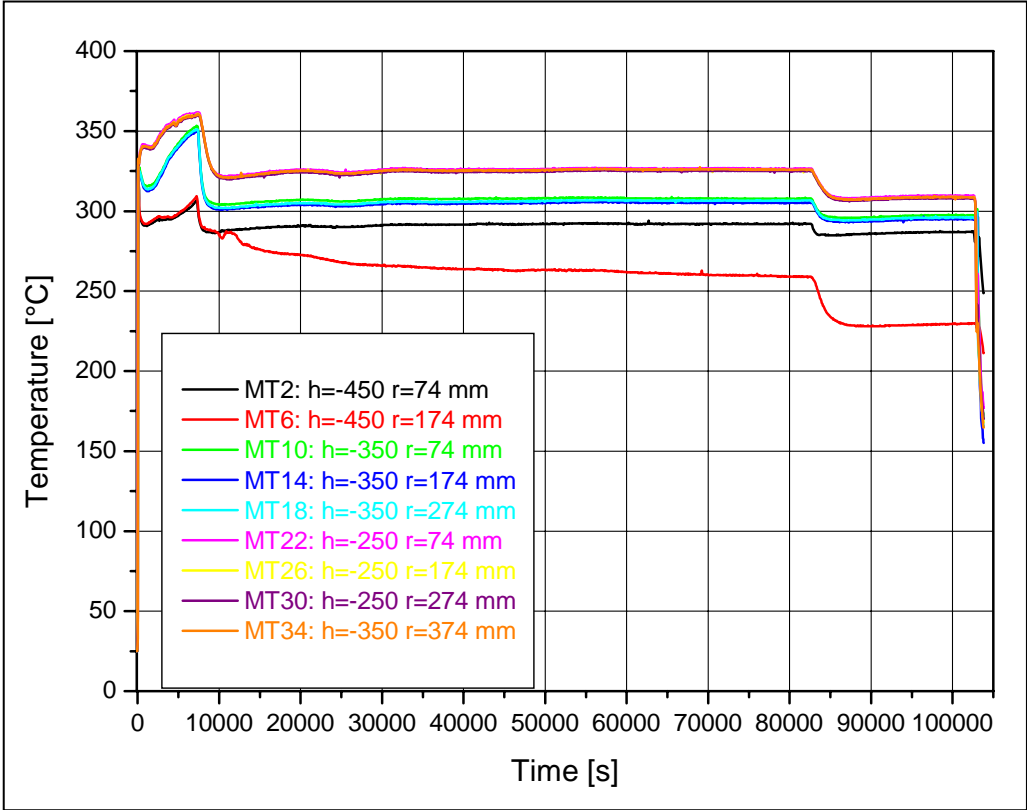


Figure C- 1: Melt pool temperatures at different elevations along the meridian at 90° in LIVE-L1

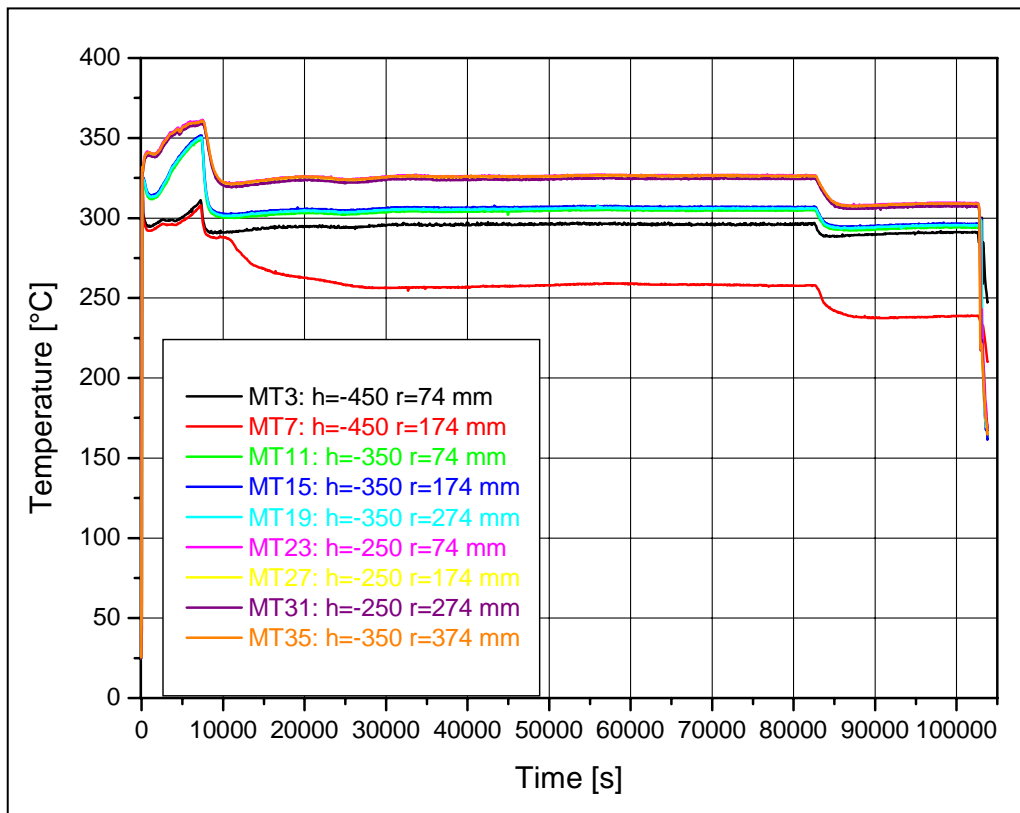


Figure C- 2: Melt pool temperatures at different elevations along the meridian at 180° in LIVE-L1

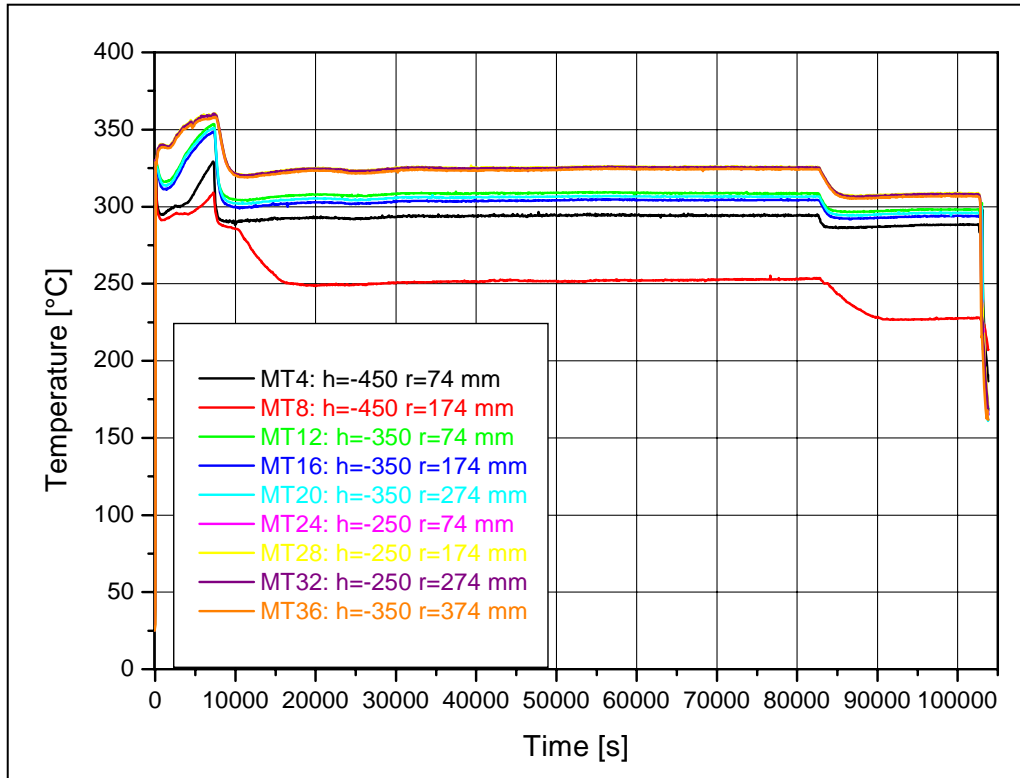


Figure C- 3: Melt pool temperatures at different elevations along the meridian at 180° in LIVE-L1

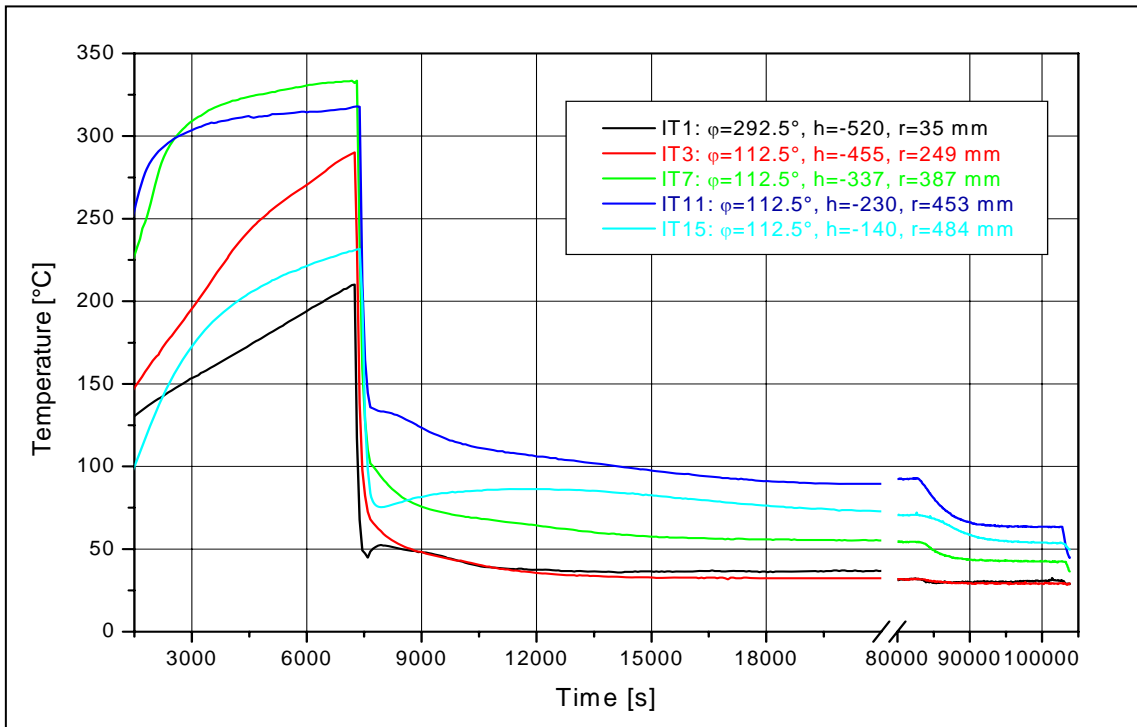


Figure C- 4: Inner temperatures of the test vessel wall at different elevations along the meridian at 112.5° in LIVE-L1. In LIVE-L1 only the meridian at 112.5° was instrumented with IT thermocouples.

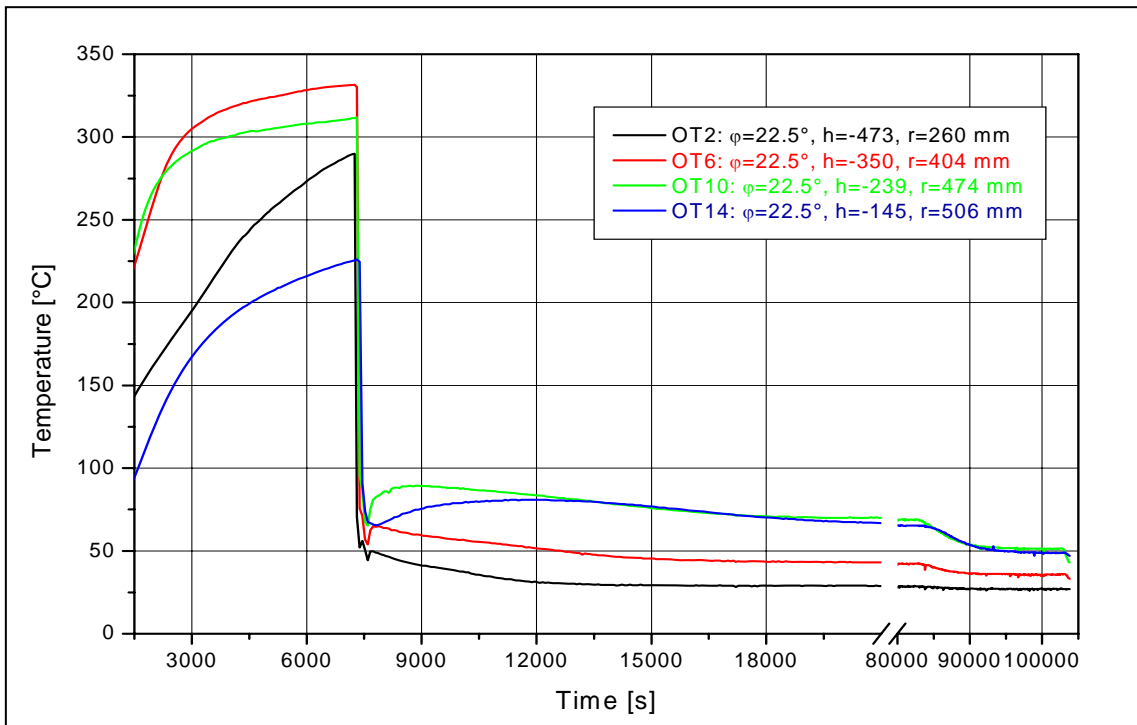


Figure C- 5: Outside wall temperatures of the test vessel at different elevations along the meridian at 22.5° in LIVE-L1

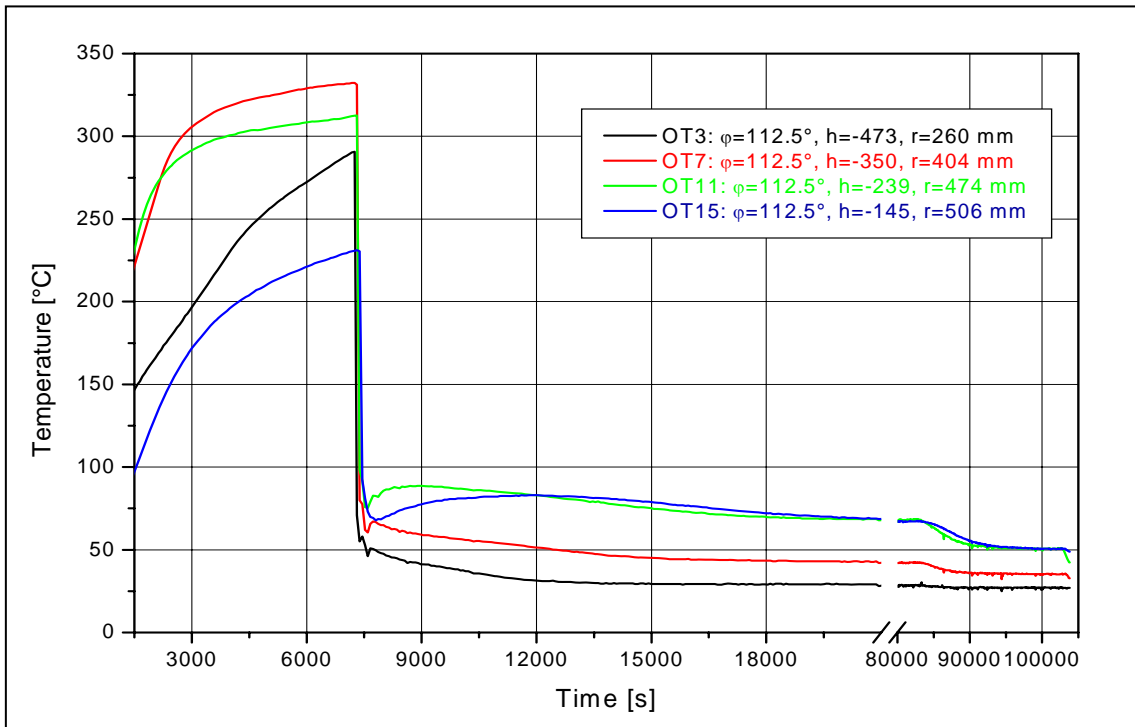


Figure C- 6: Outside temperatures of the test vessel at different elevations along the meridian at 112.5° in LIVE-L1

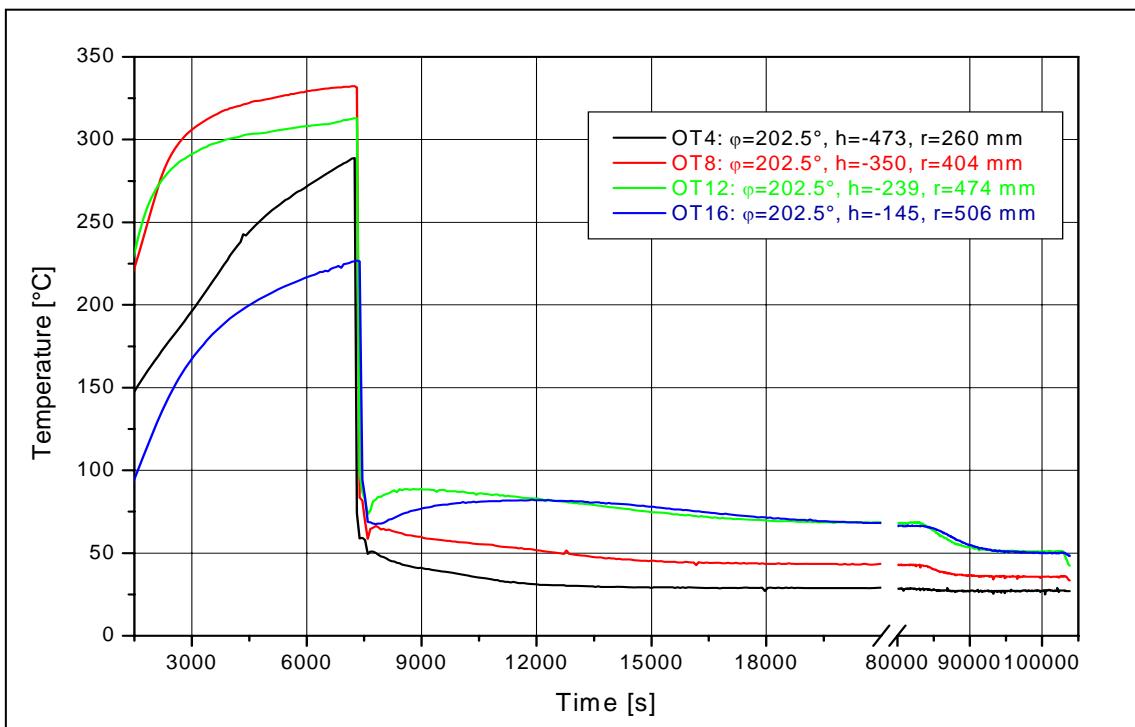


Figure C- 7: Outside temperatures of the test vessel at different elevations along the meridian at 202.5° in LIVE-L1

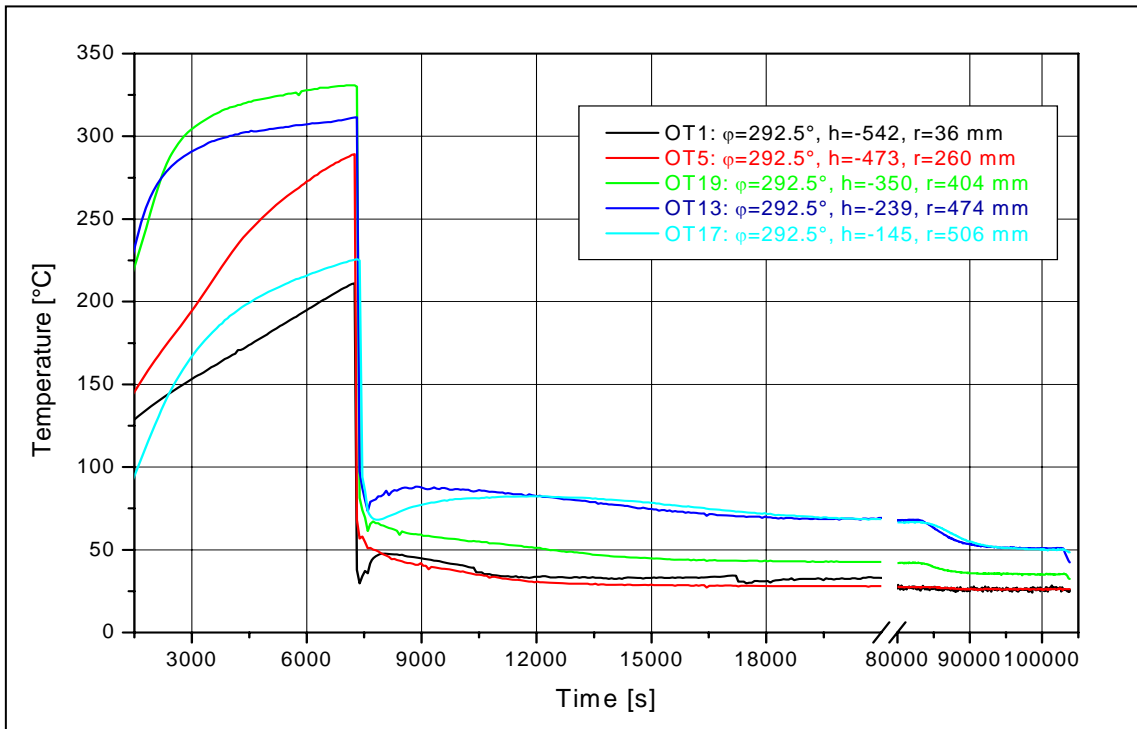


Figure C- 8: Outside temperatures of the test vessel at different elevations along the meridian at 292.5° in LIVE-L1

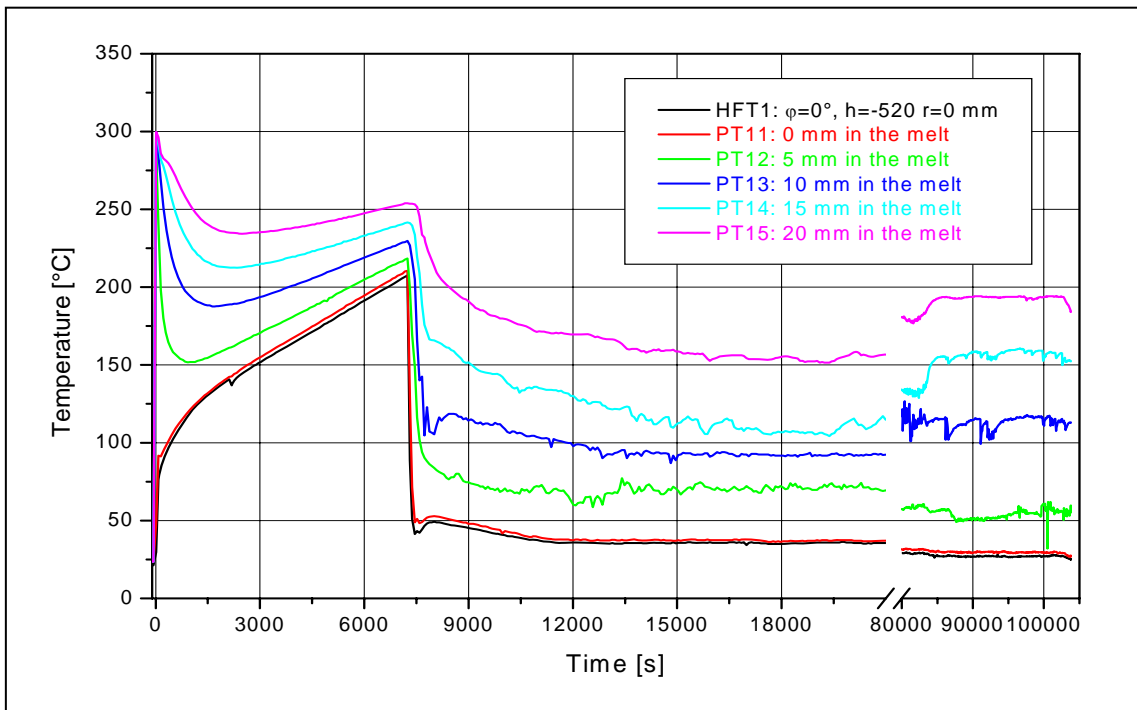


Figure C- 9: Plug and heat flux sensor temperatures in LIVE-L1, φ = 0°, h = -520.4 mm, r = 0 mm

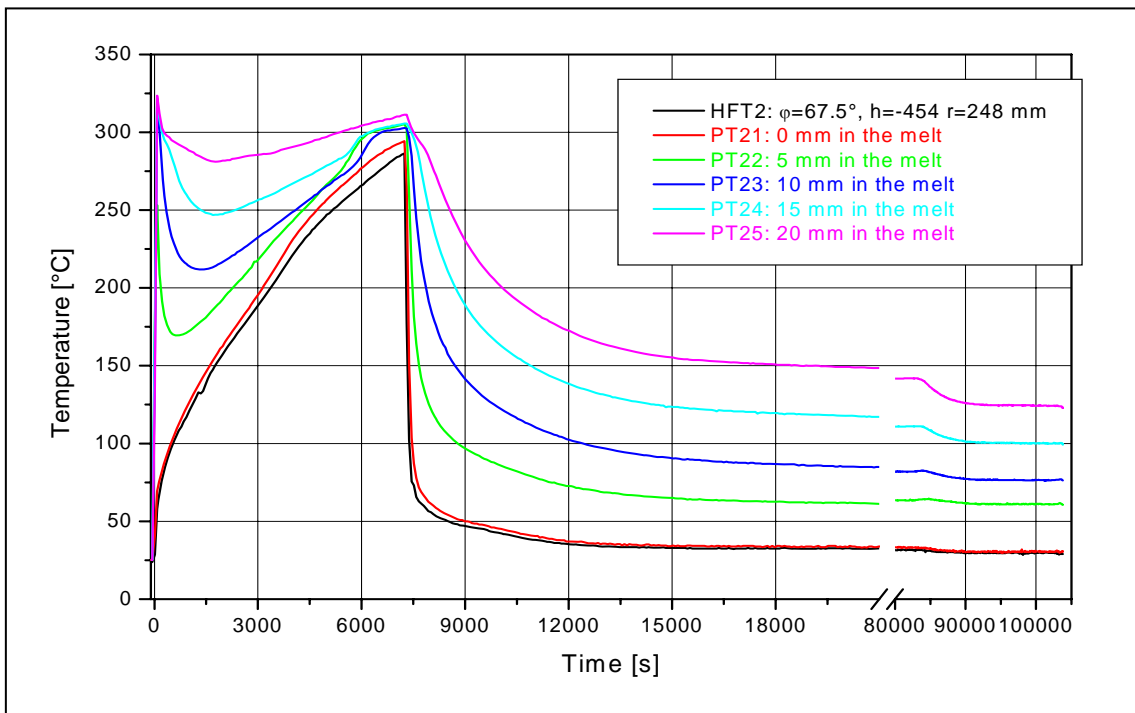


Figure C- 10: Plug and heat flux sensor temperatures in LIVE-L1, $\phi = 67.5^\circ$, $h = -454$ mm,
 $r = 248$ mm

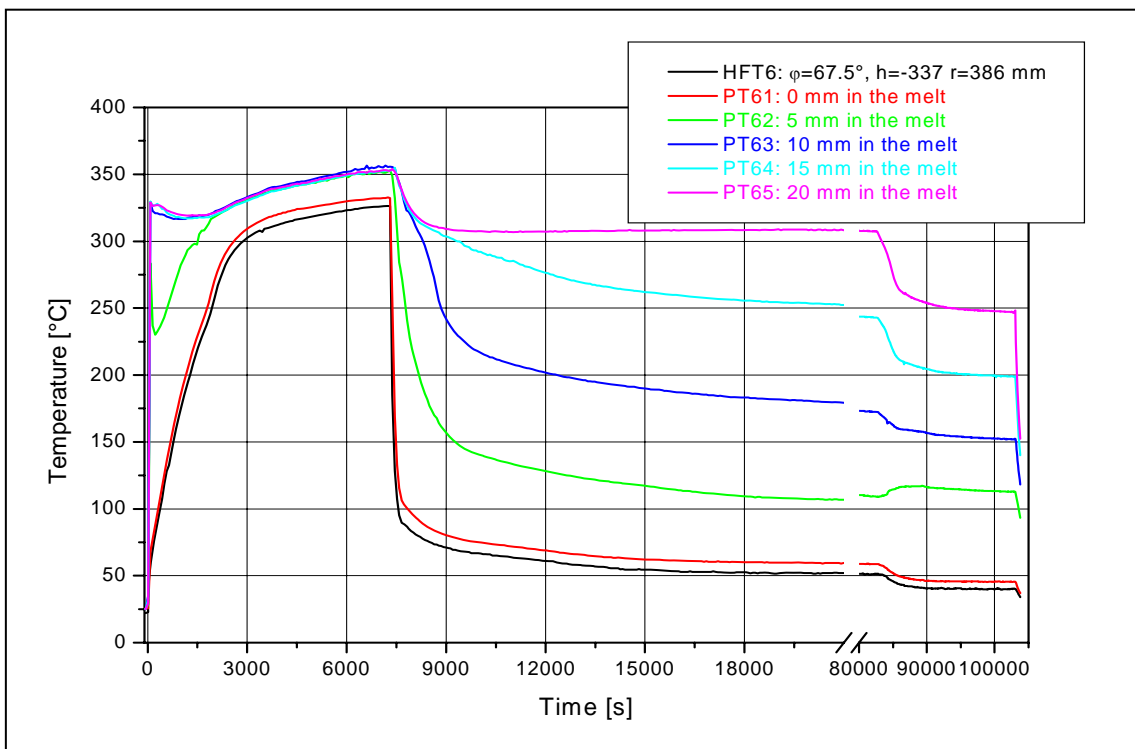


Figure C- 11: Plug and heat flux sensor temperatures in LIVE-L1, $\phi = 67.5^\circ$, $h = -337$ mm,
 $r = 386$ mm

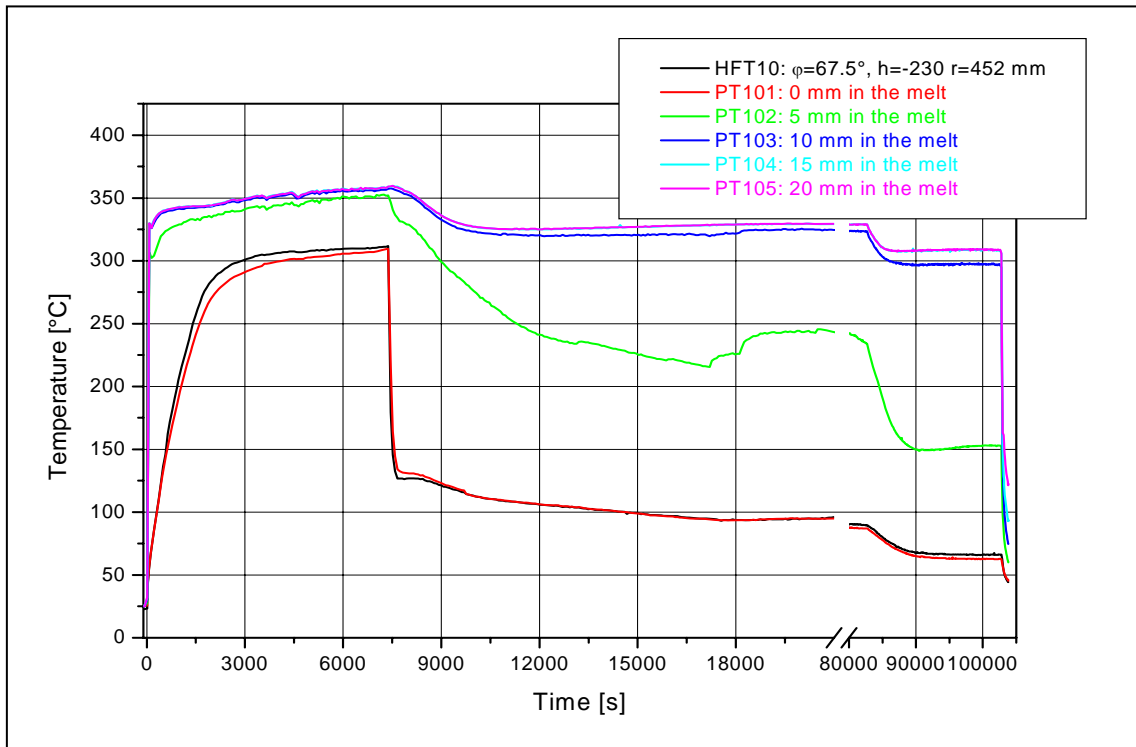


Figure C- 12: Plug and heat flux sensor temperatures in LIVE-L1, $\phi = 67.5^\circ$, $h = -230$ mm, $r = 452$ mm

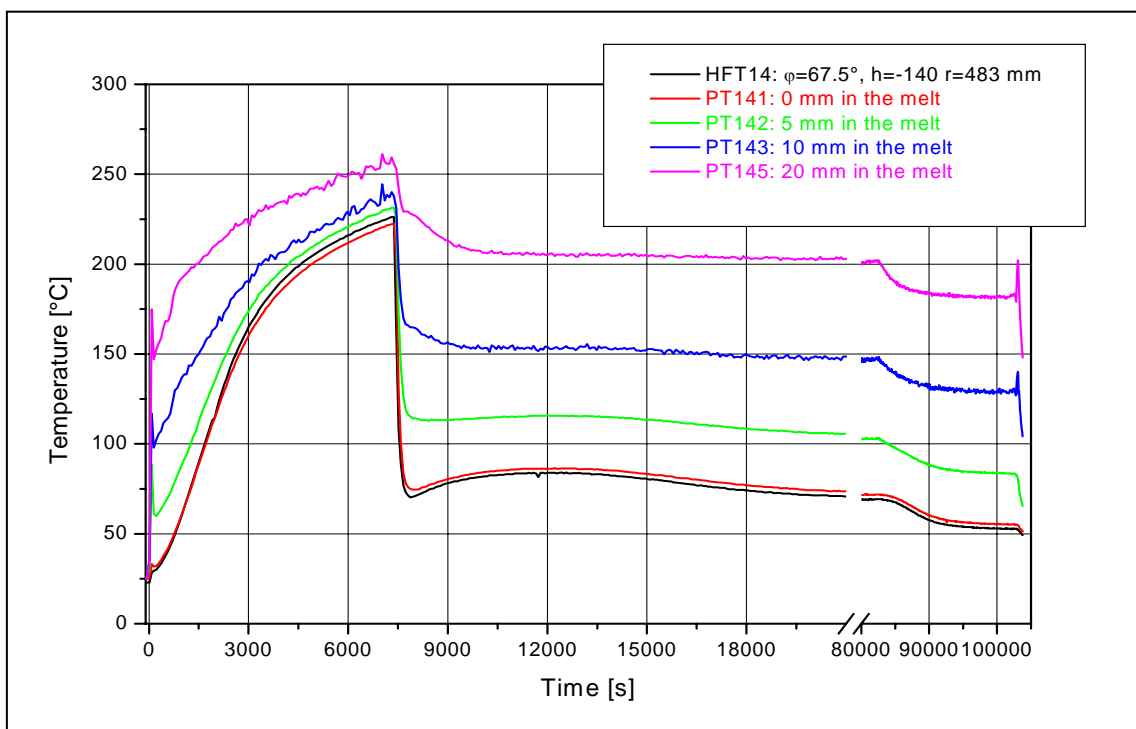


Figure C- 13: Plug and heat flux sensor temperatures in LIVE-L1, $\phi = 67.5^\circ$, $h = -140$ mm, $r = 483$ mm

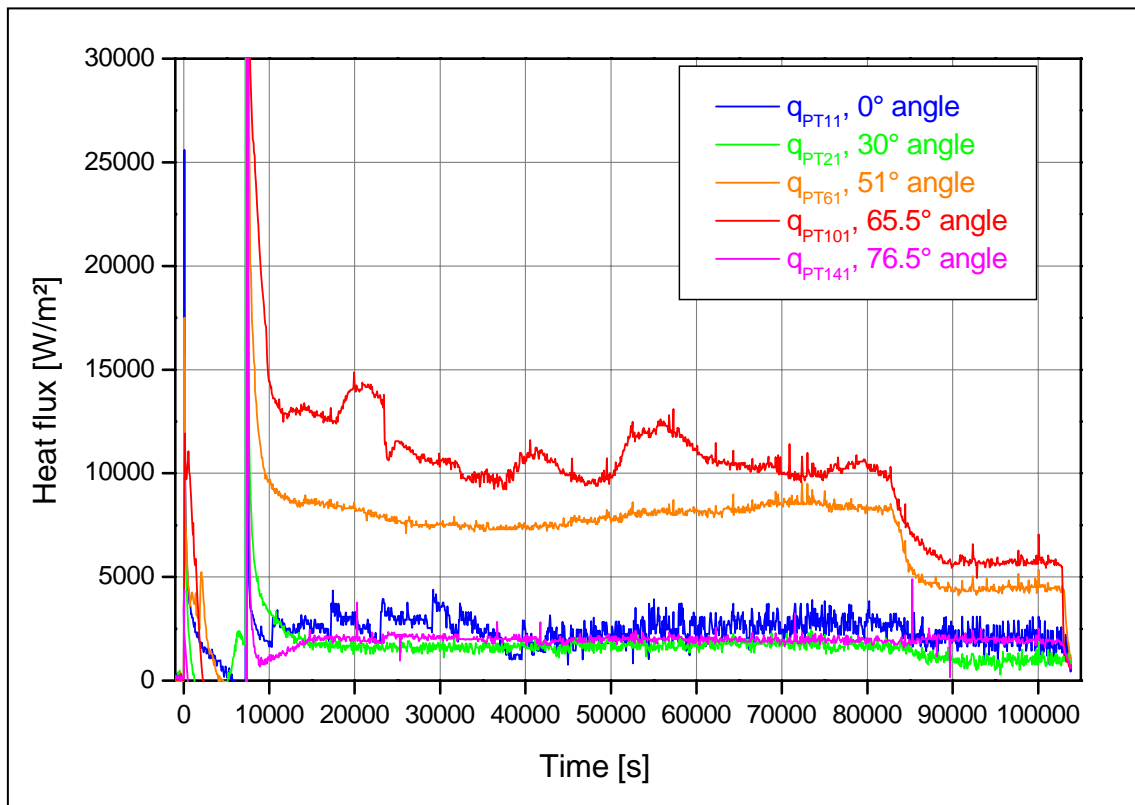
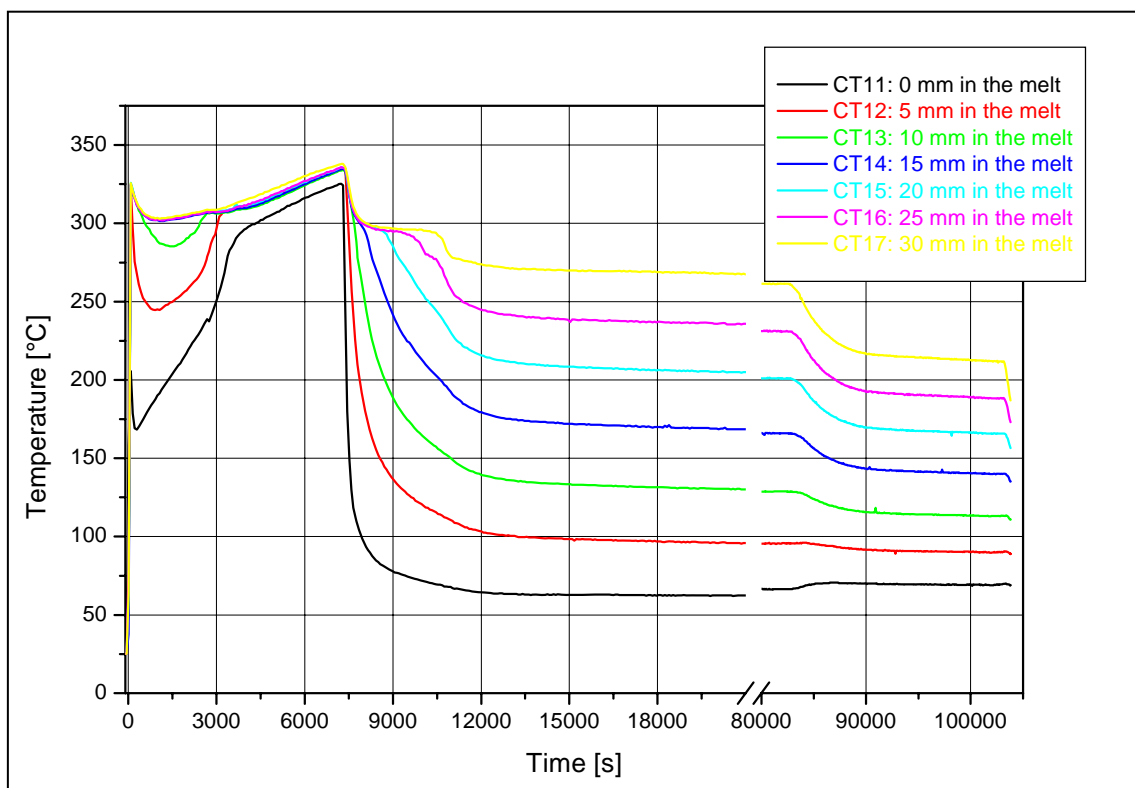


Figure C- 14: Heat flux calculated with PT/OT thermocouples in LIVE-L1

Figure C- 15: Temperature measurements of the thermocouple tree CT1 in LIVE-L1, $\phi = 35^\circ$,
 $h = -420.4$ mm, $r = 299$ mm

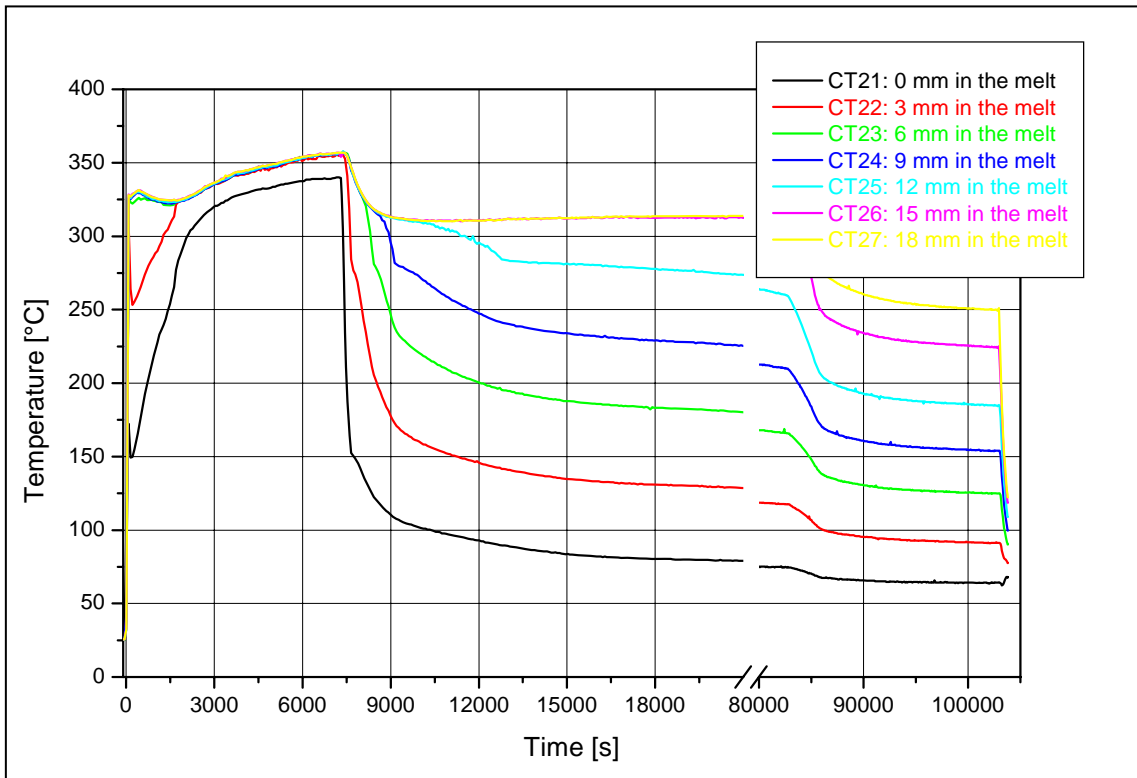


Figure C- 16: Temperature measurements of the thermocouple tree CT2 in LIVE-L1, $\varphi = 35^\circ$, $h = -320.4 \text{ mm}$, $r = 398 \text{ mm}$

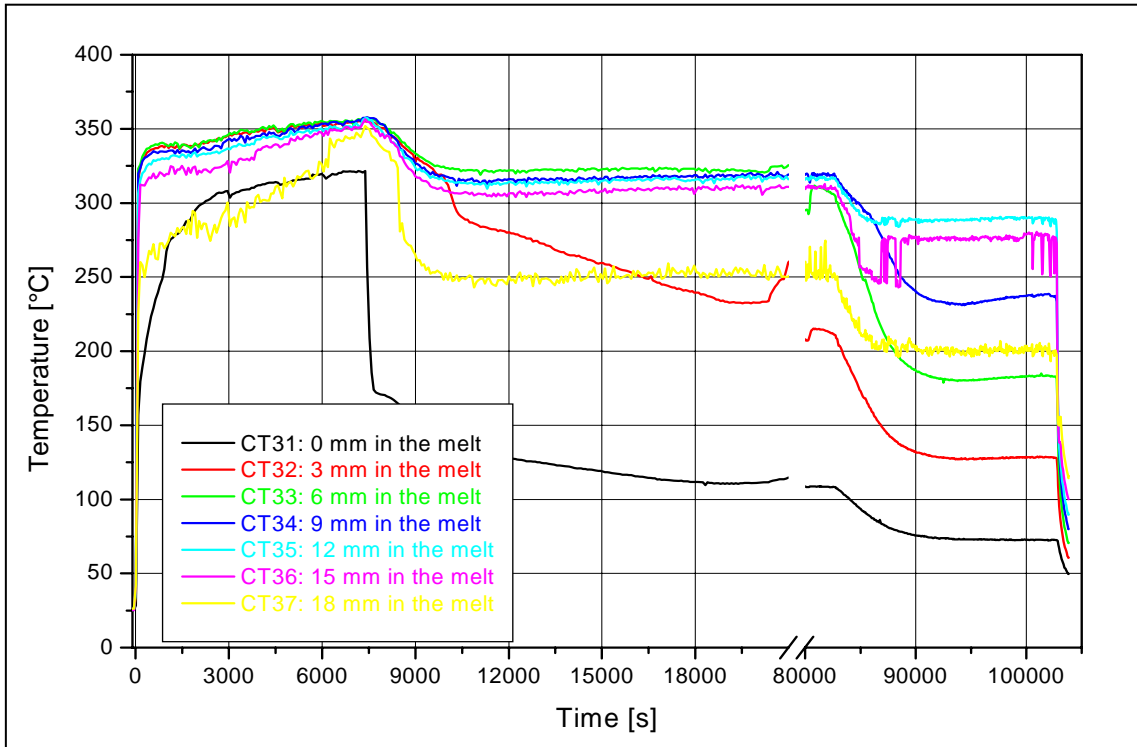


Figure C- 17: Temperature measurements of the thermocouple tree CT3 in LIVE-L1, $\varphi = 35^\circ$, $h = -220.4 \text{ mm}$, $r = 456 \text{ mm}$

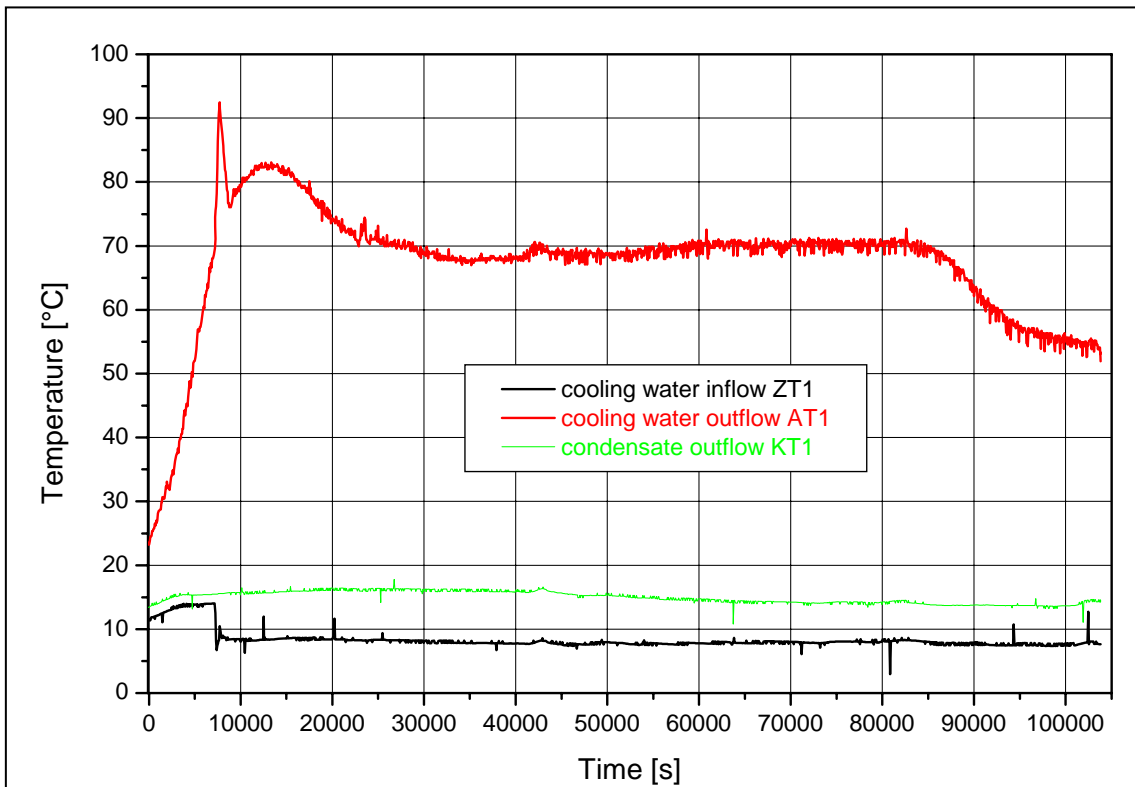


Figure C- 18: Cooling water temperatures in LIVE-L1

Annex C.2 Test data of LIVE-L3

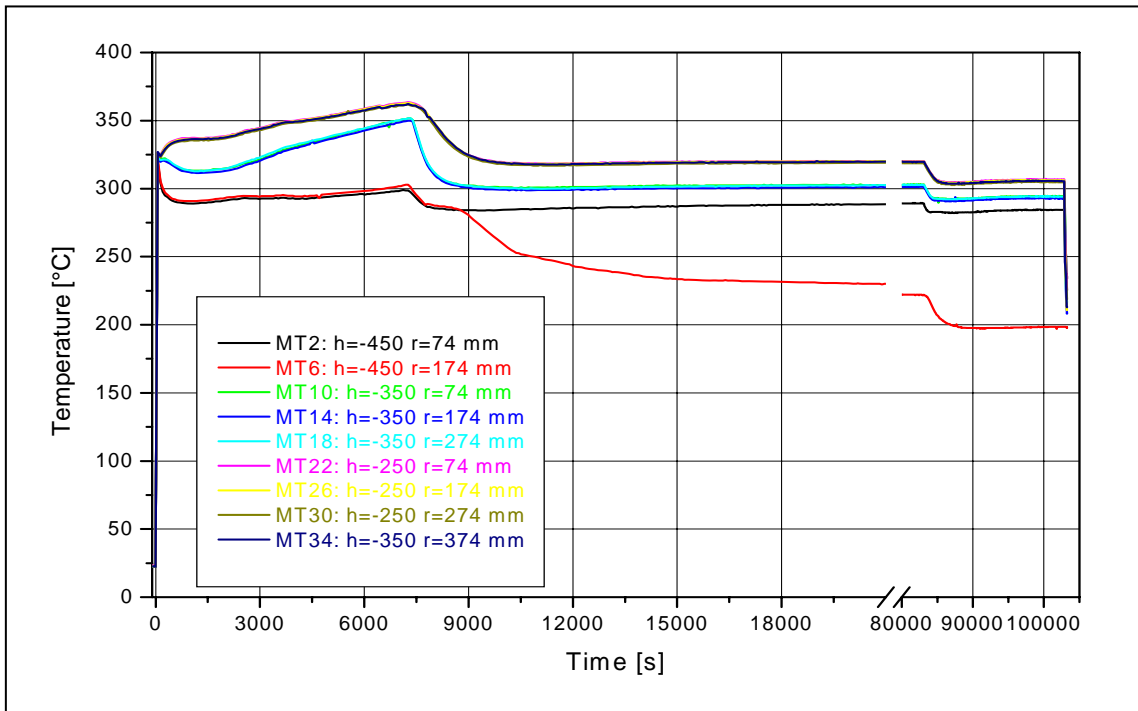


Figure C- 19: Melt pool temperatures at different elevations along the meridian at 90° in LIVE-L3

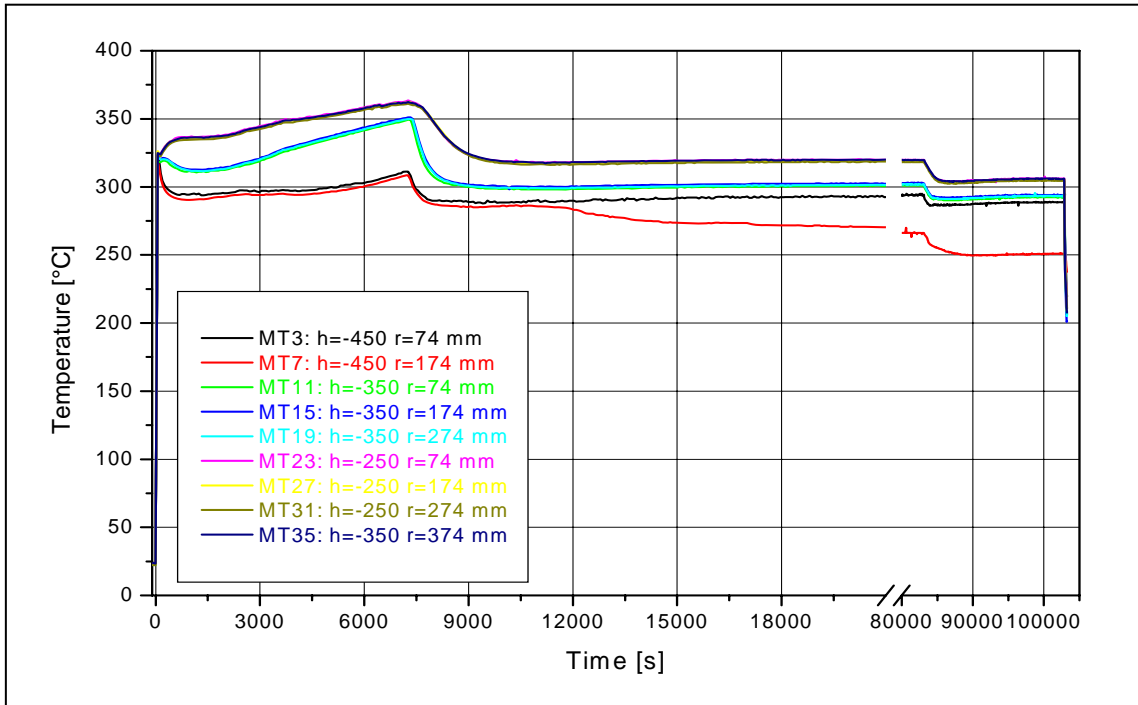


Figure C- 20: Melt pool temperatures at different elevations along the meridian at 180° in LIVE-L3

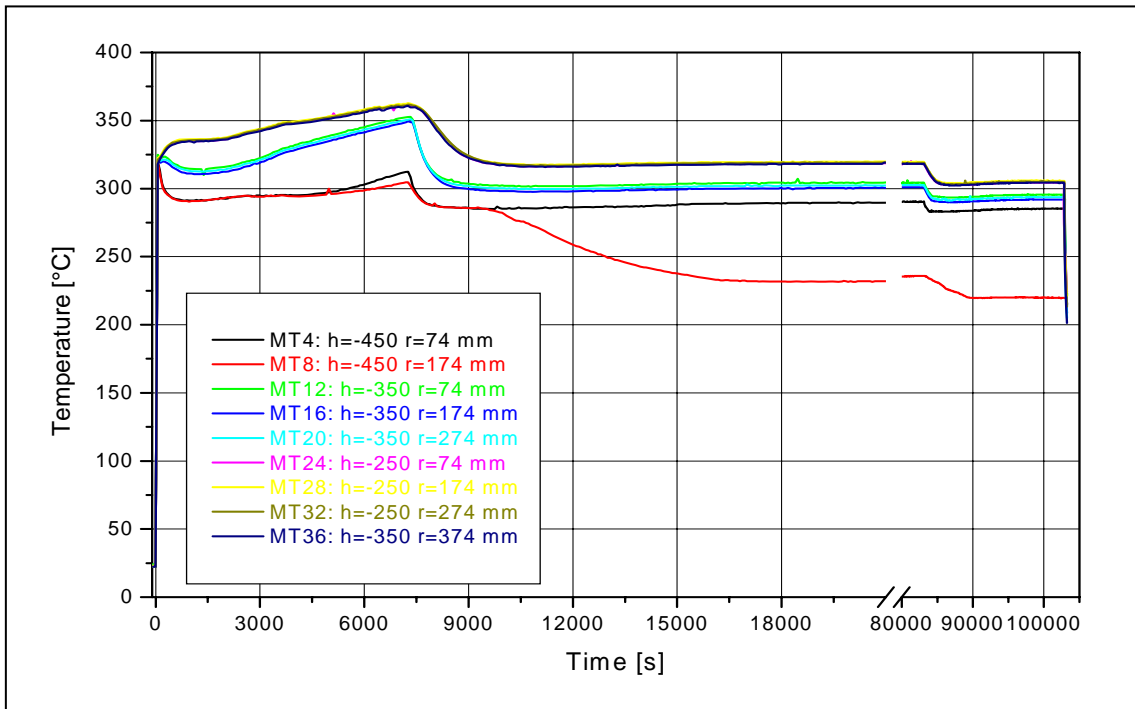


Figure C- 21: Melt pool temperatures at different elevations along the meridian at 270° in LIVE-L3

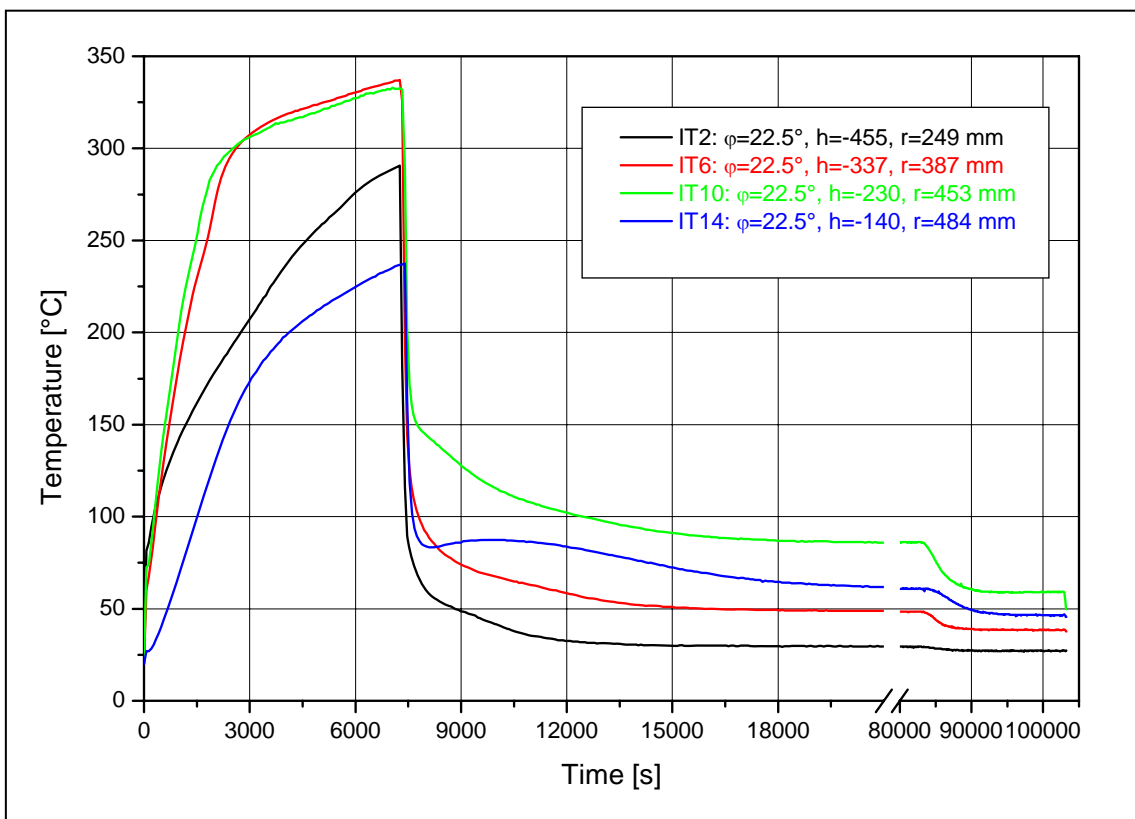


Figure C- 22: Inner wall temperatures of the test vessel at different elevations along the meridian at 22.5° in LIVE-L3

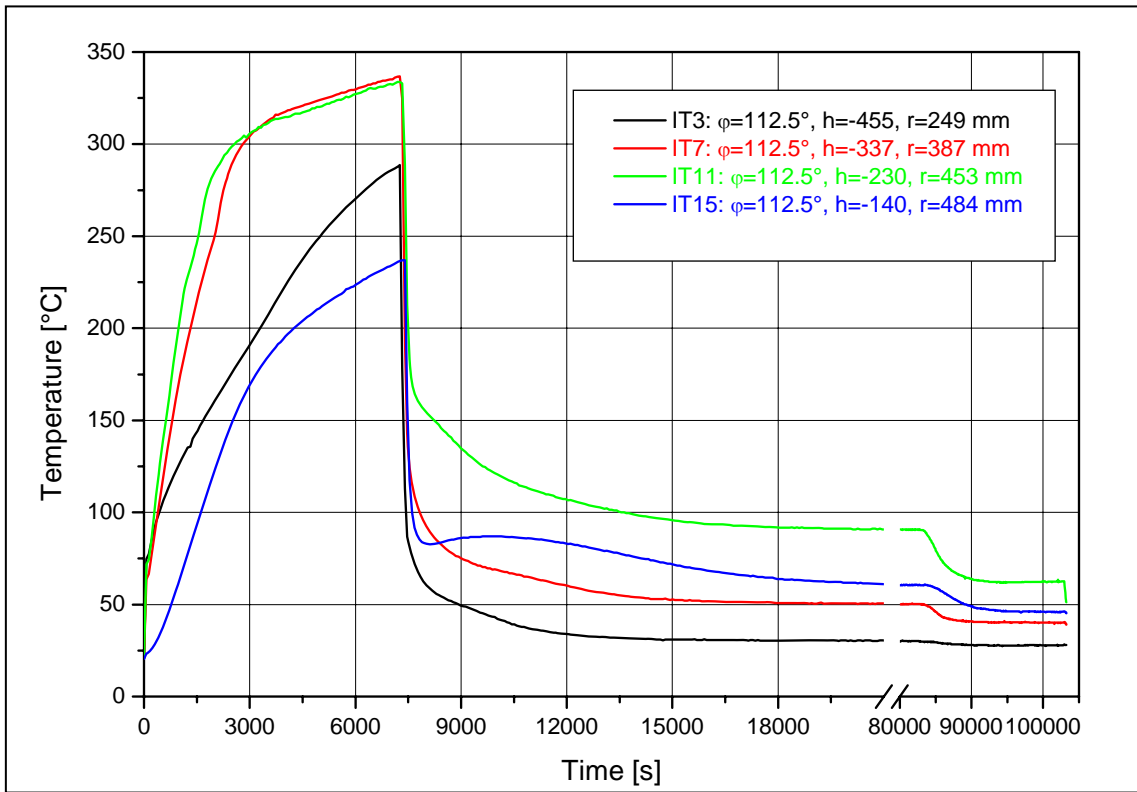


Figure C- 23: Inner wall temperatures of the test vessel at different elevations along the meridian at 112.5° in LIVE-L3

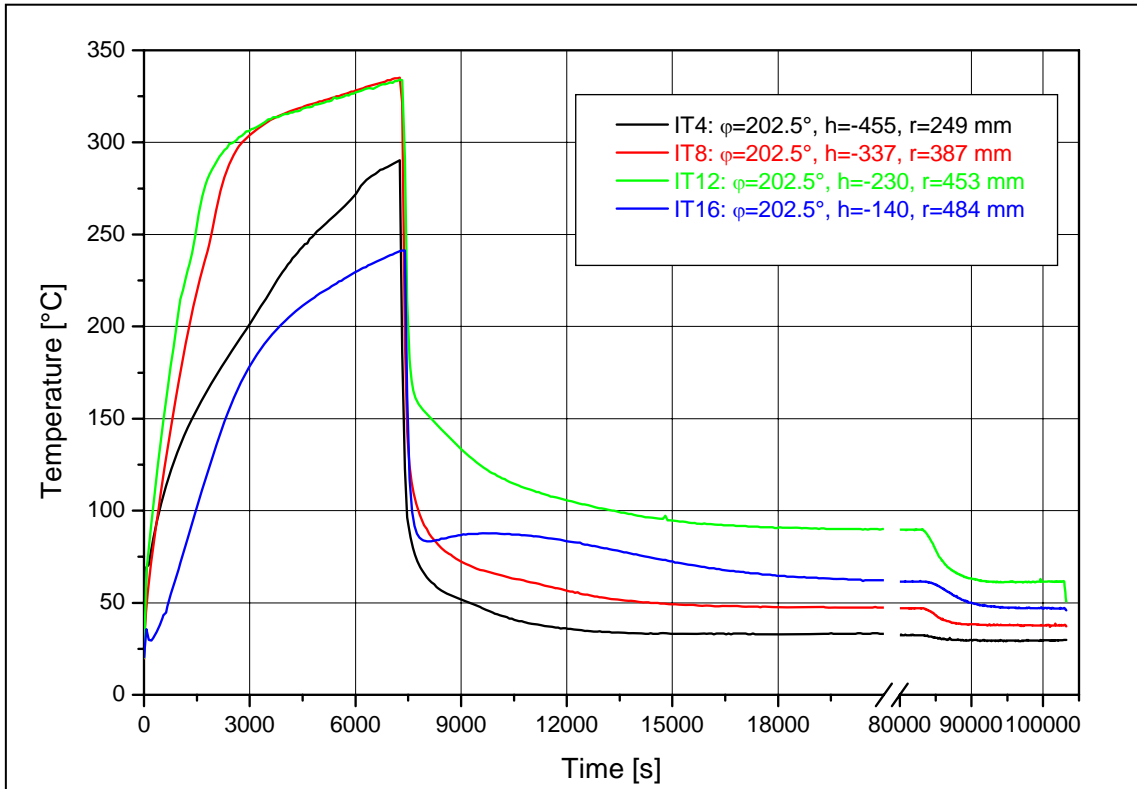


Figure C- 24: Inner wall temperatures of the test vessel at different elevations along the meridian at 202.5° in LIVE-L3

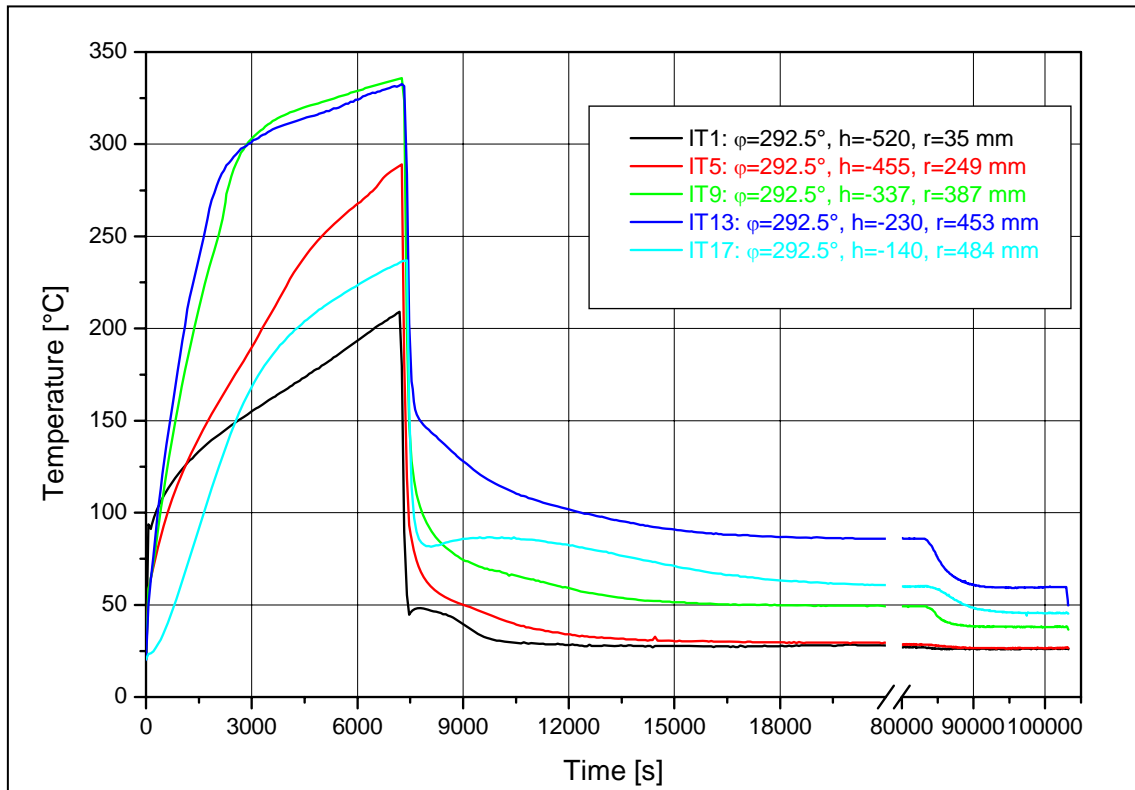


Figure C- 25: Inner wall temperatures of the test vessel at different elevations along the meridian at 292.5° in LIVE-L3

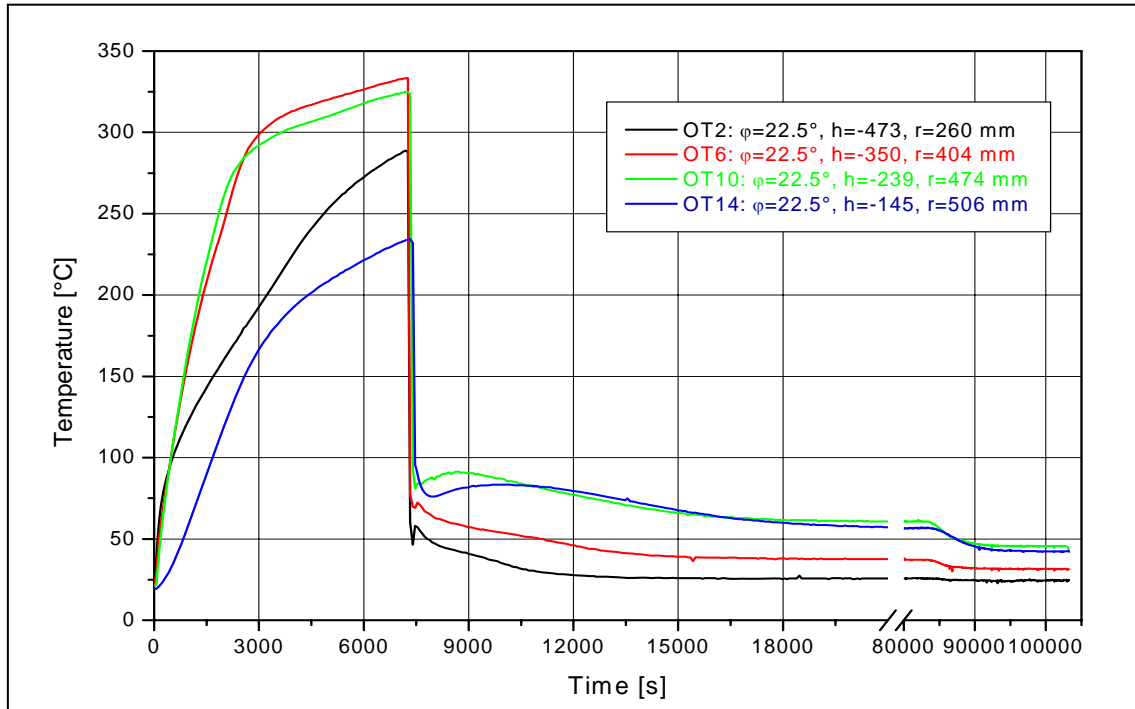


Figure C- 26: Outside wall temperatures of the test vessel at different elevations along the meridian at 22.5° in LIVE-L3

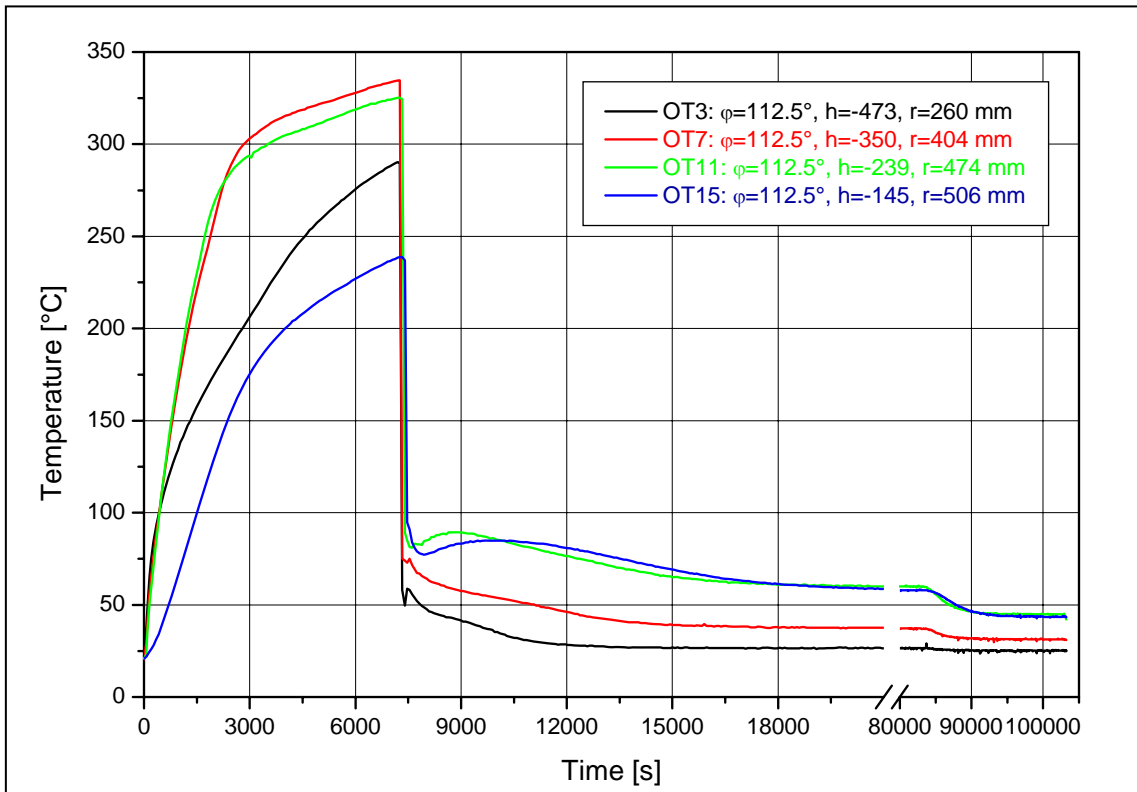


Figure C- 27: Outside wall temperatures of the test vessel at different elevations along the meridian at 112.5° in LIVE-L3

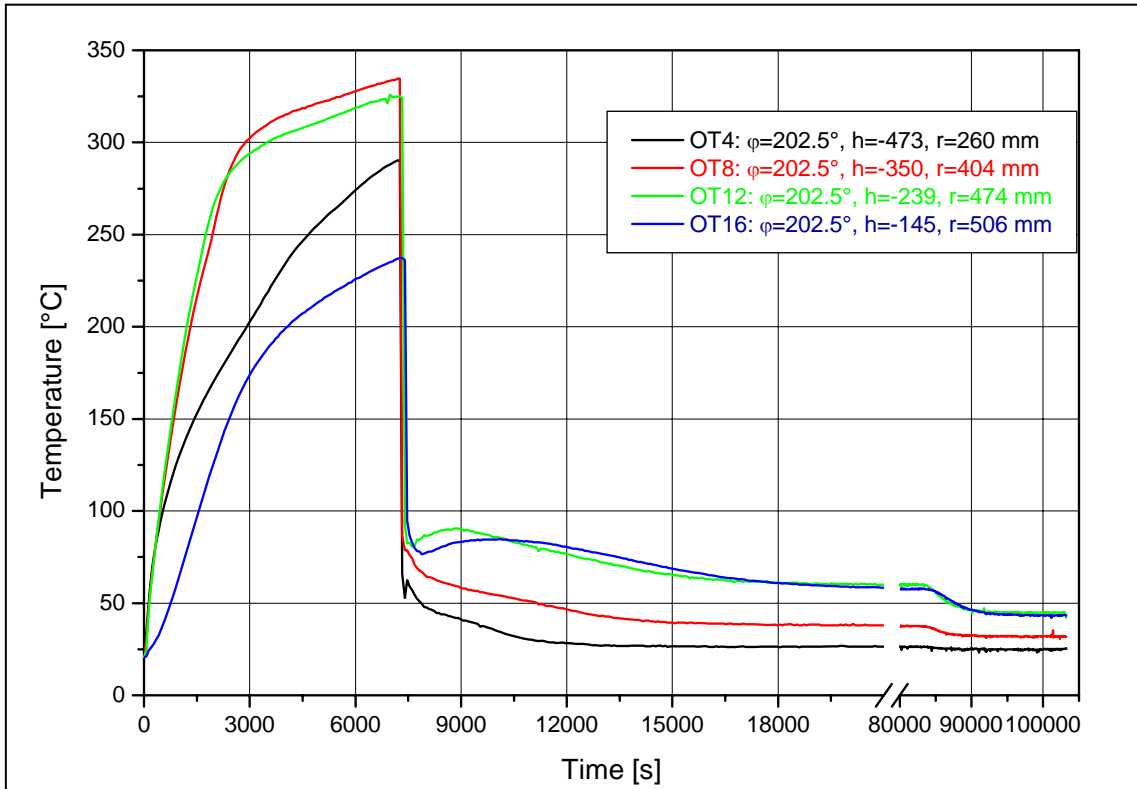


Figure C- 28: Outside wall temperatures of the test vessel at different elevations along the meridian at 202.5° in LIVE-L3

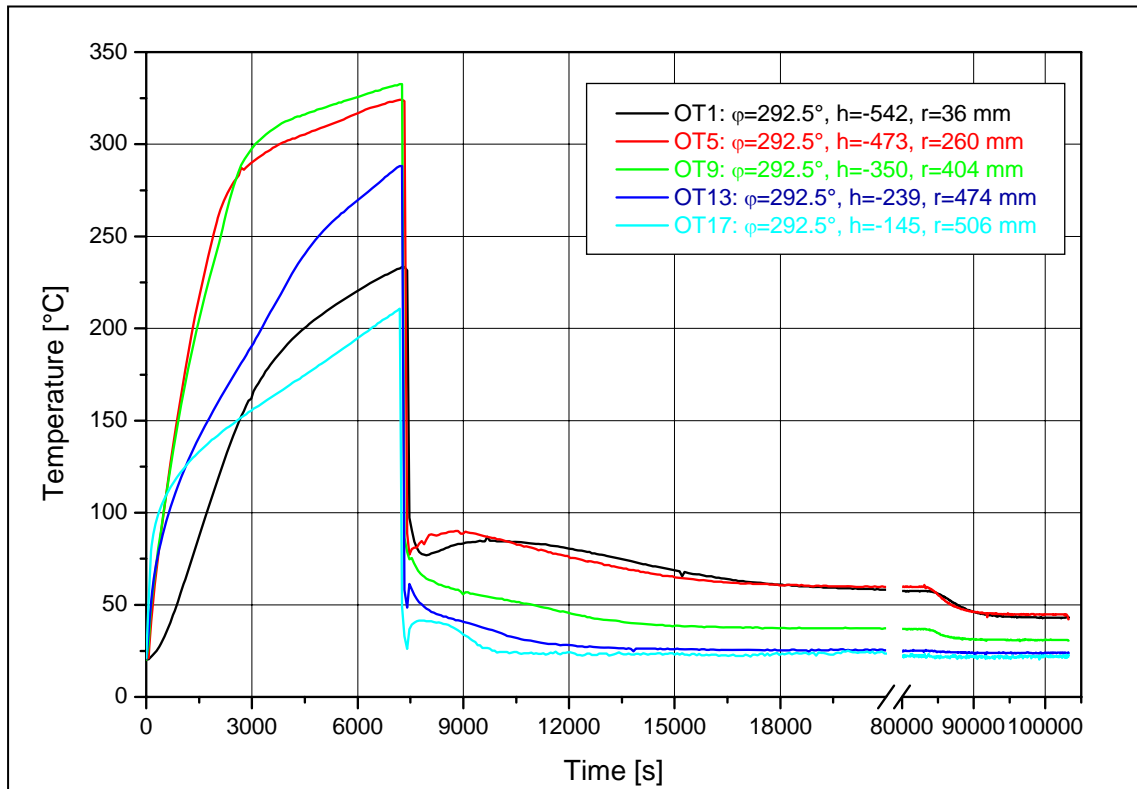


Figure C- 29: Outside wall temperatures of the test vessel at different elevations along the meridian at 292.5° in LIVE-L3

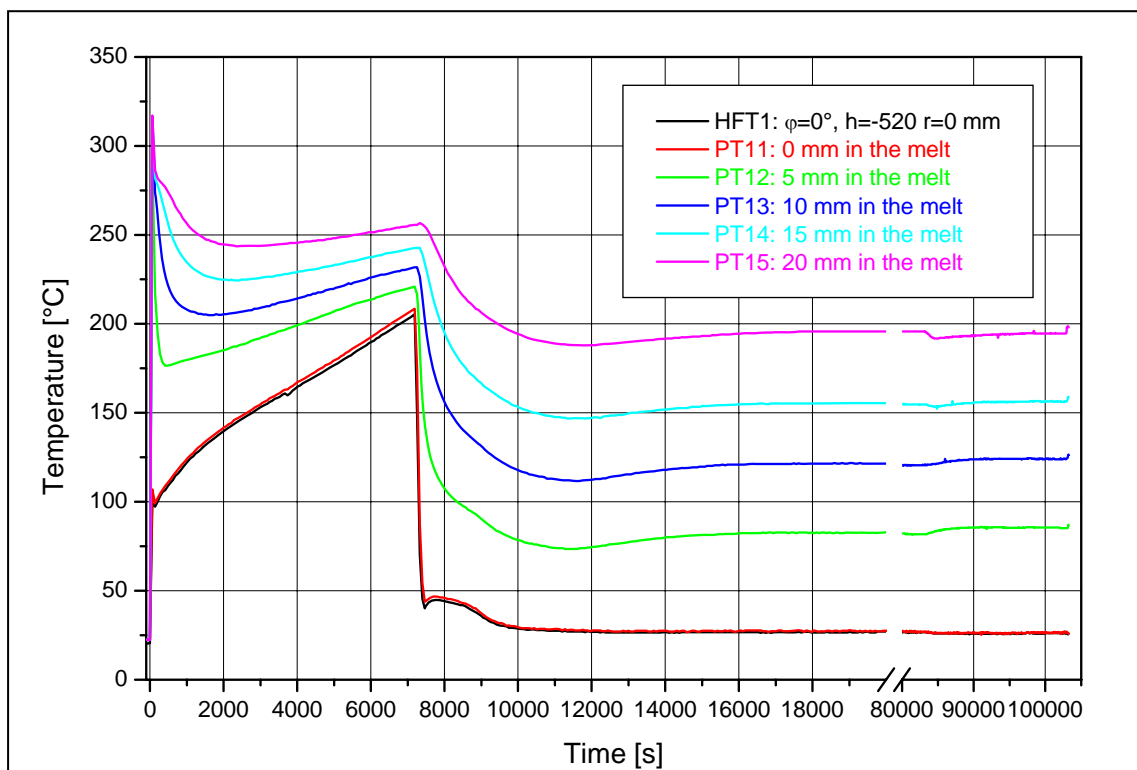


Figure C- 30: Plug and heat flux sensor temperatures in LIVE-L3, $\phi = 0^\circ$, $h = -520$ mm, $r = 0$ mm

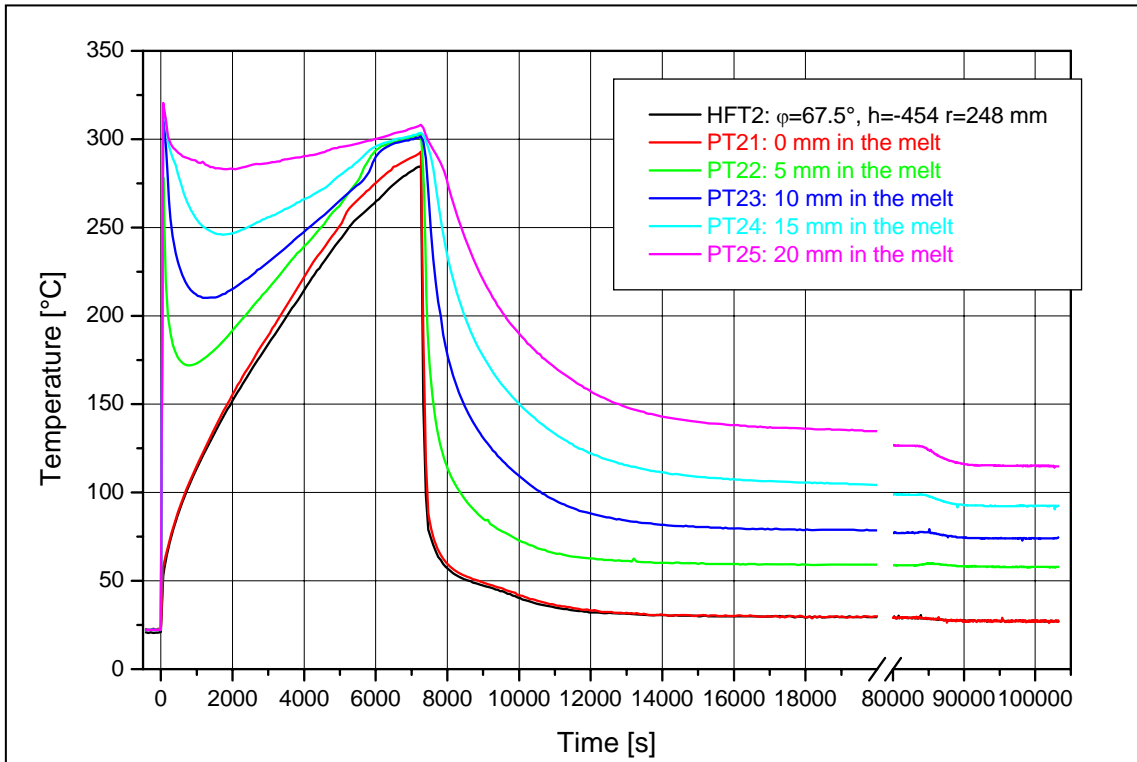


Figure C- 31: Plug and heat flux sensor temperatures in LIVE-L3, $\phi = 67.5^\circ$, $h = -454$ mm, $r = 248$ mm

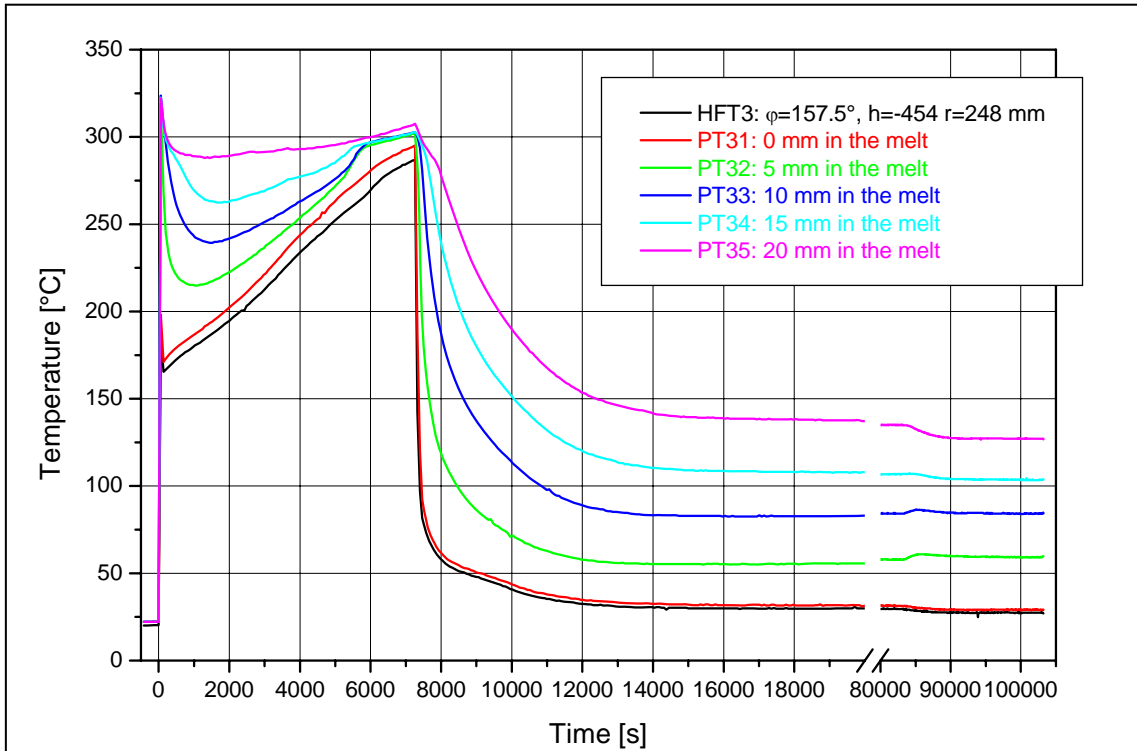


Figure C- 32: Plug and heat flux sensor temperatures in LIVE-L3, $\phi = 157.5^\circ$, $h = -454$ mm, $r = 248$ mm

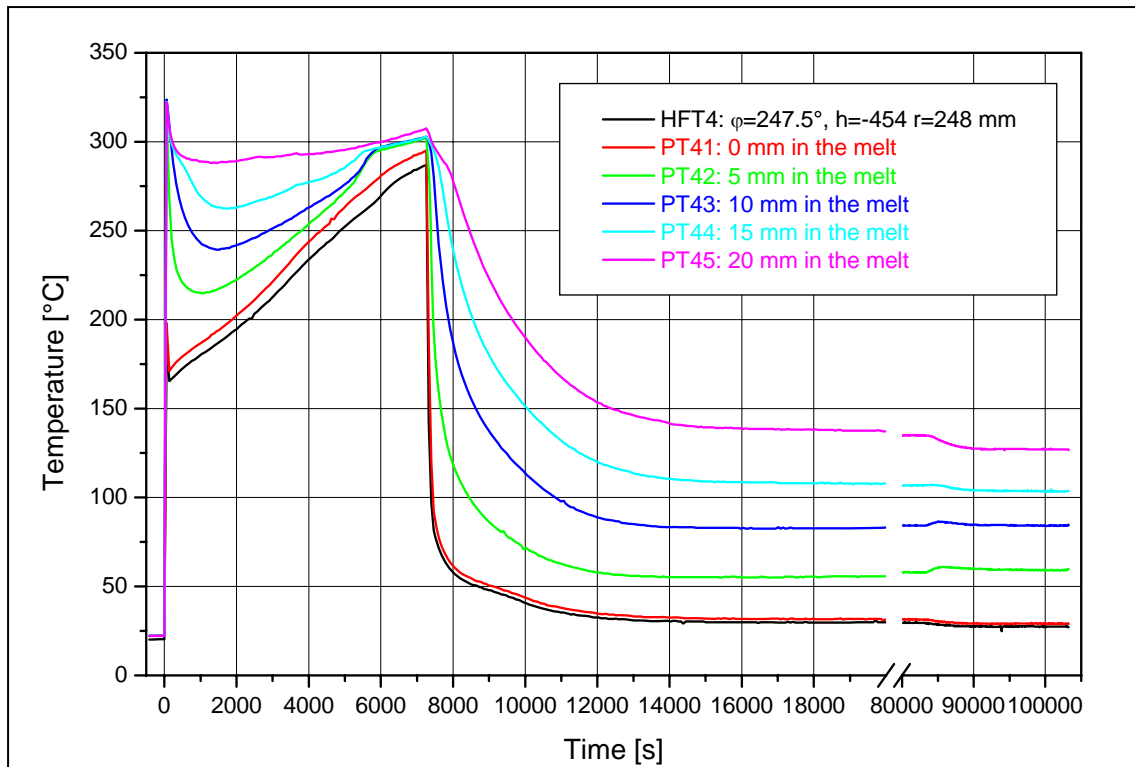


Figure C- 33: Plug and heat flux sensor temperatures in LIVE-L3, $\phi = 247.5^\circ$, $h = -454$ mm, $r = 248$ mm

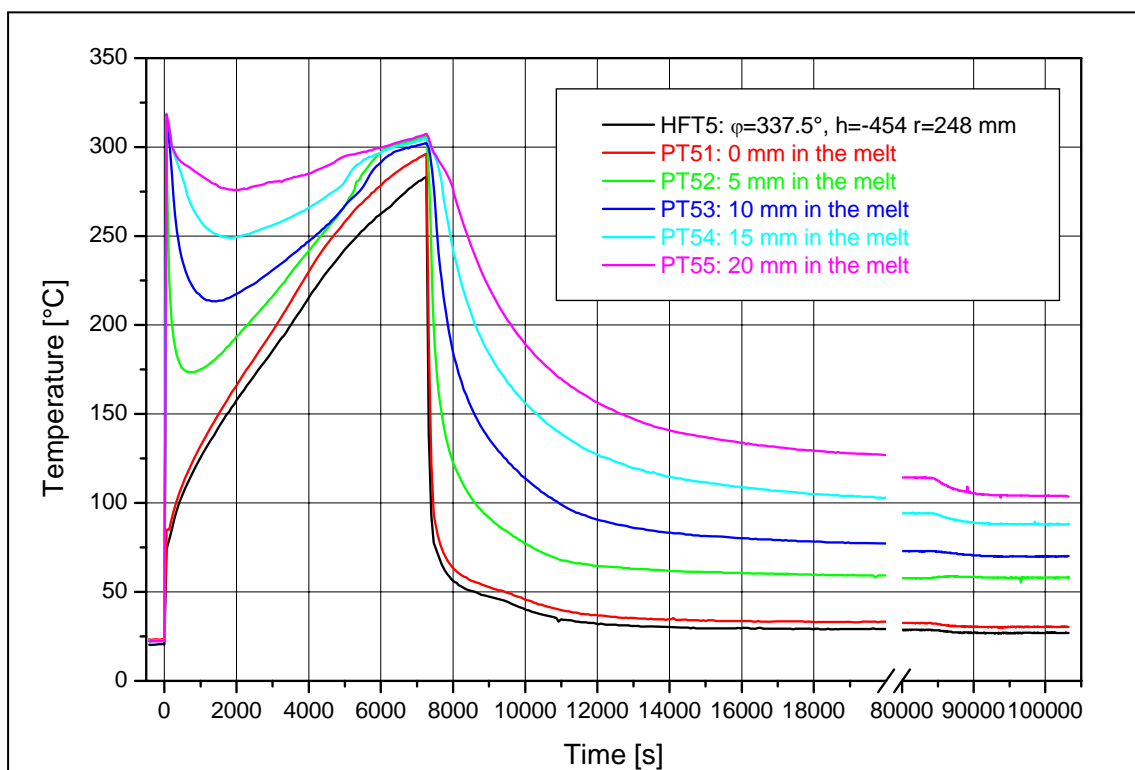


Figure C- 34: Plug and heat flux sensor temperatures in LIVE-L3, $\phi = 337.5^\circ$, $h = -454$ mm, $r = 248$ mm

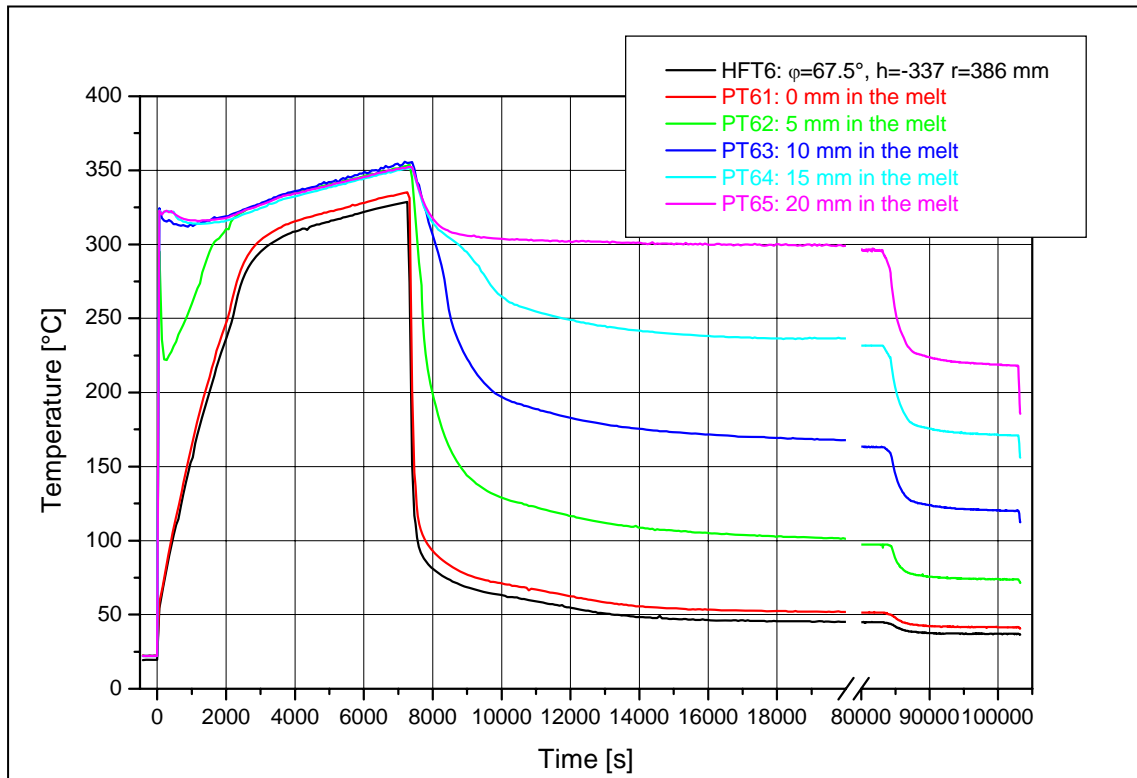


Figure C- 35: Plug and heat flux sensor temperatures in LIVE-L3, $\phi = 67.5^\circ$, $h = 337$ mm, $r = 386$ mm

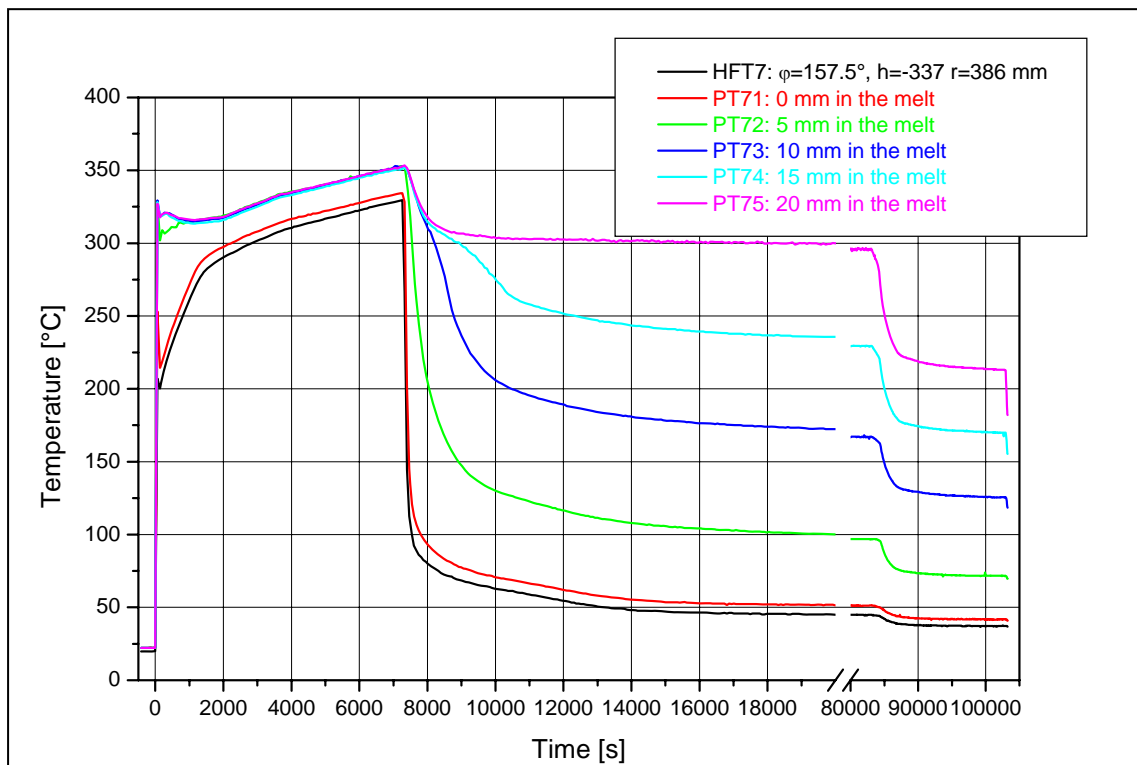


Figure C- 36: Plug and heat flux sensor temperatures in LIVE-L3, $\phi = 157.5^\circ$, $h = 337$ mm, $r = 386$ mm

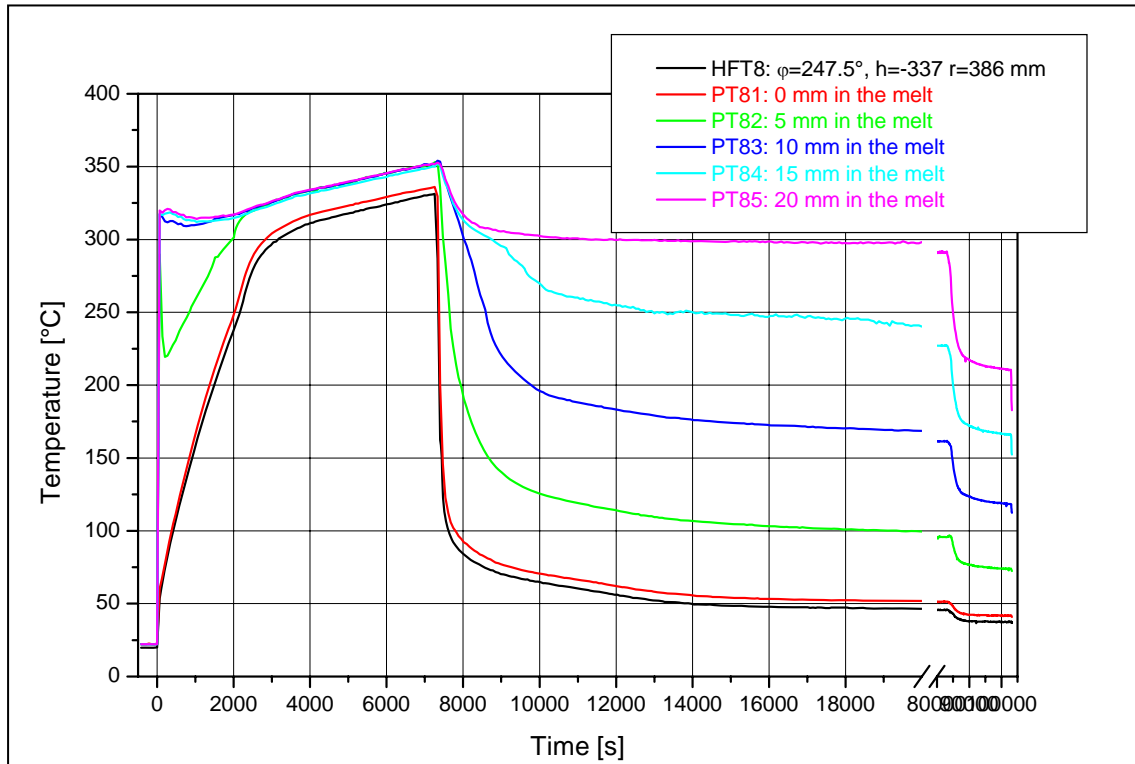


Figure C- 37: Plug and heat flux sensor temperatures in LIVE-L3, $\phi = 247.5^\circ$, $h = 337$ mm,
 $r = 386$ mm

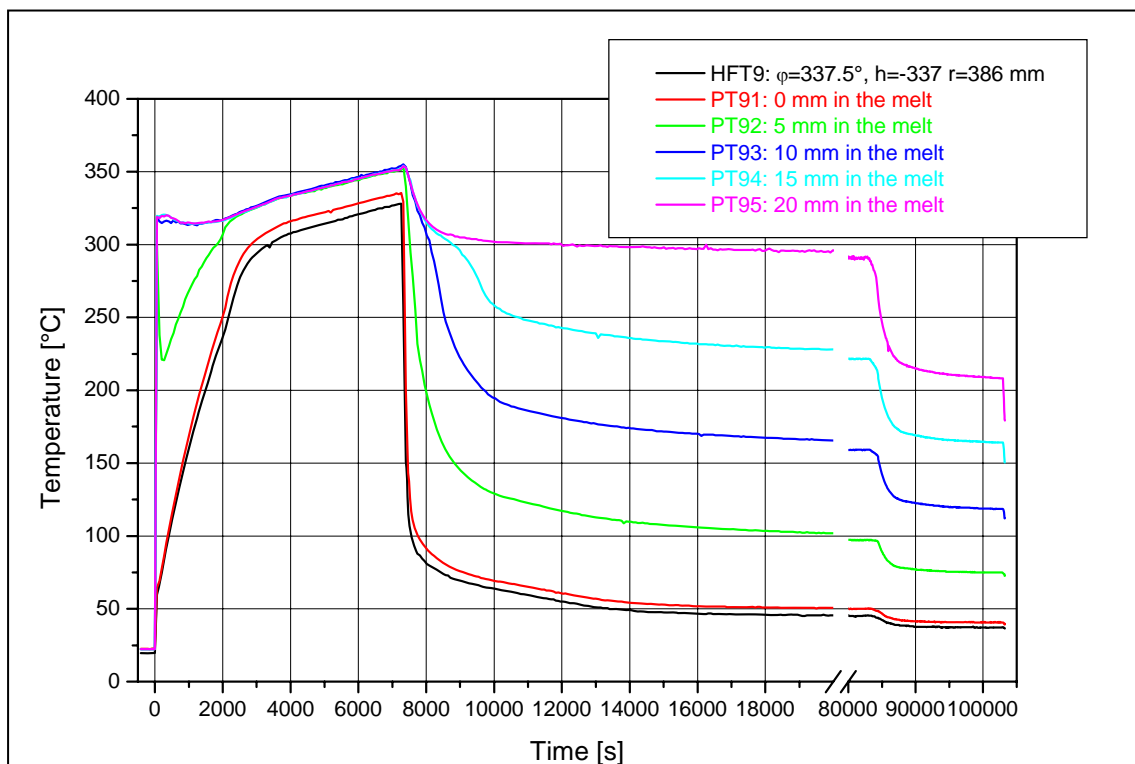


Figure C- 38: Plug and heat flux sensor temperatures in LIVE-L3, $\phi = 337.5^\circ$, $h = 337$ mm,
 $r = 386$ mm

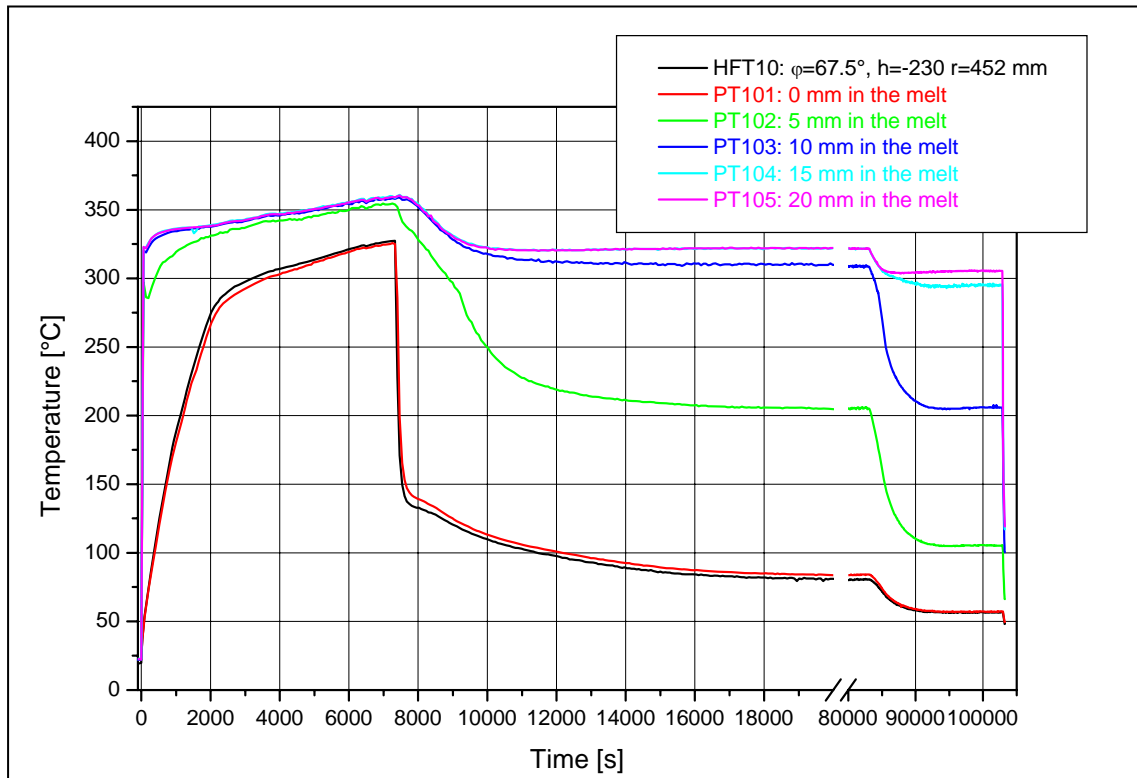


Figure C- 39: Plug and heat flux sensor temperatures in LIVE-L3, $\phi = 67.5^\circ$, $h = 230$ mm, $r = 452$ mm

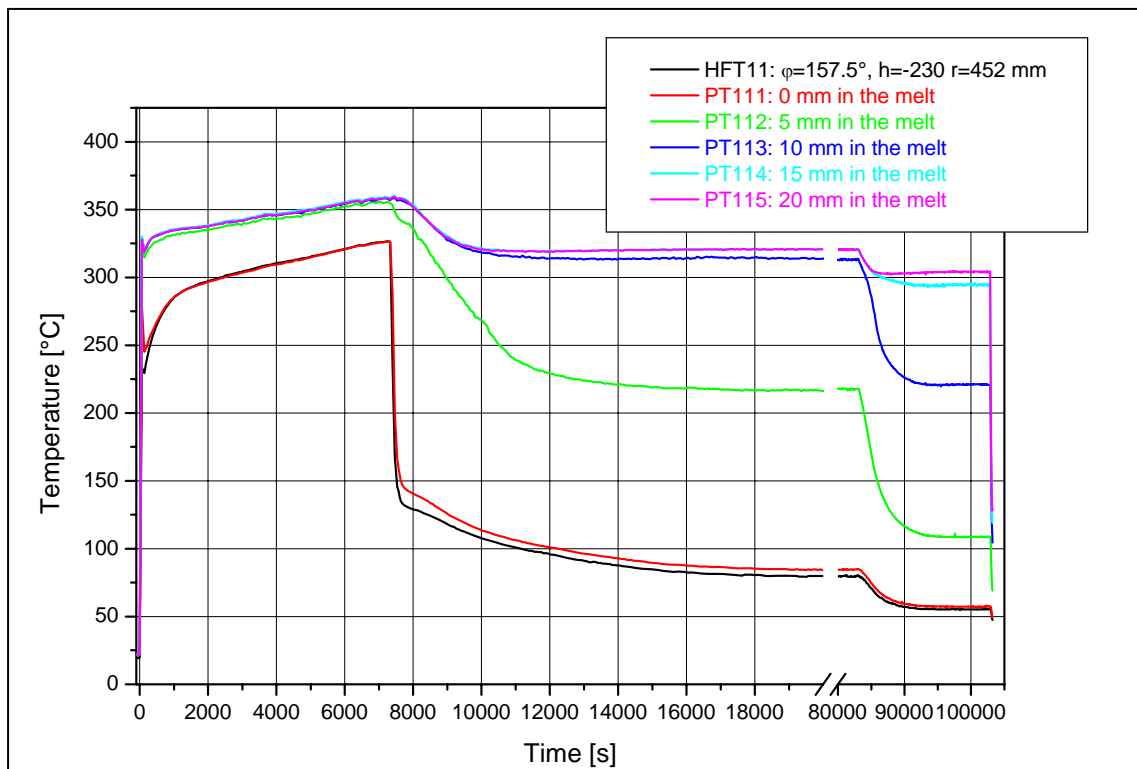


Figure C- 40: Plug and heat flux sensor temperatures in LIVE-L3, $\phi = 157.5^\circ$, $h = 230$ mm, $r = 452$ mm

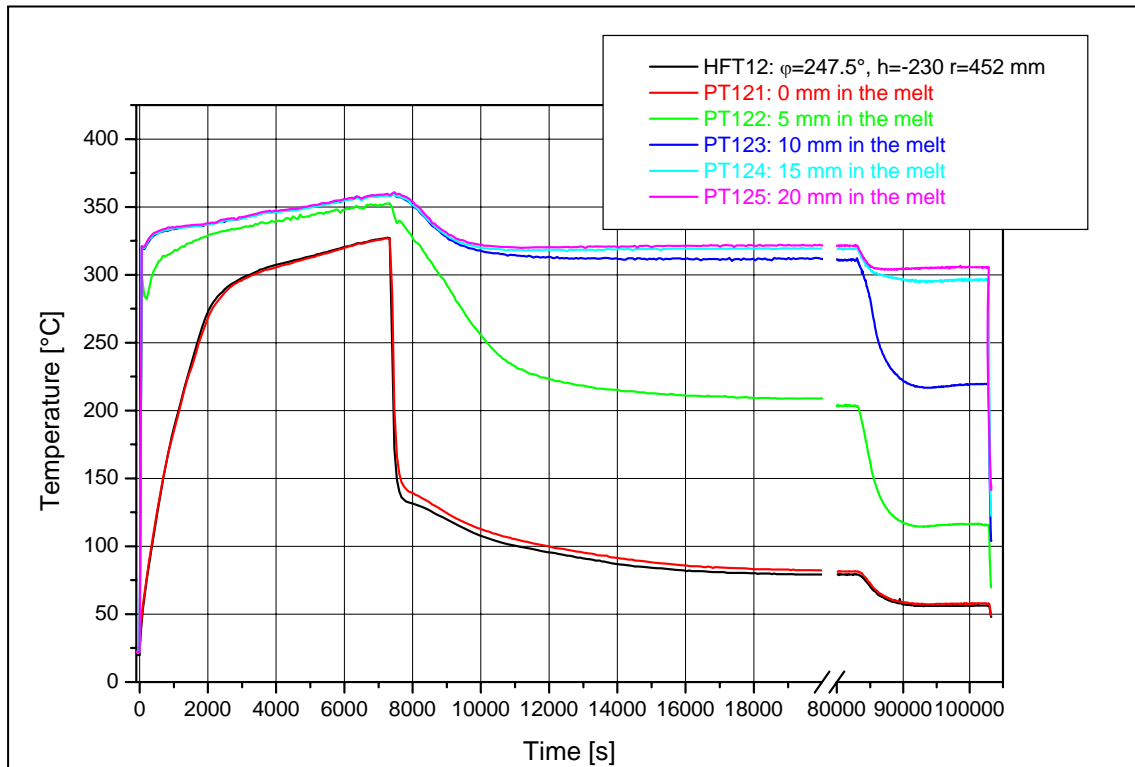


Figure C- 41: Plug and heat flux sensor temperatures in LIVE-L3, $\phi = 247.5^\circ$, $h = 230$ mm, $r = 452$ mm

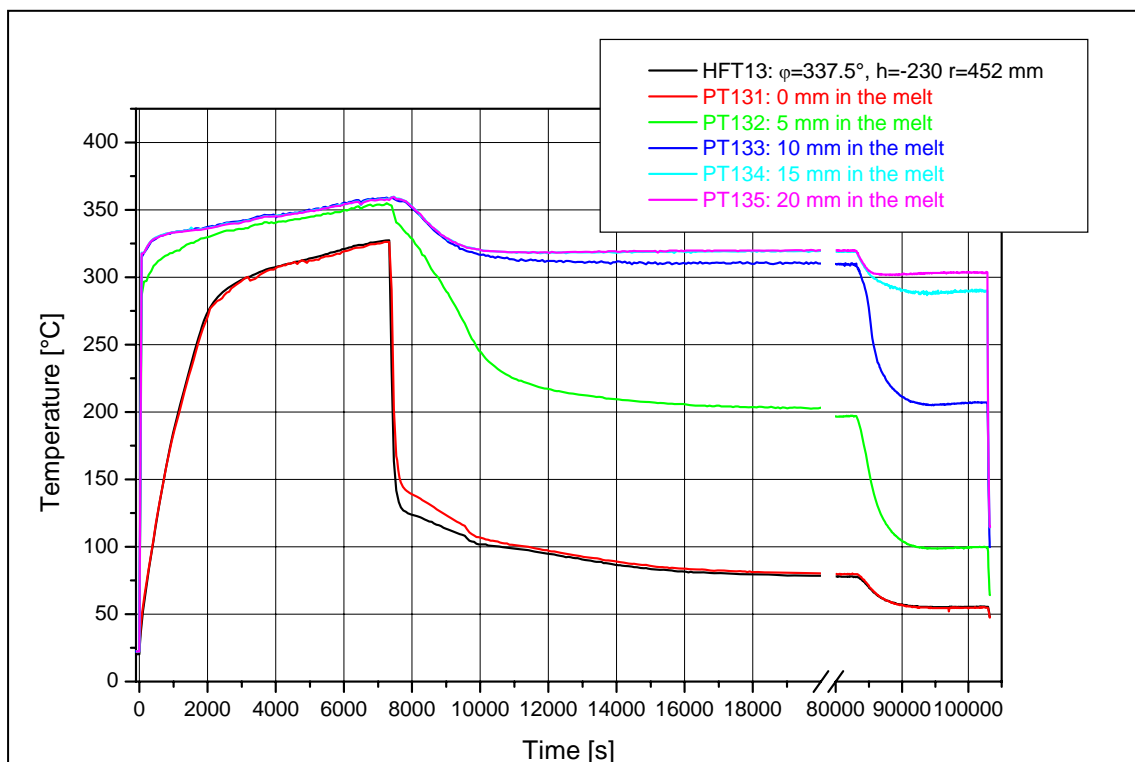


Figure C- 42: Plug and heat flux sensor temperatures in LIVE-L3, $\phi = 337.5^\circ$, $h = 230$ mm, $r = 452$ mm

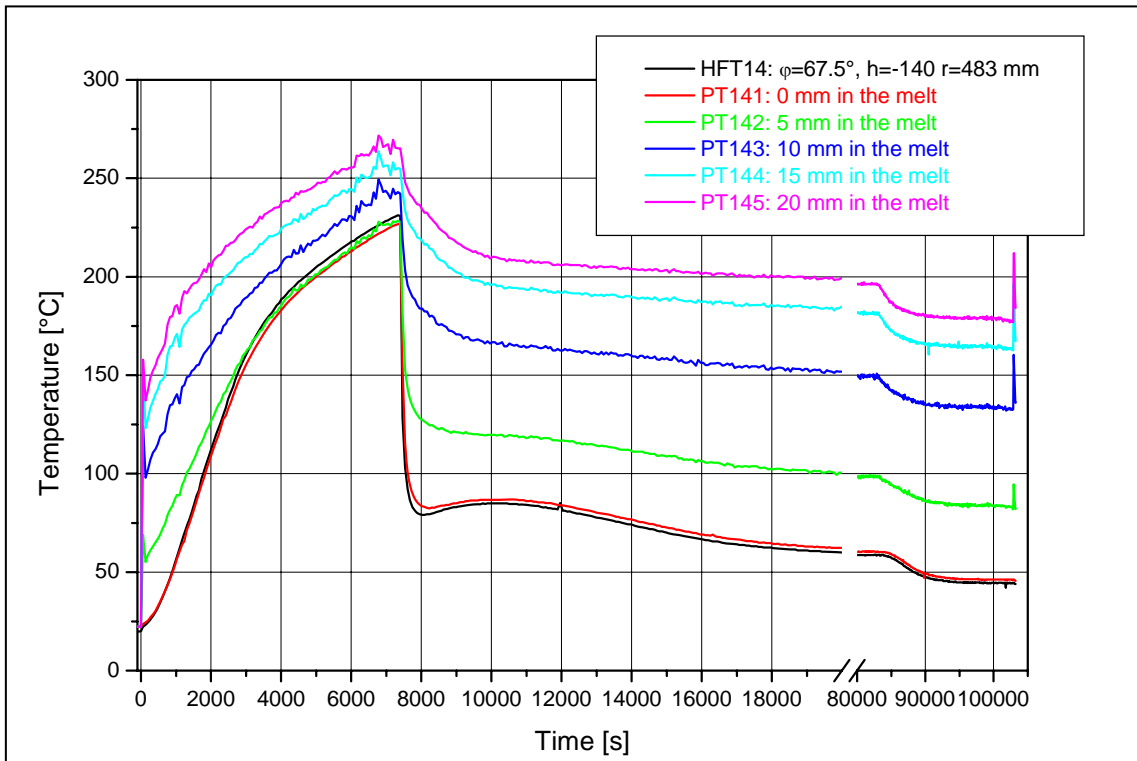


Figure C- 43: Plug and heat flux sensor temperatures in LIVE-L3, $\phi = 67.5^\circ$, $h = 140$ mm, $r = 483$ mm

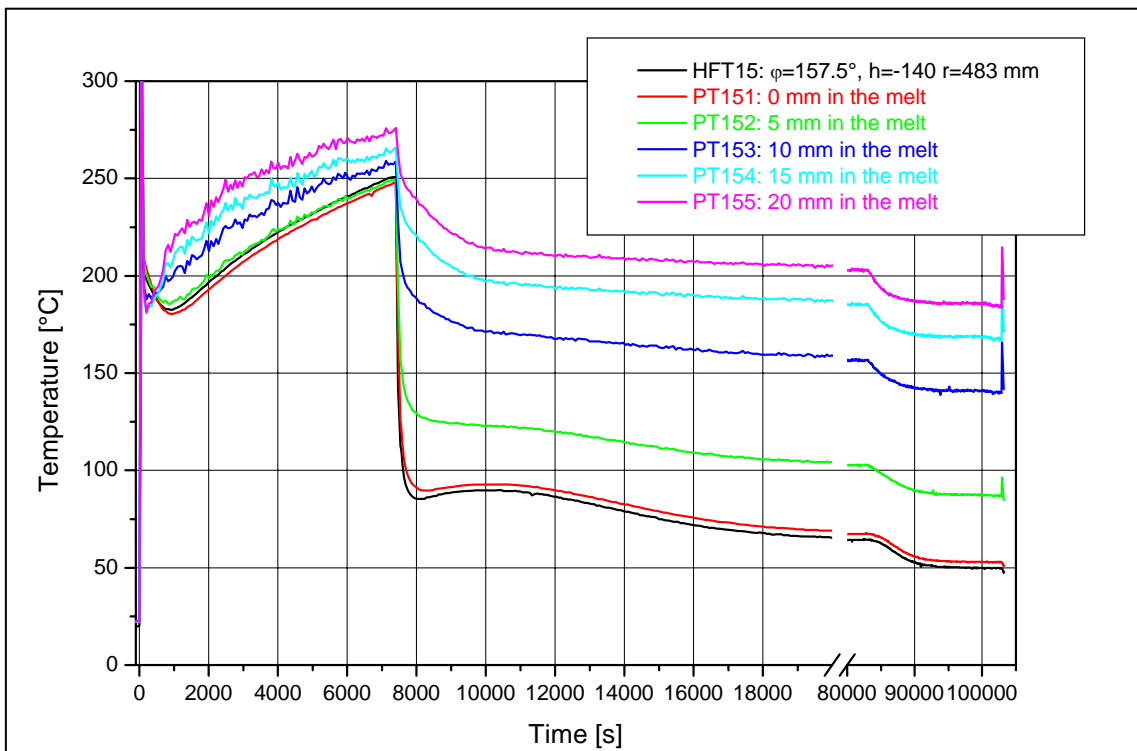


Figure C- 44: Plug and heat flux sensor temperatures in LIVE-L3, $\phi = 157.5^\circ$, $h = 140$ mm, $r = 483$ mm

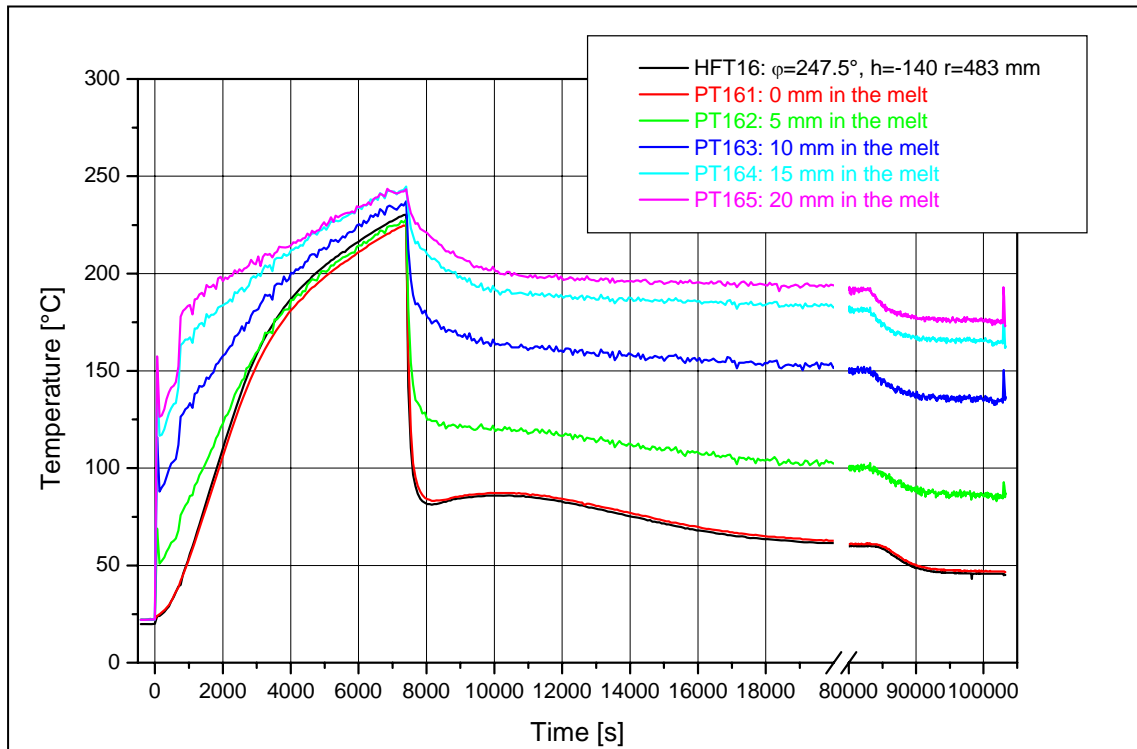


Figure C- 45: Plug and heat flux sensor temperatures in LIVE-L3, $\phi = 247.5^\circ$, $h = 140$ mm, $r = 483$ mm

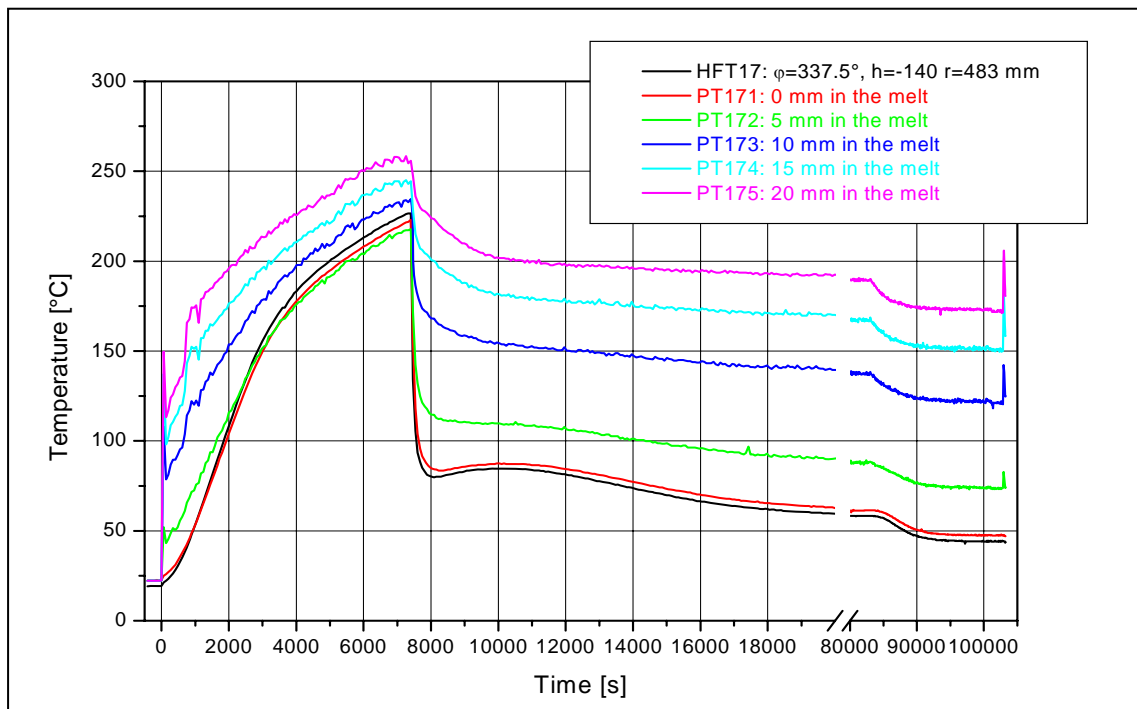


Figure C- 46: Plug and heat flux sensor temperatures in LIVE-L3, $\phi = 337.5^\circ$, $h = 140$ mm, $r = 483$ mm

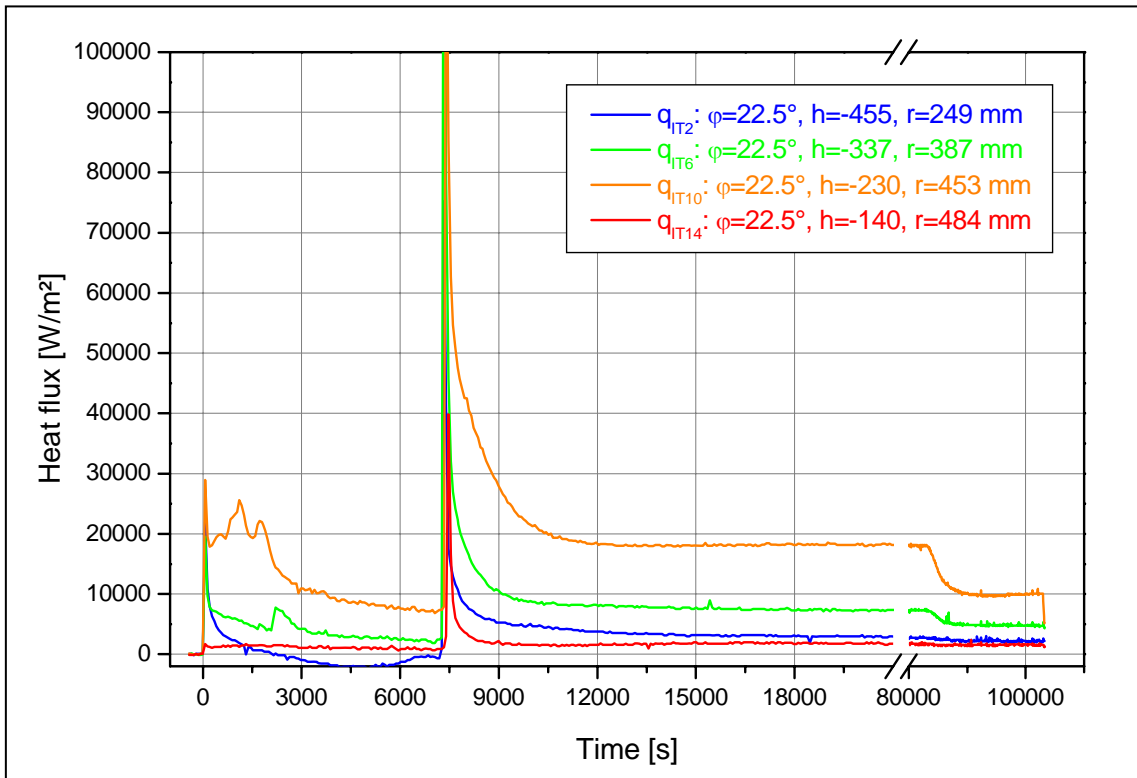


Figure C- 47: Heat flux values calculated with IT/OT thermocouples along the meridian at 22.5° in LIVE-L3

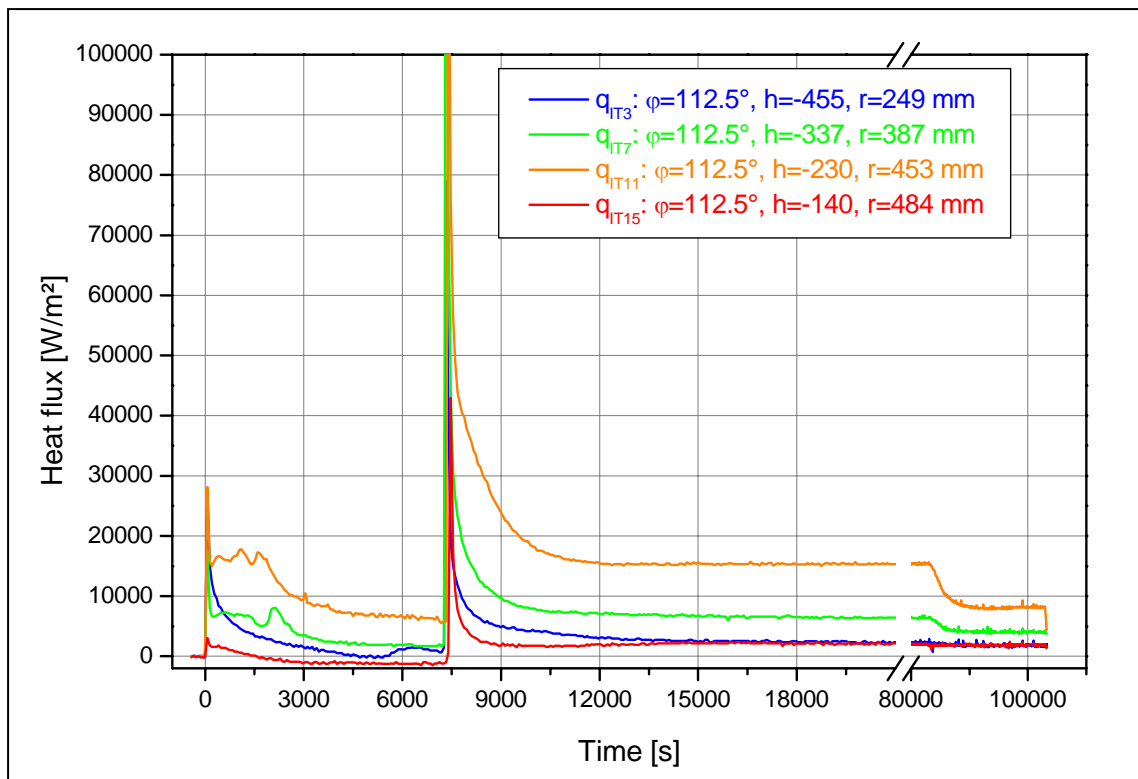


Figure C- 48: Heat flux values calculated with IT/OT thermocouples along the meridian at 112.5° in LIVE-L3

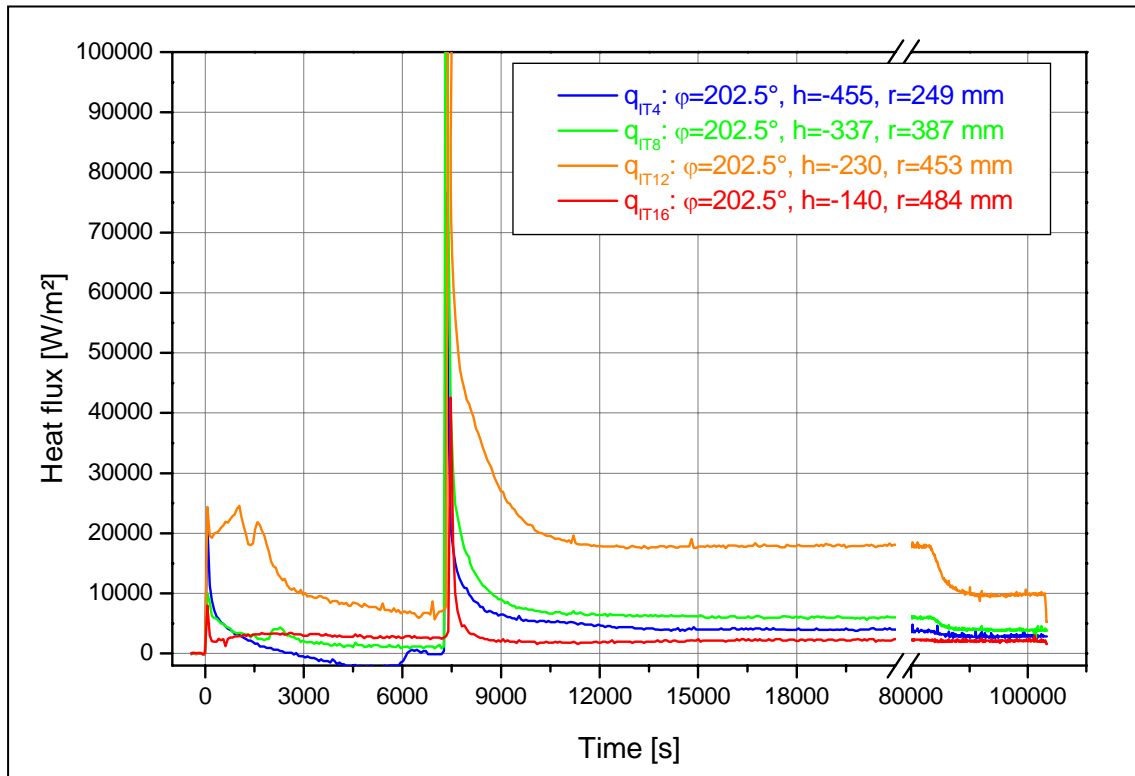


Figure C- 49: Heat flux values calculated with IT/OT thermocouples along the meridian at 202.5° in LIVE-L3

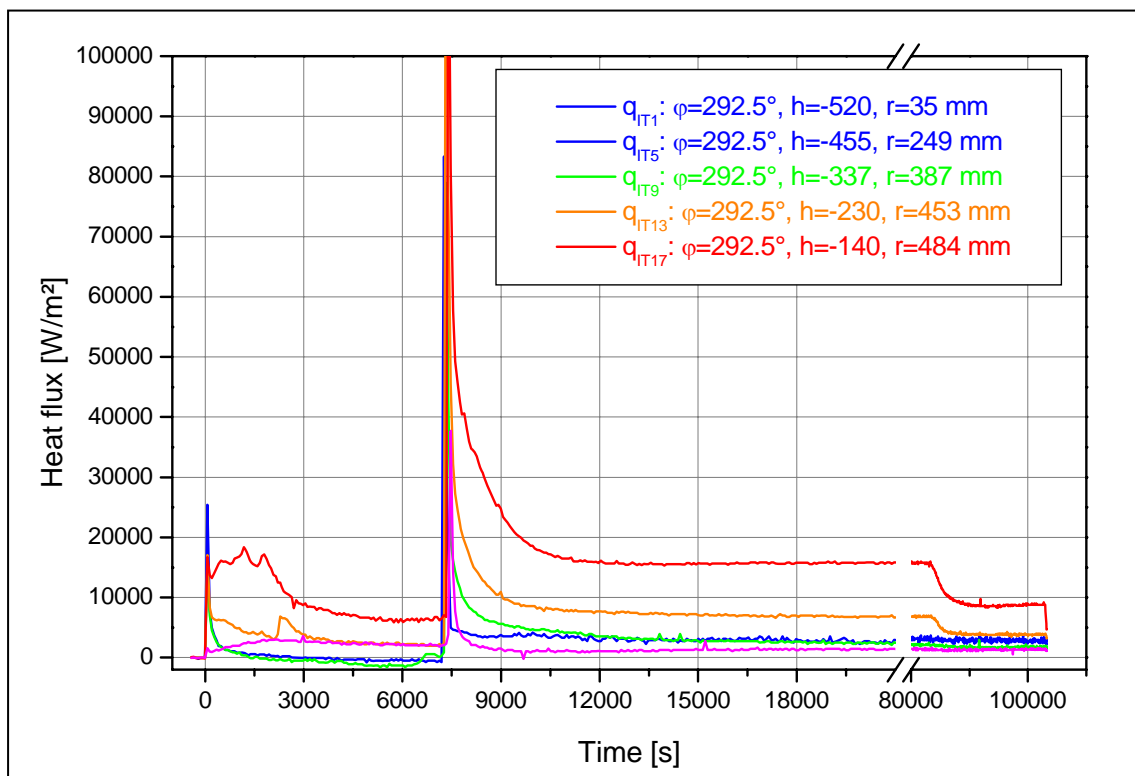


Figure C- 50: Heat flux values calculated with IT/OT thermocouples along the meridian at 292.5° in LIVE-L3

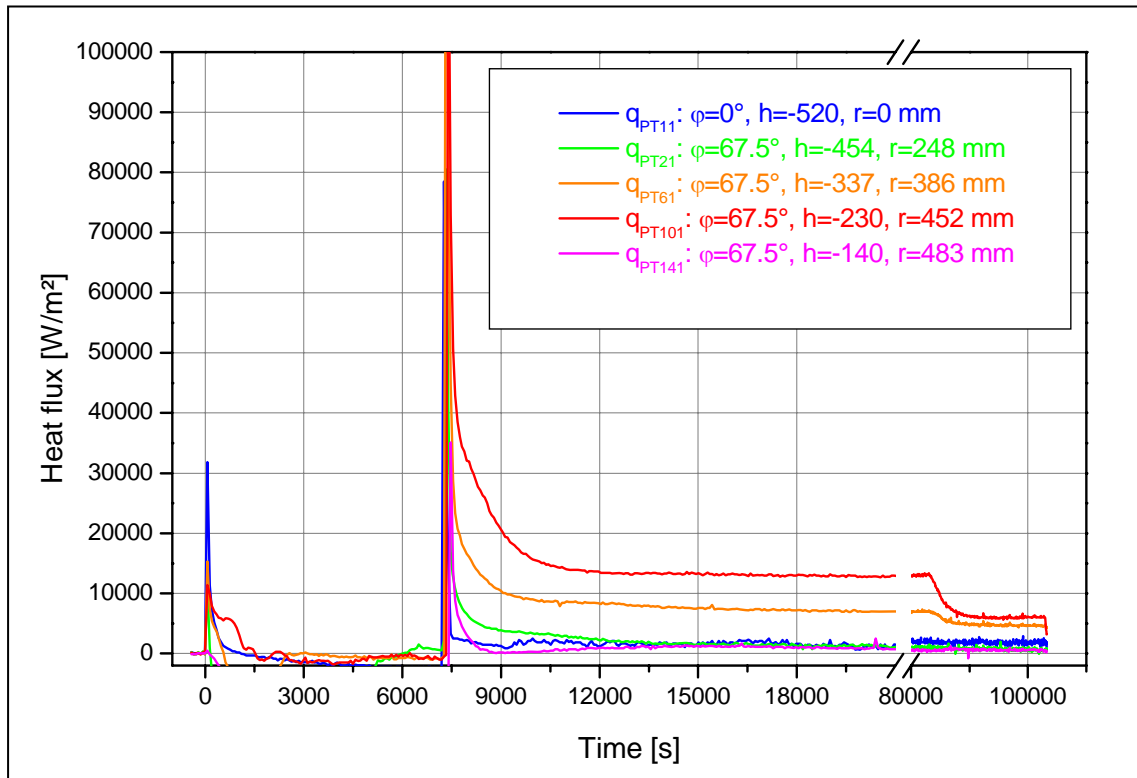


Figure C- 51: Heat flux values calculated with PT/OT thermocouples along the meridian at 67.5° in LIVE-L3

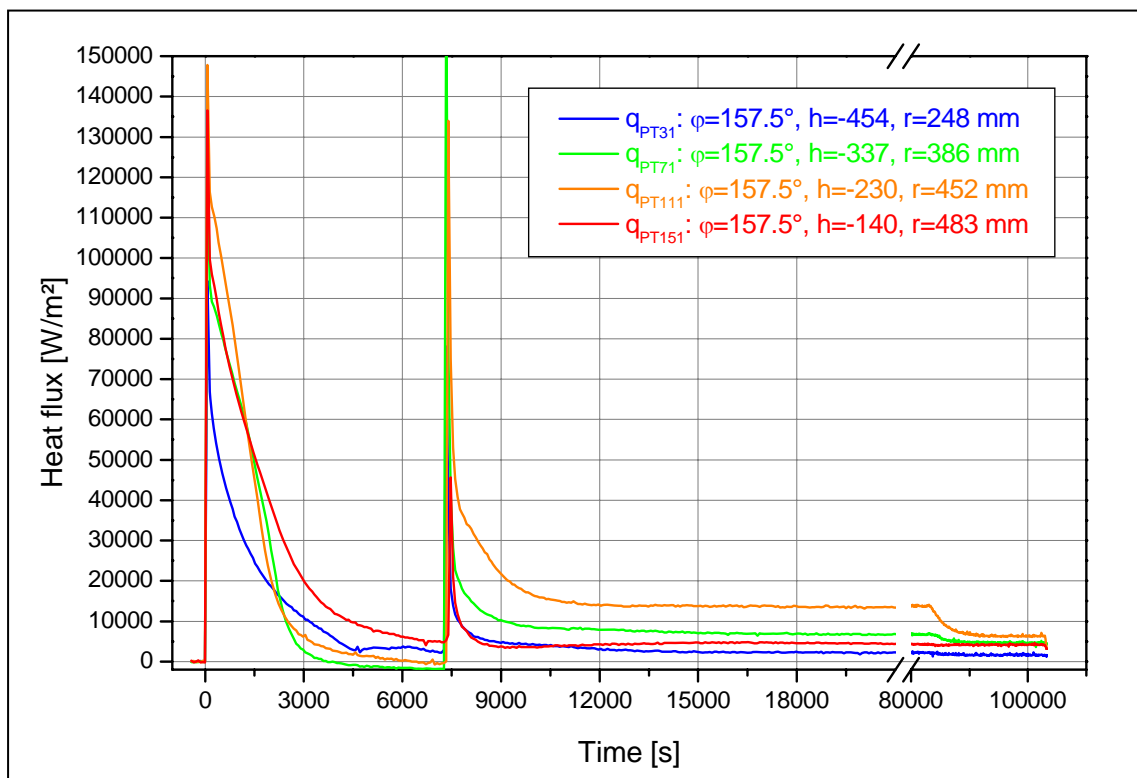


Figure C- 52: Heat flux values calculated with PT/OT thermocouples along the meridian at 157.5° in LIVE-L3

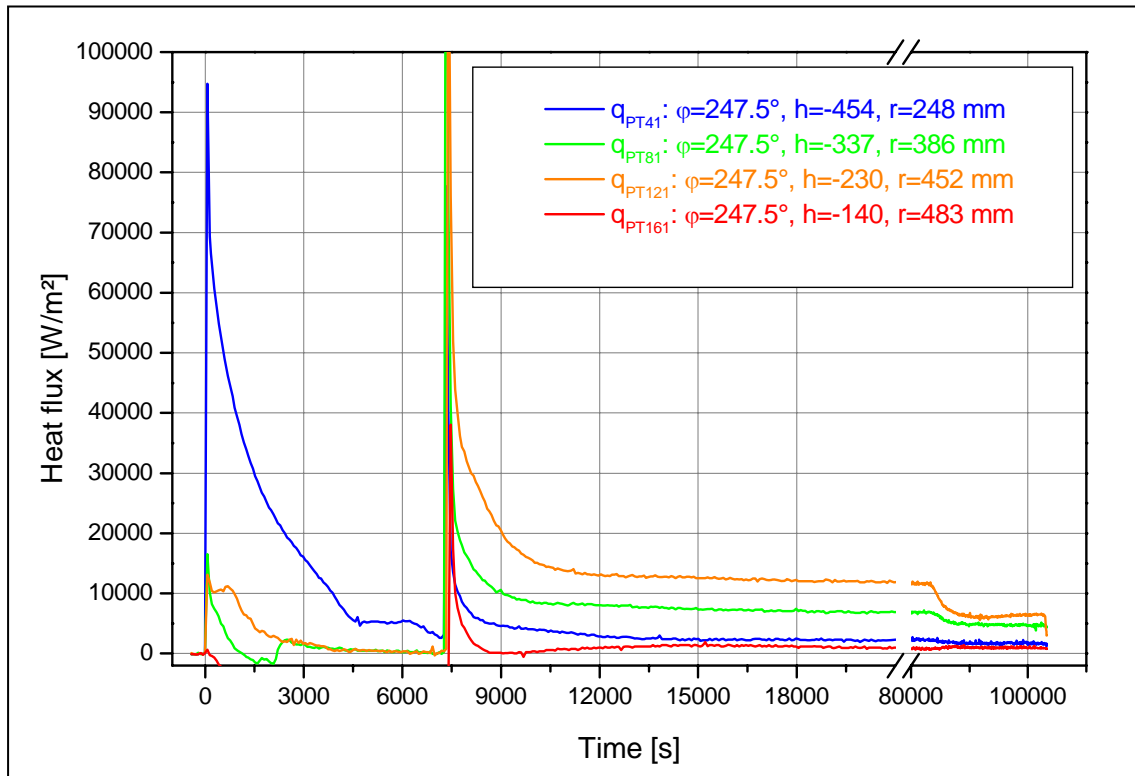


Figure C- 53: Heat flux values calculated with PT/OT thermocouples along the meridian at 247.5° in LIVE-L3

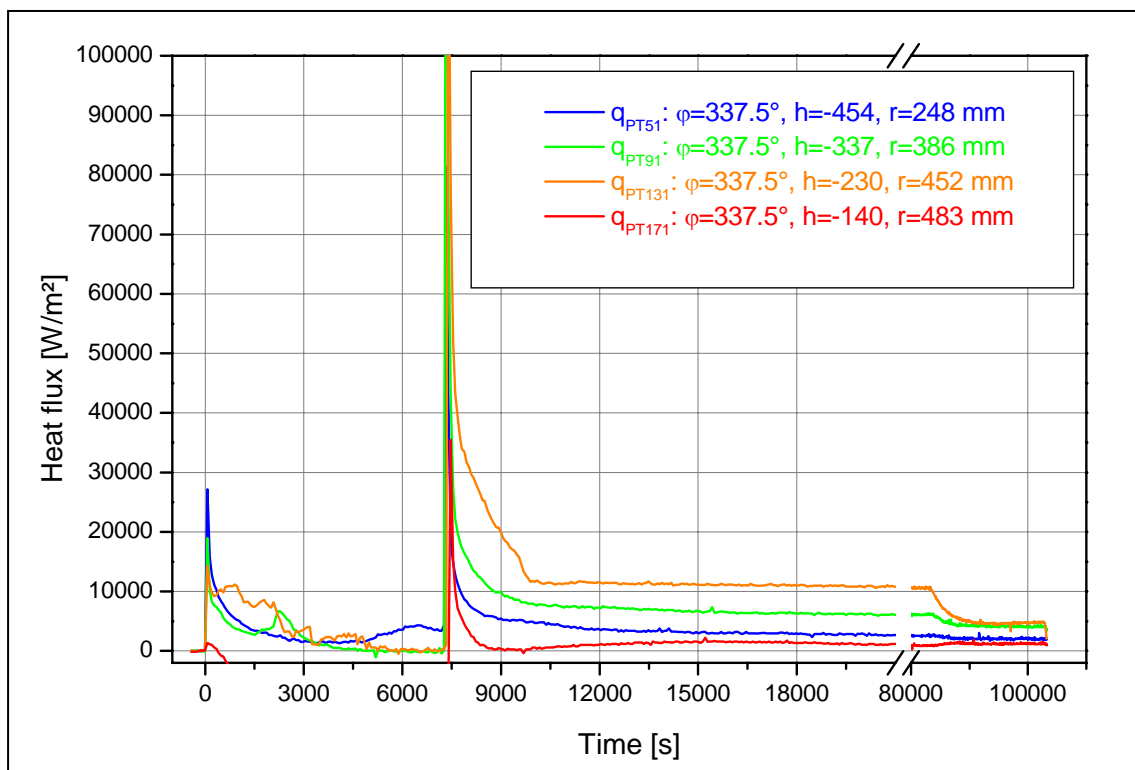


Figure C- 54: Heat flux values calculated with PT/OT thermocouples along the meridian at 337.5° in LIVE-L3

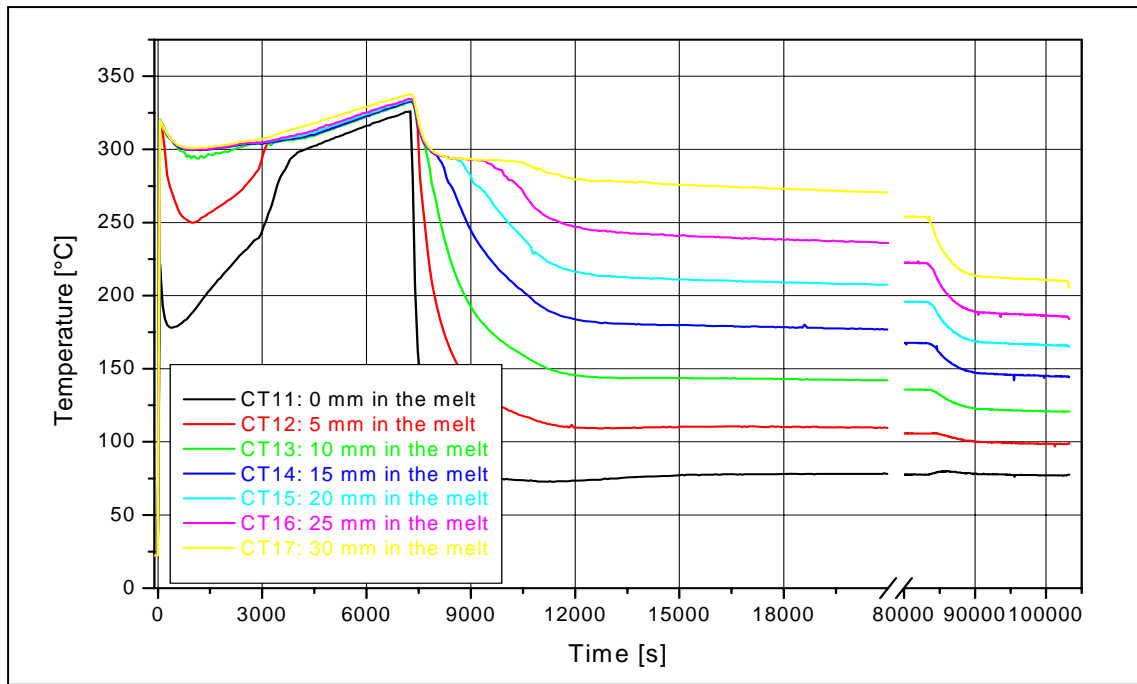


Figure C- 55: Temperature measurements of the thermocouple tree CT1 in LIVE-L3, $\varphi = 35^\circ$, $h = -420.4$ mm, $r = 299$ mm

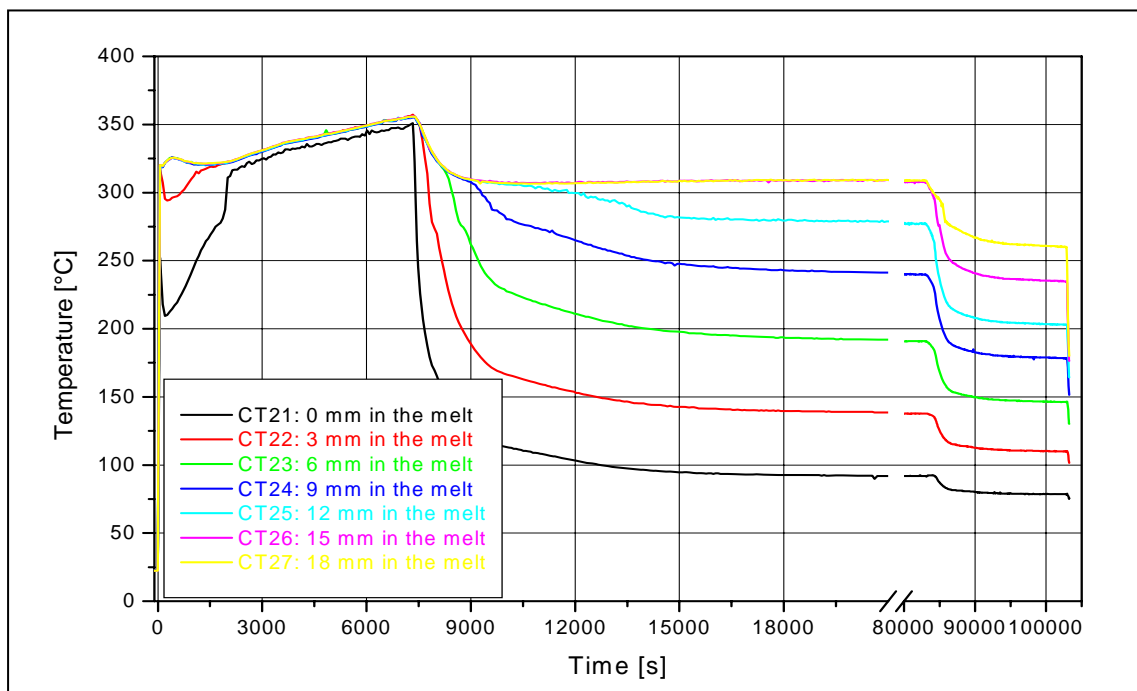


Figure C- 56: Temperature measurements of the thermocouple tree CT2 in LIVE-L3, $\varphi = 35^\circ$, $h = -320.4$ mm, $r = 398$ mm

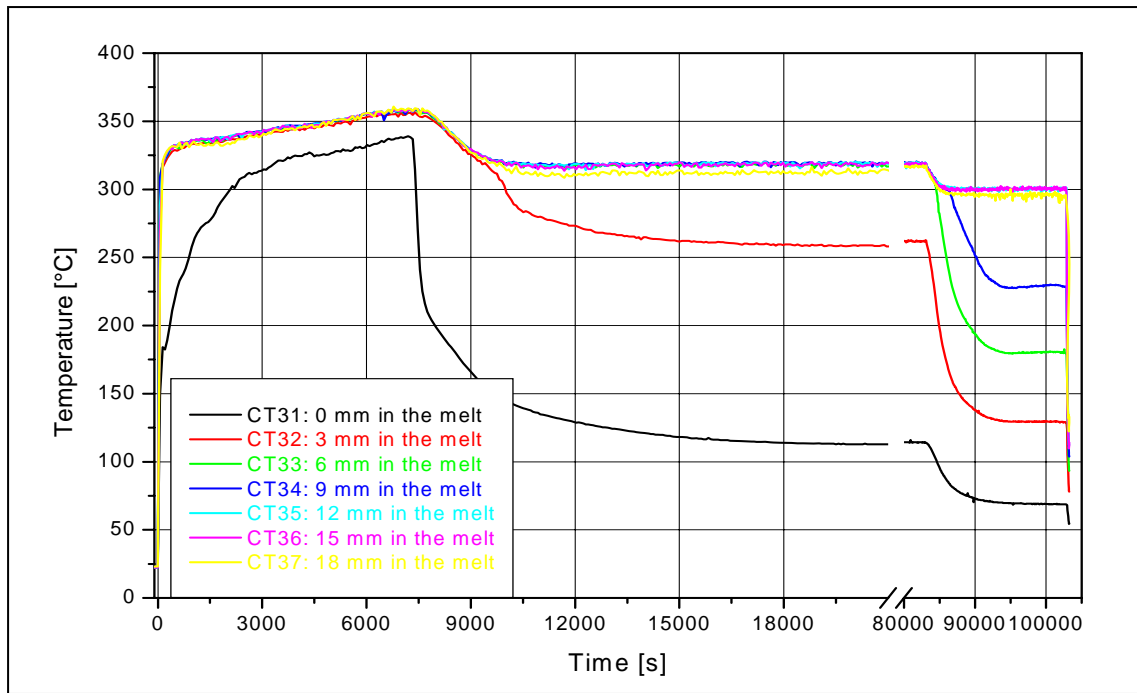


Figure C- 57: Temperature measurements of the thermocouple tree CT3 in LIVE-L3, $\varphi = 35^\circ$,
 $h = -220.4$ mm, $r = 456$ mm

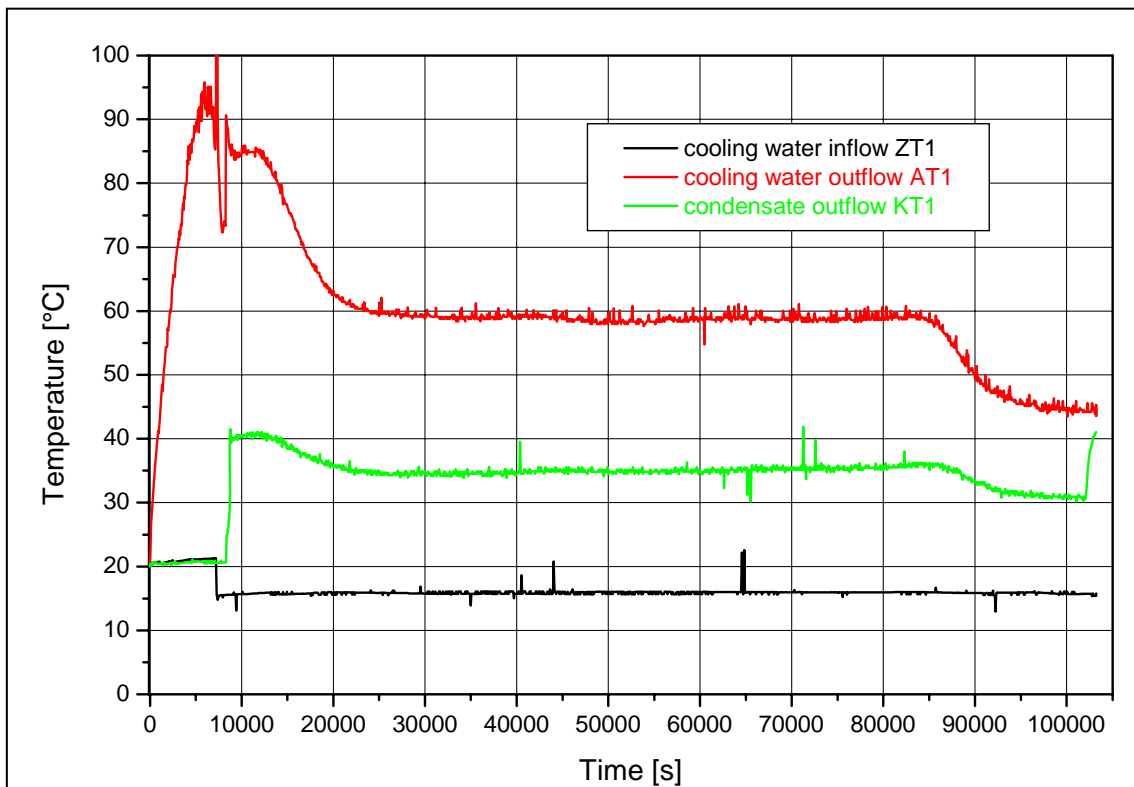


Figure C- 58: Cooling water temperatures in LIVE-L3